ADVANCED STEEL CONSTRUCTION

An International Journal

Volume 18 Number 1

March 2022

CONTENTS

Technical Papers

Website: *http://www.hkisc.org*
ISSN 1816-112X
Science Citation Index Expanded, Materials Science Citation Index and ISI Alerting
Cover: Steel structures in Stanley, Hong Kong. Photo@ Liu Yao-Peng
e-copy of IJASC is free to download at "www.ascjournal.com" in internet and mobile apps.

ADVANCED STEEL CONSTRUCTION

VOL.18, NO.1 (2022)

ADVANCED STEEL CONSTRUCTION

an International Journal

ISSN 1816-112X

Volume 18 Number 1 *March 2022*

ISSN 1816-112X

Science Citation Index Expanded, Materials Science Citation Index and ISI Alerting

Advanced Steel Construction
an international journal

Cover: Steel structures in Stanley, Hong Kong. Photo@ Liu Yao-Peng
e-copy of IJASC is free to download at "www.ascjournal.com" in internet and mobile apps.

General Information
Advanced Steel Construction, an international journal

Aims and scope

The International Journal of Advanced Steel Construction provides a platform for the publication and rapid dissemination of original and up-to-date research and technological developments in steel construction, design and analysis. Scope of research papers published in this journal includes but is not limited to theoretical and experimental research on elements, assemblages, systems, material, design philosophy and codification, standards, fabrication, projects of innovative nature and computer techniques. The journal is specifically tailored to channel the exchange of technological know-how between researchers and practitioners. Contributions from all aspects related to the recent developments of advanced steel construction are welcome.

Subscription inquiries and change of address. Address all subscription inquiries and correspondence to Member Records, IJASC. Notify an address change as soon as possible. All communications should include both old and new addresses with zip codes and be accompanied by a mailing label from a recent issue. Allow six weeks for all changes to become effective.

The Hong Kong Institute of Steel Construction
HKISC
c/o Department of Civil and Environmental Engineering,
The Hong Kong Polytechnic University,
Hunghom, Kowloon, Hong Kong, China.
Tel: 852- 2766 6047 Fax: 852- 2334 6389
Email: *ceslchan@polyu.edu.hk* Website: *http://www.hkisc.org/*
ISSN 1816-112X
Science Citation Index Expanded, Materials Science Citation Index and ISI Alerting

ISSN 1816-112X

Science Citation Index Expanded, Materials Science Citation Index and ISI Alerting

Advanced Steel Construction
an international journal

VOLUME 18 NUMBER 1 March 2022

Technical Papers

Advanced Steel Construction – Vol. 18 No. 1 (2022) 425–435
DOI:10.18057/IJASC.2022.18.1.1

BUCKLING BEHAVIOR OF A WHEEL COUPLER HIGH-FORMWORK SUPPORT SYSTEM BASED ON SEMI-RIGID CONNECTION JOINTS

Jin-Feng Dong, Hai-Qing Liu and Zhong-Wei Zhao *

School of Civil Engineering, Liaoning Technical University, Fuxin 123000, China
** (Corresponding author: E-mail: zhaozhongwei@lntu.edu.cn)*

ABSTRACT

To clarify the buckling behavior of a wheel coupler high-formwork support system with a diagonal bracing, the positive and negative bending behaviors of the connection joints of the support were systematically studied through experiments. Through a parametric analysis and a finite element analysis, a precise numerical model of the connection joints of the wheel coupler was established and verified. Based on the characteristics of the semi-rigid connections, the buckling behavior of the overall structure was analyzed. The results showed that the failure modes in the positive direction were correlated with the insertion depth of the socket into the template; the greater the depth, the more likely the socket was to fracture. The failure modes in the negative direction were closely related to the insertion depth and the bending of the vertical post. An appropriate joint density was conducive to the overall stability. In the presence of a lateral constraint at the top, the greater the angle between the diagonal bracing and the horizontal plane, the better the overall stability under the same joint density. The optimal layout of the vertical diagonal bracing was a 2-span, 4-step arrangement, and the optimal angle was in the range of 30–70°. In the absence of a lateral constraint at the top, the smaller the angle between the diagonal bracing and the horizontal plane, the better the overall stability under the same joint density. The optimal angle was approximately 30° when the lift height was moderate.

ARTICLE HISTORY

Received: 5 December 2020
Revised: 21 May 2021
Accepted: 24 May 2021

KEYWORDS

Semi-rigid connection joints;
Wheel coupler high-formwork support system;
Diagonal bracing;
Buckling behavior

1. Introduction

Wheel coupler formwork supports have been widely used in construction to support the gravity load of floor slabs. However, the reliability of their mechanical behavior has not been sufficiently studied. Existing results are mostly applicable to conventional fastener-type and bowl buckle-type formwork supports [1-3], which are not widely used as external scaffolds or formwork supports. Dou et al. [4] and Chen [5] investigated and analyzed a socket-type wheel coupler formwork support, they concluded that this support can be considered an extended version of the socket-type disc-buckle formwork support. However, the design, production, and construction of such a support cannot be implemented in accordance with the construction specification employed for disc-buckle formwork supports because of the differences in terms of the structure and calculation parameters. No relevant product standards or technical specifications have been issued. We refer to the "Safety technical specification for wheel-coupler steel pipe scaffold" issued by Guangdong Province, China [6]. Therefore, further research on the behavior aspects should be conducted.

The mechanical behavior of the connection joints of formwork supports is complex because of the need for a rapid assembly during construction. The semi-rigid joints significantly influence the bearing capacity of the overall formwork support system [7-10]. There are many studies on semi-rigid joints of steel frames [11-20]. In the classic design and calculation theory of steel structures [21], the joint between a steel frame beam and a column is considered a rigid joint or a hinge joint. The calculations in this simplified method can be easily implemented. However, it cannot reflect the true stress state of the overall structure. Therefore, it is necessary to study the semi-rigid joints of wheel coupler-type steel pipe formwork support systems, because the joint is semi-rigid in theory, mainly including the influences of joint stiffness and geometrical imperfections on the overall stability.

Current studies have mostly focused on the joints of fastener-type formwork supports [22, 23]. The results have shown that the ultimate bearing capacity of fastener-type formwork systems increases nonlinearly with the increase in the semi-rigid value. For a bowl buckle-type joint, Zou et al. [24] found that a trilinear semi-rigid joint model provides a reliable accuracy and is suitable for a refined numerical simulation of bowl buckle-type formwork supports. The bearing capacity increases with the increase in the initial bending stiffness and presents a three-stage variation. Compared with the joint stiffness of the conventional fastener-type steel pipe formwork support, the stiffness range of the connection joints of a wheel coupler formwork support varies [25], and the spacing and lift height of the vertical post significantly influence the overall stability. Yu et al. [26] and Chu et al. [27] integrated the lowest eigenmode with a column out-of-straightness magnitude of 1/1000 for the height of the scaffold units into the model. Sevim et al. [28] investigated the effects of truss height and number of tie bars on the structural behavior of suspended scaffolding systems through experiments, the results showed that a scaffolding system with 60 cm-high truss and two tie bars presents optimal safety and cost-savings. Liu et al. [29] presented a mortise–tenon steel-tube scaffold, the influencing laws of storey height, vertical member interval and other factors were determined through parameter analysis, research results provide important references for future in-depth studies and engineering applications of the mortise–tenon steel-tube scaffold.

In this work, the connection joints of a wheel coupler formwork support were studied through experiments and numerical analyses. The bending stiffness of the joints was obtained on the basis of the connection characteristics of semi-rigid joints. Fine connection joints were established using nonlinear spring elements, and the joint stiffness data were based on the experiment. A complete nonlinear buckling analysis and a first-mode buckling analysis were carried out on the numerical model of the wheel coupler high-formwork support system with a diagonal bracing. With this, we study the selection of the spatial layout of the diagonal bracing and the influences of the plane layout of the vertical diagonal bracing, the joint density between the diagonal bracing and the frame, and the angle between the diagonal bracing and the horizontal plane on the overall stability of the wheel coupler high-formwork support system. Thus, our study provides a reference for the practical applications of wheel coupler formwork supports.

2. Experimental research on flexural behavior of socket connections

2.1. Experimental survey

2.1.1. Geometrical size of socket connection

Fig. 1 illustrates the components of the socket connection, which comprises a socket and a template, wherein the socket is welded to the end of a horizontal bar, and the template is welded to a vertical post. The horizontal bar, vertical post, and template were made of Q235, and the socket was made of cast steel given its complex shape and material properties.

(a) A socket connection joint

(b) Horizontal bar

(c) Socket connection zone

Fig. 1 Formwork support connection and composition diagram

Fig. 2 shows the geometrical dimensions of the socket connection of the wheel coupler formwork support adopted in our actual project. The outer diameter of the horizontal bar and the vertical post was set to 48 mm, and the thickness was set to 3.0 mm. Figs. 2(a) and 2(b) show the detailed geometrical dimensions of the socket. The thickness was set to 7 mm, and the size of the insertion hole on the template was 14 mm × 25 mm, as shown in Fig. 2(c).

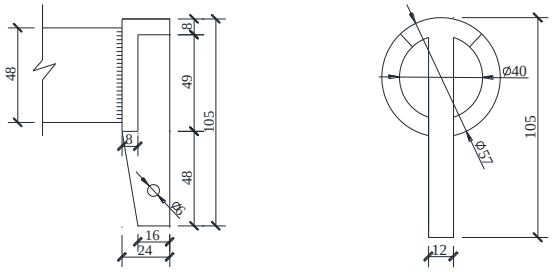

(a) Side view of the socket (b) Front view of the socket

(c) Template

Fig. 2 Geometrical dimensions of connection joints (all the dimensions in the figure are in mm).

The experimental specimen material was obtained from a construction site. The sizes of each group of experimental connection joints were different because of manufacturing errors. Fig. 3 shows the schematic of the socket insertion state.

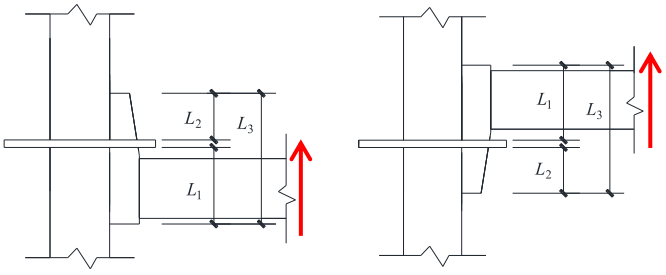

(a) Positive direction (b) Negative direction

Fig. 3 Schematic of the socket insertion state

Table 1 lists the detailed dimensions of the specimens. The letters prefixed to the specimen number indicate the loading direction, with "P'' representing a positive loading direction and "N" representing a negative loading direction. The positive loading results in a bending on the upper side of the horizontal bar, whereas the negative loading results in a compression.

Table 1
Detailed dimensions of the specimens

Specimen No.	L_1/mm	L_2/mm	L_3/mm
P-SJ1	66	30	103.0
P-SJ2	72	25	104.0
P-SJ3	73	23	103.0
P-SJ4	78	19	104.0
N-SJ1	71	26	103.0
N-SJ2	68	28	102.5
N-SJ3	62	34	104.0
N-SJ4	63	32	102.0

2.1.2. Experimental equipment and arrangement of the measuring points

Four 100 mm displacement transducers and one 200 mm displacement transducer were used to measure the displacement of the horizontal bar and the vertical post during the loading process. The distance between the upper and lower measuring points of the vertical post and the center of the joint was set to 150 mm, which were recorded as measuring point 1 and measuring point 2. The distances between the measuring point at the proximal end of the horizontal bar and the center of the joint were 85 mm and 185 mm, respectively, which were recorded as measuring points 3 and 4. The distance between the loading point at the far end of the horizontal bar and the joint center was set to 300 mm, which were recorded as measuring point 5 and used for data calibration. Fig. 4 shows the specific arrangement of the measuring points. ①~④ represent flange components.

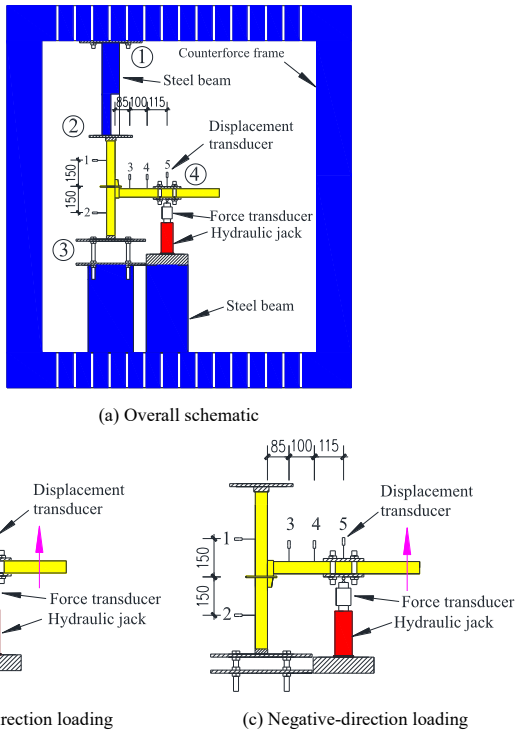

(a) Overall schematic

(b) Positive-direction loading (c) Negative-direction loading

Fig. 4 Experimental equipment and arrangement of the measuring points

2.1.3. Measurement method of joint rotational stiffness

Qian [30] employed the bending moment–rotation angle curve to measure the relevant parameters of disc-buckle type and bowl buckle-type formwork support joints. In this approach, the joint bending moment is taken as the product of the vertically concentrated load at the loading point of the horizontal bar and the distance from the loading point to the joint center, which can be calculated using Eq. (1), where F represents the vertically concentrated load at the loading point of the horizontal bar, and L represents the distance from the loading point to the joint center, which can be taken as 300 mm. The relative rotation angle of the joint can be obtained using Eq. (2). Here, Δ_1, Δ_2, Δ_3, and

Δ_4 respectively represent the displacement transducer reading data at measuring points 1, 2, 3, and 4, d_{3-4} represents the straight-line distance between the measuring points 3 and 4, d_1 and d_2 represent the distances from the measuring points 1 and 2 to the joint center, respectively, and θ_1 represents the rotation angle of the horizontal bar section relative to the joint. A section of the vertical post will produce a rotation angle relative to the joint, which is denoted by θ_2 and expressed in Eq. (2). After the influence of the deformation of the vertical post was compensated, the angle of the joint obtained was more accurate because the vertical post will also produce an elastic deformation during the loading process.

$$M = F \times L \tag{1}$$

$$\theta = \theta_1 - \theta_2 = \tan^{-1}\frac{\Delta_4 - \Delta_3}{d_{3-4}} - \tan^{-1}\frac{\Delta_2 - \Delta_1}{d_1 + d_2} \tag{2}$$

The bending moment–rotation angle curve of the joint was obtained by processing the data obtained from the experiment through Eqs. (1) and (2).

Fig. 5 shows the mechanical calculation model of the moment–rotation angle.

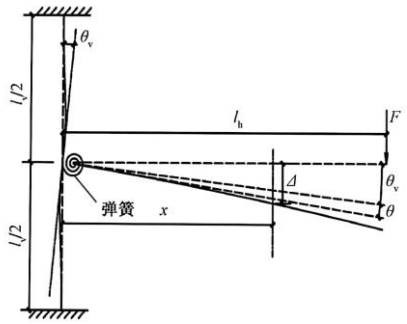

Fig. 5 Mechanical calculation model of moment–rotation angle

The vertical bending stiffness of the joint of the wheel coupler in an arbitrary stress state can be expressed as follows:

$$k = \frac{dM(\theta)}{d\theta} \tag{3}$$

The small deformation assumption is adopted to ignore the influence of component deformation on the component size. Under a vertically concentrated load, the vertical bending moment of the joint of the wheel coupler can be expressed as follows:

$$M = FL_h \tag{4}$$

Under the action of vertical bending moment, the rotation angle of the vertical pole at the joint of the wheel coupler can be expressed as follows:

$$\theta_v = \frac{ML_v}{16E_vI_v} \tag{5}$$

The spring rotation angle of the joint of the wheel coupler can be expressed as follows:

$$\theta = \frac{M}{k} \tag{6}$$

The relationship between the spring rotation angle of the joint of the wheel coupler, the vertical bending stiffness of the joint of the wheel coupler, and the vertical displacement at the measuring point is as follows:

$$(\theta_v + \theta)x + \frac{FL_hx^2}{2E_hI_h} - \frac{Fx^3}{6E_hI_h} = \Delta \tag{7}$$

By substituting (4) and (5) into (7), the relationship between the vertical bending moment and the rotation angle can be obtained:

$$M = \frac{48E_hE_vI_hI_vL_h(\Delta - \theta x)}{3E_hI_hL_hL_vx + 8E_vI_vx^2(3L_h - x)} \tag{8}$$

Here, k represents the vertical bending stiffness of the joint, $dM(\theta)$ represents the vertical bending stiffness increment of the joint, $d\theta$ represents the angle increment of the spring joint, M represents the vertical bending moment of the joint, F represents the vertically concentrated load at the loading point of the horizontal bar, L_h represents the distance between the loading point of the vertically concentrated load of the horizontal bar and the axis line of the vertical pole, θ_v represents the angle of the vertical pole at the joints, and L_v represents the length of the vertical pole, E_v represents the elastic modulus of the vertical pole, I_v represents the cross-sectional moment of inertia of the vertical pole; θ represents the spring angle of the joint, x represents the distance between the measuring point of the vertical displacement on the horizontal bar and the axis line of the vertical pole, E_h represents the elastic modulus of the horizontal bar, I_h represents the cross-sectional moment of inertia of the horizontal bar, and Δ represents the measured vertical displacement of the horizontal bar.

From Eq. (8), we find that the position of the measuring point has little influence on the bending moment–rotation angle of the joint, and the influence degree is not in the same order of magnitude.

2.1.4. Loading mechanism

The loading point was set 300 mm away from the joint on the horizontal bar, and a uniaxial loading was applied using a hydraulic jack. The loading force data were read using a force transducer connected to a computer. The experimental process included preloading, formal loading, and unloading. The step loading was carried out in the way of force control. There were four groups of parallel experiments. The loading in each step was 1/10-1/15 of the estimated ultimate load, and the load was kept in each step for 2 min. When the horizontal bar had a large rotation angle relative to the vertical post, we observed the deformation of the joint and the steel tube; the load did not increase, but the displacement continued to increase. At this point, we considered that the joint reached the ultimate failure state, and the loading was stopped. Tables 2 and 3 list the positive and negative loading mechanisms, respectively.

Table 2
Positive-direction experimental loading mechanism

Loading force /kN	0.2	0.4	...	1.4	1.6	1.7	1.8	...
Load keeping time /min	2	2	...	2	2	2	2	...

Table 3
Negative-direction experimental loading mechanism

Loading force/kN	0.7	1.4	...	6.3	7.0	7.3	7.6	...
Load keeping time /min	2	2	...	2	2	2	2	...

2.2. Experiment results and analysis

2.2.1. Failure mode analysis

A wheel coupler scaffold socket may be subjected to positive and negative bending moments because of its special structural form. The positive and negative failure modes of the socket were comprehensively analyzed. Fig. 6 shows the failure modes of the socket under a positive bending moment.

(a) P-SJ1

(b) P-SJ2

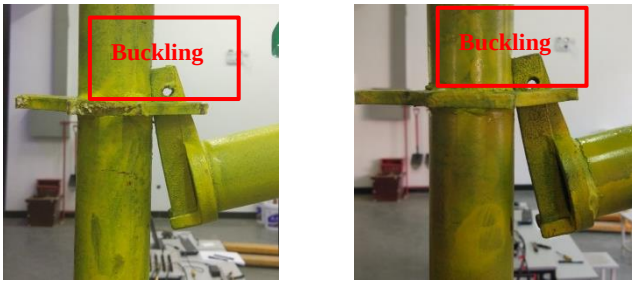

(c) P-SJ3 (d) P-SJ4

Fig. 6 Failure modes of various specimens (as listed in Table 1) in the positive direction

Fig. 6 shows that the socket in a bending state under a positive bending moment. A fracture occurred in P-SJ1 when the bending moment reached the ultimate value. No fractures occurred in P-SJ2, P-SJ3, and P-SJ4 when the bending moment reached the ultimate value. Based on the data listed in Table 1, we find that the failure modes are related to the depth of the socket inserted into the template. This is because the L_2 value of P-SJ1 was higher than that of the other specimens, and the higher the L_2 value, the easier it was for the socket to fracture. All the specimens underwent buckling at the contact position between the socket and the vertical post surface; however, the state of the socket determined the positive-direction bending capacity.

Fig. 7 shows the failure modes of the socket under a negative bending moment.

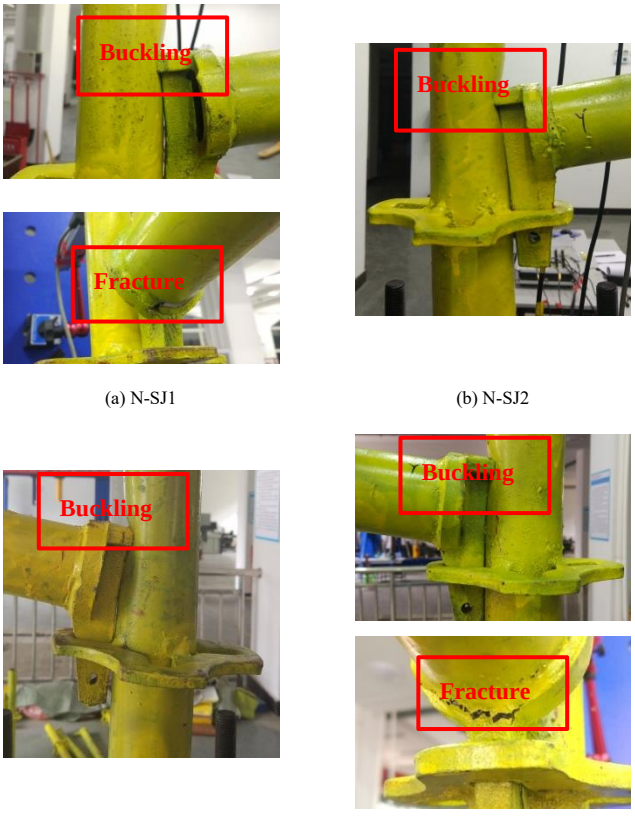

(a) N-SJ1 (b) N-SJ2

(c) N-SJ3 (d) N-SJ4

Fig. 7 Failure modes of various specimens (as listed in Table 1) in the negative direction

The failure modes of the N-SJ1 and N-SJ4 specimens were mainly fracture failure at the connection between the socket and the horizontal bar. The failure modes of N-SJ2 and N-SJ3 were mainly buckling of the vertical post. From the failure modes, we find that the negative-direction failure mode was different from the positive-direction failure mode, which was related to the depth of the socket inserted into the template and the material properties of the vertical post.

2.2.2. Bending capacity analysis

The moment–rotation angle curve was plotted by processing the data obtained from the positive-direction and negative-direction experiments. As shown in Fig. 8, the positive-direction bending capacity is largely the same at a bending moment of 0.45 kN·m; however, the initial bending stiffness in the positive direction is different, mainly because of the different L_2 values. Moreover, the negative-direction bending capacity is significantly different from the positive-direction bending capacity because of the different failure modes. The negative initial bending stiffness was unaffected by the L_2 value. By comparing the bending moment–rotation angle curves of N-SJ1 and N-SJ4, we find that the reduction in the bending stiffness was due to the initial imperfections of the vertical post. The negative-direction bending capacity and initial bending stiffness were much higher than those in the positive direction.

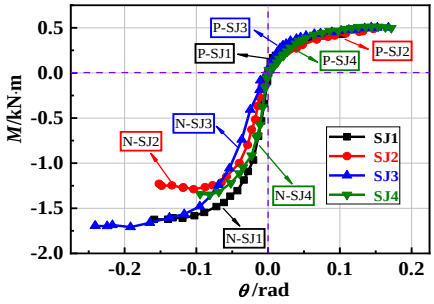

Fig. 8 Bending moment–rotation angle curve obtained experimentally

2.2.3. Constitutive model of material

Three standard arc specimens were prepared by randomly selecting a steel pipe, on which a tensile test was conducted to obtain its material properties. In accordance with the relevant requirements of GB/T 228.1-2010 “Metallic materials Tensile testing, Part 1: Method of test at room temperature” [31], the experimental specimen was prepared on the basis of the relevant requirements specified in appendix E.1, as shown in Fig. 9(a).

Assuming that the constitutive models of the horizontal bar and the vertical post are the same, the stress–strain curves of three groups of specimens are shown in Fig. 9(c). The yield strength was set to 256 MPa, and the elastic modulus was set to 2.02×10^5 MPa.

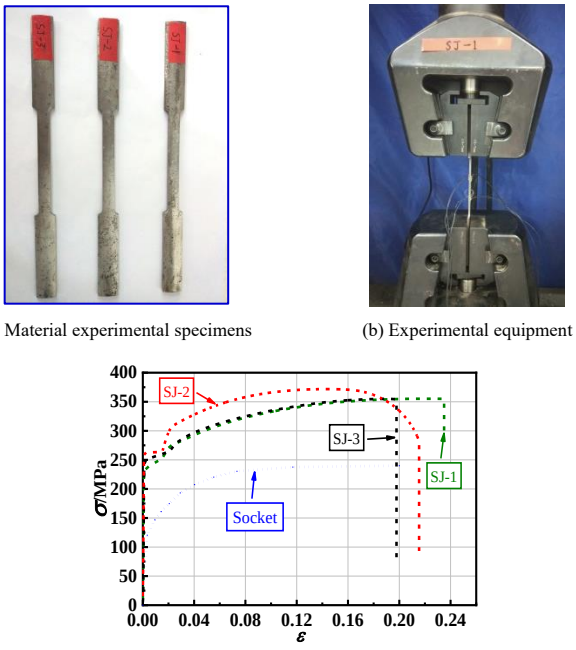

(a) Material experimental specimens (b) Experimental equipment

(c) Constitutive model of steel pipe and socket

Fig. 9 Constitutive model of material

The constitutive model of cast steel for the socket is also shown in Fig. 9(c). The constitutive model of the socket was obtained from existing literature given the difficulty in carrying out tensile tests on cast steel.

2.2.4. Verification and division of semi-rigid joints

Du [32] introduced and provided judgment criteria for the semi-rigid joint

of socket-type formwork supports when summarizing the domestic division of such joints, as shown in Fig. 10.

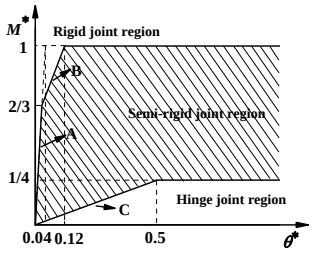

Fig. 10 Semi-rigid judgment criteria for socket-type joints

The curves in the figure were plotted using the following formula:

$$A: M^* \le 2/3, M^* = 25\theta^*;$$

$$B: 2/3 < M^* \le 1, M^* = (25\theta^* + 4)/7;$$

$$C: M^* = 0.5\theta^*。$$

$$M^* = M/M_p;\quad \theta^* = \theta/\left(M_p L_b / EI_b\right);$$

$$W_{px} = \frac{\pi}{4}(R^3 - \frac{r^4}{R});\quad I_b = \frac{\pi}{4}(R^4 - r^4).$$

Here, M_p represents the full plastic bending moment of the beam, $M_p = W_{px} \cdot f_y$, where W_{px} represents the plastic section modulus; EI_b/L_b represents the linear stiffness of the beam. I_b represents the cross-sectional moment of inertia.

The section size of the steel pipe was set to D48 mm × δ3.0 mm. E = 2.02×10^5 MPa, L_b = 0.3 m, and f_y = 256 MPa.

According to the above formula, it can be concluded that M_pL_b/EI_b = 0.01531 rad, and M_p = 1.150 kN·m.

The joint experimental data can be dimensionless–processed by the above formula, and then a curve can be drawn to divide the semi-rigid joint region, as shown in Fig. 11.

The connection joints of the wheel coupler-type formwork were typical semi-rigid connection joints based on the dimensionless bending moment–rotation angle curves of the four groups of joint experimental data shown in Fig. 11. As shown, they tend to the boundary of the hinge joint region when the joints are in the positive bending state and tend to the boundary of the rigid joint region when the joints are in the negative bending state.

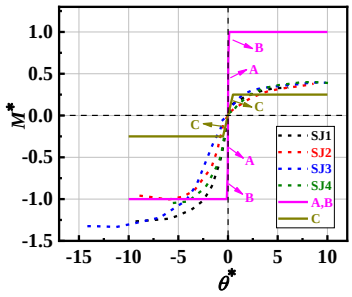

Fig. 11 Region division of semi-rigid joints

2.3. Finite element numerical analysis and verification

2.3.1. Establishing a finite element model

The finite element software ANSYS was used to establish a 3D solid model. The outer diameter and wall thickness of the steel pipe were set to 48 mm and 3.0 mm, respectively. Based on the experimental results of the material properties, the elastic modulus was set to 2.02×10^5 MPa, the Poisson's ratio was set to 0.3, the density was set to 7.85×10^{-6} kg/mm^3, and the empirical value of the friction coefficient was set to 0.2.

A refined finite element model was established in ANSYS to analyze the bending behavior of the socket connection. As shown in Fig. 12, the Solid185 element is discretized into a geometrical model, and the mesh size is set to 3.0 mm. The rigid beam scheme of MPC184 element was used to establish the loading points at both ends of the vertical post. The rigid beam scheme was used to connect the loading point with the node at the end of the steel pipe. As shown in Fig. 13, a displacement constraint is applied directly at the loading point. As shown in the red box in Fig. 13, the three translational degrees of freedom are constrained at the end of the horizontal bar. The translational degrees of freedom in the X and Y directions of the loading point were constrained at the upper end of the vertical post, and the translational degrees of freedom in the Y direction of the loading point was constrained at the lower end of the bar. The bending moment was applied by applying a displacement D in the X direction at the loading point at the lower end of the vertical post. Finally, the moment–rotation curve of the socket connection was obtained.

(a) Overall finite element model (b) CONTA174 element (c) TARGE170 element

Fig. 12 Numerical model of the socket connection

The contact elements CONTA174 and TARGE170 were used to simulate the mechanical behavior of the socket and the template, respectively, as shown in Figs. 12(b) and (c). The contact pair represents the contact and sliding between the socket element surface defined by CONTA174 and the deformable surface defined by TARGE170. The friction coefficient of the contact element was set to 0.2, and the normal stiffness was set to 1.0.

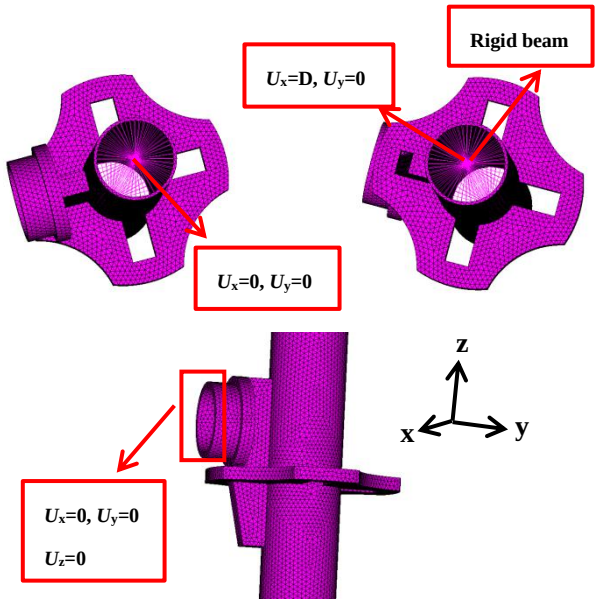

Fig. 13 Restraint condition of FE model

2.3.2. Comparative analysis of bending behavior

The results of the finite element model simulation were compared with the experimental results, as shown in Fig. 14. The finite element model can accurately predict the bending stiffness and bearing capacity in the positive direction. The finite element model can also effectively predict the bending stiffness in the negative direction. However, the finite element model cannot accurately predict the bending capacity of the socket when a fracture occurs in the experiment. Through the above results, we can verify the reliability of the finite element model in predicting the bending behavior of the connection joints of the wheel coupler-type formwork support.

For the case where the finite element results were not completely consistent with the experimental results, the failure modes of the joints in the positive and negative directions, shown in Figs. 5 and 6, indicate differences in the main components of the joints of the wheel coupler-type formwork support. When the joint was subjected to a bending moment, fracture failure easily occurs at the socket, at the connection of the socket and the horizontal

bar. The fracture failure occurs before the buckling failure of the joints. In which case, the finite element method cannot accurately simulate the buckling behavior of the joints.

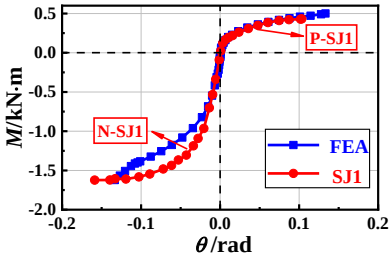

(a) SJ1

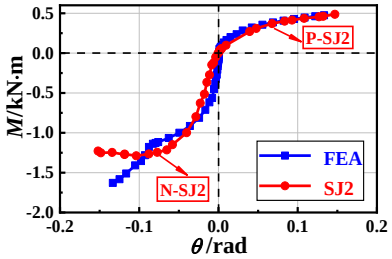

(b) SJ2

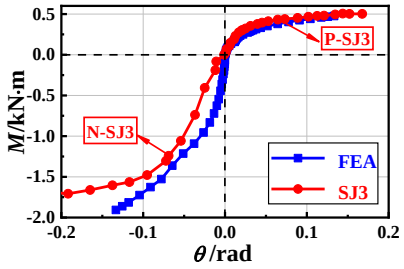

(c) SJ3

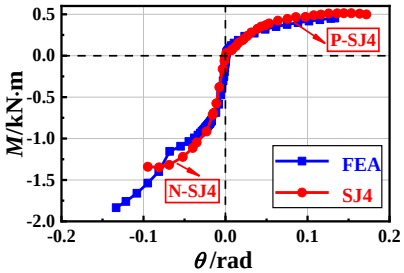

(d) SJ4

Fig. 14 Moment–rotation angle curves obtained from finite element simulation and experiments

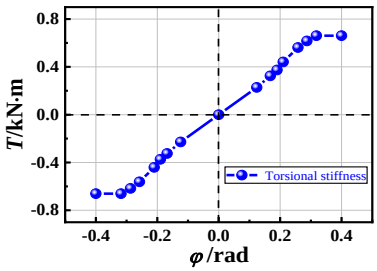

Fig. 15 Curve of torsion stiffness

2.3.3. Determination of the torsional stiffness of the socket connection

The finite element analysis software was used to analyze the torsional stiffness because the torsional stiffness of the socket connection of the wheel coupler-type formwork support cannot be accurately measured in the experiment. The complete torsional stiffness curve was obtained after analysis and processing using the same loading method as that employed for the bending stiffness, as shown in Fig. 15.

3. Parametric analysis of buckling behavior of wheel coupler-type high-formwork support system with diagonal bracing

3.1. Establishment of a finite element model

The key problem in establishing a finite element model in our study was accurately simulating the mechanical behavior of the semi-rigid socket connection. A nonlinear spring element COMBIN39 was used to simulate the bending behavior of the socket connection. The moment–rotation angle curves of SJ4 were set as the real constant of the COMBIN39 element. In addition, the "CP" command in ANSYS was used to couple the translational degrees of freedom of the nodes belonging to the horizontal bar and the vertical pole. Fig. 16(a) shows the finite element model of the socket connection. The torsion stiffness data can be analyzed through the finite element analysis results shown in Fig. 15, and the overall wheel coupler-type high-formwork support model was established using ANSYS, as shown in Fig. 16(b). The horizontal bar and vertical pole were simulated using the BEAM188 element, and the diagonal bracing was simulated using the LINK180 element. Generally, a high-formwork support system was used to bear the gravity load of the floor in construction engineering, so an overall uniform bearing load was set in the analysis, as shown in Fig. 16(c). In this section, two conditions were considered because the setting of the wall connecting pole was not always considered in actual engineering: with and without the application of a lateral constraint at the top, as shown in Fig. 16(d). First, an eigenvalue buckling analysis was carried out, and the first-order buckling mode was used as the initial geometrical imperfections. For the formwork support structure, 1/1000 of the total height was adopted as the initial imperfection [26, 27], which is a relatively conservative value in engineering. The initial imperfection value was set to H/1000, where H is the total height of the formwork support. Subsequently, a nonlinear buckling analysis of the overall formwork support was carried out to obtain the buckling coefficient. The critical load was the product of the buckling coefficient and the loading value. In this section, the buckling coefficient was used to represent the critical load. The greater the buckling coefficient, the greater the critical load, the greater the ultimate bearing capacity, and the better the overall stability. Otherwise, the worse. The magnitude of the applied load was P_w = 125.2 kN.

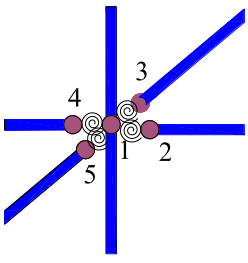

(a) Detailed connection of the FE model

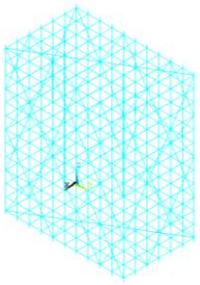

(b) Finite element analysis model

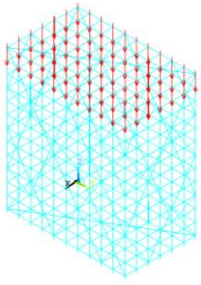

(c) Loading method

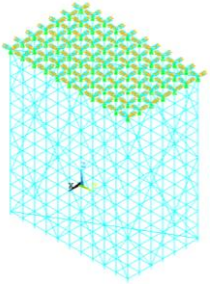

(d) Finite element analysis model with lateral constraints at the top

Fig. 16 Overall FE model

3.2. Influence of spatial layout of the diagonal bracing

Based on the specification requirements, a vertical diagonal bracing should be arranged at definite intervals along the span length in a high-formwork support system, and the vertical diagonal bracing should be arranged parallel to the short-side and long-side directions. A frame with 10×6×12 spans in the length, width, and height directions, respectively, was taken as the research object, l = w = h = 1.2 m, i.e., the transverse distance, longitudinal distance, and lift height were set to 1.2 m. The height of the frame H = 14.4 m, the width B = 7.2 m, and the aspect ratio H/B = 2 < 3, which meets the specification requirement. The plane layout of the vertical diagonal bracing has 4 spans × 6 steps. The angle between the diagonal bracing and the horizontal plane was set to 56.3°, and vertical and horizontal diagonal bracings were arranged around and up and down the frame, respectively. Fig. 17 shows the layout of the frame.

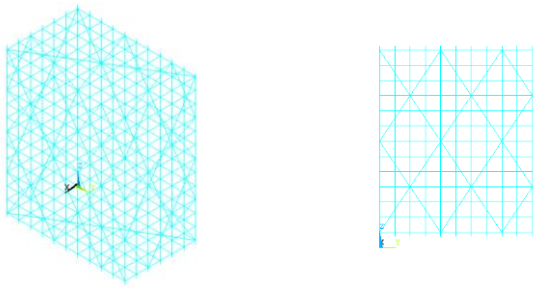

(a) Stereogram (b) Front view

Fig. 17 Layout of a 10×6×12 frame

The internal vertical diagonal bracing was arranged parallel to the short-side direction, at nine different intervals: every 1 span, every 2 spans, every 3 spans, every 4 spans, every 5 spans, every 6 spans, every 7 spans, every 8 spans and every 9 spans. When arranging parallel to the long-side direction, five intervals were considered: every 1 span, every 2 spans, every 3 spans, every 4 spans and every 5 spans. Fig. 18 shows the buckling coefficients under different conditions.

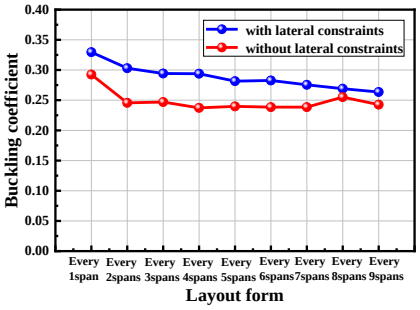

(a) Vertical diagonal bracing was arranged parallel to the short-side direction

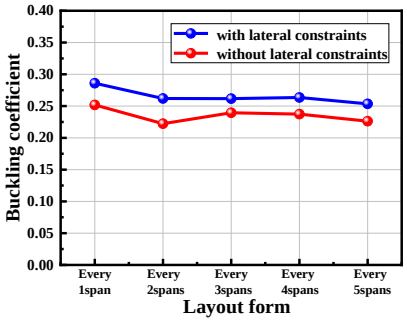

(b) Vertical diagonal bracing was arranged parallel to the long-side direction

Fig. 18 Variation in the buckling coefficients of a vertical diagonal bracing under different conditions

In summary, a comprehensive layout in which internal vertical diagonal bracings were arranged every 3 spans parallel to the short-side direction and every 3 spans parallel to the long-side direction was adopted to obtain the variation in the buckling coefficient with and without lateral constraints, as listed in Table 4.

Table 4
Variation in the buckling coefficient under parallel long- and short-side layouts of the vertical diagonal bracing

No:	Parallel short-side: every 3 spans	Parallel long-side: every 3 spans	Parallel long- and short-side: every 3 spans	Variation of buckling coefficient
With lateral constraints	0.294188	0.261688	0.320950	9.10%/ 22.65%
Without lateral constraints	0.247000	0.239500	0.257000	4.05%/ 7.31%

From Table 4, we find that the superposition layout has no significant influence on the overall stability. Therefore, considering the comprehensive economy, the internal vertical diagonal bracing can be arranged in the parallel short-side direction.

3.3. Influence of a plane layout of the vertical diagonal bracing

Currently, a large formwork system with 8×8×12 spans in the length, width, and height directions was taken as the research object, l = w = h = 1.5 m, i.e., the transverse distance, longitudinal distance, and lift height were set to 1.5 m. The height of the frame was 18 m, the width B = 12 m, and the aspect ratio H/B = 1.5 < 3, which meets the specification requirements. The vertical diagonal bracing was arranged only around the frame, whereas the horizontal diagonal bracing was arranged along the height direction of the frame every 6 steps. Six different layouts of the vertical diagonal bracing were studied: 2-span 2-step, 2-span 4-step, 2-span 6-step, 4-span 4-step, and 4-span 6-step. Fig. 19 shows the plane layout of the vertical diagonal bracing.

The buckling coefficient was obtained by a nonlinear buckling analysis of the six layouts and then compared with the buckling coefficient of the layout without the diagonal bracing. Table 5 presents the variation in the buckling coefficient.

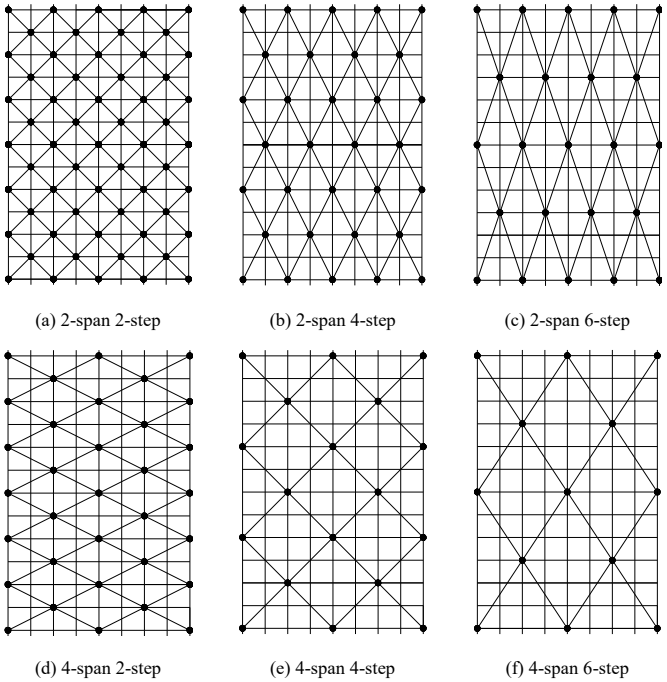

(a) 2-span 2-step (b) 2-span 4-step (c) 2-span 6-step

(d) 4-span 2-step (e) 4-span 4-step (f) 4-span 6-step

Fig. 19 Layout diagrams of the vertical diagonal bracing

Table 5
Comparison of buckling coefficients of different layouts of the vertical diagonal bracing

No:	Layouts of the vertical diagonal bracing	Number of joints on one side	Angle	Buckling coefficient with lateral constraints	Variation of buckling coefficient	Buckling coefficient without lateral constraints	Variation of buckling coefficient
	Without diagonal bracing			0.158562	0.00%	0.157400	0.00%
a	2×2	59	45°	0.223250	40.80%	0.191688	21.78%
b	2×4	32	63°	0.214980	35.58%	0.177000	12.45%
c	2×6	23	72°	0.207625	30.94%	0.179500	14.04%
d	4×2	33	27°	0.205950	29.89%	0.197200	25.29%
e	4×4	18	45°	0.199500	25.82%	0.185750	18.01%
f	4×6	13	56°	0.193763	22.20%	0.170750	8.48%

From the above table, we find that the overall stability of the high-formwork support system with a diagonal bracing was mainly affected by the joint density between the diagonal bracing and the frame, and the angle between the diagonal bracing and the horizontal plane. Next, two influencing factors were mainly explored.

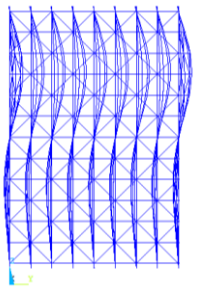

(a) With lateral constraints; 2-span 2-step

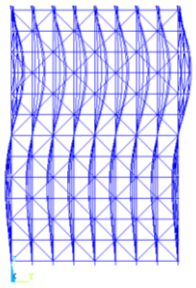

(b) Without lateral constraints; 2-span 2-step

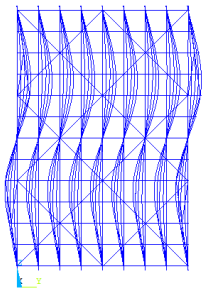

(c) With lateral constraints; 4-span 4-step

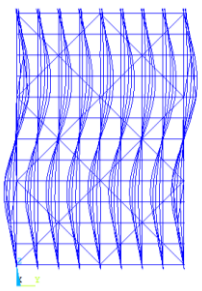

(d) Without lateral constraints; 4-span 4-step

Fig. 20 First-order buckling modes for different layouts of the vertical diagonal bracing

As shown in Fig. 20, the buckling modes of the integral formwork support in different plane layouts are bounded by the horizontal plane of the intermediate horizontal diagonal bracing. Large-wave drumbeating occurs both above and below the middle horizontal plane, and there were also conditions where large-wave drumbeating occurs above the middle horizontal plane. The deformation wavelength was related to the joint density between the diagonal bracing and the frame, and the angle between the diagonal bracing and the horizontal plane.

3.4. Influence of joint density between the diagonal bracing and the frame

To better study the influence of the joint density between the diagonal bracing and the frame on the overall stability, a series of numerical models with different joint densities were established under the same angle and height settings, and a nonlinear buckling analysis was carried out. In this section, we mainly study the numerical model of the formwork support system with two specifications, one with l = w = h = 1.5 m and the other with l = w = h = 1.2 m. Each specification has five conditions: a joint density of 27°, a joint density of 45°, a joint density of 56°, a joint density of 63°, and a joint density of 72°, as shown in Fig. 21.

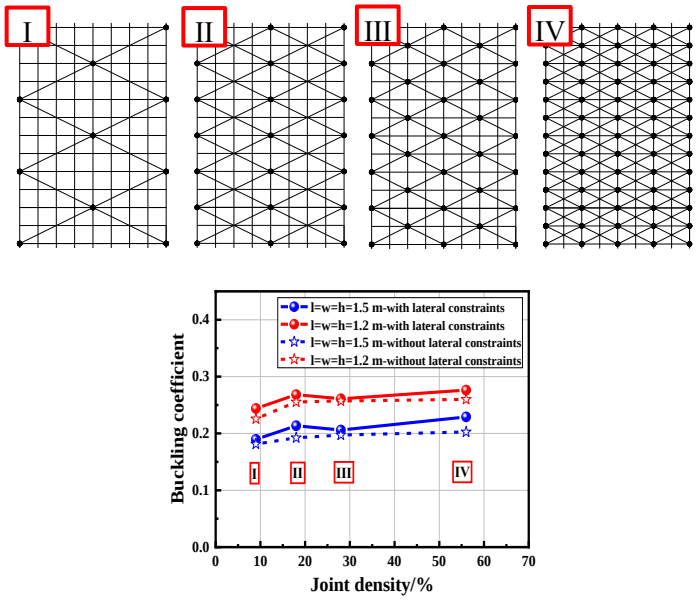

(a) 27°

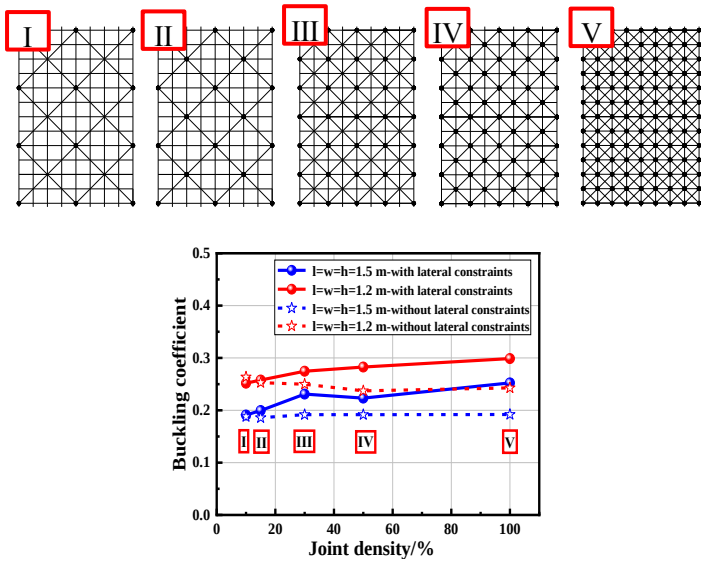

(b) 45°

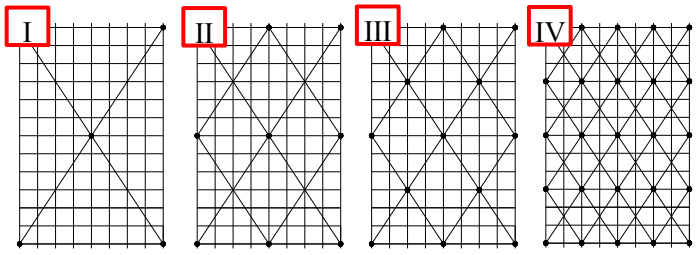

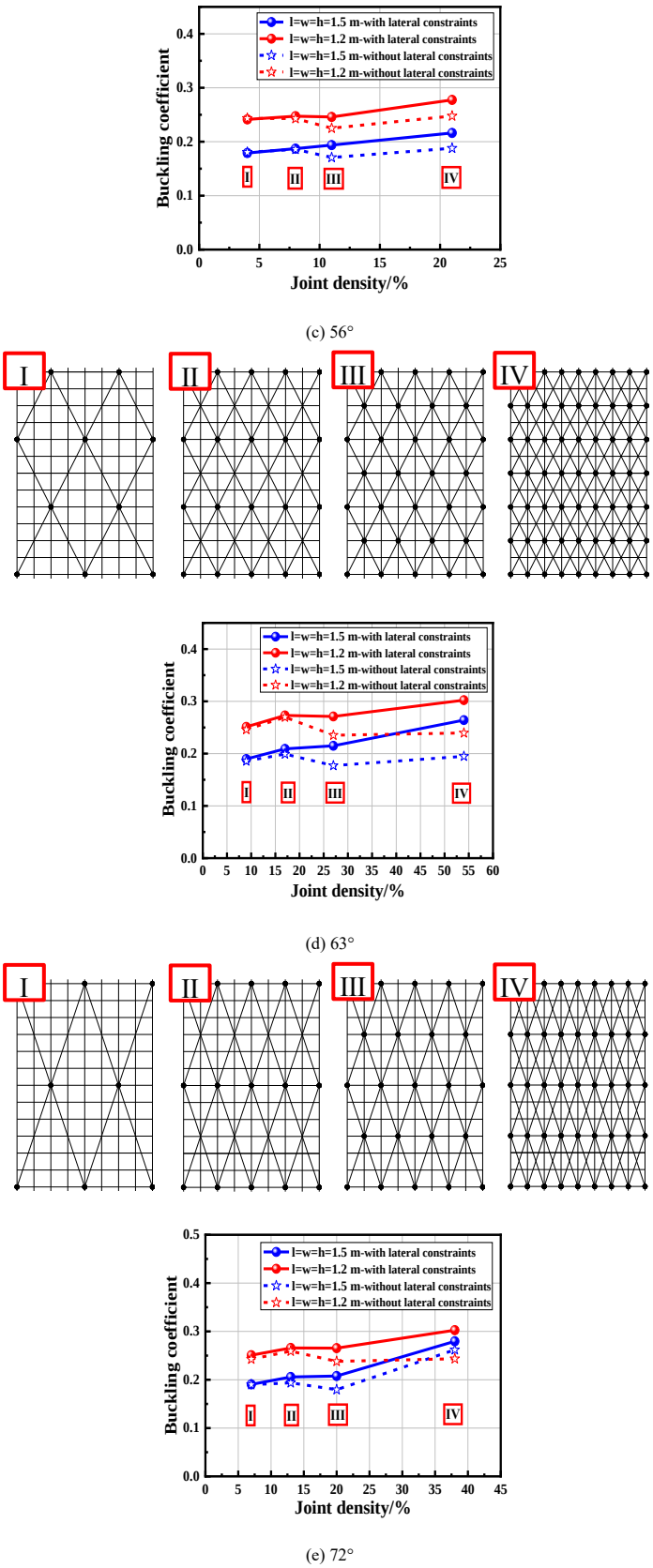

(c) 56°

(d) 63°

(e) 72°

Fig. 21 Comparison of buckling coefficients at different joint densities

The above analysis shows that with the increase in the joint density, nonlinear buckling coefficient increases gradually and that the overall stability improves while keeping the angle unchanged. However, this trend was not very evident, and the regularity was more evident when considerably increasing the joint density. From an economic perspective, an appropriate joint density connection form should be selected in the construction process.

We summarize the buckling coefficients corresponding to the joint density under five conditions of the same vertical diagonal bracing plane layout with two sizes to better illustrate the variation in the overall stability with the increase in the joint density under the same angle and vertical diagonal bracing plane layout. Fig. 22(a) shows the results in the condition of a lateral constraint at the top. Fig. 22(b) shows the results for the condition without any lateral constraints.

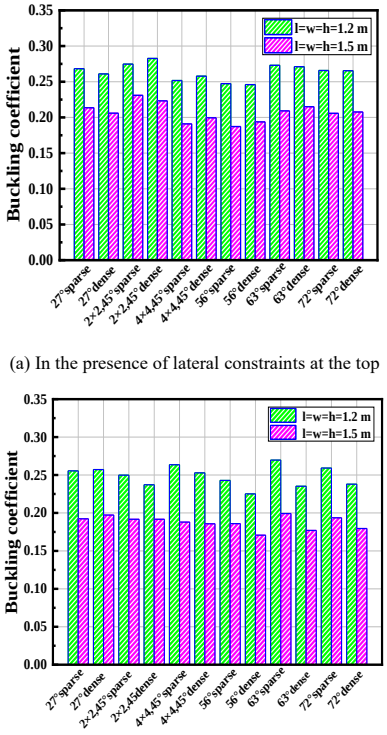

(a) In the presence of lateral constraints at the top

(b) In the absence of lateral constraints at the top

Fig. 22 Comparison of sparse buckling coefficients of the joints with and without lateral constraints at different angles and in the same layout

In summary, the higher the joint density, the better the overall stability in the presence of a lateral constraint at the top; the angle between the diagonal bracing and the horizontal plane and the layout of the vertical diagonal bracing were the same. From an economic perspective, a low joint density can meet the overall stability requirement.

Taking the high-formwork system with 8 spans × 8 spans × 12 steps as the research object, l = w = 1.5 m, the optimal plane layout and optimal angle were obtained with the variation in the lift height, as listed in Table 6.

Table 6
Optimal plane layout and optimal angle under different lift heights

Lift heights/m	Optimal plane layout	Optimal angle (°)	Optimal plane layout	Optimal angle (°)
0.3	2 spans, 4 steps	22	2 spans, 6 steps	31
0.6	2 spans, 4 steps	39	4 spans, 4 steps	22
0.9	2 spans, 4 steps	50	4 spans, 4 steps	31
1.2	2 spans, 2 steps	39	2 spans, 2 steps	39
1.5	2 spans, 2 steps	45	4 spans, 2 steps	27
1.8	2 spans, 4 steps	67	4 spans, 2 steps	31
2.1	2 spans, 2 steps	54	4 spans, 2 steps	35
2.4	2 spans, 4 steps	73	2 spans, 2 steps	58
3.0	2 spans, 4 steps	76	2 spans, 4 steps	76

With the increase in the lift height, the optimal angle increases when the lift height was small, and the optimal layout was a 2-span 4-step arrangement. With the increase in the lift height, the optimal angle increases steadily. The optimal plane layout was mostly a 2-span 4-step arrangement, though there were 2-span 2-step conditions as well. However, considering the comprehensive economy, the layout of the vertical diagonal bracing of a wheel coupler formwork support was a 2-span 4-step arrangement, and the optimal angle should be approximately in the range of 30–70°.

In the absence of a lateral constraint at the top, the optimal angle varies by approximately 30° when the lift height h was in the range of 0.3–2.1 m,

and the optimal angle was relatively large when the lift height h = 2.4 m and h = 3.0 m. The results show that the smaller the angle between the diagonal bracing and the horizontal plane, the better the overall stability in the absence of a lateral constraint at the top and when the lift height was not particularly large. The optimal angle was approximately 30°. The optimal plane layout cannot be determined, and the distribution was relatively random.

3.5. Influence of angle between the diagonal bracing and the horizontal plane

To better study the influence of the angle between the diagonal bracing and the horizontal plane on the overall stability at the top with and without a lateral constraint, the variation in the buckling coefficient at different angles was obtained, as listed in Table 7, for the same joint density but different lift heights.

Table 7
Comparison of buckling coefficients for the same joint density but different lift heights

Lift heights /m	Optimal plane layout	Number of joints on one side	Optimal angle (°)	Buckling coefficients with lateral constraints	Buckling coefficients without lateral constraints
0.3	4-span 2-step	33	6	0.695438	0.720438
	2-span 4-step	32	22	0.715950	0.716550
0.6	4-span 2-step	33	11	0.480950	0.455750
	2-span 4-step	32	39	0.498450	0.447000
0.9	4-span 2-step	33	17	0.328763	0.318875
	2-span 4-step	32	50	0.377313	0.314075
1.2	4-span 2-step	33	22	0.250125	0.234813
	2-span 4-step	32	58	0.255013	0.239075
1.5	4-span 2-step	33	27	0.205950	0.197200
	2-span 4-step	32	63	0.214980	0.177000
1.8	4-span 2-step	33	31	0.182000	0.166888
	2-span 4-step	32	67	0.193919	0.152625
2.1	4-span 2-step	33	35	0.167937	0.145437
	2-span 4-step	32	70	0.153650	0.135750
2.4	4-span 2-step	33	39	0.133406	0.124275
	2-span 4-step	32	73	0.161144	0.123250
3.0	4-span 2-step	33	45	0.104407	0.101844
	2-span 4-step	32	76	0.138250	0.109110

From Table 7, we find that in the presence of a lateral constraint at the top, the greater the angle between the diagonal bracing and the horizontal plane, the greater the buckling coefficient and the better the overall stability under the same joint density. In the absence of a lateral constraint at the top, the smaller the angle between the diagonal bracing and the horizontal plane, the greater the buckling coefficient and the better the overall stability under the same joint density.

4. Conclusions

The buckling behavior of a wheel coupler high-formwork support system with a diagonal bracing was systematically studied, and the positive and negative bending behaviors of the connection joints of the support were analyzed through experiments. A precise numerical model of the connection joints of the wheel coupler was established and verified through a finite element analysis. Based on the characteristics of the semi-rigid connections, the buckling behavior of the overall structure was analyzed. The influencing factors, such as the spatial layout of the diagonal bracing, the plane layout of the vertical diagonal bracing, the joint density between the diagonal bracing and the frame, and the angle between the diagonal bracing and the horizontal plane, were mainly studied.

1) The experimental results showed that the failure modes in the positive direction were relevant to the insertion depth of the socket into the template. The higher the L_2 value, the more likely the socket was to fracture. The failure modes in the negative direction were closely related to the insertion depth of the socket into the template and the bending of the vertical post.

2) The proposed moment–rotation curve was based on the same steel grade and component size. Further verification was required for different steel grades and component sizes. After dimensionless treatment of the experimental data, the dimensionless moment–rotation angle curve was plotted. The connection joint of the wheel coupler formwork support was a typical semi-rigid connection joint. Through a finite element analysis and parametric analysis, an accurate numerical model of the connection joint of the wheel coupler formwork support was established and verified.

3) Regardless of the application of a lateral constraint at the top, the internal vertical diagonal bracing should be arranged parallel to the short-side direction.

4) In the presence of a lateral constraint at the top, the optimal plane layout of the vertical diagonal bracing was found to be a 2-span 4-step arrangement, and the optimal angle was in the range of 30–70°. In the absence of a lateral constraint at the top, the optimal plane layout could not be determined, and when the lift height was moderate, the optimal angle was approximately 30°.

5) An appropriate joint density was conducive to the overall stability.

6) In the case of the same joint density, in the presence of a lateral constraint at the top, the higher the angle between the diagonal bracing and the horizontal plane, the better the overall stability. In the absence of a lateral constraint at the top, the smaller the angle between the diagonal bracing and the horizontal plane, the better the overall stability.

References

[1] Lu Z.R., “Experimental and theoretical study on fastener steel tube full hall formwork support system”, Tianjin: Tianjin University, 2010.
[2] Liu H.B., Zhao Q.H. and Wang X.D., et al, “Experimental and analytical studies on the stability of structural steel tube and coupler scaffolds without X-bracing”, Engineering Structures, 32(4), 1003-1015, 2010.
[3] Zhou K.Z., “Test and analysis on load-bearing capacity of steel tubular falsework with bowl-button-type connection”, Tianjin: Tianjin University, 2010.
[4] Dou G.J., Kang Y. and Zi J.T., et al, “Investigation and application analysis of socket type wheel-buckle scaffold”, Building Construction, 40(11), 1957-1958+1968, 2018.
[5] Chen M., “The study on the popularization and application of the pulley-clip high formwork in Wenzhou”, Hangzhou: Zhejiang University of Technology, 2016.
[6] Guangdong Provincial Bureau of Quality and Technical Supervision, Technical specification for safety of wheel-coupler steel tube scaffolding: DB44/T1876-2016, Guangdong, 2016.
[7] Zhao Z.W., Chen Z.H. and Yan X.Y., et al, “Simplified numerical method for latticed shells that considers member geometric imperfection and semi-rigid joints”, Advances in Structural Engineering, 19(4), 689-702, 2016.
[8] Abdel-Jaber M., Beale R.G., Shatarat N.K. and Shehadeh M.A., “Experimental and theoretical investigations of spigot connections under cyclic loading”, Advanced Steel Construction, 15(1), 37-46, 2019.

[9] Peng J.L., Wang S.H., Wang C.S. and Yang J.P., “Stability study on scaffolds with inclined surfaces and extended jack bases in construction”, Advanced Steel Construction, 17(1), 73-83, 2021.
[10] Zhao Z.W., Liu H.Q., Dong J.F. and Bian Y.X., “Buckling capacity of socket-template scaffold system without X-bracing”, Journal of Performance of Constructed Facilities, 34(1), 04019089: 1-14, 2020.
[11] Zhao Z.W., Liu H.Q., Liang B. and Yan R.Z., “Influence of random geometrical imperfection on the stability of single-layer reticulated domes with semi-rigid connection”, Advanced Steel Construction”, 15(1), 93-99, 2019.
[12] Chan S.L. and Zhou Z.H., “Second-order elastic analysis of frames using single imperfect element per member”, Journal of Structural Engineering, ASCE, 121(6), 939-945, 1995.
[13] Chan S.L. and Gu J.X., “Exact tangent stiffness for imperfect beam-column members”, Journal of Structural Engineering, ASCE, 126(9), 1094-1102, 2000.
[14] Chan S.L. and Cho S.H., “Second-order analysis and design of angle trusses Part I: Elastic analysis and design”, Engineering Structures, 30(3), 616-625, 2008.
[15] Cho S.H. and Chan S.L., “Second-order analysis and design of angle trusses, Part II: Plastic analysis and design”, Engineering Structures, 30(3), 626-631, 2008.
[16] Chan S.L., Huang H.Y. and Fang L.X., “Advanced anslysis of imperfect portal frames with semi-rigid base connections”, Journal of Engineering Mechanics, ASCE, 131(6), 633-640, 2005.
[17] Chan S.L. and Cho S.H., “Second-order P-Δ-δ analysis and design of angle trusses allowing for imperfections and semi-rigid connections”, Advanced Steel Construction, 1(1), 169-183, 2005.
[18] Chan S.L. and Chui P.P.T., “Non-Linear static and cyclic analysis of steel frames with semi-rigid connections”, Elsevier Science, 1999.
[19] Chen Z.H. and Zhao Z.W., “Analysis of door-type modular steel scaffolds based on a novel numerical method”, Advanced Steel Construction, 12(3), 316-327, 2016.
[20] Zhao Z.W., Liu H.Q. and Liang B., “Novel numerical method for the analysis of semi-rigid jointed lattice shell structures considering plasticity”, Advances in Engineering Software, 114, 208-214, 2017.
[21] Zhang Y.C., Design principle of steel structure, Beijing: Higher Education Press, 2004.
[22] Ye K., Zhao Y.Q. and Liu G., “The impact analyse between ultimate bearing capacity with semi-rigid node of fasteners template scaffold”, Journal of Civil, Architectural &Environmental Engineering, 37, 130-133, 2015.
[23] Liu H.B., Jia L. and Wen S.L., et al, “Experimental and theoretical studies on the stability of steel tube-coupler scaffolds with different connection joints”, Engineering Structures, 106, 80-95, 2016.
[24] Zou A.M., Li Q.W., He M.H. and Zhang H., “FEA on bearing behavior of cuplok scaffold based on tri-linear semi-rigid joint model”, Journal of Building Structures, 37(4), 151-157, 2016.
[25] Yang S., “The research on stability bearing capacity of wheel buckle steel tubular formwork support frame”, Changsha: Changsha University of Science & Technology, 2011.
[26] Yu W.K., Chung K.F. and Chan S.L., “Structural instability of multi-storey door-type modular steel scaffolds”, Engineering Structures, 26 (7), 867-881, 2004.
[27] Chu A.Y.T., Chan S.L. and Chung K.F., “Stability of modular steel scaffolding systems–theory and verification”, Advances in Building Technology, 1, 621-628, 2002.
[28] Sevim B., Bekiroglu S. and Arslan G., “Experimental evaluation of tie bar effects on structural behavior of suspended scaffolding systems”, Advanced Steel Construction, 13(1), 62-77, 2017.
[29] Liu H.B., Zhou Y., Chen Z.H. and Liu Q., “Structural performance and design method of new mortise–tenon full steel-tube scaffold”, Advanced Steel Construction, 14(2), 291-307, 2018.
[30] Qian X.J., “Experimental research and technical application of joint mechanical behavior of disk lock and cuplok steel tubular falsework”, Nanjing: Southeast University, 2016.
[31] Metallic materials–Tensile testing–Part 1: Method of test at room temperature: GB/T 228.1–2010. Beijing: China Standards Press, 2010.
[32] Du R.J., “Scientizing and standarding regulations on design and calculation of construction falsework in scaffold structure(2)”, Construction Technology, 39(2), 110-116, 2010.

Advanced Steel Construction – Vol. 18 No. 1 (2022) 436–445
DOI:10.18057/IJASC.2022.18.1.2

THE SEISMIC PERFORMANCE OF DOUBLE TUBE BUCKLING RESTRAINED BRACE WITH CAST STEEL CONNECTORS

Zhan-Zhong Yin [1, 2, *], Da-Zhe Feng [1], Bo Yang [1] and Chao-Chao Pan [1]

[1] *School of Civil Engineering, Lanzhou University of Technology, Lanzhou 730050, China*
[2] *Western Engineering Research Center of Disaster Mitigation in Civil Engineering of Ministry of Education, Lanzhou University of Technology, Lanzhou 730050, China*
[*] *(Corresponding author: E-mail: yinzhanzhong@lut.edu.cn)*

ABSTRACT

The special concentrically braced frame (SCBF) is an aseismic structure, but its bracing system exhibits brittle failure and premature buckling connected with the weld fracture of the gusset plate and the post-buckling of the braces; thus, maximizing the role of energy dissipation is difficult. Here, this paper proposes a system of double-tube buckling-restrained brace with cast steel connectors for steel SCBFs. The large inelastic deformation of the bracing system is mainly concentrated in the ductile cast connectors under the earthquake, and the degree of buckling and post-buckling of braces can be reduced. Cyclic loading tests were conducted on two groups of specimens with different parameters, then the deformation trend, stress distribution, energy dissipation capacity, and stiffness degradation of the specimens were analyzed. The improved measures of increasing the width–thickness ratio of the energy dissipation plate and stiffener and casting the end right-angle tip tightly for a certain length of cast connector in Group 2 specimens, which overcomes the brittle fracture caused by the crack of the connection segment due to flexural buckling in Group 1 specimen tests, was evaluated. The cast steel connector conducts the main energy dissipation member that exhibits good ductile and energy absorption performance, and the advantages of using improved ductile cast steel connectors to obtain the energy dissipation of BRBs are illustrated. The test results provided direct evidence that the seismic performance of specimens is closely associated with the length of the energy dissipation segment of the cast connector and the overstrength factor of axial force. Also, the strength, rigidity, deformation, and energy dissipation performance of the members can be independently controlled by reasonably designing the cast connector. Our results provide the underlying insights needed to guide the design of the bracing connector.

ARTICLE HISTORY

Received: 17 April 2021
Revised: 24 May 2021
Accepted: 24 May 2021

KEYWORDS

Buckling restrained brace;
Cast steel connector;
Cyclic loading test;
Seismic performance;
Special concentrically braced frame

1. Introduction

A special concentrically braced frame (SCBF) [1] is a steel structural system with a high bearing capacity and a large lateral stiffness. However, the Kobe earthquake in 1995 [2] exposes the problem of SCBF structures inevitably suffering from buckling and fracture of the bracing system. Notably, an intensive review found that the fracture failure of bracing mainly occurs at the end connection. Before that, Goel et al. studied the concentrically braced frame system with various types of supports connected by gusset plates and found that gusset plates are prone to brittle failure [3,4]. Subsequently, several studies and reviews focused only on the mechanical behavior of gusset plate connectors [5-9], whereas the effects of support on the gusset plate have not been considered for many years. These trends led to a proliferation of studies on the yield mechanism, inelastic deformation capacity, and ultimate failure mode of bracing members with end connectors over the past two decades. Tremblay et al. conducted extensive research on the mechanical properties of steel bracing under cyclic loading [10] and found that the aspect ratio and slenderness ratio are the most important parameters that affect the life of the support. Similar work was conducted by Shaback and Brown [11], who proposed the calculation formula of the life of hollow structural steel section (HSS) support. Tests were conducted on a two-layer frame with an HSS cross-section brace by Uriz et al. [12], who found that this brace would lead to fracture at the beam-column joints. Moreover, Roeder et al. [13,14] studied the seismic design of frame support structures and found that the lateral displacement capability and the ductility of the structure can be greatly improved by controlling the yielding of braces and connectors. Although the frame structure has certain ductility, the deformation capacity of the brace is often limited due to premature yielding [15].

The problem of insufficient energy dissipation of bracing system has attracted considerable attention to the performance of support, which is another key factor that affects the seismic performance of the SCBF structural system. Compared with traditional braces, buckling-restrained braces (BRB) are a kind of brace that relies on its core component that could be confined with a peripheral component from buckling to achieve full-section yield [16-18]. To release expansion and contraction of the core component in the vertical and horizontal directions, the core component and the peripheral component are required to retain a certain gap [19]. The gap is generally filled with filler materials to provide better-confined action [20-21]. As a part of their study, Sridhara et al. [22] proposed a brace with a casing pipe that confined the bending of the core member, thereby squeezing the peripheral pipe to generate flexural stress. The yield strength of the sleeve is greater than the flexural stress, thus improving the compressive bearing capacity of the core member. A comparison of different types of BRBs is given in [23], where the author claimed that the lack of adhesive materials such as mortar and concrete will lead to premature local buckling of the core component. This issue has been considered by recent work [24], in which the frictional force in the contact area of the core component increased and the strain distribution along the core member was not uniform, which were closely associated with increased clearance between the core component and the limiter under compressive load. This finding established that the clearance between the core component and the limiter plays an important role for evaluating the seismic performance of BRB. A proposed double steel tube buckling-restrained brace simplified the structure of the brace and made field installation more convenient [25,26]. Since then, Yin et al. [27] added a contact ring between the inner and outer components to improve the double-tube BRB. Finite component analysis and tests showed that this support has good energy dissipation performance, and the lateral stiffness of the inner tube confined with the contact rings is significantly improved [28,29]. Hence, this BRB could be introduced to SCBF systems to replace the traditional support to address the limitation of premature buckling.

Nonetheless, the energy dissipation performance of BRB has not yet been fully utilized due to the brittle failure of the gusset plate. A ductile connector is urgently needed instead of the gusset plate to avoid brittle failure of structural joints. Fleischman et al. [30] proposed a modular cast steel connector for steel moment frames, and the later work of [31] extended the ductility of the connector by geometrically based techniques. A conceptually similar study was conducted by [32], in which the cast connector was used as the end connector for HSS braces to avoid brittle failure. Gray et al. [33] offered a yielding brace system that dissipates seismic energy by flexural yielding of special cast connectors. The advantages of prefabricated modular steel construction in industrial technique enhanced productivity, site safety, and construction quality is evident. More recent work in this area [34] extends the methods by using a new type of bolted joint for modular steel building, which indicated that the joints have stable bearing capacity with adequate ductility and seismic performance. A similar connecting method was proposed in tests by [35], which considered that a connection with slot bolt holes revealed the potential application of these connections for a dual-function component in a structure to simultaneously provide stiffness and energy dissipation capacity.

Current research on modular ductile connectors tends to focus on beam-column joints or traditional braces rather than BRBs. However, it has not explicitly addressed the issue of premature buckling and low dissipation of the brace. A systematic understanding of how ductile cast connector contributes to the BRB is still lacking. Considering the assembling of prefabricated buildings need for a precise connecting system to ensure structural integrity and effective

transfer of loads and moments, an assembling modular connector for BRBs needs to be developed. This paper presents a bracing system of buckling-restrained brace with cast connectors (CBRB), where ductile cast steel connectors are used for double-tube BRB with contact rings instead of the gusset plate to alleviate the stress concentration of the joint. Low cycle loading tests were performed on the members, and the impact of different parameters of cast connectors on the mechanical properties and energy-dissipating performance for specimens were analyzed. Using the excellent ductility of cast connectors to avoid brittle failure of connector for the brace enabled the BRB to fully exert energy dissipation. An equally important detail is that the cast connector can act as the main energy dissipation component to concentrate most of the inelastic deformation of members, which enables the structure to dissipate energy in stages and prolongs the time course of energy dissipation. In addition, the cast connector can be a "fuse" for easy replacement to reduce the inspection time and repair cost of structures after an earthquake. This work provides a new idea for the application of assembled connectors, which has important theoretical significance and broad engineering application prospects.

2. Theoretical analysis for design of cast connector

The energy-dissipating brace is an axially deformable member that provides lateral stiffness for SCBFs. Therefore the design method based on the lateral stiffness ratio could be applied for the steel frame system with BRB. As shown in Fig. 1, the configuration after deformation is identical to the initial configuration of the frame on the basis of an assumption concerning the small deformation in the theory of elastoplasticity. Therefore, the angle between the support and the horizontal direction, θ, in the structure can be assumed to be the same before and after deformation. Theoretically, the axial displacement of support ΔL can be calculated according to Equation (1)

$$\Delta L = \cos\theta = \frac{FL}{EA} \tag{1}$$

In Equation (1), F is the axial force in the support, A is the cross-sectional area of the support, and E is the Young's modulus. Thus, the horizontal component for the axial force of brace is

$$F_n = F\cos\theta = \frac{EA\cos^2\theta}{L} \tag{2}$$

The lateral stiffness of BRB is

$$K_D = F_n/1 = EA\sin\theta\cos^2\theta/h \tag{3}$$

The nominal rigidity ratio is defined as $k = K_D/K_f$. K_f is the lateral stiffness of steel frame obtained by the D-value method with $K_f = 12\gamma E_c I_c/h^3$, γ is the correction coefficient, E_c is the Young's modulus of the column, I_c is the moment of inertia of the column, and h is the height of the column. The effect of reasonable lateral stiffness ratio on the seismic behavior of steel frame structures with braces is self-evident. According to the finite component analysis of the influence of the lateral stiffness ratio on the whole steel frame structure was completed by Liu [36], support does not affect the whole frame, as the lateral stiffness ratio exceeds 2.5. According to the above statement, the sectional area of the inner tube of BRB can be obtained, that is,

$$A = k\cdot K_f\cdot h/E\sin\theta\cos^2\theta \tag{4}$$

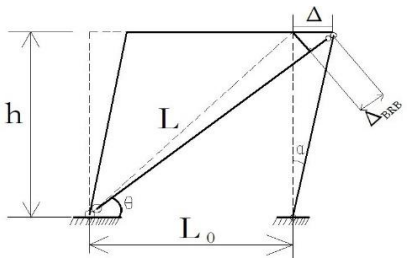

Fig. 1 Schematic of BRB deformation

As minor deformation occurs, Fig. 1 shows that $\Delta = h\tan\alpha$, $\cos\theta = L_0/L$ and $L = \sqrt{L_0^2 + h^2}$. Thus, the total deformation of a single diagonal BRB can be expressed as

$$\Delta_{BRB} = \Delta\cos\theta = h\tan\alpha\cos\theta = \tan\alpha L_0 h/L \tag{5}$$

According to Equation 5, the story drift, α, can be used to calculate the deformation of the bracing member. It is important to highlight that the elastic–plastic story drift of 1/50 specified in the Chinese code [37] should be adopted to design deformable components, while the elastic story drift under the frequent earthquakes does not ensure that all energy-dissipating members yielded. Thus, as the axial displacement of the support, $\Delta_{plastic}$, is

As shown in Fig. 2, both ends of BRB are connected with the frame through ductile cast connectors arranged at the connection zone to form an SCBF system. Using the ductile cast connector instead of the gusset plate is advantageous for energy dissipation. Therefore, the plastic deformation of the system could be concentrated on the ductile cast connector as much as possible through a reasonable detailed design of the energy dissipation member. Fig. 3 presents a schematic of the structure of ductile cast connector and cross-sectional shape of energy dissipation segment. The ductile cast connectors can be designed into a cross-section with three parts: L1 is the connection segment, which was designed as a right-angle tip for easy frame connection; L2 is the actual energy dissipation segment that drawing on the "dog bone" idea of the weakened segment; and L3 is the transition segment connecting with the brace. The energy dissipation segment enhances the strength of the connection and transition segments to a certain extent. Therefore, the stress distribution of the beam-column joint will not change due to the large stiffness of the connection segment as the brace is damaged.

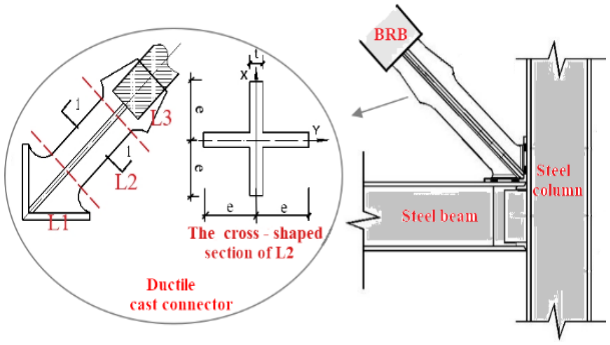

Fig. 2 Schematic of ductile cast connector

The deformation of the cast connector is mainly concentrated on the energy dissipation segment, of which the section is cross-shaped and prone to torsional buckling. For cross-section, its torsional buckling load P_{cr} is as follows:

$$P_{cr} = \frac{GI_t}{i^2}\left(1 + \frac{\pi EI_w}{GI_t l^2}\right) \approx \frac{GI_t}{i^2} \tag{6}$$

In Equation (6), i is the radius of polar rotation of the star section with respect to the shear center; I_t is the torsional moment of inertia of the section; I_w is the warping moment of inertia of the cross-section; and G is the shear modulus. As a result of the pimping moment of warping inertia of the section is small, it can be ignored. Therefore, the ultimate load of torsional instability of the section can be approximately expressed as GI_t/i^2. where $G = E/2(1+\nu)$; $i^2 = \left(I_x + I_y\right)/A$. The torsional buckling stress of cast connector can be expressed as

$$\sigma_{cr} = \frac{P_{cr}}{A} = \frac{GI_t}{Ai^2} = \frac{E\cdot\frac{4}{3}et^3}{2(1+\nu)\cdot\frac{4}{3}e^3 t} = \frac{E}{2.6}\left(\frac{t}{e}\right)^2 \tag{7}$$

where e is the extended length of the cross-section, and t is the width of the plate for the cross-section. To avoid torsional buckling of ductile cast connectors, a necessary step is to ensure that $\sigma_{cr} \geq f_y$, in which f_y is the yield strength of cast connectors. Thus, $e/t \leq \sqrt{E/2.6 f_y}$ can be obtained. Assuming that all plastic deformation is concentrated on the weakened energy dissipation segment of the cast connector at both ends of the support, the minimum length of the energy dissipation segment of the cast connectors can be ascertained as

$$L_{2,\min} = \Delta_{plastic} / \delta \tag{8}$$

In Equation (8), δ is the elongation of the steel. The energy dissipation segment is the main axially compressed member, and the slenderness ratio λ_{L2} can be calculated as

$$\lambda_{L2} = \mu L_2 / i \tag{9}$$

where μ is the effective length factor. In this paper, μ=2 .

3. Experimental program

3.1. Test specimens

The specimen is based on a single-layer special concentrically braced frame with a span of 6 m and a height of 4. 5 m, in which the beams and columns are both H-section and rigidly connected, and both ends of the brace are hinged with beam-column joints. The beam and column dimensions are H400×300×10×16 and H400×400×12×20, respectively, and the lateral stiffness ratio K = 2. 8 of the frame was selected for brace validity. To further study the energy dissipation performance of cast connectors, the inner tube sections of BRBs for all specimens were designed to the same specification. The cross-sectional area of the inner tube was calculated as 2541 mm^2 by Equation (4) to this end. Fig. 3 provides an overview of double steel tube BRBs. The seamless steel tubes are used for all parts, and then both ends of BRB are provided with end plates to facilitate connection with cast connectors by high-strength bolts. The tests were performed with half of the whole member based on the symmetry of the system to help fix the specimen on the loading frame. The specific parameters are obtained from the geometric dimensions of BRBs in Table 1.

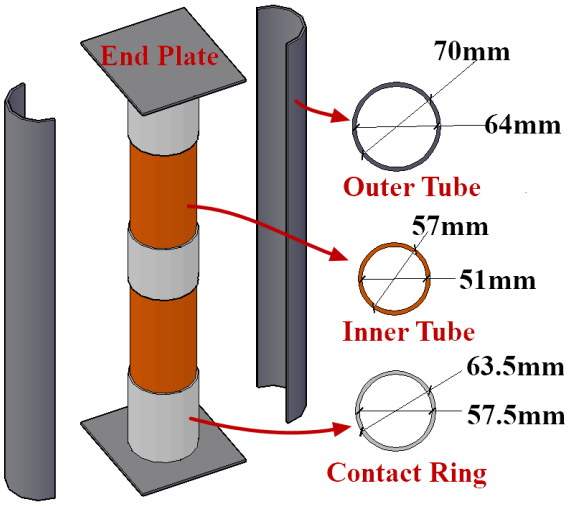

(a) Section design

(b) Member

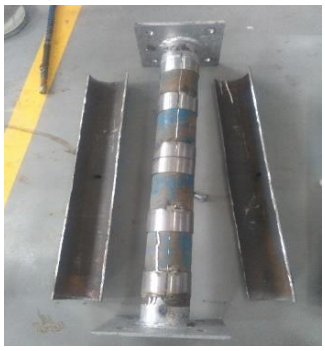

(c) Inner tube with contact rings

Fig. 3 Photo of BRB component

Table 1
Parameter table of BRBs

Inner tube section	Inner tube length/mm	Outer tube section	Outer tube length/mm	Contact ring section	Number of contact rings
Φ121×5.5	1300	Φ140×6.5	1180	Φ127×3	5

For the same reason, the end part of the transition section is provided with a connecting end plate where the cast connector is connected with BRB by a high-strength bolt to facilitate the replacement and repair of the cast connector. As shown in Table 2 and Fig. 4, eight cast connectors were made based on dimensions and length of the cross-shaped section, of which the wedge plate inscribed with the two legs of the right-angle steel is the main deformable component to dissipate energy, and the plate in the other direction could act as a stiffener. The direction along the energy dissipation plate is defined as x-axis corresponding to the direction along the stiffener as y-axis in the cross-section. The width–thickness ratios of stiffeners and energy dissipation plates can be used as a section parameter for easy analysis. The specific focus in Fig. 4a is the right-angle tip of the cast connector for some of the specimens. This right-angle tip was cast tightly below a certain height of L1 for end reinforcement, and the width–thickness ratios of the stiffeners and energy dissipation plates improved. This result occurred because the cast connectors in the Group 1 specimens exhibited untimely fracture during the loading process due to the flexural buckling of the connection segment. We expect our proposed solution will help address this issue. For this reason, only two specimens in Group 1 were taken for analysis, and the remaining improved six specimens were labeled as Group 2 for later tests. The corresponding yield load of each energy-dissipating component for designed specimens was obtained by performing finite component numerical simulation. The axial force overstrength coefficient of specimens, n , is defined as follows:

$$n = P_{y,c} / P_{y,b} \tag{10}$$

In Equation (10), $P_{y,b}$ is the axial yield load of the BRB, and $P_{y,c}$ is the axial yield load of the cast connector.

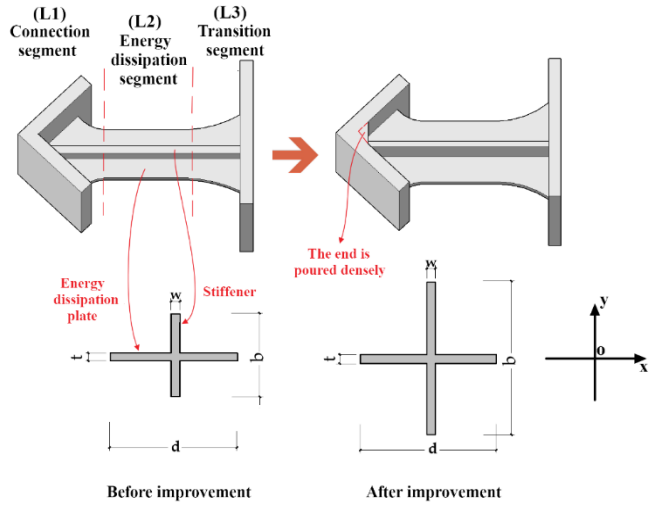

(a) Section design and improvement

(b) Specimens before improvement

(c) Specimens after improvement

Fig. 4 Cast steel connectors

Table 3 provides the material properties for the steel samples measured by the tensile coupon test. The test was conducted according to the Chinese “Metallic materials—Tensile testing at ambient temperature” (GB/T 228–2002) [38]. Fig 5 presents an overview of steel samples for components, and the representative value of each material property index was taken as the average value of the test results of each test sample. The samples for cast connectors are made of low-yield-point steel, whose strength is lower than that of BRB.

Table 1
Parameter table of specimens

Specimen grouping	Specimen Number	Specification of Cast connectors /mm							Total Length (mm)	Slenderness ratio of L2 λ_{L2}	Overstrength Coefficient n	Area ratio	End Reinforcement
		L1	L2	L3	t	w	b	d					
Group 1	CBRB-1	150	150	90	18	18	36	66	390	36.51	0.786	0.595	×
	CBRB-2	150	150	90	18	18	46	66	390	29.24	0.797	0.666	×
Group 2	CBRB-3	150	100	140	20	14	82	74	390	11.64	0.817	0.924	√
	CBRB-4	150	150	90	20	14	82	74	390	17.47	0.817	0.924	√
	CBRB-5	110	200	80	20	14	82	74	390	23.29	0.817	0.924	√
	CBRB-6	150	150	90	20	12	80	80	390	19.22	0.805	0.913	√
	CBRB-7	150	150	90	22	16	80	68	390	17.14	0.841	0.954	√
	CBRB-8	150	150	90	20	16	82	72	390	16.72	0.845	0.957	√

Note: "Area ratio" denotes "the ratio of the cross-sectional area of the energy dissipation segment to the inner tube of the BRB"

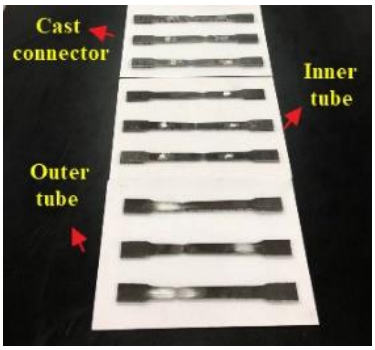

Fig. 5 Photo of steel samples

Table 3
Material parameters

Sample category	Steel grade	Yield strength (MPa)	Ultimate strength (MPa)	E_s (GPa)	Elongation (%)
Cast connectors	Q235	264	500	206	20
Inner tube	Q345	350	510	206	25
Outer tube	Q345	340	500	206	26

3.2. Instrumentation, test device, and loading protocol

Fig. 6 shows the loading device, which consists of a vertical portal loading frame, a hydraulic jack, a right-angle support, and a rigid base, where the right-angle support is a right-angle surface that simulates the beam-column joint. The two ends of the rigid base are fixed on the ground through pressure beams to prevent out-of-plane displacement of the member. The right-angle support and rigid base are connected by 10.9-grade high-strength bolts to fix the lower end of the specimens to ensure vertical loading. A heavy hammer line was hung in the vertical direction to observe the degree of inclination of the specimen during the loading process. To observe the deformation of the specimens in the vertical direction and the horizontal direction during the test more intuitively, horizontal and vertical guiding rulers are respectively arranged at the matching position of the cast connector and the lower end of the BRB.

Fig. 6a shows that 10 displacement meters are erected around the cast connector and BRB, and the deformation of the global specimen could be known by the displacement meter readings. To determine the stress distribution of the specimen during the test, resistance strain gauges are arranged on the cast steel connectors and BRBs. As shown in Fig. 7, strain gauges are arranged on both sides of the energy dissipation plate and stiffener of the ductile cast connector, which is mainly used for detecting various stress changes of the energy dissipation segment during the test. Also, strain rosettes are arranged on the connection segment and the transition segment to detect the stress at the portion where the sectional shape is changed. Given that the inner tube of BRB is the main energy-dissipating component, strain gauges are arranged along the length direction of the extended parts of the inner tube at both ends of the BRB.

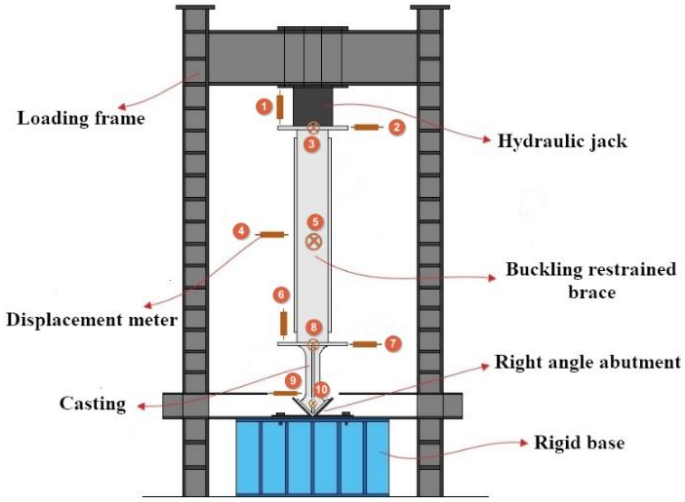

(a) Vertical portal loading frame and displacement meter arrangement

(b) Photo of the vertical portal loading frame

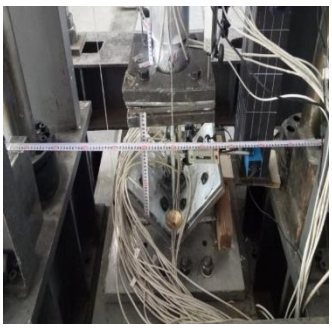

(c) Heavy hammer line and guiding rulers

Fig. 6 Loading device

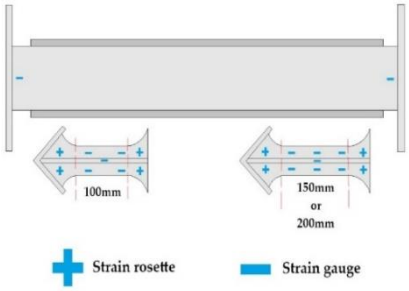

Fig. 7 Measuring arrangement of strain gauge and strain rosette

In the test, a 1000 kN electro-hydraulic servo system was used for axial cyclic loading to examine the hysteretic performance of cast connectors. The loading pattern in Fig. 8 shows the loading method of displacement control with

amplitudes of 2 mm, 4 mm, 6 mm, 8 mm ..., and each amplitude is loaded for three cycles at a time until the specimen is damaged. The axial compression and elongation rate of the total specimen, $\delta^{\pm}$, are defined as the ratio of the displacement exerted by the actuator to the total length of the specimen.

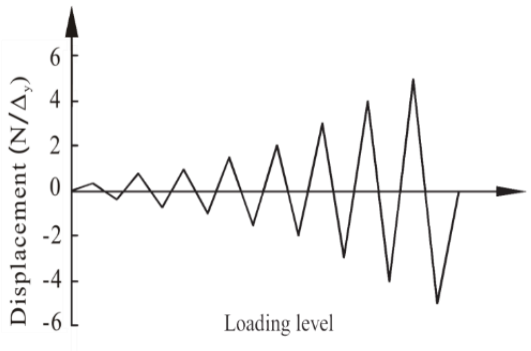

Fig. 8 Loading pattern

4. Experimental results and discussion

4.1. Damage processes and failure mode

All the specimens were in the elastic stage during the first two cycles of 2 mm loading displacement ($\delta^{\pm}=1/880$), and no obvious test phenomenon was observed. Starting from the third cycle, closer inspection of readings of both Nos. 9 and 10 displacement meters showed that the connection segment of CBRB-1 shifted for an approximately 2 mm out-of-plane displacement in the X and Y direction. Accordingly, the observed parallel results were that nearly 5 mm out-of-plane displacement of the upper end of BRB was measured by the No. 3 displacement meter. Similarly, these findings were observed in the testing of CBRB-2, and the out-of-plane displacement increases with the test process. This finding, while preliminary, suggests that flexural buckling occurred, which skewed the specimen toward the out-of-plane. From the data in vertical displacement meters, it is apparent that each component of the specimen begins to undergo axial tension and compression deformation. A review of the readings showed that the deformation increases with the raising of the test load. As the loading displacement approached 6 mm ($\delta^{\pm}=1/293$), the transverse cracks appeared at the coating of the connection segment of cast connectors of the specimen CBRB-2 and CBRB-1 successively. The cracks continued to develop and increase, and a slight coating warping was found around the cracks as the test progressed. Further comparison of displacement meter readings revealed that the compression and elongation of BRBs are less than those of ductile cast connectors. When the loading displacement reached 6.6 mm ($\delta^{-}=1/267$), a crack was found at one side of the energy dissipation plate axis of connection between the connection segment and the right-angle steel of CBRB-2. This result could be attributed to the inclination of the cast connector mainly on one side of the Y direction. After a short time, the coating bulged in the energy dissipation segment and cracks appeared gradually, and numerous cracks were significant at $\delta^{\pm}=1/196$. The endplate between the BRB and the cast connector of CBRB-1 skewed 4 mm toward the out-of-plane in the direction of the x-axis at the moment. As the loading displacement further increased, the cast connector of CBRB-2 was excessively stretched vertically. When the displacement finally reached −10 mm ($\delta^{-}=1/176$), the cracks at the paint coating of the energy dissipation plate widened, and the paint skin began to fall off in a large area. Subsequently, the crack on one side of the end of the connection segment of the cast connector ran through, and then the crack developed in the other side afterward. When the hydraulic jack finally returned to the equilibrium position, one side of the end of the CBRB-2 connection segment fractured (Fig. 9c). Meanwhile, the specimen CBRB-1 was severely inclined (Fig. 9a). As shown in Fig. 9b, cracks appeared at both sides of the energy dissipation plate axis of connection between the connection segment and the right-angle steel and widened as the loading progressed. The connection segment bent obviously, and its paint coating peeled off in a large area at that time. The end of the connection segment fractured at the loading displacement with a length of −12 mm ($\delta^{-}=1/147$). The width–thickness ratio of stiffener increased, resulting in the asymmetry of the bending deflection of the connection segment, which may explain the difference between the CBRB-1 and the CBRB-2.

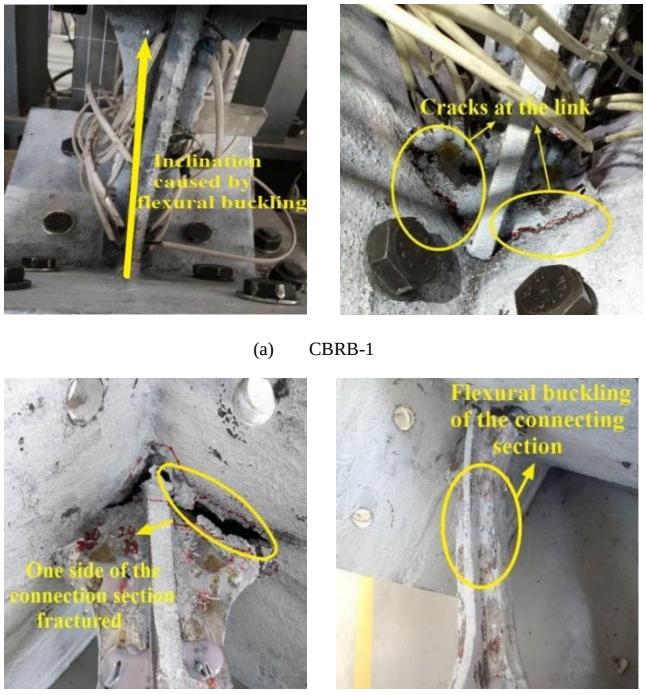

Fig. 9 Failure modes of Group 1 specimens at the final stage

The second set of tests examined the performance of the improved specimens, and all showed similar phenomena. The tension and compression deformation of all specimens had a fairly stable growth with the increase in loading displacement. No significant bending of connection segment was found during the test loading process, which is consistent with the smaller out-of-plane displacement than that of the Group 1 specimens, as detected by the Nos. 9 and 10 transverse displacement meters. These findings suggest that an improved method of increasing the width–thickness ratio of energy dissipation plate and stiffener may help prevent the local buckling of connection segments effectively. The selected typical test phenomena of CBRB-4 are further discussion in detail. At a loading displacement of 12 mm ($\delta^{\pm}=1/147$), the exposed part of the inner tube at the lower end of the BRB showed a slight swelling of paint (Fig. 10a). The same phenomenon with a few cracks of paint was found near the weld of BRB and flange plate at the upper end (Fig. 10b). The order of specimens observed these findings is as follows: CBRB-8, CBRB-7, CBRB-3, CBRB-4, CBRB-5, and CBRB-6. This finding suggests that a smaller axial force overstrength coefficient means that the BRB enters the plastic stage at a later point. These findings were not obvious in the first set of testing. Overall, these results demonstrate that the improved cast connector can better maintain the plastic deformation and damage accumulation of BRB. As shown in Fig. 10c, the coating paint of the energy dissipation segment of the CBRB-4 bulged slightly as the compression rate reached approximately 1/126. Some were accompanied by slight coating cracks, such as CBRB-7 and CBRB-8. As the test continued, cracks in the paint skin at the energy dissipation segment of each specimen began to develop and increase in number gradually. Also, the upper exposed part of the inner tube showed obvious bulging, and the lacquered skin of the lower exposed part began to peel off, as shown in Figs. 10d and 10e, respectively. Only a few cracks appeared at the connection segment, and no crack appeared at the link between the angle steel and the end of the connection segment unlike with the Group 1 specimens even though it was also detected some out-of-plane displacements of the members. The results indicate that end reinforcement may help prevent fracture due to the buckling of the connection segment. When the displacement was about 18 mm ($\delta^{+}=1/98$), the bearing capacity of CBRB-3 was reduced, the inner tube bulged seriously, and the loading stopped. When the elongation rate was about 1/88, the bearing capacity of CBRB-4 and CBRB-6 was reduced. The bearing capacity of CBRB-8 decreased at the displacement of −24 mm ($\delta^{-}=1/73$), while that of CBRB-5 and CBRB-7 decreased until the displacement reached 26 mm ($\delta^{+}=1/68$). The striking aspect of the results is that the improved specimen has better ductility and stronger deformability.

The failure mode of the Group 1 specimens belongs to the fracture caused by cracks of the cast connector end due to the flexural buckling of the connection segment. A possible reason may be that the smaller width–thickness ratio of the stiffener and energy dissipation plate led to the flexural buckling of

the connection segment under compressive loading. Another reason for this condition is that a weak link may exist between the energy dissipation plate and the angle steel because the end was not poured tightly. As can be seen from Fig. 9d, cracks produced easily in the weak link, resulting in fracture under eccentric loading caused by the out-of-plane inclination of the specimen, especially after bending of the connection segment. Unlike the Group 1 specimens, the Group 2 specimens did not exhibit a significant bending deflection of the connection segment (Fig. 10f). A large number of paint cracks were found at the energy dissipation segment. Moreover, the bulge at the exposed part of the inner tube indicated that local buckling had occurred. These results provide further support for the idea that the ductility of all members of improved specimens was fully utilized. The tests ended with the decreased bearing capacity of these specimens, and the low cycle fatigue is their main failure mode.

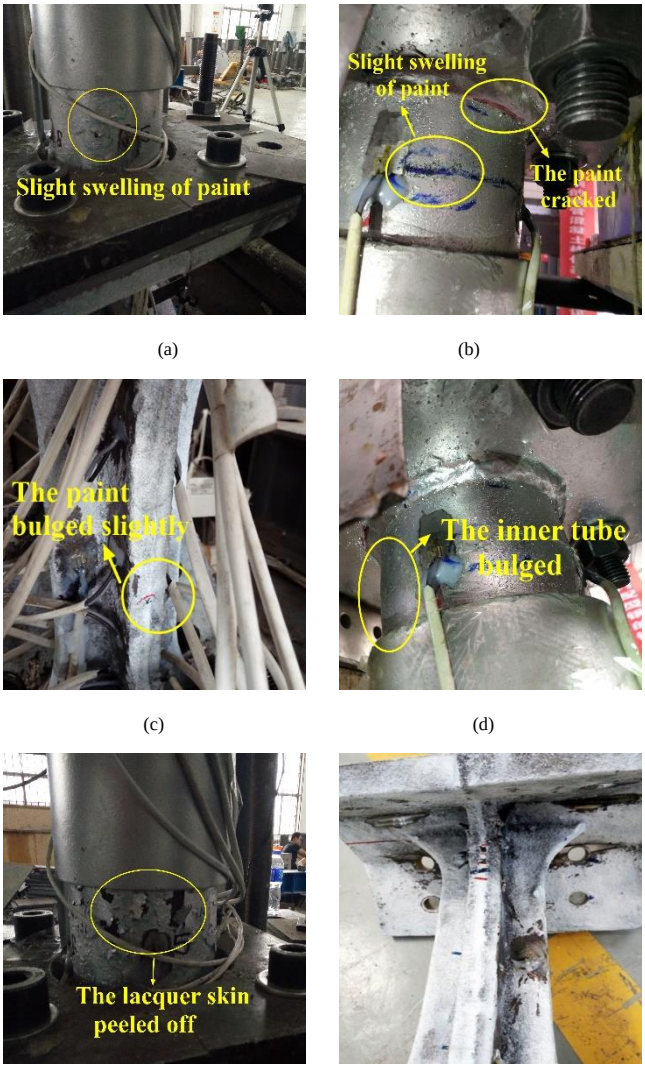

Fig. 10 Failure modes of CBRB-4 in Group 2

4.2. Deformation analysis

Fig. 11 provides the axial deformation of all specimens under the peak displacement of tension and compression load from the reading of vertical displacement meters. The entire deformation of the specimen is controlled by the ductile cast connector and the inner tube of BRB. The percentage of cast connector deformation in total deformation of the Group 1 specimens varies from 50% to 83%, while that of the Group 2 specimens varies from 59% to 92%. This finding suggests that most of the deformation of the specimen is mainly concentrated on the cast connector. The most obvious finding is that the energy dissipation time of the Group 2 specimens is longer, and the loading displacement of the cast connector deformation is significantly larger than that of the Group 1 specimens, which indicates that the cast connectors of the improved specimens have better plastic deformation and accumulation ability. Another important finding is that the displacement exerted by the actuator from the start of loading in the test of Group 1 specimens is significantly larger than the axial entire deformation of the specimen and is more obvious under compressive load. This inconsistency may be due to different degrees of flexural buckling of cast connectors, which caused the specimen to tilt and produce non-axial displacement. This result agrees well with the test phenomena of the first set. The occurrence of this phenomenon in the second set is obviously delayed, and the maximum non-axial displacement is 61% lower than that in the first set. The data from this figure can be combined with the data in Fig. 12, which shows the out-of-plane displacements of cast connectors along the x-axis (energy dissipation plate) and y-axis (stiffener) under compressive load from the readings of the Nos. 9 and 10 displacement meters. Notably, the local buckling of the Group 2 specimens occurs after 8 mm loading displacement ($\delta^{+}=1/220$), and the bending degree in two directions is reduced compared with that of the Group 1 specimens. These results further indicate that the improved method of increasing the width–thickness ratio of stiffeners and energy dissipation plates can slow down the flexural buckling degree of cast connectors. Interestingly, no difference is found in the width–thickness ratios of the energy dissipation plate between the CBRB-1 and CBRB-2, whereas the x-axis deformation of CBRB-1 decreases by 41% on average compared with CBRB-2. This finding is unexpected and suggests that a larger width–thickness ratio in a certain axial direction corresponds to larger deformation in the axis of symmetry.

In the range of tensile and compressive rates from 1/880 to 1/440, the percentage of the deformation of the cast connector to the total deformation of the specimen increases with the loading displacement, and the inner tube of BRB is in the elastic deformation stage. After the loading displacement of 4 mm, Fig. 11 shows that the percentage of the axial deformation of the cast connector to the total deformation exhibits a clear trend of decreasing first and then increasing gradually. This result can be explained by the rapid increase in the deformation of the BRB inner tube caused by the overstrength effect of the parts of the energy dissipation segment that has entered the plastic phase. The ratio of the cross-sectional area of the energy dissipation segment to the inner tube of the BRB in this test was controlled within the range of 0.595 to 0.957. Therefore, the cast connector and the BRB are connected in series, ensuring that the energy dissipation segment can yield before the inner tube during the axial force transfer in this bracing system. The hardening of the energy dissipation segment is similar to turning on the energy dissipation switch of the BRB, causing the inner tube to perform supplementary energy dissipation, thus achieving a two-stage energy dissipation mechanism. Subsequently, the deformation of the inner tube gradually stabilized after yielding, while the deformation of the cast connectors continued to grow steadily. These results show that the cast connector can ensure the BRB dissipates energy continuously and stably. At the late loading stage of Group 1 specimens, the percentage of cast connector deformation of CBRB-1 and CBRB-2 in total deformation are maintained at about 69% and 59%, respectively. The percentage of the deformation of cast connectors in the total deformation of Group 2 specimens is still increasing steadily, and evidence that the deformation of cast connectors can reach 82% of the entirety of component deformation on average is found when the specimens were damaged. Overall, these results further support that the improved cast connector has better ductility and stable energy dissipation.

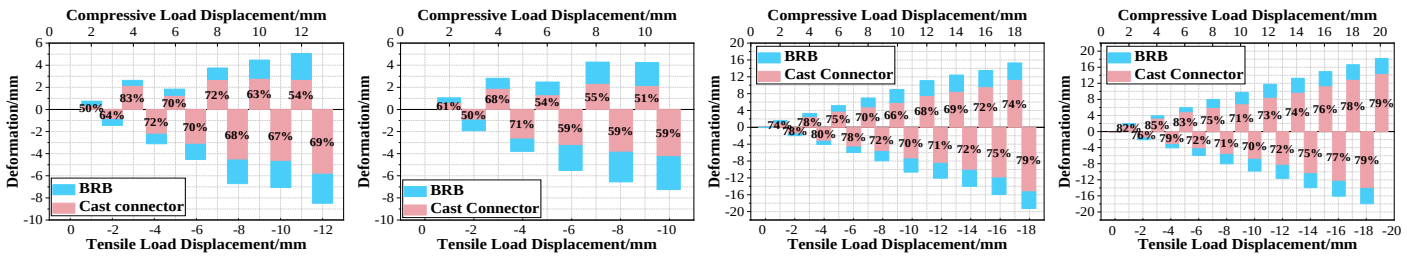

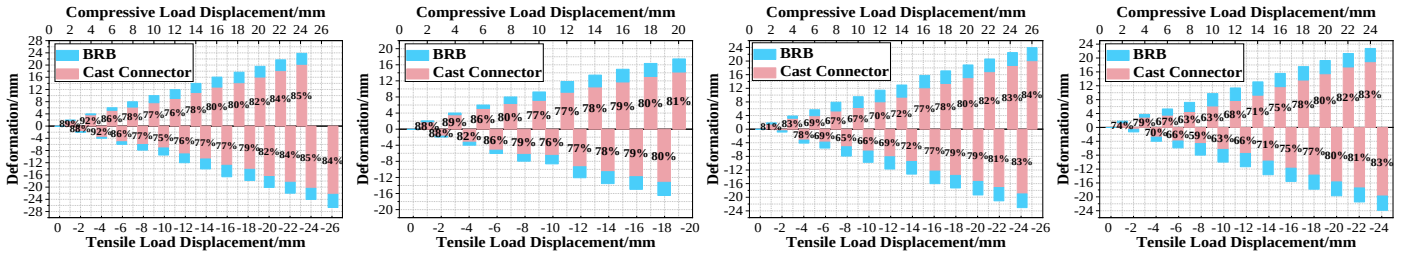

(e) CBRB-5 (f) CBRB-6 (g) CBRB-7 (h) CBRB-8

Fig. 11 Axial deformation of specimens

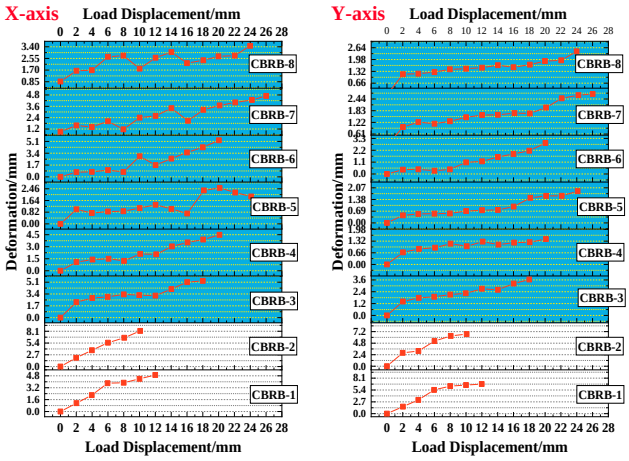

(a) (b)

Fig. 12 Deformation trend diagram of energy dissipation plates and stiffeners

We now focus on experimental evidence of the influence of design parameters on the deformability of members. A striking observation from the data comparison is that the axial deformation of cast connectors from CBRB-3, CBRB-4, and CBRB-5 increased in turn under the pressure at each loading stage, which is likely to be related to the length of the energy dissipation segment. Interestingly, the differences between displacement exerted by the actuator and the entire deformation of the specimen are highlighted with the decrease in the length of the energy dissipation segment. The higher non-axial displacement may be due to the decrease in the stiffness of the cast connector with the length of the energy dissipation segment, and a larger stiffness easily causes instability of the end for the cast connector. This finding indicates that the long energy dissipation segment can delay the local buckling of the connection segment. A closer inspection of Fig. 11 shows that the inner tube of BRB deforms more and tends to stabilize relatively later with the overstrength coefficient of the axial force. This finding matches the order of specimens where paint swelling was observed among the test phenomena. The reason for this special phenomenon is that the large overstrength effect of the cast connector causing the assembled BRB to enter the plastic stage early. The correlation between the deformation of the cast connector and the overstrength coefficient is interesting because the deformation of the cast connector decreases at the early stage and increases at the middle and late stages of loading with the overstrength coefficient. A clear benefit of increasing the overstrength coefficient in the development of plastic deformation of the energy dissipation segment can be identified in this analysis.

4.3. Stress distribution

The stress on each component of the specimen is calculated according to Hooke's law by using the strain from results measured by the strain collection device, and the yield mechanism for components can be determined by whether the stress value is currently above or below the yield strength. No significant difference was found among the stress distribution rules of eight specimens. Therefore, only the member stresses of CBRB-1 and CBRB-6 under different loading displacements are considered, as shown in Fig. 13, to facilitate the illustration of some main characteristics of the stress distribution for two sets of specimens. The stress of each part of the specimen is very small at δ=1/880, and the global specimen is in the elastic stage at this time. Afterward, the specimen is in the elastoplastic stage at δ^{+}=1/293. Notably, the stress value of L2 exceeds the yield strength, that is, the energy dissipation segment occurs the inelastic deformation to dissipate energy at the moment, while the rest of the components are maintained in the elastic phase. The stress of the connection segment (L1) of CBRB-6 is far less than the yield stress and is compared with that of CBRB-1, which reached the yield strength under compressive load. This disparity implies that the improved specimen can better alleviate stress concentration of the joint connected with the right-angle support. In addition, the stress difference between the energy dissipation segment and the BRB inner tube at δ=1/293 loading displacement is significantly increased compared with that at δ=1/880. This condition was sufficient to demonstrate that the inner tube starts to participate in energy dissipation at this time. Furthermore, the tensile and compressive stresses of each part of the specimen are inconsistent especially in the L1 from δ=1/293 onwards. The stress under pressure load is significantly greater than that under tension load, which indicates that material hardening occurs under the pressure load. The energy dissipation segment entered the full section, dissipating energy as the δ reached 1/176, whereas the stress of the connection segment and the transition segment of CBRB-6 were both still in the elastic stage. A detail that should be clarified is that the stress of the inner tube increases obviously as the stress difference between the energy dissipation segment and BRB begin to decrease. An implication of this condition is that the cast connector and the BRB are jointly involved in energy dissipation at this time. The stress in the energy dissipation segment increases continuously due to the effect of the overstrength. Fig. 13b clearly shows that the stress of the inner tube of CBRB-6 exceeded the yield load to dissipate energy at δ=1/147, where both L1 and L3 remained in the elastic phase and the stress variation began to level off. As a corollary, even when the energy dissipation segment of the cast connector increased closer to the ultimate strength, corresponding to the transition segment, it can stably transfer load and the connection segment can alleviate the stress concentration of the connection that is connected with the frame. The fracture of the specimen CBRB-1 occurred due to flexural buckling of the connection segment at δ^{-}=1/147, which matches the observation that the stress value of the L1 is close to that of L2, but BRB had not yet yielded.

Significantly, the energy dissipation segment (L2) is the region of maximum stress for the whole specimen in any loading phase, which suggests the feasibility of protecting the other components by weakening the cross-section of L2 to concentrate most of the stresses in the energy dissipation segment. The stress distribution result shows that the L1 and L2 of the improved cast connector are consistently maintained in elasticity, which ensures stable force transmission in the CBRB system while avoiding brittle fracture due to residual stress in traditional welded gusset plates. The energy dissipation segment of the cast connector first turns into plasticity and is followed by the inner core of BRB in a plastic state. This condition achieves the goal of the system to dissipate earthquake energy by stages.

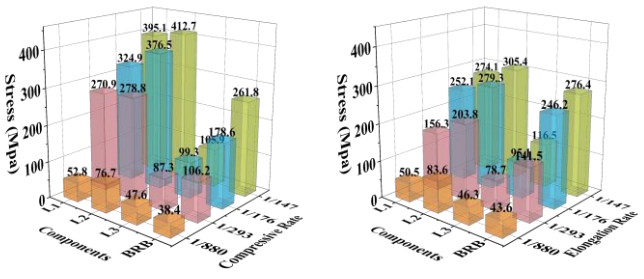

(a) CBRB-1

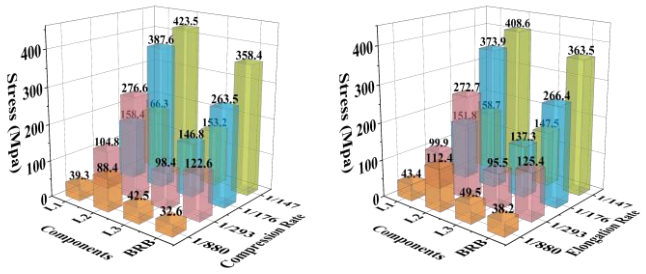

(b) CBRB-6

Fig. 13 Comparison of stress distribution of components for CBRB-1 and CBRB-6

4.4. Energy dissipation behavior

The key point of this research is to examine the energy dissipation capacity of specimen by utilizing hysteretic curves. Fig. 14 provides experimental loops for both loading histories of all specimens, where the hysteresis loop is very narrow during early cycles when the specimen is in the elastic stage and the energy dissipation is small. As the loading progresses, the specimen starts to dissipate large quantities of energy. Thus, the hysteresis loop becomes full. These curves shows a slight slip spring as specimens under tensile–compressive transformation are noticeable. A possible explanation for this condition may be that certain gaps are inevitably left during the assembly of each component. The hysteresis loop of the improved specimen is full, in which the ultimate bearing capacity increases loop by loop and the energy dissipation performance is better than that of the hysteresis loops of the specimens CBRB-1 and CBRB-2, which exhibit a scattered distribution in curves. This discrepancy could be attributed to the flexural buckling that occurred before a large amount of energy was dissipated in the plastic stage for the Group 1 specimens, which leads to severe stiffness degradation of the cast connector. Tension–compression imbalance remains most marked in the early loading process.

Data of CBRB-3–CBRB-5 show that the hysteresis loop becomes long and narrow, exhibiting a more obvious pinching phenomenon as the length of the energy dissipation segment increases. The main cause for this condition is that the bending behavior gradually predominates axial behavior as the slenderness ratio of the energy dissipation segment increased. Another important finding is that the imbalances between the tension and compression loading worsened as the length of the energy dissipation segment increased. This condition happens in the long energy dissipation segment, which generates a certain buckling when compressed, resulting in a few softened regions that are not conducive to transfer tensile loads. The specific focus is that the total area of hysteresis loops increases with the length of the energy dissipation segment at that time for the same cross-sectional area of the energy dissipation segment. This idea suggests that the energy absorption capacity of the specimen benefited from the increasing length of the energy dissipation segment. To ensure that a certain axial deformation capacity of the cast connector can dissipate a large amount of energy without instability, the slenderness ratio of the energy dissipation segment should be maintained at 16.72–17.47. Remarkably, the hysteresis loop area increases with the increase in the axial force overstrength coefficient, but this result is not significant at CBRB-8 (n = 0.845). This special phenomenon occurred because the rigidity of the cast connector reached a level that caused the assembled BRB to become a weak member, thus resulting in local instability at the late loading stage, which is unfavorable to the continuous energy dissipation for the specimen. Therefore, the axial force overstrength coefficient should be set within a reasonable range to ensure the energy dissipation performance of cast connectors. The hysteresis loop area also tends to increase with the increase in the cross-section area of the energy dissipation segment. Also, with the influence of the axial force overstrength coefficient on the energy dissipation of the system in stages taken into consideration, the optimal ratio of the cross-sectional area of the energy dissipation segment to the cross-sectional area of the inner tube should be in the range of 0.924–0.954.

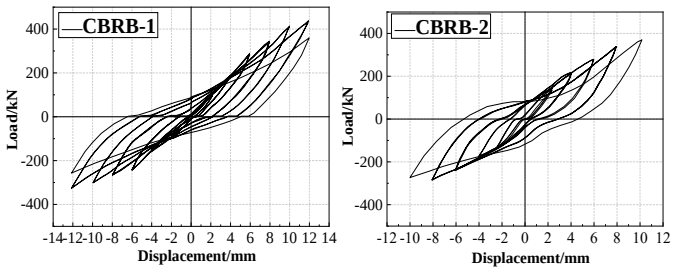

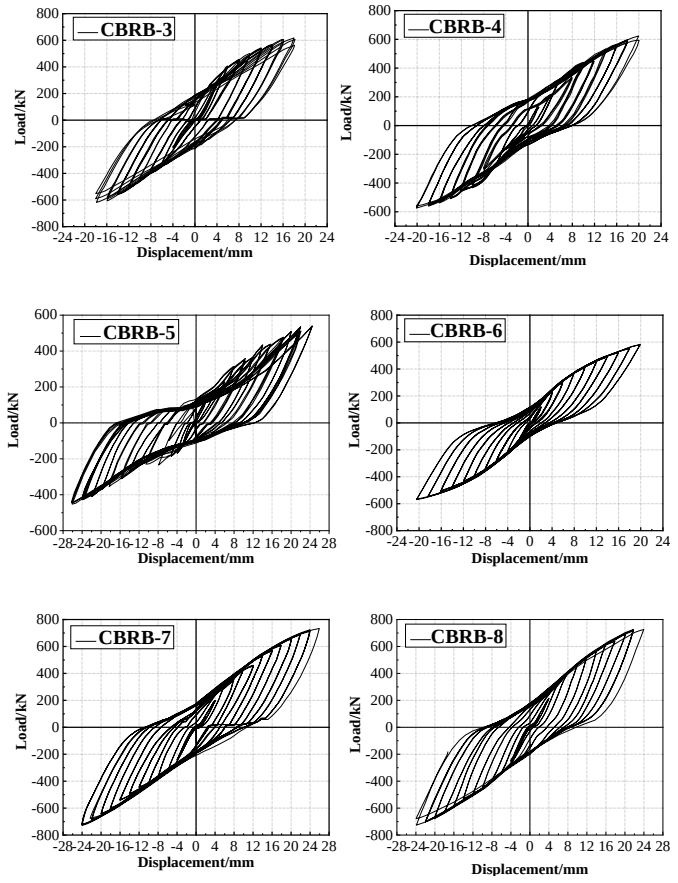

Fig. 14 Hysteretic curves of specimens

The energy dissipation coefficient, E , may have a large significance for the energy dissipation performance of the member, which can be obtained by the calculation diagram as shown in Fig. 15.

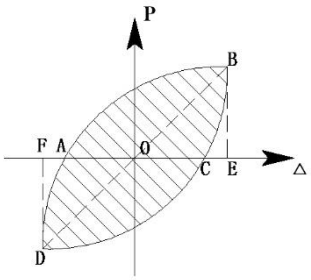

Fig. 15 Calculation diagram of energy dissipation coefficient E

where $S_{ABC+CDA}$ is the area enclosed by the hysteresis loops. $S_{\Delta OBE+\Delta ODF}$ is the sum of the areas of ΔOBE , and ΔODF can be calculated according to Equation (11)

$$E=\frac{S_{ABC+CDA}}{S_{\Delta OBE+\Delta ODF}} \tag{11}$$

Table 4 compares the energy dissipation coefficient of all specimens. The energy dissipation coefficient of the improved specimens is in the range of 1.23–1.48, which is larger than the energy dissipation coefficients of 1.06 and 1.18 of the specimens before the improvement. Evidence from this condition suggests that the improved method for reinforcing the end and improving the cross-shaped section area of the cast connector strengthens the energy dissipation performance of the specimens. Notably, data from CBRB-3–CBRB-5 show that the energy dissipation coefficient E increases with successive 50 mm increases in the length of the energy dissipation segment. Table 4 shows the positive correlation between the overstrength coefficient and energy dissipation capacity before the overstrength coefficient reaches 0.845. The overstrength coefficient affects the axial deformation of the cast connector observed in Fig. 11, yet its

increase will also increase the space for plastic development in the energy dissipation segment. These findings are in line with the data from the total area of hysteresis loops.

Table 4
The energy dissipation coefficient

Number	CBR B-1	CBR B-2	CBR B-3	CBR B-4	CBR B-5	CBR B-6	CBR B-7	CBR B-8
E	1.06	1.18	1.33	1.38	1.43	1.23	1.48	1.42

4.5. Skeleton curves

The ultimate bearing capacity of specimens identified in these cycle responses is presented in Fig. 16. The skeleton curves of the specimens with different parameters have a similar variation trend, including elastic, hardening, and plastic stages. The specimens are all elastically deformed within 4 mm displacement, and the ultimate bearing capacity basically increases linearly with displacement. The specimens entered the elastic–plastic stage, and the bearing capacity grows at a slower rate with loading displacements. In the plastic stage, the growth of the bearing capacity of the specimen was reduced obviously until the load finally reached the maximum. Notably, the displacement of Group 2 specimens entering the plastic stage is greater than that of the Group 1 specimens, thereby showing that the improved specimens have higher ductility. The results demonstrate that the process of increasing the width–thickness ratio of energy dissipation plate and stiffener and casting the right-angle tip tightly within a certain length of the cast connector is useful in developing the plasticity of the energy dissipation segment and increasing the bearing capacity of the member. For CBRB-3–CBRB-5, a clear trend of the decreased bearing capacity is found, along with the component entering the plastic stage later as the length of energy dissipation segments increases. Furthermore, the changing trend of bearing capacity for CBRB-3 and CBRB-4 is similar, where the curves come closest to coinciding in shape. Yet, the bearing capacity of CBRB-5, which has a long energy dissipation segment. is dramatically lower than that of CBRB-3 and CBRB-4, which have a short energy dissipation segment. These results represent the only a small part of the tension–compression region of the energy dissipation segment entering the plastic stage and reaches the ultimate strength where the bearing capacity is reduced significantly as the energy dissipation segment increases once a certain threshold of the slenderness ratio is achieved. The skeleton curves of the specimens CBRB-6, CBRB-4, CBRB-7, and CBRB-8 are symmetrical in compression and tension. The single most striking observation to emerge from the data comparison is that no significant differences were found in the development trend of skeleton curves of these specimens at the elastic stage and are followed by a positive correlation between the overstrength coefficient of axial force and bearing capacity at the plastic stage, as shown in Fig. 16c. This finding further confirms the association between the overstrength coefficient of axial force and bearing capacity, namely, that a high overstrength coefficient of axial force corresponds to a severe degree of plastic development of the energy dissipation segment.

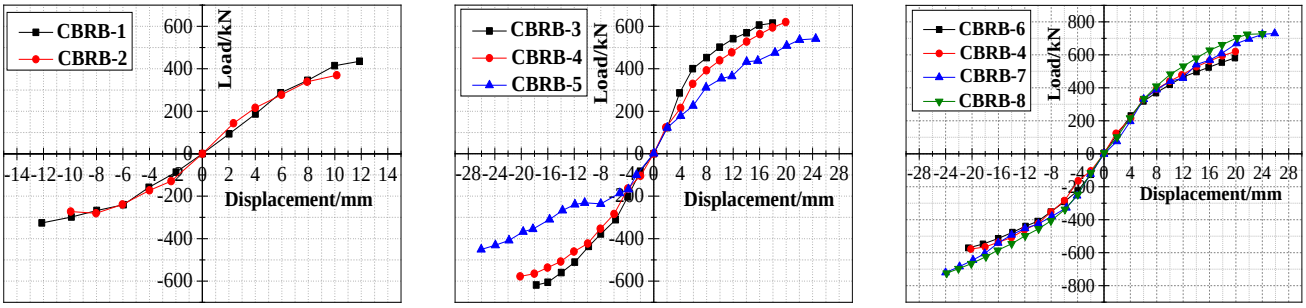

(a) CBRB-1 and CBRB-2 (b) CBRB-3~CBRB-5 (c) CBRB-6~CBRB-8

Fig. 16 Skeleton curves of specimens

4.6. Stiffness degradation

To further describe the degree of stiffness degradation of the specimen during the test, an average stiffness degradation curve is presented. The average stiffness is defined as the ratio of the sum of absolute values of tensile and compressive load peaks to the sum of corresponding displacement extremes. The average stiffness K_i can be expressed as

$$K_i = \frac{|P_i^+| + |P_i^-|}{|\Delta_i^+| + |\Delta_i^-|} \tag{12}$$

where $|\Delta_i^{\pm}|$ and $|P_i^{\pm}|$ are the extreme displacement and peak load in tension and compression at i loading cycle, respectively. Fig. 17 shows the summary of the stiffness degradation for each specimen. This figure clearly shows that the stiffness degradation rate at the initial stage of loading is fast, which corresponds to the fact that the cast connector bore the brunt of energy dissipation, and then gradually slows down as a result of the inner tube of BRB for supplementary energy dissipation. Afterward, the inner tube yielded and the cast connector entered the plastic stage, which corresponds to the slight acceleration of the stiffness degradation rate of the specimen. Fig. 17b also shows that the value of the initial stiffness of the specimen decreased with the increase in the length of the energy dissipation segment. No significant differences were found between stiffness degradation rates for these specimens at the initial stage of loading. The rigidity degeneration curve of CBRB-5 is less steep compared with that of CBRB-3 and CBRB-4 in the late loading stage, which may be due to the bending behavior gradually predominating the axial behavior of energy dissipation segment, thereby causing the slower development of plasticity. A closer comparison of the curves in Fig. 17c shows that the trend of stiffness degradation of those specimens is approximate, and the stiffness degradation trend appeared to be unaffected by the overstrength coefficient of axial force.

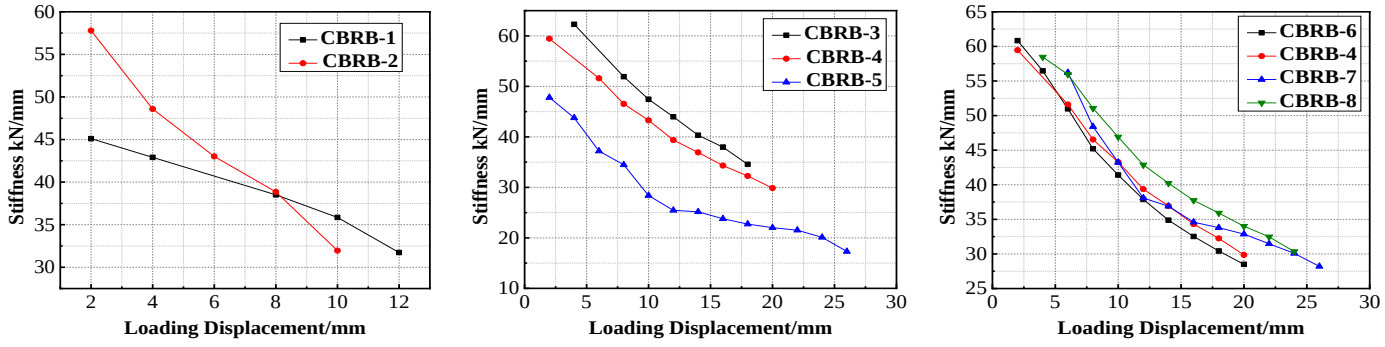

(a) CBRB-1 and CBRB-2 (b) CBRB-3~CBRB-5 (c) CBRB-4, CBRB-6~CBRB-8

Fig. 17 Stiffness degradation curves

5. Conclusions

A type of BRB with ductile cast connectors was developed to address the inability of the conventional brace system to fully perform energy dissipation due to premature buckling of the brace and the brittle fracture of the gusset plate. The seismic behavior of the proposed members was evaluated by testing two groups of full-scale specimens before and after improvement subject to cyclic loadings. The main parameters are the lengths of energy dissipation segment and axial force overstrength factors, and their influences on the seismic behavior of specimens were investigated. The major findings of this study are summarized as follows:

(1) The failure mode of the Group 2 specimens belongs to ductile failure, whereas the Group 1 specimens suffered brittle fracture at an early stage, thereby confirming that the improved method for reinforcing the end and improving the cross-shaped section area of the cast connector can help prevent the local buckling of connection segments and strengthen the seismic performance of the specimens effectively.

(2) The greatest axial deformation of the CBRB system was concentrated on the cast connector, which ensures continuous and steady energy dissipation for BRB. The maximum stress position of the whole specimen is in the energy dissipation segment, which maintains the connection and transition segments in an elastic phase at all times, thereby enabling the transition segment to transfer load stably and relieving the stress concentration in the connection segment, thus avoiding the fracture of the gusset plate of SCBFs.

(3) The increase in the length of the energy dissipation segment enhances the energy dissipation capacity of the specimen considerably, whereas the axial deformability and the bearing capacity are reduced with as the energy dissipation segment increases once a certain threshold of the slenderness ratio is achieved. The results of this study demonstrate that the members with energy dissipation segments with slenderness ratios in the range of 16.72–17.47 have the best seismic performance.

(4) The axial force overstrength factor represents a space for plastic development in the energy dissipation segment, which is proportional to the cross-sectional area of the energy dissipation segment. However, an excessively large axial force overstrength factor is unfavorable for energy dissipation of the specimen in stages and should be less than 0.845. The optimal ratio of the cross-sectional area of the energy dissipation segment to that of the inner tube should be in the range of 0.924–0.954.

(5) All specimens showed obvious stiffness degradation, and the stiffness degradation law is closely related to the phased energy dissipation of the member. A longer energy dissipation segment corresponds to a lower value of the initial stiffness of the specimen.

This study provides a comprehensive assessment of the seismic performance of buckling-restrained brace with ductile cast connectors, and the findings of this research provide insights for future work into assembly ductile connectors of bracing systems. A limitation of this study is that the cast connector is made of Q235 steel, and more research using controlled tests is needed for cast connectors made of different materials, such as low-yield-point steel. Unfortunately, although the increase in the length of the energy dissipation segment improves the energy absorption capacity to a certain extent, it also enhances the bending behavior. To address this issue, an effective way is to use a ferrule to add to the energy dissipation segment of the ductile cast connector to improve the axial compression behavior of the long energy dissipation segment. Further studies are needed to validate whether this measure can improve the stability of the energy dissipation segment to reduce the effect of the excessively long energy dissipation segment on the energy dissipation of the CBRB system.

Acknowledgment

Financial support for this research is provided by the National Natural Science Foundation of China (51968044, 51568040) and the National Key R&D Program of China (2019YFD1101003). Test conditions were supplied by the Engineering Research Center of the Ministry of Education for Earthquake Prevention and Disaster Reduction of Civil Engineering in Western China.

References

[1] Sabelli R., Roeder C.W. and Hajjar J.F., “Seismic design of steel special concentrically braced frame systems: a guide for practicing engineers”, NEHRP Seismic Design Technical Brief No.8, Gaithersburg, MD, 2013.
[2] Park R., Billings I.J., Clifton G.C., Cousins J. and Walker G., “The Hyogo-Ken Nanbu earthquake (the Great Hanshin Earthquake) of 17 January 1995”, Bulletin of the New Zealand Society for Earthquake Engineering, 28(1), 1-98, 1995.
[3] Astaneh-Asl A., Goel S.C. and Hanson R.D., “Cyclic out-of-plane buckling of double-angle bracing”, Journal of Structural Engineering, 111(5), 1135-1153, 1985.
[4] Goel S.C. and El-Tayem A.A., “Cyclic load behavior of angle x-bracing”, Journal of Structural Engineering, 112(11), 2528-2539, 1986.
[5] Rabinovitch J.S. and Cheng J.J.R. “Cyclic behavior of steel gusset plate connectors”, Structural Engineering Report No. 191, University of Alberta, Alberta, Canada, 1993.
[6] Cheng J.J.R, Yam M.C.H. and Hu S.Z., “Elastic buckling strength of gusset plate connectors”, Journal of Structural Engineering, 120(2), 538-559, 1994.
[7] Brown V.L.S. Stability of gusseted connections in steel structures, D.E., Department of Civil Engineering, University of Delaware, Delaware, USA, 1998.
[8] Walbridge S.S., Grondin G.Y. and Cheng J., “An analysis of the cyclic behaviour of steel gusset plate connections”, Journal of Constructional Steel Research, 46(1), 449-450, 1998.
[9] Sheng N., Yam C.H. and Lu V.P., “Analytical investigation and the design of the compressive strength of steel gusset plate connections”, Journal of Constructional Steel Research, 58(11), 1473-1493, 2002.
[10] Tremblay R., “Inelastic seismic response of steel bracing members”, Journal of Constructional Steel Research, 58(5), 665-701, 2002.
[11] Shaback B. and Brown T., “Behaviour of square hollow structural steel braces with end connections under reversed cyclic axial loading”, Canadian Journal of Civil Engineering, 30(4), 745-753, 2003.
[12] Uriz P. and Mahin S.A., “Seismic performance assessment of concentrically braced steel frames”, Proceedings of the 13th World Conference on Earthquake Engineering, Vancouver, BC, Canada, 2004.
[13] Roeder C.W., Lehman D.E., Clark K., Powell J. and Wei C.Y., “Influence of gusset plate connections and braces on the seismic performance of X-braced frames”, Earthquake Engineering & Structural Dynamics, 40(4), 355-374, 2011.
[14] Roeder C.W., Lumpkin E.J. and Lehman D.E., “A balanced design procedure for special concentrically braced frame connections”, Journal of Constructional Steel Research, 67(11), 1760-1772, 2011.
[15] Lehman D.E. and Roeder C.W., “Improved Seismic Design of Concentrically Braced Frames and Gusset Plate Connections”, American Society of Civil Engineers Structures Congress, Vancouver, British Columbia, Canada, 1-10, 2008.
[16] Yoshino T. and Karino Y., “Experimental study on shear wall with braces: Part 2. Summaries of technical papers of annual meeting”, Architectural Institute of Japan, Structural Engineering Section, Tokyo, Japan, 11, 403-404, 1971.
[17] Clark P.W., Aiken I.D., Kasai K., Ko E. and Kimura I., “Design procedures for buildings incorporation hysteretic damping devices”, Proceedings of the 69th Annual SEAOC Convention, Sacramento, USA, 355–372, 1999.
[18] Nakamura H., Maeda Y. and Sasaki T., “Fatigue Properties of Practical-Scale Unbonded Braces”, Nippon Steel Technical Report, 82, 51-57, 2000.
[19] Koetaka Y., Narihara H. and Tsujita O., “Experimental study on buckling restrained braces”, Proceedings of the Sixth Pacific Structural Steel Conference, Beijing, China, 15-17, 2001.
[20] Wakabayashi M., Nakamura T., Kashibara A., Morizono T. and Yokoyama H, “Experimental study of elasto-plastic properties of precast concrete wall panels with built-insulating braces”, In: Summaries of Technical Papers of Annual Meeting, Architectural Institute of Japan, Structural Engineering Section, Tokyo, Japan, 10, 1041-1044, 1973.
[21] Mochizuki S., Murata Y., Andou N. and Takahashi S., “Experimental study on buckling of unbonded braces Under axial forces: Parts 1&2. Summaries of technical papers of annual meeting” , Architectural Institute of Japan, Structural Engineering Section, Tokyo, Japan, 1623-1626, 1979.
[22] Sridhara B.N., “Sleeved column-as a basic compression member”, Proceedings of the 4th International conference on steel structures and space frames, Singapore, 181-188, 1990.
[23] Iwata M., Kato T. and Wada A., “Buckling-restrained braces as hysteretic dampers”, Proceedings of the Behavior of Steel Structures in Seismic Areas: STESSA 2000, Montreal, Canada, 33-38, 2000.
[24] Xie L.Q., Wu J., Shi J.H. and Zhu Y.Q., “Influence of the core-restrainer clearance on the mechanical performance of sandwich buckling-restrained braces”, Advanced Steel Construction, 16(1), 37-46, 2020.
[25] Tada M., Kuwahara S. and Yoneyama T., “Horizontally loading test of the steel frame braced with double-tube members”, Annual Technical Papers of Steel Structures, 1, 203-208, 1993.
[26] Lai J.W. and Tsai K.C., “Research and application for buckling restrained braces in Taiwan”, 2004 ANCER Annual Meeting: The Sheraton Princess Kaiulani, Honolulu, Hawaii, 2004.
[27] Yin Z.Z. and Wang X.L., “Finite component analysis of constrained buckling support with contact ring”, Journal of Lanzhou University of Technology, 34(5), 122-126, 2008. (in Chinese)
[28] Yin Z.Z. and Bu F.C., “Overall stability analysis of improved buckling restrained braces”, The Open Civil Engineering Journal, 10(1), 61-75, 2016.
[29] Yin Z.Z., Chen W., Chen S.L. and Wang X.L., “Experimental study on buckling support of improved double steel tube”, Journal of Building Structures, 35(09), 90-97, 2014.
[30] Fleischman R.B., Sumer A. and Li X.J., “Development of modular connections for steel special moment frames”, American Society of Civil Engineers Structures Congress 2004, Nashville, Tennessee, United States, 1-9, 2004.
[31] Fleischman R.B. and Sumer A., “Optimum arm geometry for ductile modular connectors”, Journal of Structural Engineering, 132(5), 705-716, 2006.
[32] Oliveira J.C.D., Packer J.A. and Christopoulos C., “Cast steel connectors for circular hollow section braces under inelastic cyclic loading”, Journal of Structural Engineering, 134(3), 374-383, 2008.
[33] Gray M.G., “Cast steel yielding brace system for concentrically braced frames”, School of Graduate Studies - Theses, 2012.
[34] Khan K. and Yan J.B., “Numerical studies on the seismic behaviour of a prefabricated multi-storey modular steel building with new-type bolted joints”, Advanced Steel Construction, 17(1), 1-9, 2021.
[35] Hou Z.X., Gong C., Zhang Y., Sun Y.Z., Jiang J. and Li G.Q., “Seismic behavior of bolted connections with slot bolt holes at ambient and elevated temperature”, Advanced Steel Construction, 14(4), 651-667, 2018.
[36] Liu J.B. Theoretical study on design of anti-buckling support and buckling support frame, D.E., Tsinghua University, Beijing, China, 2005.
[37] GB50017-2003. Code for design of steel structures, China Architecture & Building Press, Beijing, China, 2006.
[38] GB/T 228–2002. Metallic materials-tensile testing at ambient temperature, China Standard Press, Beijing, China, 2002.

Advanced Steel Construction – Vol. 18 No. 1 (2022) 446–452
DOI:10.18057/IJASC.2022.18.1.3

TEACHING-LEARNING BASED OPTIMIZATION METHOD CONSIDERING BUCKLING AND SLENDERNESS RESTRICTION FOR SPACE TRUSSES

Felipe Faustino Kunz [1], Patrick dos Santos e Santos [2], Emanuely Ugulino Cardoso [3], Rene Quispe Rodríguez [4, *], Lucas Queiroz Machado [5] and Alana Paula da Costa Quispe [6]

[1] *Department of Civil Engineering, Mato Grosso State University, Brazil*
[2] *Department of Mechanical Engineering, Santa Catarina State University, Brazil*
[3] *Faculty of Technology, University of Brasilia, Brazil*
[4] *Department of Mechanical Engineering, Federal University of Santa Maria, Brazil*
[5] *IMPEE, Heriot-Watt University, Edinburgh, UK*
[6] *Department of Civil Engineering, Federal University of Santa Maria, Brazil*
* *(Corresponding author: E-mail:* rene.rodriguez@*ufsm.br)*

ABSTRACT

The structural performance of a building is a function of several parameters and constraints whose association may offer non unique solutions which, however, meet the design requirements. Therefore, an optimization routine is needed to determine the best solution within the set of available alternatives. In this study, the TLBO method was implemented for weight-based optimization of space trusses. The algorithm applies restrictions related to the critical buckling load as well as the slenderness ratio, which are the basis to obtain reliable and realistic results. To assess the capability of the TLBO method, two reference cases and a transmission tower are subjected to the optimization analysis. In the transmission tower analysis, however, a more realistic approach is adopted as it also considers, through a safety factor, the plastic behavior in the critical buckling load constraint. With no optimization, the ideal weight increases by 101.36% when the critical buckling load is considered in the first two cases, which is consistent with the expected behavior. If the slenderness of the elements is also restricted, the ideal weight now rises by 300.78% from the original case and by 99.04% from the case where only the critical buckling load restriction is applied. Now, considering the critical buckling load and slenderness restriction with the TLBO method applied, a 18.28% reduction in the ideal weight is verified. In fact, the proposed optimization procedure converged to a better solution than that of the reference study, which is based on the genetic algorithms method.

ARTICLE HISTORY

Received: 8 August 2020
Revised: 24 May 2021
Accepted: 25 May 2021

KEYWORDS

3D truss;
TLBO;
Critical buckling load;
Slenderness ratio

1. Introduction

The design process requires a series of steps in order to deliver an outcome which is efficient regarding material consumption and cost, and, along with it, meets the design and safety standards. Optimization efforts are generally applied to identify the most suitable solution to the problem from a wide set of design alternatives subjected to restrictions and constraints [1]. The solution can be obtained by minimizing or maximizing an objective function defined according to the governing parameters and imposed restrictions. The optimization routine can be driven by diverse leading and, sometimes, competing fields, so that the objective function can assume distinct formats depending on the driving parameter, e.g., weight, displacement, natural frequency, tension, buckling, etc.

Currently, there is a vast collection of optimization methods applicable to a multitude of problems, especially the nature-inspired meta-heuristic methods. Most well-known and explored processes are based on the genetic algorithms (GA), as proposed by Holland [2]. It belongs to a wider category of evolutionary algorithms which are based on the theory of evolution presented by Darwin, i.e., that evolution occurs through the selection of the most suitable individual. Holland [2] points out that methods such as GA, although effective, require many control parameters, whose ideal values are difficult to determine. Addressing this limitation, Rao et al. [3] presented the teaching-learning-based optimization (TLBO) algorithm, which emulates the teaching interaction between teacher and student, and seeks to solve problems and obtain results with low computational cost and high consistency. Camp and Farshchin [4] modified the method to allow its application to the optimization of space trusses and verified that it was able to provide better results when compared to other population-based techniques. The TLBO method presents attractive features such as easy implementation, versatility, does not require design parameters to direct the search, and has low computational cost.

Lattice structures are widely applied in engineering as they provide excellent resistance/weight ratio. Despite the advantage presented by steel structures, this structural system is prone to collapse due to buckling, as the structure can suddenly or partially collapse without warning [5]. The buckling phenomenon is characteristic of thin sections in compression zones where the overall buckling depends on the attributes of their individual components, which are related with each other influencing the buckling loads [7].

Buckling failure is a critical factor when it comes to slender structures, which is a characteristic feature of metal structures. Caglayan and Yuksel [6] investigated a roof structure failure due to overload caused by the accumulation of snow. Augente and Parisi [7] investigated the failure of a roof structure in the construction phase due to a gust of wind. They pointed out in their results that the steel lattice structure collapsed due to buckling, which propagated causing its total collapse. Episodes like this justify the special attention that must be paid to the buckling restrictions imposed on the structures.

Moreover, there are vast references in the application of optimization methods in the design of steel structures. Safari and Maheri [8] used graph theory for improving the GA and applied it for searching the optimal brace position in 2D steel frames. Fawzia and Fatima [9] presented a parametric optimization methodology for finding the optimum position of steel outrigger systems in high composite buildings, analyzing buildings with 28, 42 and 57 floors. Doğan et al. [10] investigated the effect of the behavior of joints into the design of steel frames using the Hunting Search Algorithm (HSA) to this end. They presented a set of optimum design structures and compared them with the ones obtained by the Particle Swarm Optimization method (PSO) available in the literature. More recently, Gomez et al. [11] applied topology optimization to high buildings under wind stochastic loads. In this study the optimization was accounted using a gradient-based method, demonstrating high efficiency for tall buildings as well.

Haghpanah and Foroughi [12] analyzed the optimization of space trusses using the TLBO method considering critical buckling load restriction values and their percentages to simulate imperfection effects.

In this work, the TLBO was used to optimize space trusses with the objective of minimizing the total weight of the structure. The main focus was to verify the effect of considering critical buckling load and slenderness restrictions on the optimization results. First, a brief theoretical concept is presented followed by a description of the TLBO method including the changes made by Camp and Farshchin [4], which were also considered of this study. Lastly, three case studies are presented to validate and assess the method.

2. Theoretical foundation

2.1. Truss

The truss is a practical and economical structural solution in many applications, e.g., construction of bridges, roof structures, transmission telecommunications towers, among others. By definition, trusses are structures that consists of bars, straight and rigid, subjected to loading at the nodes. Taking into account

that truss elements are connected by frictionless hinged joints at their ends, they do not experience bending moments nor shear forces, i.e., truss members only experience axial forces [13]. However, in practice, trusses can have welded or non frictionless bolted joints in addition to imperfections, which can generate bending moments in the structure and induce non-linear behavior [14]. Since truss structures are in general composed of thin elements and can only support a small lateral load, they are liable to the occurrence of buckling [15].

2.2. Buckling

Some structural elements may be subjected to compressive loads which, depending on the length and slenderness of the part, are sufficient to cause a lateral deflection. This phenomenon is referred to as buckling and the maximum load that an element can withstand on the buckling threshold is called critical load (P_{cr}), also known as Euler load [16].

The part will be in stable equilibrium if $P \leq P_{cr}$ and in neutral equilibrium if $P = P_{cr}$. However, if $P \geq P_{cr}$ it is said that the element is in unstable equilibrium. At stable equilibrium, the element remains in the initial position without experiencing lateral displacement. In the case of an ideal column, theoretically, it would remain straight even with the increase of load until its rupture or yielding. However, when the load P_{cr} is reached, a small lateral force F is able to bend the element and it will remain in the bent position even with the removal of the force F. The element will only to return to its initial position if the load in relation to the critical load is reduced [16].

Clearly, the point at which the state changes from stable to unstable is a bifurcation point, which is represented by the critical load. In structural design, the stress state in all elements is expected to fall within the stable equilibrium domain, so that $P \leq P_{cr}$. Since the buckling is related to the flexural strength, the P_{cr} value can be determined by the beam's differential equation, which relates the element's internal bending moment M to its deflected position, given by equation (1):

$$EI\frac{d^2v}{dx^2} = M \tag{1}$$

Applying the considerations for the deflected bars and the moment at the joints equal to zero as a boundary condition, equation (2) yields the following solution:

$$P_{cr} = \frac{\pi^2 EI}{L^2} \tag{2}$$

Thus, the critical buckling stress for the bars can be expressed by equation (3):

$$\sigma_{cr} = \frac{\pi^2 E}{\lambda^2} \tag{3}$$

$$\lambda = \frac{L}{r} \tag{4}$$

where, E is the elastic modulus of the material, I is the moment of inertia of the cross section, L is the length of the column, λ is the slenderness index, r is the radius of rotation of the bar, P_{cr} is the critical buckling load and σ_{cr} is the critical buckling stress. Therefore, the column will buckle around the axis with the lowest moment of inertia [12].

The theory presented so far applies to the ideal case. However, as already mentioned, in practice the structures can present residual stresses caused by geometric imperfections from the manufacturing and construction processes, and eccentricities from the imposed loads [16]. In the case of metallic truss structures, the nonlinear behavior of the model is difficult to be implemented, as it requires the combination of nonlinear sources, the definition of specific parameters, and high computational experience [14]. Thus, safety factors are introduced to compensate these differential effects and provide a more realistic calculation. These factors are specified in the American Institute of Steel Construction (AISC) [17] and are described by equations (5) to (8). The calculation of the safety factor varies according to the value of the slenderness index of the column. These considerations were used in problem 3 of this study.

If $\lambda \geq C$

$$\sigma_{cr} = \frac{12\pi^2 E}{23\lambda^2} \tag{5}$$

If $\lambda \geq C$

$$\sigma_{cr} = \sigma_y\left(1 - \frac{\lambda^2}{2C^2}\right)n \tag{6}$$

$$n = \frac{5}{6} + \frac{3\lambda}{8} - \frac{\lambda^3}{8C^3} \tag{7}$$

$$C = \sqrt{2\pi^2 E/\sigma_y} \tag{8}$$

The Brazilian technical standard that regulates the elaboration of steel structure projects is the NBR 8800 [18], applied to structures formed by rolled or welded steel profiles, of tubular section and with connections made with welding or screws. It is recommended that the slenderness index of the bars should not exceed 300, and that the slenderness index of the compressed bars should not be higher than 200 [18]. These parameters are adopted as the slenderness restrictions in the problems analyzed in this study.

2.3. Problem formulation

Structural optimization procedures, in general, focus on determining the set of parameters that minimizes the weight of the structure. When the geometry of the structure is fixed, the problem focuses on finding the cross sections for the elements in a way that minimizes the weight of the structure while respecting the restrictions. The available cross-sectional areas can be restricted to a range of values, being obtained in a discrete or continuous manner at the beginning of the process. The structure of the optimization problem can be described by the following mathematical formulation.

Objective function:

$$W = \sum_{i=1}^{m} \gamma A_i L_i \tag{9}$$

Constraints:

$$\sigma^L \leq \sigma_i \leq \sigma^U \tag{10}$$

$$\sigma^{cr} \leq \sigma_j \leq 0 \tag{11}$$

$$\delta^L \leq \delta_k \leq \delta^U \tag{12}$$

$$\lambda_i \leq \lambda_{j,t}^U \tag{13}$$

$$A_L \leq A_i \leq A_U \tag{14}$$

$$i \in \{1,2,\dots,m\},\ j \in \{1,2,\dots,m\},\ t \in \{1,2,\dots,m_t\},\ k \in \{1,2,\dots,n\}$$

where W is the weight function, m is the number of components,n is the number of nodes, γ is the specific gravity of the material. For each member i, A_i is the area of the cross section, L_i is the length, σ_i is the stress, and λ_i is the slenderness index. Regarding the constraints, σ^L is the lower limit stress that is equivalent to the maximum compressive stress, σ^U is the upper limit stress that is equivalent to the maximum tensile stress, j designates that the element is under compression andσ^{cr} is the critical buckling stress described in section 2.2. A_L and A_U are the minimum and maximum areas, respectively, for each node $k$analyzed. δ^L and $\delta^U$are the lower and upper displacement limits, which are associated with the negative and positive coordinate displacements, respectively. t indicates the members subjected to traction. $\lambda_j^U$and λ_t^U are the slenderness limits for members under compression and tension, respectively.

In this process, a mechanism known as penalty function is implemented to verify if the model complies with the restrictions. If an arrangement violates the restrictions, a penalty is applied to the result of the objective function for that case. The penalty will be proportional to the value of the sum of the violations. According to Camp [19], the penalized result helps to direct the focus of the research. The amount of penalties is calculated according to the following equations:

The deflection penalty is calculated as:

$$if: \sigma_L \leq \sigma_{cr}\ then\ \sigma_L = \sigma_{cr} \tag{15}$$

$$if: \sigma_L \leq \sigma_i \leq \sigma_U\ then\ \emptyset_\sigma^i = 0 \tag{16}$$

$$if: \sigma_i < \sigma_L\ or\ \sigma_i > \sigma_U\ then\ \emptyset_\sigma^i = \left|\frac{\sigma_i - \sigma_{L,U}}{\sigma_{L,U}}\right| \tag{17}$$

The total voltage penalty for design k is:

$$\emptyset_\sigma^k = \sum_{i=1}^{m} \emptyset_\sigma^i \tag{18}$$

The deflection penalty is calculated as follows:

$$if: \delta_L \leq \delta_{i(x,y,z)} \leq \delta_U\ then\ \emptyset_\delta^i = 0 \tag{19}$$

$$if: \delta_L < \delta_{i(x,y,z)} \; or \; \delta_{i(x,y,z)} > \delta_U \; then \; \emptyset_\delta^i = \left|\frac{\delta_i - \delta_{L,U}}{\delta_{L,U}}\right| \quad (20)$$

The total deflection penalty for design k is:

$$\emptyset_\delta^k = \sum_{i=1}^{m}\left[\emptyset_{\delta(x)}^i + \emptyset_{\delta(y)}^i + \emptyset_{\delta(z)}^i\right] \quad (21)$$

The calculation of the slenderness penalty is:

$$if: \lambda_i \leq \lambda_{j,t}^U \; then \; \emptyset_\lambda^i = 0 \quad (22)$$

$$if: \lambda_i > \lambda_{j,t}^U \; then \; \emptyset_\lambda^i = \left|\frac{\lambda_i - \lambda_{U(j,t)}}{\lambda_{U(j,t)}}\right| \quad (23)$$

The total slenderness penalty for design k is:

$$\emptyset_\lambda^k = \sum_{i=1}^{m} \emptyset_\lambda^i \quad (24)$$

The total penalty amount for the truss design k is the result of the sum of the penalties:

$$c^k = \left(1 + \emptyset_\sigma^k + \emptyset_\delta^k + \emptyset_\lambda^k\right)^\varepsilon \quad (25)$$

where ε is the positive penalty exponent, defined as 2 in this work, as also adopted by Camp and Farshchin [4]. Lastly, the penalty amount is applied to the weight determined for the truss design k:

$$F^k = w^k c^k \quad (26)$$

3. Teaching-learning-based optimization

The TLBO method is an optimization method whose main inspiration is the process of teaching and learning. It takes place in a classroom and resembles the relationship between teacher and student, as its ultimate goal is to make students increase their level of knowledge. It is assumed that the teacher is the most instructed individual in the class and will try to share his knowledge with the students so that they increase their level of knowledge. Rao et al [3] showed that the result is proportional to the level of the teacher, so he is able to increase the knowledge of a class from an initial level to a higher level.

In addition to the phase where the teacher is the vector guiding the process, it is understood that students can interact with each other. In this phase, they will be protagonists of the process by sharing knowledge collaboratively, which also contributes to raising the level of knowledge of the class. The evaluation of the performance of each student is carried out through an exam and the result is the grade. The final performance of the class can be described by the normal probability curve.

As previously mentioned, the method is divided into two phases, the teacher phase and the student phase. Next, both phases will be described in accordance with Rao et al [3], including the changes proposed by Camp and Farshchin [4].

3.1. Teacher Phase

In this phase, the method tries to model the influence of the teacher on the students of the class in such a way that the students try to update their knowledge according to the information provided by the teacher. At the teacher's phase, the students will increase their knowledge, that is, all students are influenced by the teacher. In practice, a teacher can only move the level of the classroom to a limited stage which is proportional to his capacity. This process is modeled by the following mathematical expressions:

$$X_{new}^k(j) = X_{old}^k(j) \pm \Delta(j) \quad (27)$$

$$\Delta(j) = T_F * r|M(j) - T(j)| \quad (28)$$

where, $X^k(j)$ is the student's grade k in the discipline j, which is, by analogy, the design variable j of the solution vector k. T_F is the teaching factor, r is a random number in the range between [0 1], $M(j)$ is the class average, and $T(j)$ is the teacher's status. The teaching factor T_F decides the average that will be changed and represents the teacher's ability. Its value can be chosen as 1 or 2, or randomly by the expression:

$$T_F = round[1 + rand(0,1)\{2-1\}] \quad (29)$$

The studies by Togan and Mortazavi [20] compared the use of the three possibilities for the value assumed by T_F, i.e., 1, 2 or a randomly generated number (equation 29), concluding that any of the three choices do not interfere in the final optimization result. For this work, the value 2 was used, the same used by Camp and Farshchin [4].

The work of Rao et al [21] and Rao and Patel [22] emphasize that the value of T_F is not a parameter, since an input value is not mandatory, as occurs in genetic algorithms, and because its value can be generated randomly by equation (29).

In this work, the TLBO method modified by Camp and Farshchin [4] was used, which provides or calculates the average of the average of students with weighted average, a principle calculated by Rao et al [3] in an arithmetic way. The M value is determined by the following expression:

$$M(j) = \frac{\sum_{k=1}^{N} \frac{X^k(j)}{F^k}}{\sum_{k=1}^{N} \frac{1}{F^k}} \quad (30)$$

where F^k is the weight of the penalized structure (Eq. (26)), and N is the population number.

The updated $X_{new}^k(j)$ value for each student will be accepted if the update value is better than the old $X_{old}^k(j)$. All values updated at the end of the teacher phase are retained and become input values for the student phase.

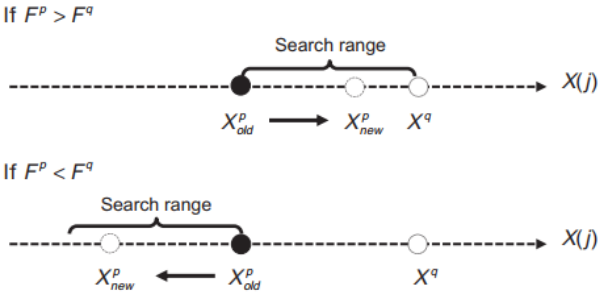

Fig. 1 Learner phase, [4]

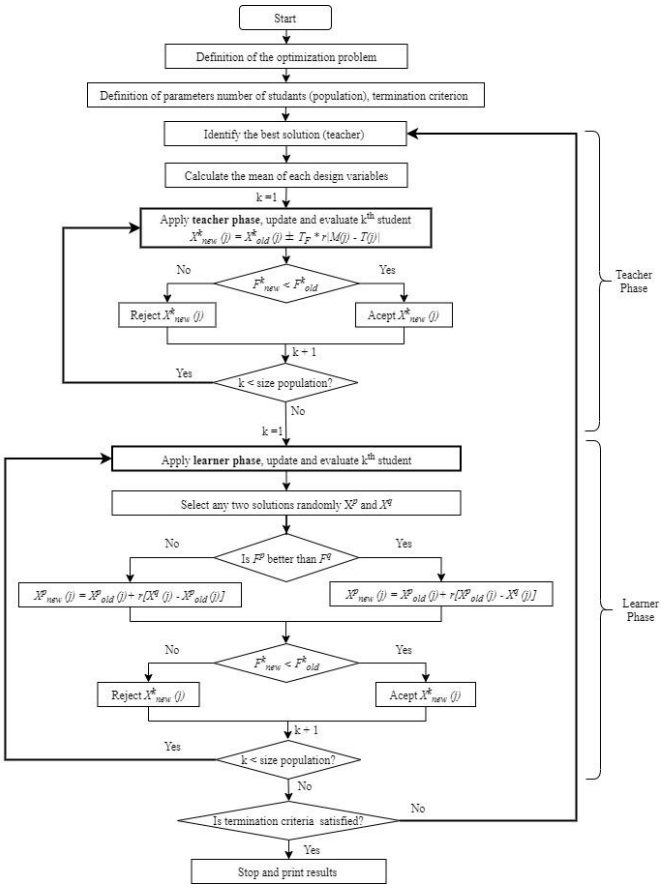

Fig. 2 Flowchart - TLBO Method, [3]

3.2. Learner Phase

This phase corresponds to the stage at which students learn through the interaction between themselves. At this stage, each student in the class randomly

interacts with another student. It is understood that a student will learn new things from another who has more knowledge. In this phase, each student is compared with another student in the class. The learning process in this phase occurs as follows:

(a) A student p is selected randomly in the class;
(b) A second student q is selected randomly, with $q \neq p$;
(c) F_p^k and F_q^k are calculated;

$$X_{new}^{p}(j) = \begin{cases} X_{old}^{p}(j) + r\left[X_{old}^{p}(j) - X^{q}(j)\right] \; if \; F_p^k < F_q^k \\ X_{old}^{p}(j) + r\left[X^{q}(j) - X_{old}^{p}(j)\right] \; if \; F_p^k \geq F_q^k \end{cases} \quad (31)$$

where, r is a random number in the range [0.1]. Fig. 1 illustrates the behavior of students in the process.

Fig. 2 presents a flowchart that describes the process of operation of the TLBO method.

3.3. Operation of the method

The computational procedure mimics the process described above, divided into the teacher and student phases. The TLBO method is a population-based method. According to Togan [23], the following analogy can be established between the TLBO and the ideal configuration of the structure: the students in the class represent the candidate configurations, each discipline represents the design variable (the steel section), and its combinations represent the variables of the project.

Next, the procedure for implementing the TLBO method will be described as presented by Rao et al [21].

Initialization of the problem:

Step 1: define the optimization parameters, number of students - population (*Pn*), number of groups - number of design variables (*Dn*), number of generations (*Gn*) and the limits of the design variables described in section 2.3.

The optimization problem is defined by the maximization function *w(x)* subjected to $x = x1, x2,...,xDn$. Where x_i are the design variables that must comply with the imposed restrictions.

Step 2: The population is initialized randomly according to its size, the number of design variables, and the design variables available.

$$population = \begin{bmatrix} x_{1,1} & x_{1,2} & \cdots & x_{1,D} \\ x_{2,1} & x_{1,1} & \cdots & x_{2,D} \\ \vdots & \vdots & \vdots & \vdots \\ x_{Pn,1} & x_{Pn,2} & \cdots & x_{Pn,D} \end{bmatrix} \begin{matrix} \rightarrow w_1(x) \\ \rightarrow w_2(x) \\ \rightarrow \quad \vdots \\ \rightarrow w_{Pn}(x) \end{matrix} \quad (32)$$

Step 3: teacher phase.

First, the weighted average grade of the population is calculated in rows and this will yield the class average grade in each discipline resulting in a $M_D = [m_1, m_2, \ldots, m_{Dn}]$. The best solution will interact with a teacher and try to evolve the students' knowledge towards their own level of knowledge. At this stage, the knowledge of each student will be influenced by the teacher (equation 27). Updated students are accepted if their knowledge is improved.

Step 4: learner phase.

The code receives the updated population vector (students) from the teacher phase. Students interact with each other randomly, as described in the student phase (section 3.2).

Step 5: stop criteria.

There two stop criteria, i.e., when the maximum iteration limit is reached at 200 or when the restrictions imposed by the optimization problem is met, see section 2.3. In this method, a penalty is applied to solutions that exceed the imposed restrictions (see section 3). If it does not meet the stop criteria, the process returns to step 3.

All the work was done using Matlab commercial software. The Matlab is a well known software that works to solve problems based on matrix analysis. The structural analysis process was implemented using the finite element method (FEM). The implemented program followed the following procedure: First, a code was created to insert the data, coordinates, incidence, loads, boundary conditions, division of groups and restrictions. Second, the structural analysis by the FEM is carried out, which includes calculation of the stiffness matrix, displacement, tension and penalty. This process works in parallel with the TLBO method, teacher and student phases.

4. Results and discussions

Three examples are addressed for discussion, where the first two are reference examples and the third is a tower approached by Galante and Onate [24] and Rajeev and Krishnamoorthy [25]. In the first two examples, the obtained results are compared against those published by Camp and Farshchin [4] to validate the code. The first is a 25-bar truss divided into 8 groups, the second a 72-bar truss divided into 16 groups, and the third a 160-bar tower divided into 16 groups. The population of 75 students was adopted, which, according to Camp and Farshchin [4], is an ideal value to obtain good results with low computational cost. The TLBO algorithm was implemented to perform a maximum of 200 iterations if convergence is not reached by then, which is the same criterion used by Camp and Farshchin [4]. The results are presented in the form of cross sections and ideal weight.

In addition, for each case, the optimization was repeated one hundred times in order to verify the uniformity of the results. The analyses studied in this paper were carried out in a laptop model I14-2640P, with Core i5 processor and 8GB RAM.

4.1. Problem 1: 25-bar tower

The 25-bar truss tower is shown in Fig. 3 and the applied loads are shown in table 1. For the optimization problem, the following parameters were assumed: elastic modulus of 68.95 GPa, density 2767.99 kg/m³, maximum nodal displacement of 8.89 mm and maximum permissible stress of 275.79 MPa. More details about the structure can be found in Camp and Farshchin [4].

To validate the code, the cross sections given by Camp and Farshchin [4] were used, ranging from 0.645 cm² to 21.935 cm², with an increase of 0.645 cm². For application of the buckling conditions, 50 corner profiles with equal leg angles were used, as provided in the catalog of the company Gerdau - Catalog of equal leg angles - with cross sectional area varying from 0.7 cm² to 73.81 cm².

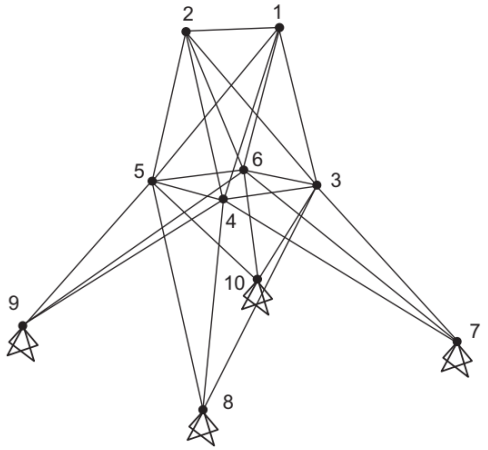

Fig. 3 25-bar tower, [4]

Table 1
Applied Loads on the 25-bar tower, [12]

Node	Fx (kN)	Fy (kN)	Fz (kN)
1	4.448	-44.482	-44.482
2	0	-44.482	-44.482
3	2.224	0	0
6	2.669	0	0

The optimization results are shown in table 2. To validate the code, the case addressed by Camp and Farshchin [4] was applied without applying the buckling restrictions. The present work converged to the same total weight of the structure obtained by Camp and Farshchin [4], i.e., 219.93 kg. These results can be seen in column 3 and 4 of Table 2.

After validating the code, three situations were analyzed for the problem, case 1: without applying the buckling and slenderness restriction, case 2: applying the critical buckling load restriction, and case 3: considering the critical load restriction including buckling and slenderness. For case 1, the TLBO obtained a value of 212.54 kg. For case 2, the result converged to 343.12kg, which represents an increase of 56.02% compared to case 1. For case 3, the ideal weight obtained was 353.70 kg, i.e., an increase of 60.83% compared to case 1.

For case 1, 15 bars were compressed, of which 12 presented stresses greater than the critical buckling load and 10 reached slenderness above 200. 5 of the tensioned bars presented slenderness above 300, in both the slenderness reaches 1437.8. For case 2, there was a reduction in the slenderness index of the bars, 12 were compressed, of which 4 showed slenderness above 200 reaching 250.66, and 3 of the compressed bars have slenderness above 300, reaching 762.

Table 2
TLBO results for the 25-bar tower

Variables		Cross-sectional areas (cm²)				
Group	Members	Camp and Farshchin [4]	Validation	Present		
				Normal	With σ_{cr}	With $\sigma_{cr} + \lambda$
1	1	0.645	0.645	0.700	0.700	1.930
2	2-5	1.935	1.935	0.700	12.510	12.510
3	6-9	21.935	21.935	24.190	15.730	15.730
4	10,11	0.645	0.645	0.700	0.700	1.930
5	12-13	13.548	13.548	13.500	2.320	4.580
6	14-17	6.452	6.452	5.220	15.480	15.730
7	18-21	3.226	3.226	0.900	15.730	19.500
8	22-25	21.935	21.935	24.190	23.290	19.500
Weight (kg)		219.924	219.926	212.539	343.118	353.701
Average weight (kg)		219.951	219.980	212.791	362.875	385.537
N° analyses		4910	6664	6623	12004	13674
Average time (s)		-	32.436	31.987	54.803	61.857

4.2. Problem 2: 72-bar tower

Fig. 4 illustrates the 72-bar truss configuration. For optimization, the following data were considered: maximum allowable stress of 172.37 MPa, maximum nodal displacement of 6.35 mm, material density 2768 kg/m³, material elastic modulus of 68.95 GPa and loading at node 17 with 22.241 kN, 22.241 kN and -22.241 kN in the x, y and z directions, respectively.

For this case, the code was validated using a discrete variation in cross-sectional area with an interval ranging from 0.645 cm² to 19.355 cm² at an increment of 0.00645 cm². Camp and Farshchin [4] used the same interval with continuous variation. In this case, the method converged to an ideal weight of 167.698 kg, less than the value of [4], i.e.,172.198 kg. The optimization results are described in table 3.

For this problem, the same analysis performed in the previous problem was repeated here, and the same profiles were also used. For case 1, the method obtained a value of 169.69 kg, a slight reduction in weight compared to the validation case, which was due to the use of smaller profile areas. For case 2, the result converged to 341.68 kg, which represents an increase of 101.36% compared to case 1. For case 3, a significant increase occurred as the solution converged to the weight of 680.07 kg, representing an increase of 300.78% in relation to case 1.

For case 1, the tower contained 36 bars under compression, 29 exceeding the critical buckling load, 30 of the compressed bars reached slenderness above 200 and 34 compressed bars presented slenderness above 300, in both cases the slenderness reaches 1724.2. For case 2, the tower started to present 41 compressed bars, of which 27 reached slenderness above 200 reaching 952.5, and 10 of the compressed bars showed slenderness above 300, continuing to reach the value of 1724.2

Table 3
TLBO results for the 72-bar tower

Variables		Cross-sectional areas (cm²)				
Group	Members	Camp and Farshchin [4]	Validation	Present		
				Without σ_{cr}	With σ_{cr}	With $\sigma_{cr} + \lambda$
1	1-4	12.1335	12.000	11.480	7.030	7.030
2	5-12	3.3174	3.226	3.420	7.030	12.510
3	13-16	0.6452	0.645	0.700	1.930	10.900
4	17,18	0.6452	0.645	0.700	0.700	7.030
5	19-22	8.2006	8.194	7.670	5.800	7.030
6	23-30	3.3232	3.290	3.100	7.030	10.900
7	31-34	0.6452	0.645	0.700	1.930	15.480
8	35,36	0.6452	0.645	0.700	2.320	10.900
9	37-40	3.4303	3.226	3.420	4.580	4.000
10	41-48	3.3123	3.226	3.420	7.030	15.480
11	49-52	0.6452	0.645	0.700	0.900	5.800
12	53,54	0.6452	0.645	0.700	2.710	10.900
13	55-58	1.0097	0.645	0.700	4.580	4.580
14	59-68	3.5026	3.355	3.420	9.290	10.900
15	67-70	2.6329	2.516	2.770	5.800	12.510
16	71,72	3.6987	3.613	3.420	10.900	19.500
Weight (kg)		172.198	167.698	169.688	341.677	680.070
Avarage weight (kg)		172.256	167.732	169.887	369.003	892.896
N° Analyses		21542	12989	10350	21692	16949
Avarage time (s)		-	185.542	141.247	285.149	213.472

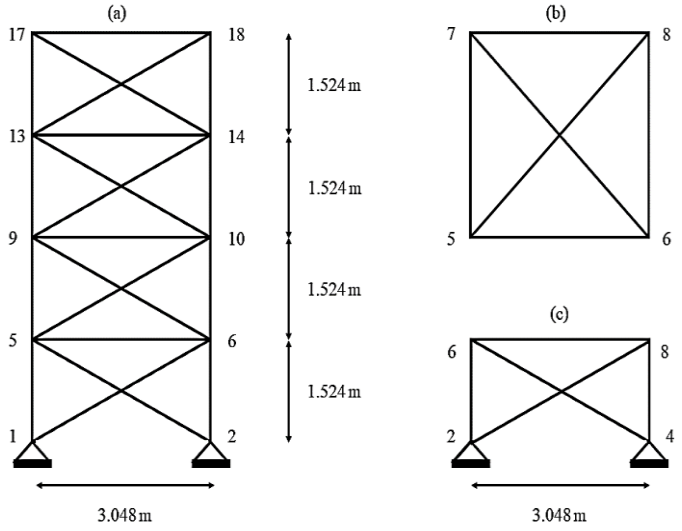

Fig. 4 72-bar tower: a) front view b) cross section c) side view, [8]

4.3. Problem 3: 160-bar tower

The 160-bar truss tower is illustrated in Fig. 5. This truss was solved by Rajeev and Krishnamoorthy [25], using GA to minimize weight without buckling. Galante and Onate [24] also analyzed the same structure using GA, optimizing it for the case where buckling and slenderness restrictions are applied. Both authors used 32 variations of cross-sectional areas taken from the AISC manual, which are also used in this problem. Galante and Onate [24] divided the structure into 16 groups, the author proposed this division in order to obtain a structure with little variation in profiles in order to find a structure that facilitates construction.

In this problem, the same values proposed by Rajeev and Krishnamoorthy [25] and Galante and Onate [24] were considered: elastic modulus of 208 GPa material, steel density of 7850 kg / m³, allowable stress of 147.15 MPa and maximum nodal displacement of 0.1 m. The assumed loads are shown in table 4. The structure was divided into 16 groups, as adopted by Galante and Onate [24]. More details about the structure can be found in Galante and Onate [24].

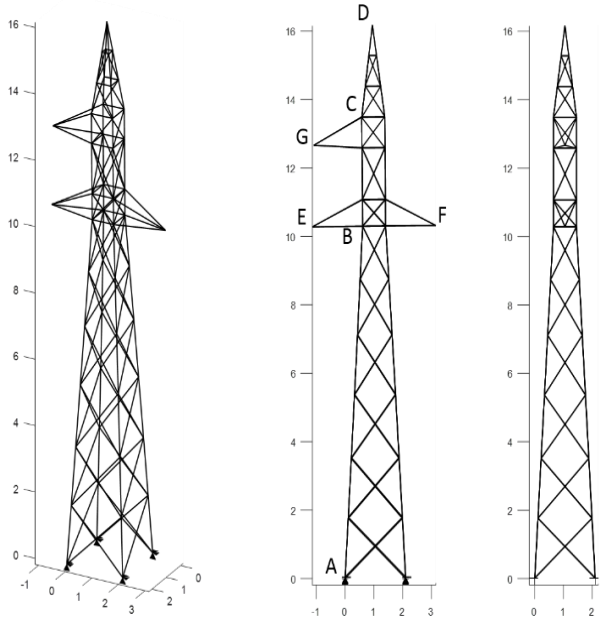

Fig. 5 160-bar tower

Table 4
Loading 160-bar tower, [20]

Node	Fx (N)	Fy (N)	Fz (N)
D	-10702.7	0	-5356.26
E	-10702.7	0	-5356.26
F	-9770.76	0	-5356.26
G	-8515.08	0	-4816.71

The optimization results can be seen in table 5. For the case when buckling and slenderness are disregarded, the TLBO obtained the ideal weight of 577.22 kg, which was between the values found by Rajeev and Krishnamoorthy [25] and Galante and Onate [24], i.e., 662.3 kg and 547.4 kg, respectively.

Table 5
Results for the 160-bar tower

Variables		**Cross-sectional areas (cm²)**			
Group	**Members**	**Galante and Onate [24] Without buckling**	**Present Without buckling**	**Galante and Onate [24] With $\sigma_{cr} + \lambda$**	**Present With $\sigma_{cr} + \lambda$**
1	1-24	-	9.290	12.5161	9.290
2	25-36	-	3.632	7.6774	4.613
3	37-48	-	2.800	4.6129	1.716
4	49-56	-	1.510	4.6129	7.032
5	57-64	-	1.510	4.6129	5.819
6	65-72	-	1.510	4.6129	7.032
7	73-80	-	1.510	4.6129	7.032
8	81-88	-	1.510	4.6129	3.123
9	89-96	-	1.510	4.6129	5.819
10	97-104	-	1.510	4.6129	2.800
11	105-112	-	1.510	4.6129	3.123
12	113-120	-	1.510	4.6129	3.123
13	121-128	-	1.510	4.6129	1.510
14	129-136	-	1.510	4.6129	1.510
15	137-148	-	1.510	4.6129	1.510
16	149-160	-	1.510	4.6129	4.613
Weight (kg)		547.400	577.217	1293.800	1057.266
Avarage weight (kg)		-	578.196	-	1180.162
N° Analyses		-	5196	-	19384
Avarage time (s)		-	135.615	-	531.863

For the case considering the critical buckling load restrictions described in section 2.2, as used by Galante and Onate [24], the TLBO reached the ideal weight of 1057.27 kg, which is below the value of 1293.8 kg reached by Galante and Onate [24] using GA, representing a reduction of 18.28%. Similarly to the two previous problems, it is possible to notice that the ideal structure undergoes a considerable increase in the ideal weight when considering the critical load restrictions imposed by buckling and slenderness.

Analyzing the behavior of the structure, it can be seen that, in the first case, without considering the restrictions of critical load of buckling and slenderness, 80 bars are subject to compressive stress, of which 27 have a compressive stress greater than the critical buckling stress specified in AISC manual (Eqs. (5) to (8)). Analyzing all the compressed bars, 43 exceed the slenderness limit of 200. In the case of compressed bars, 35 exceed the slenderness limit of 300. In both cases, the slenderness reaches 532.62. Therefore, the structure obtained when disregarding the buckling effect is not a proper structural load system, as it would not meet normative restrictions and would probably collapse [24].

5. Conclusion

Through this work, it is verified that the buckling effect plays a significant role in the optimization of truss structures, as it provides more realistic results due to the increased ideal weight of the structure. As indicated in section 2.2, depending on the geometric characteristics and on the modulus of elasticity, the critical buckling load may be less than the allowable stress for the material, therefore, larger sections are required to withstand the acting stresses, which justifies the increase in ideal weight.

It can be seen that, by restricting the critical buckling load, this resulted in a reduction in the slenderness index of some compressed elements, which is justified by the fact that the critical buckling load, in some bars, is below the allowable stress for the material, therefore requiring more robust sections. Thus, by limiting the slenderness of the parts, the standard regulation further restricts the support capacity of the structure, which is equivalent to the application of an additional safety factor.

For the optimized cases, in which the critical buckling load and slenderness restrictions were not considered, several elements violated the critical conditions, which would probably cause the collapse of these structures. This fact confirms Galant and Onate's conclusion, which states that meeting the critical load restrictions imposed by the buckling and slenderness index is fundamental for a safe and more realistic project [24].

Computational codes are available under request (only for academic purposes). Please contact the corresponding author for more information.

References

[1] TOĞAN, V.; DALOĞLU, A. T. Optimization of 3d trusses with adaptive approach in genetic algorithms. Engineering Structures, v. 28, n. 7, p. 1019–1027, 2006.

[2] HOLLAND, J. H. Adaptation in natural and artificial systems. The University of Michigan Press, Ann Arbor, 1975.

[3] RAO, R. V.; SAVSANI, V. J.; VAKHARIA, D. P. Teaching-learning-based optimization: A novel method for constrained mechanical design optimization problems. CAD Computer Aided Design, v. 43, n. 3, p. 303–315, 2011.

[4] CAMP, C. V.; FARSHCHIN, M. Design of space trusses using modified teaching-learning based optimization. Engineering Structures, v. 62–63, p. 87–97, 2014.

[5] VATANSEVER, C. Investigation of buckled truss bars of a space truss roof system. Engineering Failure Analysis, v. 106, n. August 2016, p. 104156, 2019.

[6] CAGLAYAN, O.; YUKSEL, E. Experimental and finite element investigations on the collapse of a Mero space truss roof structure - A case study. Engineering Failure Analysis, v. 15, n. 5, p. 458–470, 2008.

[7] AUGENTI, N.; PARISI, F. Buckling analysis of a long-span roof structure collapsed during construction. Journal of Performance of Constructed Facilities, v. 27, n. 1, p. 77–88, 2013.

[8] SAFARI, D.; MAHERI, M. R. Genetic Algorithm search for optimal brace positions in steel frames. Advanced Steel Construction, v. 2, n. 4, p. 400-415, 2006.

[9] FAWZIA, S.; FATIMA, T. Optimum position of steel outrigger system for high rise composite buildings subjected to wind loads. Advanced Steel Construction, v. 12, n. 2, p. 134-153, 2016.

[10] DOĞAN, E.; SEKER, S.; SAKA, M. P.; KOZANOĞLU, C. Investigating the effect of joint behavior on the optimum design of steel frames via hunting search algorithm. Advanced Steel Construction, v. 14, n. 2, p. 166-183, 2018.

[11] GOMEZ, F.; SPENCER, JR.; CARRION, J. Topology optimization of buildings subjected to stochastic wind loads. Probabilistic Engineering Mechanics, v. 64, 2021.

[12] HAGHPANAH, F.; FOROUGHI, H. Size and Shape Optimization of Space Trusses Considering Geometrical Imperfection-Sensitivity in Buckling Constraints. Civil Engineering Journal, v. 3, n. 12, p. 1314, 2018.

[13] SUSSEKIND, J.C. Structural Analysis Course: Isostatic Structures. 6. ed. Porto Alegre: Globo, 1981. 1. v.

[14] AUGENTI, N.; PARISI, F. Buckling analysis of a long-span roof structure collapsed during construction. Journal of Performance of Constructed Facilities, v. 27, n. 1, p. 77–88, 2013.

[15] BEER, F. P. et al. Vector mechanics for engineers. 9 ed. São Paulo: AMGH, 2009.

[16] HIBBELER, R. C., Strength of Materials. 5. ed. São Paulo: Person Prentice Hall, 2010.

[17] AMERICAN INSTITUTE OF STEEL CONSTRUCTION (AISC) - Specification for Structural Steel Buildings: Allowable Stress Design and Plastic Design. Chicago, 2001.

[18] BRAZILIAN ASSOCIATION OF TECHNICAL STANDARDS. NBR 8800 - Design of steel structures and mixed steel and concrete structures for buildings. Rio de Janeiro, 2008.

[19] CAMP, C. V. Design of space trusses using big bang-big crunch optimization. Journal of Structural Engineering, v. 133, n. 7, p. 999–1008, 2007.

[20] TOĞAN, V.; MORTAZAVI, A. Sizing optimization of skeletal structures using teaching-learning based optimization. An International Journal of Optimization and Control: Theories & Applications (IJOCTA), v. 7, n. 2, p. 130, 2017.

[21] RAO, R. V.; SAVSANI, V. J.; VAKHARIA, D. P. Teaching-Learning-Based Optimization: An optimization method for continuous non-linear large scale problems. Information Sciences, v. 183, n. 1, p. 1–15, 2012.

[22] RAO, R. V.; PATEL, V. An improved teaching-learning-based optimization algorithm for solving unconstrained optimization problems. Scientia Iranica, v. 20, n. 3, p. 710–720, 2013.

[23] TOĜAN, V. Design of planar steel frames using Teaching-Learning Based Optimization. Engineering Structures, v. 34, p. 225–232, 2012.

[24] GALANTE, M.; OÑATE, E. Genetic algorithms as an approach to optimize real-world trusses. International Journal for Numerical Methods in Engineering, v. 39, n. 3, p. 361–382, 1996.

[25] RAJEEV, S.; KRISHNAMOORTHY, C. S. Discrete Optimization Of Structures Using Genetic Algorithms By. S. Rajeev 1 and C. S. Krishnamoorthy 2. October, v. 118, n. 5, p. 1233–1250, 1992.

Advanced Steel Construction – Vol. 18 No. 1 (2022) 453–464
DOI:10.18057/IJASC.2022.18.1.4

EXPERIMENTAL, NUMERICAL, AND THEORETICAL STUDY ON STATIC BEHAVIOUR OF NOVEL STEEL DOVETAIL JOINT SUBJECTED TO AXIAL TENSILE LOAD

Waleed Mashrah [1], Zhi-Hua Chen [1, 2, 4], Hong-Bo Liu [3, *] and Mohammed Ameen Amer [1]

[1] *Department of Civil Engineering, Tianjin University, Tianjin 300072, China*
[2] *State Key Laboratory of Hydraulic Engineering Simulation and Safety, Tianjin University, Tianjin 300072, China*
[3] *Department of Civil Engineering, Hebei University of Engineering, Handan 056000, China*
[4] *Key Laboratory of Coast Civil Structure and Safety of Ministry of Education, Tianjin University, Tianjin 300072, China*
** (Corresponding author: E-mail: hbliu@tju.edu.cn)*

ABSTRACT

In this study, two types of socket joints manufactured based on a simple design concept and bearing load principle are proposed. The design concept, design method, test program, and FE modelling method for a novel steel dovetail joint without teeth pattern (Interlock type I) and with teeth pattern (Interlock type II) are also discussed. In addition, the tests and numerical analyses of four specimens were conducted to investigate the bearing capacities and failure modes of the new joint systems under axial tensile loads. The test results indicated that the specimens with and without teeth patterns exhibited different tensile bearing capacities: the specimens with teeth patterns generated twice the tensile load capacity of those without teeth patterns. This result can be attributed to the fact that the interlock type-II specimens rely on the teeth pattern, edges of the hub keyway, and hub ring to bear the load, whereas interlock type-I specimens rely only rely on the edges of the hub keyway and hub rings. Further, the two types of specimens have the same failure modes when the beam-inserted end (tail) is pulled out of the hub keyway. In addition, shear failure occurs on the teeth pattern of the hub keyways and beam-inserted ends of the interlock type-II specimens. Two FE models are established to verify the results of the tests, and the related equations are derived and calculated. The results obtained from the numerical analysis using the equations were compared with the test results. Finally, it was concluded that the results obtained using the three analysis methods adopted in this study agree very well, with high calculation validity and efficiency.

ARTICLE HISTORY

Received: 10 February 2021
Revised: 26 May 2021
Accepted: 26 May 2021

KEYWORDS

New socketed join;
Novel steel dovetail joint;
H-shaped beam;
Tensile bearing capacity;
Failure mode

1. Introduction

In the past two decades, single-layer grid shell structures with complex curved surfaces have been designed for structural application in leisure destinations, transportation, theatres, airports, museums, and so on, demonstrating outstanding architectural and structural representation at reasonable cost [1]. Therefore, the design and optimisation of a joint system for single-layer grid shells has become one of the most active research topics in spatial structures [2]. The grid shells rely on the connection type to transfer loads. Therefore, the mechanical performance of the joint system directly impacts the bearing capacity and safety of the grid shells [3]. The joints used in these structures can be classified into assembled and welded joints [4]. Further, the assembled joints can be categorised as bolted and socketed joints.

Traditional welded joints are widely used in steel structures, particularly in welded hollow spherical joints, which have been in service for more than 54 years [5][6], and tubular joints [7]. However, because of the difficulties and challenges of using welded joint systems, several engineers have proposed a new type of bolted joint system to secure the quick development of steel structures including single-layer grid shells such as bolted joints (Fig. 1), mero joints [8], bolt–ball joints [9], bolted beam-to-column connections [10], double-ribbed reinforced beam–column connections [11], and tremor joints of aluminium (Fig. 2) [12] and a few types of socketed joints such as socket [13][14] and triodetic joints [15].

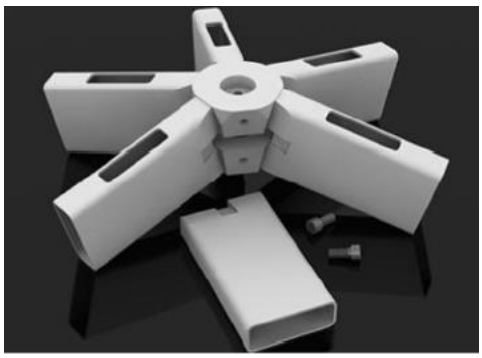

Fig. 1 Bolted joint [1]

Fig. 2 Greenhouse exhibition hall in a botanical garden in Shanghai, China [12]

Recently, numerical and experimental approaches have been employed to investigate the mechanical performance of steel structure joints under various load conditions. Qiao et al. [16] examined the moment–rotation relationship of steel sleeve beam- column joints using interference FITs. Shen Yan et al. [17] carried out a series of tests to study the full-range behaviour of steel beam-to-column connections. Zhe et al. [18] carried out a numerical study based on the test results of previous studies on the behaviour of Temcor joints under bending and axial loads. Han et al. [3][19] conducted experiments to examine the behaviour of assembled joints (AHs) under tension, compression, and bending moments. In their study, the results of the FE and theoretical analyses matched well with the elastic stiffness and bearing capacities of the assembled joint specimens in the tests. Ma et al. [20] performed a series of tests on a gear–bolt joint, considering various design parameters. Oyeniran et al. [21] experimentally and numerically studied the performance of aluminium bolted joints (HBJs) under axial loads. Fan et al. [22] adopted an experimental approach to investigate the moment–rotation relationship for a semirigid joint system connector under various loading schemes. Ma et al. [23] used experimental and numerical approaches to investigate the mechanical performance of new semirigid joints by considering different design parameters. They also adopted the same approaches to investigate the gear–bolt and bolt–column (BC) joint behaviours under a bending moment. In addition, several joints were designed using the various shapes of the sections of members, such as circular tubes, rectangular tubes, and H-shaped members. Ma et al. [4] investigated the static behaviour of bolt–column joints with

rectangular section members under in-plane direction bending. Konstantinos et al. [24] Ma et al. [25], and Han et al. [2][3][19] designed and tested various types of joints with rectangular section members. A joint with a circular section is the most popular one and applicable to single-layer grid shells. Xue et al. [26] performed experimental and numerical analyses to investigate a new type of single-layer reticulated shell connection (TCS) under a bending moment. Liu et al. [5] experimentally and numerically investigated the residual behaviour of welded hollow spherical joints under corrosion and de-rusting. Thus, various connections with circular tube members have been developed and investigated, such as bolt–ball joints with circular steel tubes [27], semirigid joints [22], socket joints [13], and welded hollow spherical joints [28]. In contrast, a few joints are designed using H-section beams; these exclude the Temcor (Figs 3 and 4) [29][30] and welded hollow spherical joints (Fig. 5) [31].

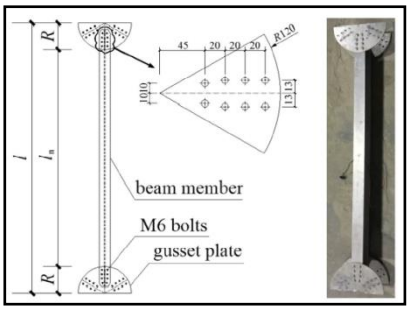

Fig. 3 Beam member of Temcor joint [29]

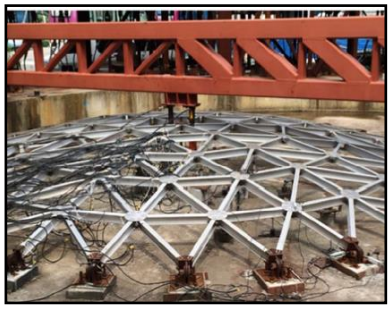

Fig. 4 Temcor joint experimental shell [30]

Fig. 5 Welded hollow spherical joint with H-section beam [31]

H-shaped members present the advantages of reducing the material, weight, and cost of the structure because they have weak and strong axes of inertia moment. However, the only assembled joint that is designed and developed using an H-shaped beam is a Temcor joint. Joints such as Temcor only connect the upper and lower flanges of the H-shaped beam with the upper and lower gusset plates without connecting the H-shaped beam; thus, a weak shear deformation can occur in this type of joint. In this study, a novel steel dovetail joint with the H-shaped beam and socket concept was proposed to avoid the problems encountered using the other types of joints.

2. Concept of novel steel dovetail joint

Two types of novel steel dovetail joints have been designed in this study using H-shaped members, combining the hub and socket concepts. The dovetail mortise–tenon concept is generally used in connections among timber structures, such as those among the ancient Chinese timber structures (Fig. 6) [32][33][34]. In this hub system, the hub or joint plate is placed at the centre of the joint, and the elements connect to the centre as rays, as illustrated in the hub joint of steel and triodetic joint of aluminium (Fig. 7). Novel steel dovetail joints with interlocks type I (NDJs) and type II (NDJGs) are designed based on these two concepts (Fig. 8).

The novel steel dovetail joint contains a hexagonal hub with three removed areas (Figs 9 and 10) to reduce the self-weight of the hub. The second component of this novel steel dovetail joint is an H-shaped beam with four main parts: an H-shaped member with curved flanges, throat web, throat neck, and beam-inserted end (tail). The beam throat is welded to the H-shaped member; thereafter, the beam end is inserted into the hub keyway. The joint is completed when two cover plates with the same shape as that of the extrude hub are arranged at the ends of the hub and a screwed bolt passed through the hub centre to connect the cover plates. Two types of novel steel dovetail joints are designed based on the same concept and specifications; the only difference is the interlock system: the interlock type-I specimens (NDJs) are designed using the standard dovetail shape (Fig. 11), whereas the interlock type-II specimens (NDJGs) are designed with teeth patterns in their interlock system (Fig. 12).

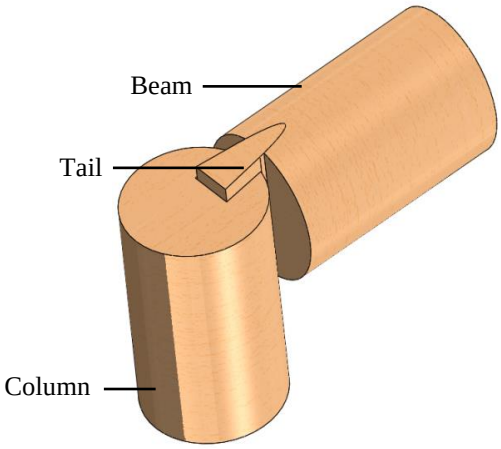

Fig. 6 Mortise–tenon system

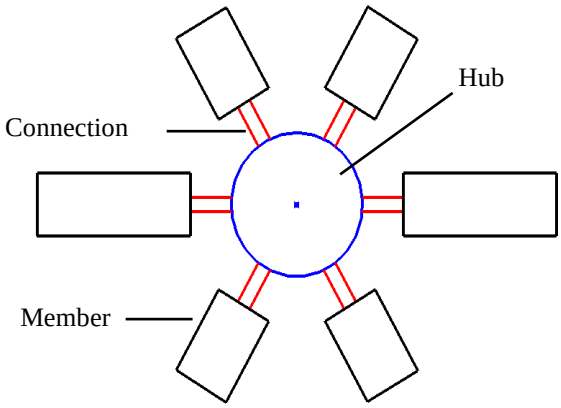

Fig. 7 Hub system

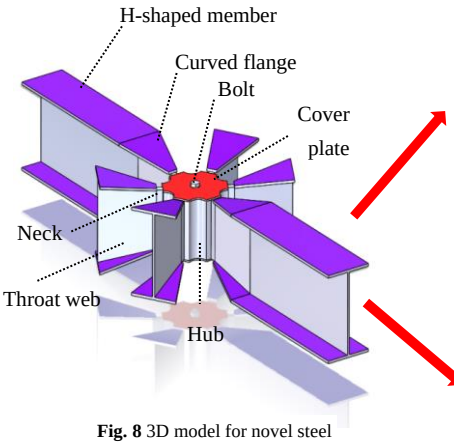

Fig. 8 3D model for novel steel dovetail joint system

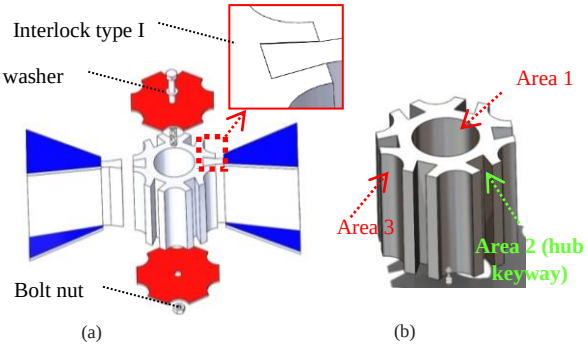

Fig. 9 3D model for novel steel dovetail joint (NDJ type): (a) Interlock type I, (b) hub type I

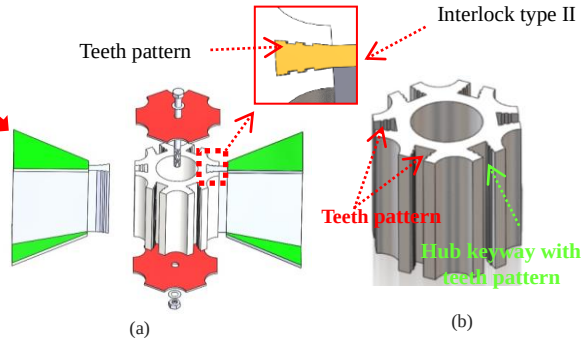

Fig. 10 3D model for novel steel dovetail joint (NDJG type): (a) Interlock type II, (b) hub type II

.

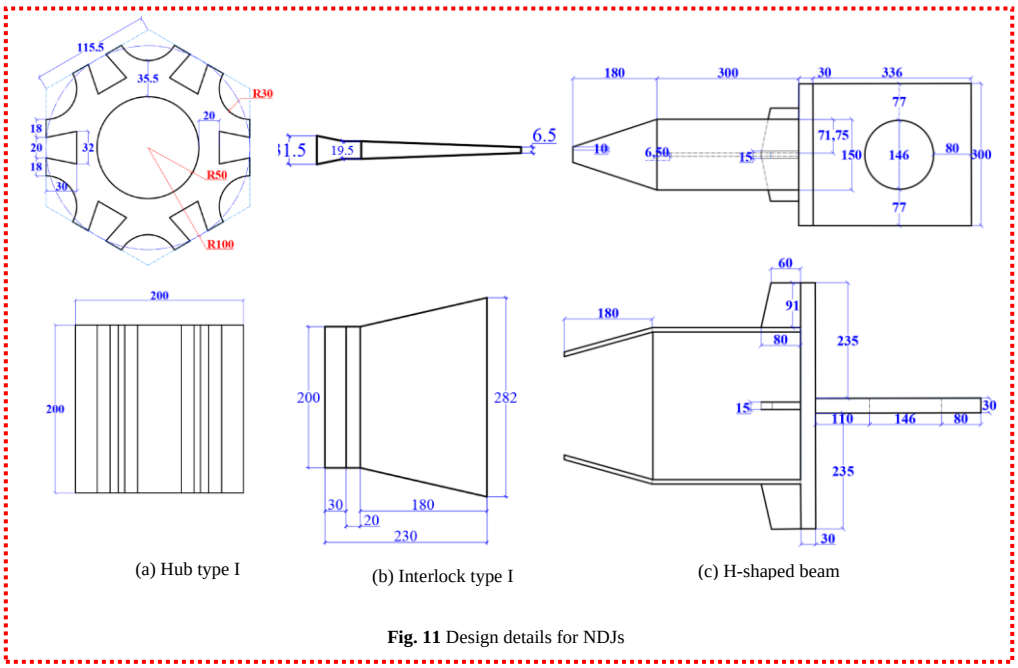

Fig. 11 Design details for NDJs

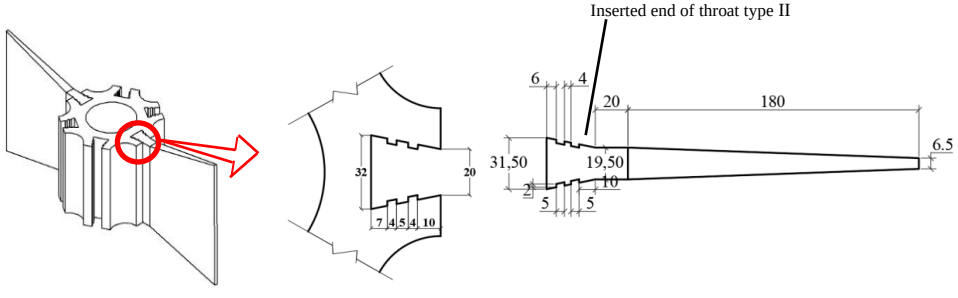

Fig. 12 Design details for NDJGs

3. Test program

3.1. Design of specimens

In this section, the investigation of the mechanical performance and failure modes of the new joint system under axial tensile load is described. Two specimens each of the novel steel dovetail joint with interlock type I (NDJ-1 and NDJ-2) and interlock type II (NDJG-1 and NDJG-2) were designed. The four specimens were assembled after fabrication and transported to the Tianjin University laboratory (Fig. 13 (a) and (b)). Thereafter, NDJG-1 and NDJG-2 were designed using interlock type II with teeth patterns to improve the performance of this new joint system under tensile load. After the specimens were assembled, all the test preparations were completed, and the specimens were placed in the test machine (Fig. 13 (c) and (d)).

Tension loads were applied to the novel steel dovetail joints using a horizontal hydraulic jack with a load capacity of 15000 kN. Therefore, to investigate the tensile bearing capacities and failure modes of these new joints, all the test specimens were designed with a loading plate and circular opening at the centre to fit the connecting elements of the loading machine (Fig. 13 (b) and (d)).

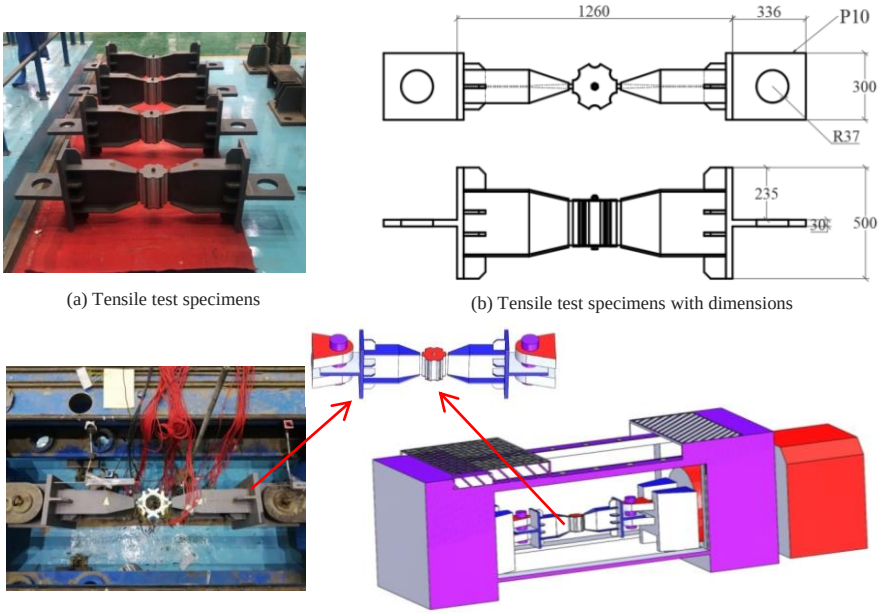

(a) Tensile test specimens

(b) Tensile test specimens with dimensions

(c) Loading the test specimen

(d) Tensile test machine

Fig. 13 Test program for novel steel dovetail joint

3.2. Arrangement of measuring points

The applied load was measured by the load sensor in the loading machine, and four displacement sensors were used to measure the axial deformation of the specimens under axial tension load (DG1 to DG4) (Fig. 14). Simultaneously, to measure the strain, 42 gauges were arranged on the test specimens, as displayed in Fig. 14 (a) and (b). The strain gauges were set mainly on the internal and external faces of the hub ring, beam neck, H-shaped beam web, and curved flanges and around the throat with the beam-welded area.

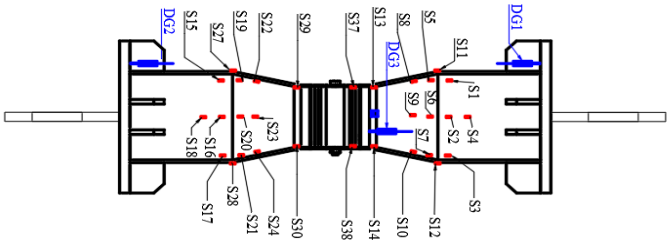

(a) Side view

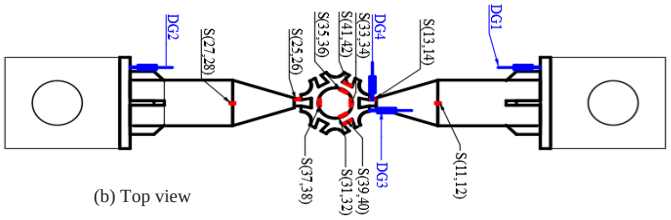

(b) Top view

Fig. 14 Arrangement of measurement points

3.3. Material test

All the components of the novel steel dovetail joint were designed using steel Q345. The material test is one of the most essential tests in structural engineering research. Therefore, to determine the stress–strain behaviour of the materials, a standard material tensile test should be conducted. Four groups of specimens were tested for the hub, throat, H-shaped beam flanges, and H-section beam web (Fig. 15). The material test model parameters and results are presented in Table 1 and Fig. 16. The material shear strength f_v was calculated according to the shear strength of the materials as specified in the Chinese code for the design of steel structures (GB 50017-2003) [35].

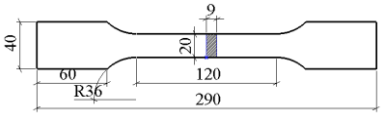

(a) Specimen design for flange

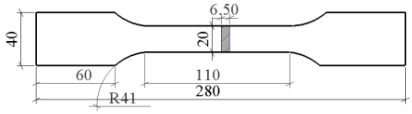

(b) Specimen design for web

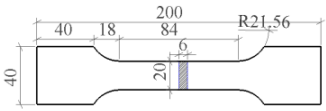

(c) Specimen design for hub

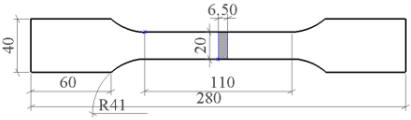

(d) Specimen design for throat

Fig. 15 Specimens for material tensile test

Table 1
Results of material tests

Component	Thickness (mm)	E (10^5 MPa)	f_y (MPa)	f_v (MPa)	f_u (MPa)	f_y/f_u
Throat	6	2.07	370		470	0.78
Hub	6.5	2.05	335	175	464	0.72
Flange	9	2.04	372		560	0.66
Web	6.5	2.07	370		550	0.67

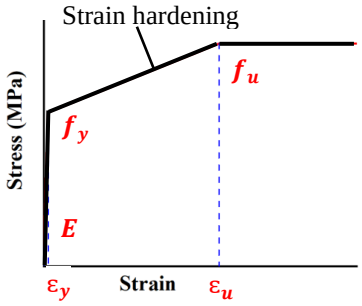

Fig. 16 Material model for components of novel steel dovetail joint

4. Test results and discussion

In this study, the mechanical performance and deformation mechanisms of the two main components of a novel steel dovetail joint system, including the throat and hub, are investigated. Four joint specimens for the two types of interlocks were tested under axial tensile loads. The test program in this study consists of two scenarios: tests of interlock type-I (NDJ) specimens and those of interlock type-II (NDJG) specimens.

4.1. Test results for NDJ specimens

Axial tensile tests were performed on two specimens (NDJ-1 and NDJ-2). The bearing capacity and failure mode were investigated and discussed. At the beginning of the test, a small preload was applied to the specimens to reduce the gap between the beam-inserted end and the keyway of the hub. Thereafter, the working loads were applied through displacement control in the test machine. As the loading increased continuously, the beam end slid slightly, pushing the edges of the keyway in the *Z*-direction (Fig. 17 (a) and (b)). As the loading was continuously applied, the beam-inserted ends (tails) continued to move out, and the hub ring started to expand in the direction of the load (Fig. 17 (c) and (d)). The load–displacement curves of the test, presented in Fig. 18 (a), depict the stiffness and axial tensile bearing capacity of the novel steel dovetail joint.

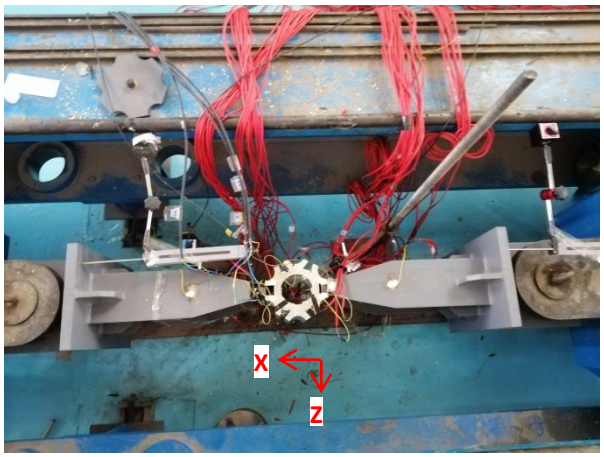

(a) Failure mode of NDJs during the tensile test

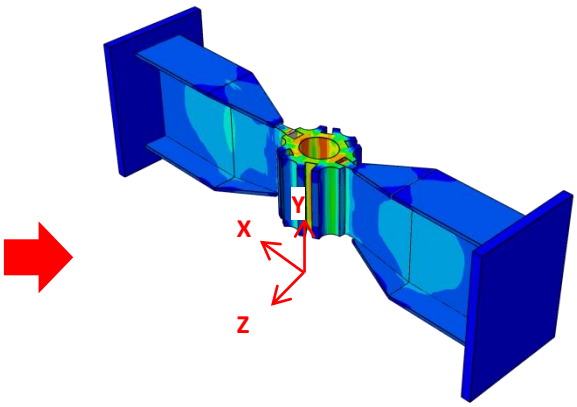

(b) Failure mode of NDJs during the FE analysis

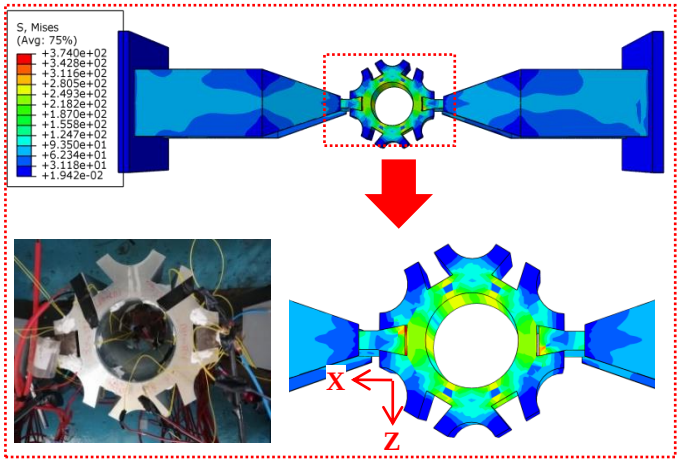

(c) First stage of the failure mode and stress distribution of the NDJs

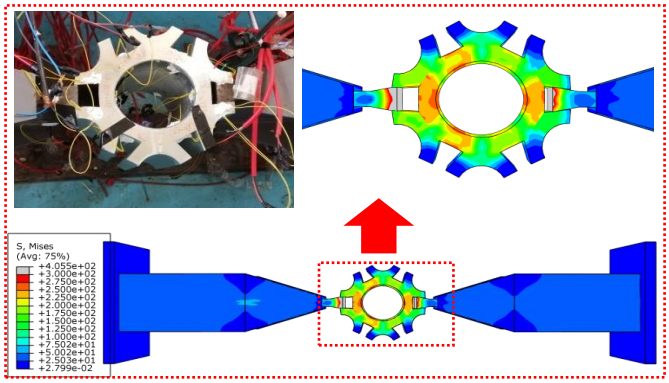

(d) First stage of the failure mode and stress distribution of the NDJs

Fig. 17 Failure modes and stress distributions of NDJs under tensile test and FE analysis

Therefore, it can be seen that the interlock type-I specimens illustrated three load-bearing capacities, including the elastic (N_E^T), yield (N_P^T), and ultimate (N_U^T) capacities; the three capacities for NDJ-1 were 76, 226, and 288 kN, respectively, and 55, 229, and 282.4 kN for NDJ-2. The strain exceeded the yield strain at the measuring points S31, S32, and S39 (in Fig. 18 (b)) and S33, S37, and S38 (in Fig. 18 (c)) of the hub. One side of the interlock component reached the yield capacity in the early loading stage. Therefore, the beam end on this side continued moving out whereas the interlock on the other side stopped moving out. Thus, the hub expanded more on one side than on the other (Fig. 17 (d)). A look at the load–strain curves at the beam measuring points (Fig. 18 (d), (e), and (f)) indicated no deformation in the H-shaped beams of NDJ-1 and NDJ-2 during loading.

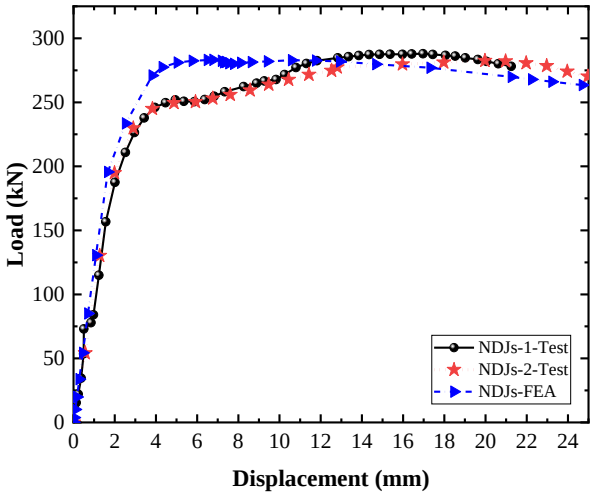

(a) Load–displacement curves

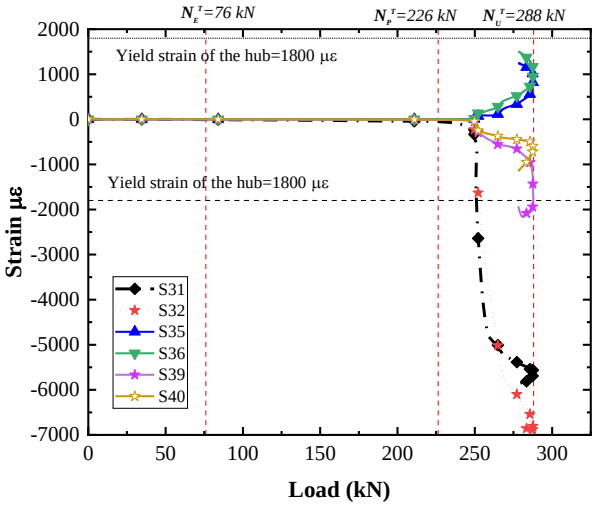

(b)Strain–load curves for the hub

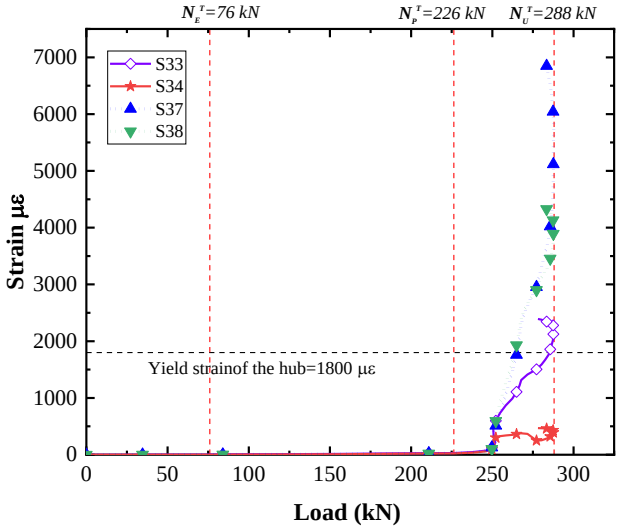

(c) Strain–load curves for the hub

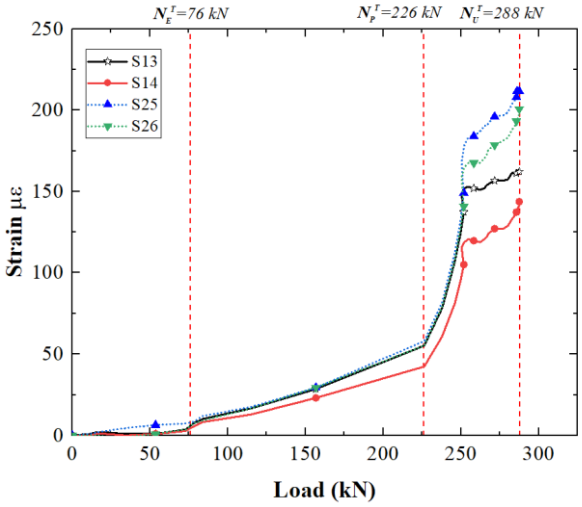

(d) Strain–load curves for the H-shaped beam

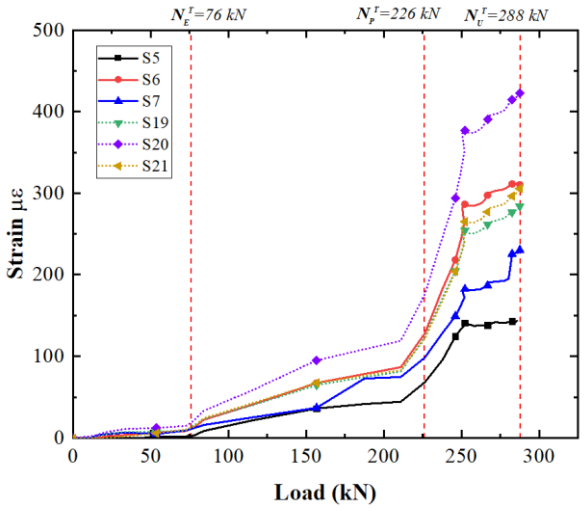

(e) Strain–load curves for the H-shaped beam

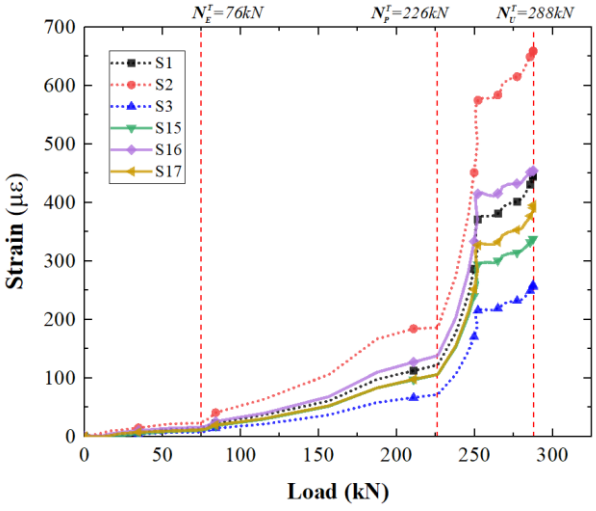

(f) Strain–load curves for the H-shaped beam

Fig. 18 Load–displacement and strain–load curves for the specimens NDJ-1 and NDJ-2

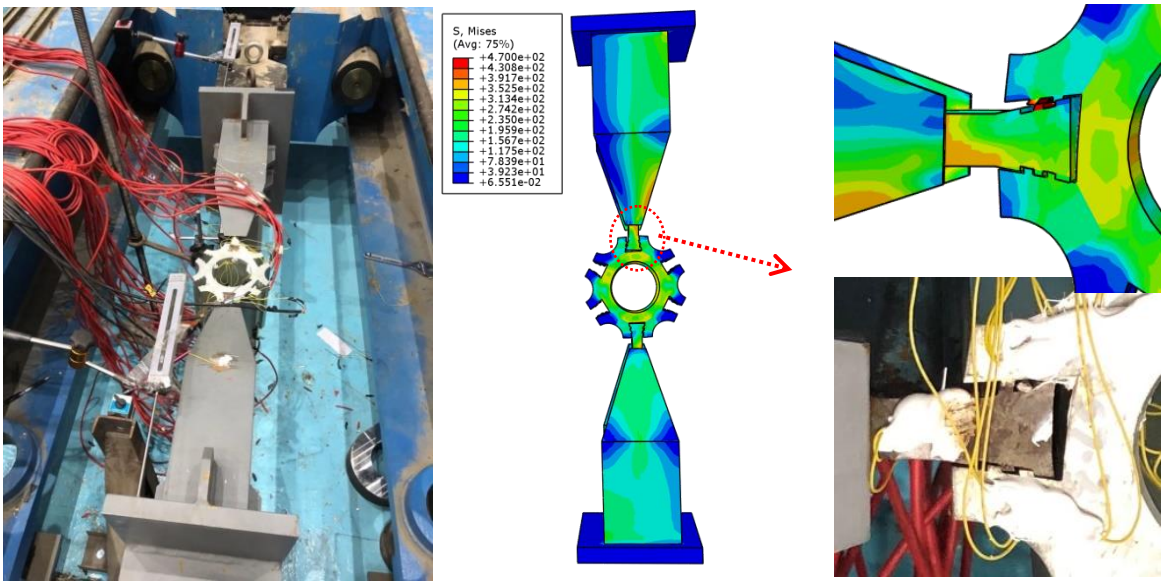

(a) Failure modes of NDJGs during tensile test and FE analysis

(b) First stage of the failure mode and stress distribution

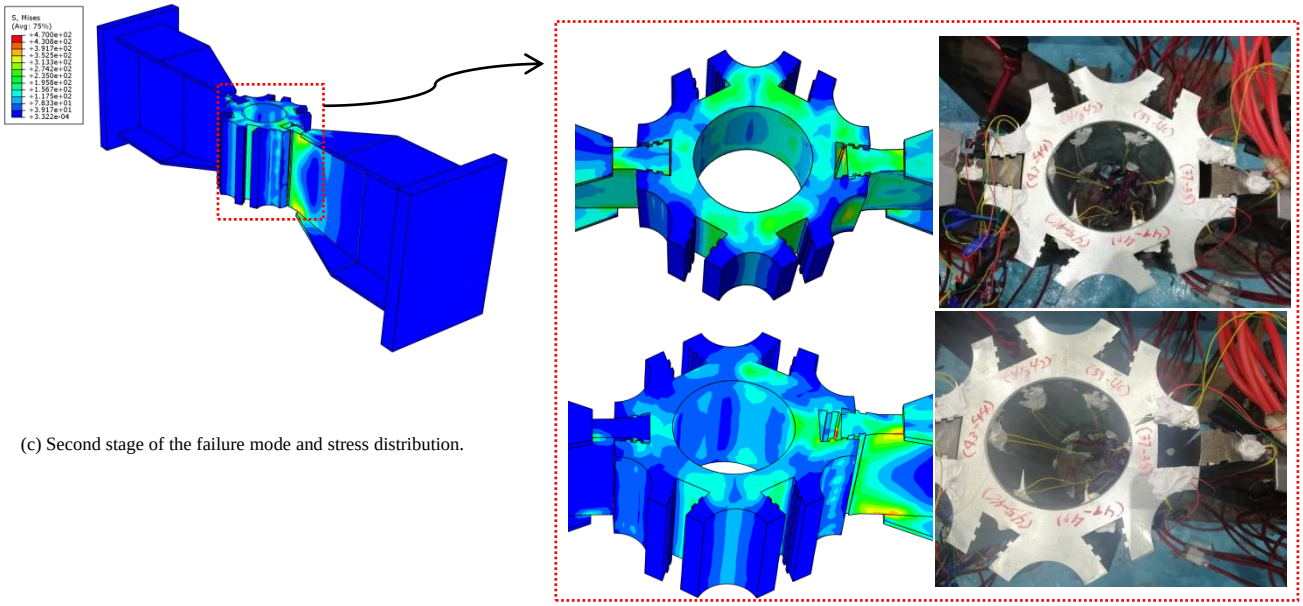

(c) Second stage of the failure mode and stress distribution.

Fig. 19 Failure modes and stress distributions of NDJGs under axial tensile load

4.2. Test results for NDJG specimens

The interlock type-II novel steel dovetail joint specimens (NDJG-1 and NDJG-2) were designed with teeth patterns to increase their bearing capacity and stiffness under axial tensile load. The specimen installation, boundary conditions, and loading process were the same as those described for the interlock type-I specimens in Section 4.1. A preload was applied to set the specimens in the correct loading position and create tightness between the teeth pattern of the interlock component. Thereafter, the working loads were applied by adopting displacement control in the test machine (Fig. 19 (a)). As the loading process continued, the teeth pattern at the beam-inserted end interacted with that in the hub keyway, and the load began to increase. The failure mechanism of the NDJGs was different from that of the NDJs: the latter rely on the friction between the hub keyway and the beam end surfaces to bear the load, whereas the former rely on the friction between the hub keyway and the beam-inserted end as well as on the teeth pattern shear strength. Therefore, shear deformation occurred in the teeth pattern after it reached the material yield capacity (Fig. 19 (b) and (c)).

The elastic (N_E^T), yield (N_P^T), and plastic (N_U^T) capacities for NDJG-1 were 131, 597, and 707 kN, respectively, and 115, 542, and 656 kN for NDJG-2 (Fig. 20 (a)). Specimens with a teeth pattern demonstrated yield and ultimate bearing capacities higher than those without a teeth pattern in the first scenario, where the yield and ultimate tensile bearing capacities of the NDJGs are equal to 2.6 and 2.5 times those of the NDJs. According to the strain results at the measuring points, the neck and teeth pattern of the beam end yielded first, when the strain in the strain gauges S13 and S14 reached the yield capacity (Fig. 20 (b)), whereas the hub had a slide that expanded in the load direction. The interlock teeth pattern on one side reached the yield strength and deformed before that on the other side. Thus, it got cut off and fell down. At that moment, considerable sounds were heard, and the load curves indicate a downward trend when the strain at the measuring points S33, S34, S35, S36, S37, S38, S41, and S42 reached the yield capacity. Further, the hub expanded to increase the space between the edges of the hub keyway (Fig. 20 (c) and (d)). The strains in the beams of NDJG-1 and NDJG-2 were higher than those in the NDJs, particularly around the H-shaped beam with the throat welding area (Fig. 20 (e) and (f)).

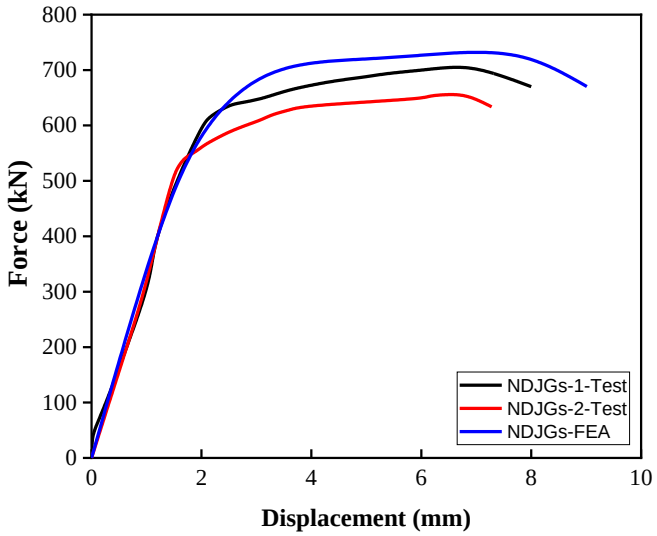

(a) Load–displacement curves

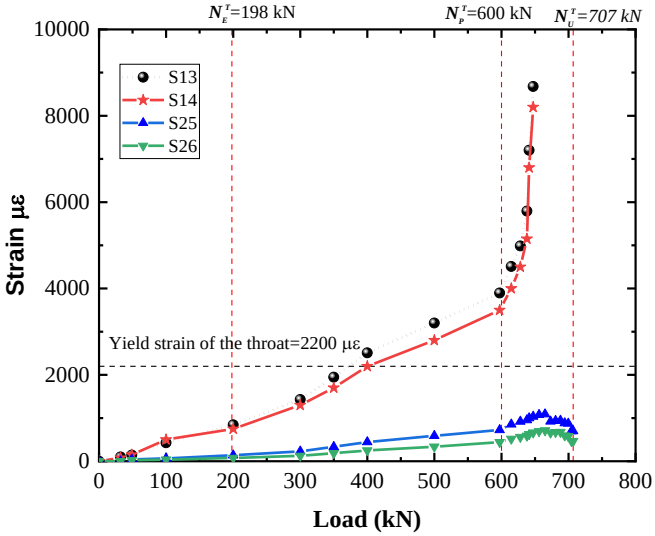

(b) Strain–load curves for the beam

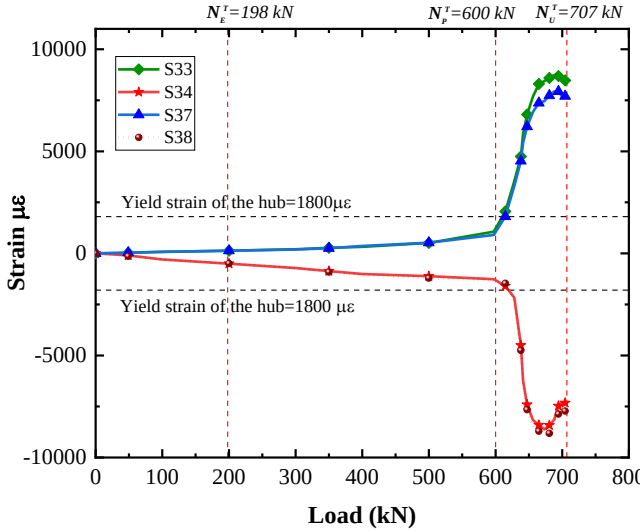

(c) Strain–load curves for the hub ring internal

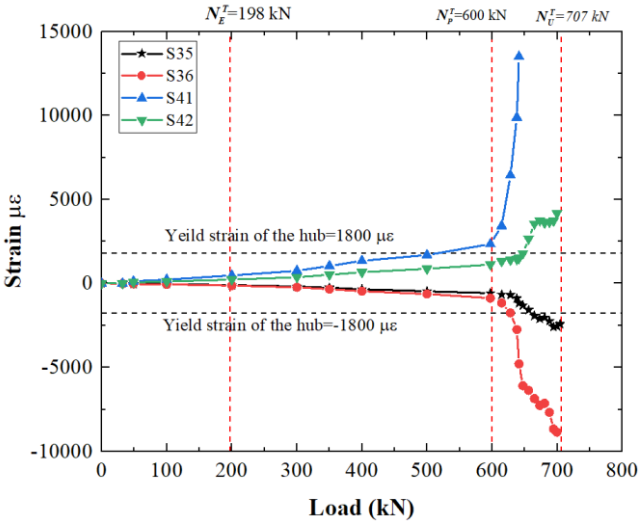

(d) Strain–load curves for the hub ring internal

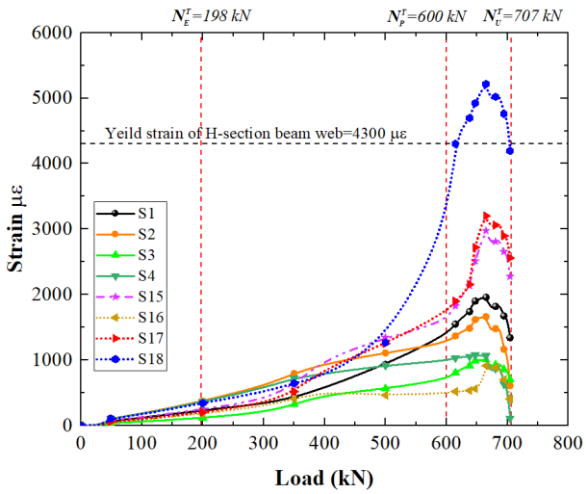

(e) Strain–load curves for the H-shaped beam

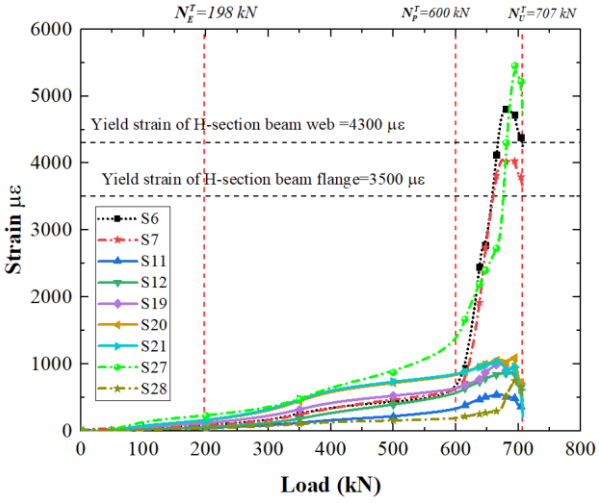

(f) Strain–load curves for the H-shaped beam flanges and welding area

Fig. 20 Load-displacement and strain load curves for specimens NDJG-1 and NDJG-2

5. FE modelling

Based on a dynamic explicit analysis step, full FE models for the NDJs and NDJGs were established using Abaqus software. Because the cover plates, bolts, nuts, and small washers do not affect the tensile bearing capacity of the joints, only hub, throat, and H-section beams were considered in the FE analysis. In the FE analysis, the tensile load was applied to one end of the joint, whereas the other end was fixed. To simplify the FE models, two reference points R1 and R2 were created at the ends of each beam to replace the loading plates in the tests. Based on the test specimen design, a tie contact was adopted

in the Abaqus software to simulate the weld connection in the tested specimens (Figs 21 (a) and Fig. 22 (a)).

5.1. Establishment of FE models

The Solidworks software was used to draw and establish the components of the specimens, including the hubs, throats, and H-shaped beams. All the components of the FE models with interlock type I (NDJ-FE) and interlock type II (NDJG-FE) were imported to Abaqus as Parasolid files for assembly and processing. The material properties for the FE model components are defined according to the material test results presented in Table 1. Before running the analysis, the components were partitioned and meshed with the Hex C3D8R element of all the components (Fig. 23 (a) and (b)). Subsequently, to simulate the boundary conditions in the test, two reference points were defined, and coupling contacts were created between the reference points and the beam ends. Thereafter, contact pair interactions developed in the interlock between the hub and beam-inserted ends. The interactions of NDJ-FE and NDJG-FE were different under tensile loads, where the interaction of surface 2 was suppressed in the interlock system of NDJ-FE, whereas surfaces 1 and 3 were activated. In contrast, the contacts of surfaces 1, 3, and 5 were suppressed, whereas the interactions of surfaces 2 and 4 were activated in the interlock system of NDJG-FE (Figs 21 (b) and 22 (b)).

5.2. Load and boundary conditions

The load and boundary conditions for the FE models of the novel steel dovetail joint were defined based on the boundary conditions (BCs) specified in the test. However, only two BCs were defined for R1 and R2 (Figs 21 and 22). The axial tensile load was applied to R1 as a displacement (U1 = 100 in the *X*-direction), whereas U2 = U3 = UR1 = UR2 = UR3 = 0. In contrast, R2 was considered as a fixed end to allow the joint to move only in the *X*-direction (Fig. 24 (a) and (b)).

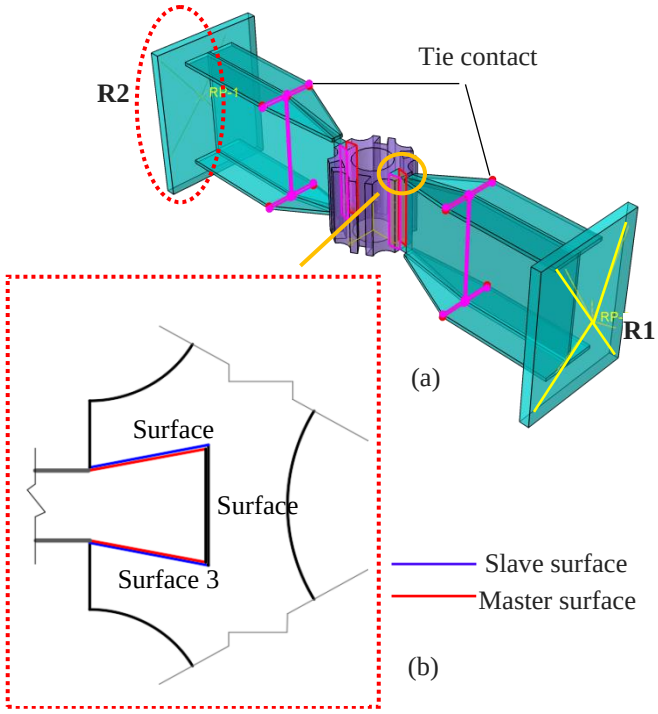

Fig. 21 Interaction details for NDJs: (a) Surface-to-surface, tie, and coupling contacts, (b) interactions in interlock type I

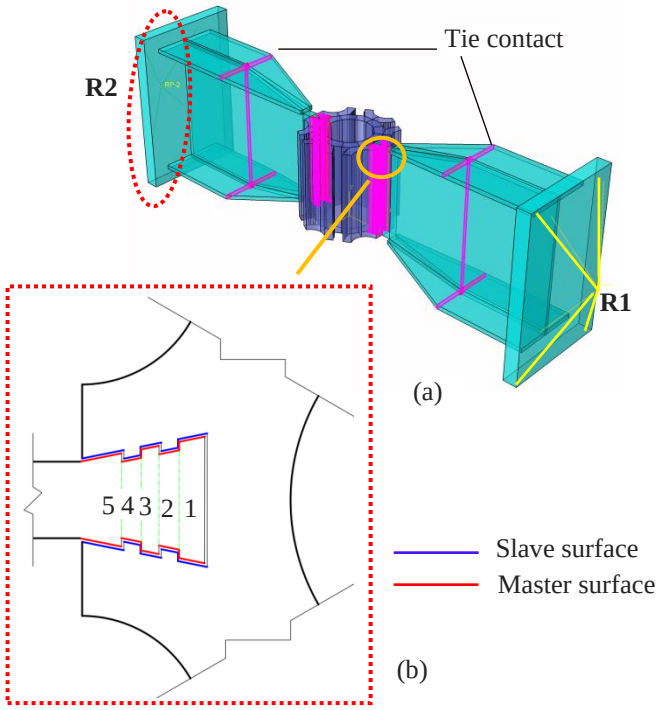

Fig. 22 Interaction details for NDJGs: (a) Surface-to-surface, tie, and coupling contacts, (b) interactions in interlock type II.

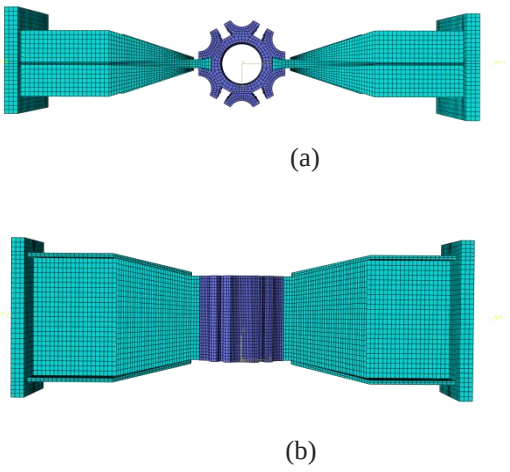

Fig. 23 Mesh for FE models: (a) Top view, (b) side view

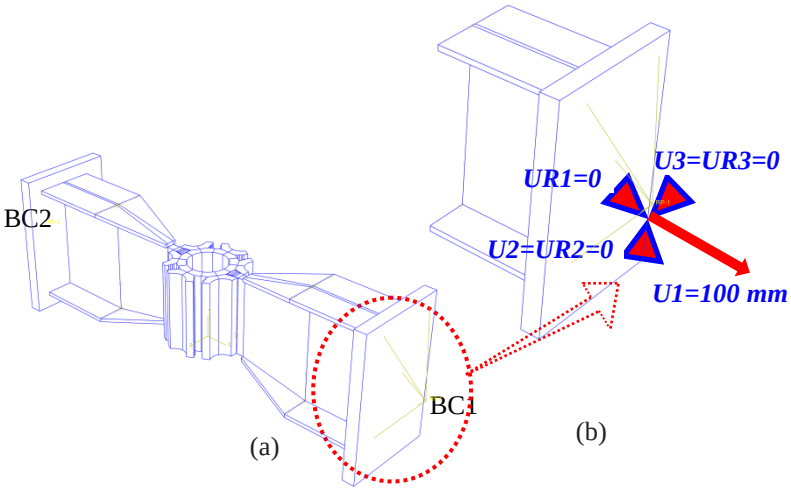

Fig. 24 Load and boundary conditions of FE models: (a) BC1 and BC2, (b) defined load

5.3. FE analysis—results and discussions

The FE models for novel steel dovetail joints without (interlock type I) and with (interlock type II) teeth patterns were analysed to verify the test results of this study. The failure modes and stress distributions of the models were compared with those obtained in the test. The FE model yielded the same stress distribution and failure mechanism (Fig. 17). Moreover, the yield capacity (233 kN) and ultimate tensile bearing capacity (282 kN) obtained using the NDJ-FE were compared with the test results (Fig. 18 (a)); the capacities were very close to the experimental results. In contrast, the

NDJG-FE yielded the same stress distributions and failure modes of the specimens as in the test (Fig. 19). Comparing the tensile capacity results of the FE analysis with the test results (Fig. 20 (a)), the yield capacity for NDJG-FE was 600 kN, which was the same as the yield capacity of NDJG-1 and 1.1 times the yield capacity of NDJG-2. Further, the ultimate capacity for the same model was 733 kN, which is equal to 1.03 times that of NDJG-1 and 1.11 times that of NDJG-2.

The results of the tests and numerical analyses for all the joints are summarised in Fig. 25 and Table 2. It is worth noting that the results of the FE analysis matched well with the test results, with high validity and efficiency.

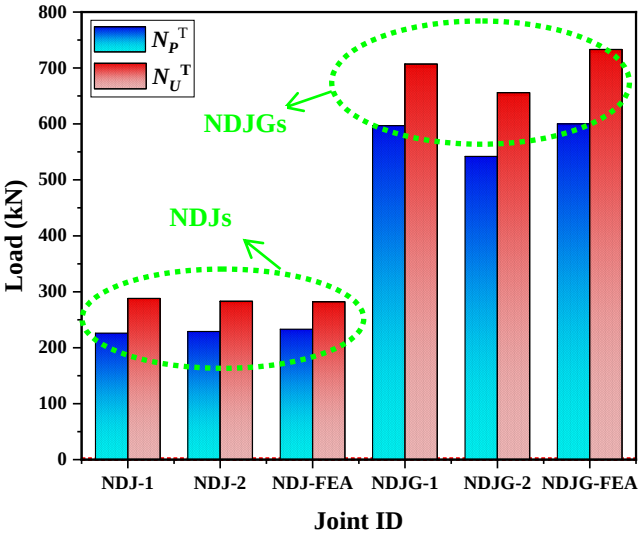

Fig. 25 Comparison of yield and ultimate bearing capacity for NDJs and NDJGs obtained in the test and FE analysis

Table 2
Comparison of yield and ultimate bearing capacities for NDJs and NDJGs obtained in the test and FE analysis

Joint ID	N_P^T times	N_U^T times
NDJG-1/NDJ-1	2.64	2.45
NDJG-1/NDJ-2	2.6	2.5
NDJG-1/NDJG-2	1.06	1.07
NDJG-2/NDJ-1	2.4	2.3
NDJG-2/NDJ-2	2.36	2.33
NDJ-1/NDJ-FEA	0.97	1.02
NDJ-2/NDJ-FEA	0.98	1
NDJG-1/NDJG-FEA	1.0	0.96
NDJG-1/NDJG-FEA	0.9	0.9
NDJG-FEA /NDJ-FEA	2.57	2.6

6. Theoretical analysis for novel steel dovetail joint

Based on the results of the test and FE analysis for the two types of novel steel dovetail joints under axial tensile load, one main failure occurred in NDJ-1 and NDJ-2 when the hub expanded and the beam end was pulled out. In contrast, NDJG-1 and NDJG-2 exhibited the same failure modes noticed in the NDJs accompanied by shear deformation in the interlock teeth. Therefore, theoretically relevant equations of yield and ultimate tensile bearing capacities of the NDJs and NDJGs were derived for the components, considering the design parameters (Figs 26 and 27).

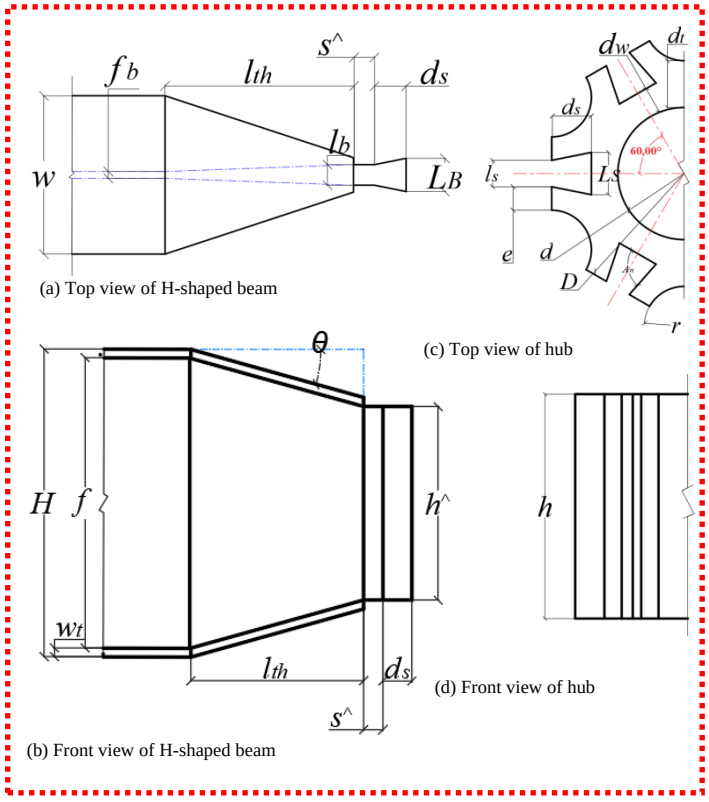

Fig. 26 Design parameters for interlock type-I joints (NDJs)

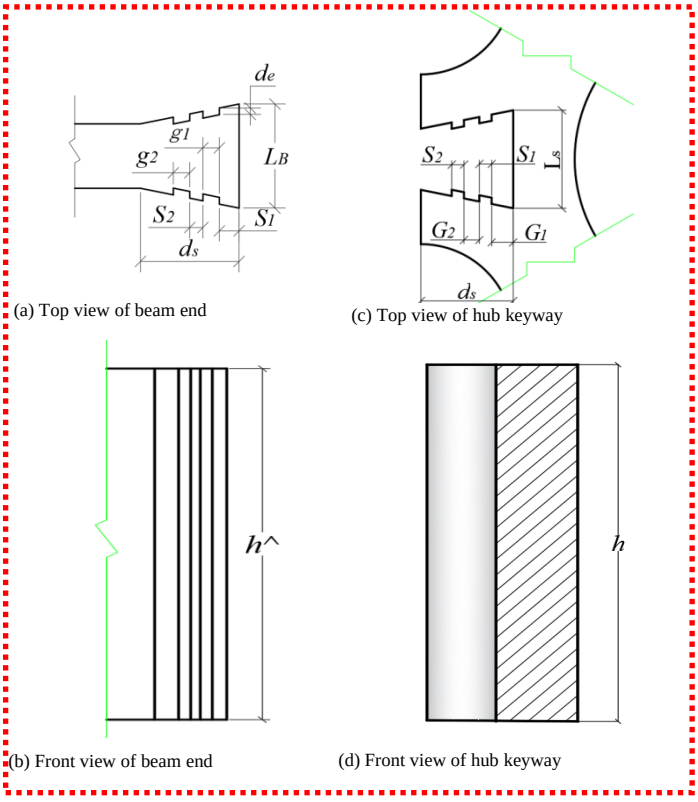

Fig. 27 Design parameters for interlock type-II joints (NDJGs)

6.1. Theoretical analysis of NDJs

Because the shapes of the hub and beam of the novel steel dovetail joint are special, the ring thickness d_w is designed to be the same or larger than the width of the beam neck l_b. Consequently, the following assumptions were adopted to derive the equations for the tensile bearing capacity:

1. The failures in the two edges of the hub keyway occurred simultaneously and had the same magnitude.
2. Based on the results of the test and FE analysis, the failure of the NDJs under tensile load occurred at the hub ring and edges of the hub keyway, where the hub ring is thicker than the neck width ($d_w \geq l_b$). Therefore,

$$T_{\text{neck}}^{Y} = 0.9\, A_{\text{neck}}\, f_y \quad (1)$$

where

$$A_{\text{neck}} = l_b\ h^{\wedge} \quad (2)$$

and $T_{\text{neck}}^{U} = 0.9\, A_{\text{neck}}\, f_u$

where T_{neck}^{Y} and T_{neck}^{U} indicate the tensile yield and ultimate capacities for the beam neck, A_{neck} is the effective area of the beam neck, l_b denotes the width of the beam neck, $h^{\wedge}$is the neck height, and f_y and f_u are the material yield and ultimate strength, respectively.

3. The deformed section area of the edges of the hub keyway was assumed to be equal to the thickness of the hub ring. Therefore, the tensile yield-bearing capacity of hub type I, where $d_{\text{m}} = d_{\text{w}} = 0.2d = 0.1D \geq l_b$, can be expressed as follows:

$$N_{P,\text{th}}^{T} = \frac{0.11\ d_m\ d_w\ h^{\wedge}\ f_v\ d_s}{D} \quad (3)$$

and the ultimate tensile bearing capacity can be expressed as follows:

$$N_{U,\text{th}}^{T} = \frac{1.5\ d_m\ d_w\ h^{\wedge}\ f_u}{D} \quad (4)$$

6.2. Theoretical analysis of NDJGs

The NDJGs rely on the hub ring, edges of the hub keyway, and teeth patterns to bear the tensile load. The tensile bearing capacity of NDGs is 2.5 times higher than that of the NDJs. Based on the results of the test and numerical analysis, the NDJG-type combined hub ring, hub keyway edge failures, and teeth pattern shear failures under axial tensile load. However, the tensile yield capacity of the NDJGs can be expressed as follows:

$$N_{P,\text{th}}^{T} = \left(\frac{(1.4\ D\ (l_n)^2)+(0.11\ d_m\ d_w\ (d_s)^2)}{D\ d_s}\right) h^{\wedge}\ f_v \quad (5)$$

Moreover, the ultimate tensile bearing capacity can be expressed as follows:

$$N_{U,\text{th}}^{T} = \left(\frac{(0.63\ D\ (l_n)^2)+(1.5\ d_m\ d_w\ d_s\ )}{D\ d_s}\right) h^{\wedge}\ f_u \quad (6)$$

where l_n is the total width of the teeth:

$$l_n = S_1 + S_2 + \ldots + S_n$$

7. Validations of test, FE analysis, and theoretical analysis

This section presents the calculations and comparisons of the results of the test and the numerical and theoretical analyses of the novel steel dovetail joint, as summarised in Table 3. The results of the analyses of the three approaches adopted in this study were validated by calculating the mean values of the ratios of the theoretical to test, theoretical to numerical, and test to numerical results for the NDJs and NDJGs. Based on the results of the comparison of the three methods of analysis, the standard deviation (Std v) was also calculated; its maximum value was 0.056. The tensile yield and ultimate bearing capacities of the NDJs and NDJGs obtained by adopting the three methods of analysis matched well with each other and indicated very high efficiency and validity.

Table 3
Comparison of the results of the test, FE analysis, and theoretical analysis for tensile bearing capacity

Item	$N_{P,t}^{T}$	$N_{P,n}^{T}$	$N_{P,\text{th}}^{T}$	$N_{P,\text{th}}^{T}$ /$N_{P,t}^{T}$	$N_{P,\text{th}}^{T}$ /$N_{P,n}^{T}$	$N_{P,t}^{T}$/ $N_{P,n}^{T}$	$N_{U,t}^{T}$	$N_{U,n}^{T}$	$N_{U,\text{th}}^{T}$	$N_{U,\text{th}}^{T}$ /$N_{U,t}^{T}$	$N_{U,\text{th}}^{T}$ /$N_{U,n}^{T}$	$N_{U,t}^{T}$/ $N_{U,n}^{T}$
NDJ-1	226	233	231	1.02	0.99	0.97	288	282	282	0.98	1	1.0
NDJ-2	229	233	231	1.01	0.99	0.98	283	282	282	0.99	1	1.003
NDJG-1	597	600	598	1.0	0.99	0.99	707	733	726	1.02	0.99	0.96
NDJG-2	542	600	598	1.1	0.99	0.90	656	733	726	1.10	0.99	0.89
Average				1.03	0.99	0.96				1.03	0.99	0.97
Std v				0.047	0.003	0.041				0.056	0.005	0.056

8. Conclusions

The single-layer lattice steel structure system is one of the most developed and young systems in the field of steel structures. Various types of joints with various types of structural element sections and materials have been designed and studied to fulfil the structural requirements. In this study, interlock type-I () and interlock type-II () novel steel dovetail joints (NDJs and NDJGs, respectively) were proposed and tested. Based on the results of the analysis, the following conclusions were drawn:

1. The novel steel dovetail joint design concept, design method, FE modelling method, and test program have been proposed and discussed using an H-shaped beam to gather and present detailed information on the new joint system.
2. The test and FE analyses were carried out on novel steel dovetail joints with different interlock-type systems. The two types presented different tensile bearing capacities: the tensile yield and ultimate bearing capacities of the interlock type-II specimens were 2.4–2.64 times those of the interlock type-I specimens.
3. Based on the results of the test and FE analysis, the NDJs and NDJGs presented different deformation modes based on their respective failure mechanisms: The NDJs rely on the interlock system and hub ring to bear the load. Therefore, a major failure occurred in the hub ring. In contrast, the NDJGs rely on the interlock system, hub ring, and teeth patterns to bear the load. Therefore, the NDJGs combined two failure modes: the hub ring expanding failure and teeth pattern shear failure.
4. The related equations for the tensile yield and ultimate bearing capacities of the NDJs and NDJGs were proposed and calculated. As experimental, numerical, and theoretical approaches were adopted to investigate the mechanical performance and failure modes of the novel steel dovetail joints, the theoretical and numerical results for the two groups verified the experimental results. All the results obtained using the three approaches in this study matched very well and indicated high analysis validity and efficiency.

Acknowledgements

This study was financially supported by the Natural Science Foundation of Hebei Province (Grant No. E2021402006).

List of symbols

NDJs	Novel steel dovetail joint without teeth pattern (interlock type I)	$s^{\wedge}$	Neck's length (mm)
		t_h	Length of H-shaped beam end (mm)
NDJGs	Novel steel dovetail joint with teeth pattern (interlock type II)	θ	Slope angle of throat
Design NDJ symbols		$S_1,\ S_2$	Teeth width (mm)
D	External diameter of hub (mm)	G_1, G_2	Groove in hub keyway (mm)

d	Internal diameter of hub (mm)	g_1, g_2	Groove in beam end (mm)
d_s	Keyway length of hub (mm)	d_e	Groove depth (mm)
d_w	Thickness of hub ring (mm)	***Theoretical analysis symbols***	
d_t	Maximum thickness of hub (mm)	l_n	Total width of teeth pattern (mm)
r	Diameter of removed area (mm)	$T^Y_{\mathbf{neck}}$	Beam neck tensile yield-bearing capacity
L_s	Maximum width of hub keyway (mm)	$A_{\mathbf{neck}}$	Section area of beam neck
l_s	Minimum width of hub keyway (mm)	$T^U_{\mathbf{neck}}$	Beam neck ultimate tensile bearing capacity
h	Hub height (mm)	$N^T_{P,\mathrm{th}}$	Yield capacity in equations
e	Width of edge of hub keyway (mm)	$N^T_{P,t}$	Yield bearing capacity in test
H	Height of H-shaped beam (mm)	$N^T_{P,n}$	Yield bearing capacity of FE analysis
$\mathrm{h}^{\wedge}$	Height of H-shaped beam end (mm)	$N^T_{U,t}$	Ultimate bearing capacity in test
L_B	Maximum width of beam end (mm)	$N^T_{U,n}$	Ultimate bearing capacity in FE analysis
l_b	Minimum width of beam end (mm)	$N^T_{U,\mathrm{th}}$	Ultimate bearing capacity in equations
f_b	Thickness of H-shaped beam web (mm)	E	Elastic modulus
w_t	Thickness of H-shaped beam flange (mm)	f_y	Material yield strength (kN)
w	Flange width of H-shaped beam (mm)	f_u	Material ultimate strength (kN)
f	Web height of H-shaped beam (mm)	f_v	Material shear strength (kN)
l_{th}	Length of throat (mm)	ε_y	Material yield strain

References

[1] R. qiang Feng, X. Wang, Y. Chen, and Q. Cai, "Static performance of double-ring joints for freeform single-layer grid shells subjected to a bending moment and shear force," Thin-Walled Struct., vol. 131, no. December 2017, pp. 135–150, 2018, doi: 10.1016/j.tws.2018.06.038.

[2] Q. Han, C. Wang, Y. Xu, X. Zhang, and Y. Liu, "Mechanical performance of AH joints and influence on the stability behaviour of single-layer cylindrical shells," Thin-Walled Struct., vol. 146, no. June 2019, p. 106459, 2020, doi: 10.1016/j.tws.2019.106459.

[3] Q. Han, Y. Liu, J. Zhang, and Y. Xu, "Mechanical behaviors of the Assembled Hub (AH) joints subjected to bending moment," J. Constr. Steel Res., vol. 138, pp. 806–822, 2017, doi: 10.1016/j.jcsr.2017.08.026.

[4] Y. Y. Ma, H. H. Ma, F. Fan, and Z. W. Yu, "Experimental and theoretical analysis on static behavior of bolt-column joint under in-plane direction bending in single-layer reticulate shells," Thin-Walled Struct., vol. 135, no. November 2018, pp. 472–485, 2019, doi: 10.1016/j.tws.2018.11.009.

[5] H. Liu, H. Chen, and Z. Chen, "Residual behaviour of welded hollow spherical joints under corrosion and de-rusting," J. Constr. Steel Res., vol. 167, p. 105977, 2020, doi: 10.1016/j.jcsr.2020.105977.

[6] J. Lu, H. Liu, and Z. Chen, "Behavior of welded hollow spherical joints after exposure to ISO-834 standard fire," J. Constr. Steel Res., vol. 140, pp. 108–124, 2018, doi: 10.1016/j.jcsr.2017.10.026.

[7] H. Nassiraei, M. A. Lotfollahi-Yaghin, H. Ahmadi, and L. Zhu, "Static strength of doubler plate reinforced tubular T/Y-joints under in-plane bending load," J. Constr. Steel Res., vol. 136, no. April, pp. 49–64, 2017, doi: 10.1016/j.jcsr.2017.05.009.

[8] S. Stephan, K. Knebel, and J. Sanchez-Alvarez, "Reticulated Structures On Free-Form Surfaces," Stahlbau, vol. 73, no. April, pp. 562–572, 2004.

[9] Ma. H, Fan. F, & Shen. S, "NUMERICAL PARAMETRIC INVESTIGATION OF SINGLE-LAYER LATTICED DOMES WITH SEMI-RIGID JOINTS, " J. Journal-International Association for Shell and Spatial Structures, 49, 99-110.

[10] A. L. Zhang, G. H. Shangguan, Y. X. Zhang, Q. B. Wang, and W. C. Cai, "Experimental study of resilient prefabricated steel frame with all-bolted beam-to-column connections," Adv. Steel Constr., vol. 16, no. 3, pp. 255–271, 2020, doi: 10.18057/IJASC.2020.16.3.7.

[11] H. W. Ma, H. Zheng, W. Zhang, and Z. Z. Tang, "Experimental and numerical study of mechanical properties for the double-ribbed reinforced beam-column connection," Adv. Steel Constr., vol. 16, no. 4, pp. 297–309, 2020, doi: 10.18057/IJASC.2020.16.4.2.

[12] H. Ma, L. Yu, F. Fan, and Z. Yu, "Mechanical performance of an improved semi-rigid joint system under bending and axial forces for aluminum single-layer reticulated shells," Thin-Walled Struct., vol. 142, no. May, pp. 322–339, 2019, doi: 10.1016/j.tws.2019.05.003.

[13] H. Ma, F. Fan, G. Chen, Z. Cao, and S. Shen, "Numerical analyses of semi-rigid joints subjected to bending with and without axial force," J. Constr. Steel Res., vol. 90, pp. 13–28, 2013, doi: 10.1016/j.jcsr.2013.07.017.

[14] M. Ahmadizadeh and S. Maalek, "An investigation of the effects of socket joint flexibility in space structures," J. Constr. Steel Res., vol. 102, pp. 72–81, 2014, doi: 10.1016/j.jcsr.2014.07.001.

[15] Zhao. C, Liu. W, Zhao. H, Elastic Plastic Analysis and Experimental Research on New Joint of Reticulated Shells ," J. Journal of Southeast University, Vol.28 No.2 Mar .1998. [in Chinese]

[16] W. T. Qiao, R. J. Zhu, D. Wang, J. Li, and J. W. Yuan, "Study on moment-rotation relationship of steel sleeve beam-column joint with interference fit," Adv. Steel Constr., vol. 16, no. 4, pp. 337–345, 2020, doi: 10.18057/IJASC.2020.16.4.6.

[17] S. Yan, K. J. R. Rasmussen, L. L. Jiang, C. Zhu, and H. Zhang, "Experimental evaluation of the full-range behaviour of steel beam-to-column connections," Adv. Steel Constr., vol. 16, no. 1, pp. 77–84, 2020, doi: 10.18057/IJASC.2020.16.1.9.

[18] Z. Xiong, X. Guo, Y. Luo, and H. Xu, "Numerical analysis of aluminium alloy gusset joints subjected to bending moment and axial force," Eng. Struct., vol. 152, pp. 1–13, 2017, doi: 10.1016/j.engstruct.2017.09.005.

[19] Q. Han, Y. Liu, Y. Xu, and Z. Li, "Mechanical behaviours of assembled hub joints subjected to axial loads," J. Constr. Steel Res., vol. 153, pp. 667–685, 2019, doi: 10.1016/j.jcsr.2018.11.007.

[20] H. Ma, Y. Ma, Z. Yu, and F. Fan, "Experimental and numerical research on gear-bolt joint for free-form grid spatial structures," Eng. Struct., vol. 148, pp. 522–540, 2017, doi: 10.1016/j.engstruct.2017.06.076.

[21] G. Oyéniran ADEOTI, F. Fan, M. A. Huihuan, and S. Shen, "Investigation of aluminium bolted joint (HBJ) system behavior," Thin-Walled Struct., vol. 144, no. June 2016, p. 106100, 2019, doi: 10.1016/j.tws.2019.03.059.

[22] F. Fan, H. Ma, G. Chen, and S. Shen, "Experimental study of semi-rigid joint systems subjected to bending with and without axial force," J. Constr. Steel Res., vol. 68, no. 1, pp. 126–137, 2012, doi: 10.1016/j.jcsr.2011.07.020.

[23] H. Ma, S. Ren, and F. Fan, "Experimental and numerical research on a new semi-rigid joint for single-layer reticulated structures," Eng. Struct., vol. 126, pp. 725–738, 2016, doi: 10.1016/j.engstruct.2016.08.028.

[24] K. D. Tsavdaridis, R. Feng, and F. Liu, "Shape Optimization of Assembled Single-Layer Grid Structure with Semi-Rigid Joints," Procedia Manuf., vol. 44, no. 2019, pp. 12–19, 2020, doi: 10.1016/j.promfg.2020.02.199.

[25] Y. Y. Ma, H. H. Ma, S. Ren, and F. Fan, "Hysteretic behavior of a new assemble joint under out-of-plane bending: Experimental and numerical studies," J. Constr. Steel Res., vol. 167, pp. 1–14, 2020, doi: 10.1016/j.jcsr.2020.105959.

[26] S. D. Xue, S. Y. Li, X. Y. Li, and C. Yao, "Behaviour and mathematical model for semi-rigid threaded-sleeve connection," Adv. Steel Constr., vol. 15, no. 2, pp. 123–128, 2019, doi: 10.18057/IJASC.2019.15.2.1.

[27] H. Wang, Q. Wu, H. Qian, K. Han, and F. Fan, "Buckling behavior of a circular steel tube with a bolt–ball joint under installation eccentricity," Eng. Struct., vol. 197, no. July, p. 109407, 2019, doi: 10.1016/j.engstruct.2019.109407.

[28] H. Chen, H. Liu, and Z. Chen, "Compressive strength of corroded special-shaped welded hollow spherical joints based on numerical simulation," Thin-Walled Struct., vol. 149, no. May 2019, p. 106531, 2020, doi: 10.1016/j.tws.2019.106531.

[29] H. Liu, Y. Ding, and Z. Chen, "Static stability behavior of aluminum alloy single-layer spherical latticed shell structure with Temcor joints," Thin-Walled Struct., vol. 120, no. June, pp. 355–365, 2017, doi: 10.1016/j.tws.2017.09.019.

[30] Z. Xiong, X. Guo, Y. Luo, S. Zhu, and Y. Liu, "Experimental and numerical studies on single-layer reticulated shells with aluminium alloy gusset joints," Thin-Walled Struct., vol. 118, no. March, pp. 124–136, 2017, doi: 10.1016/j.tws.2017.05.007.

[31] H. Liu, Y. J. Zhang, L. Wang, Y. Zhao, and Z. H. Chen, "Mechanical performance of welded hollow spherical joints with H-beams after elevated temperatures," Eng. Struct., vol. 222, no. January, p. 111092, 2020, doi: 10.1016/j.engstruct.2020.111092.

[32] X. Li, J. Zhao, G. Ma, and W. Chen, "Experimental study on the seismic performance of a double-span traditional timber frame," Eng. Struct., vol. 98, pp. 141–150, 2015, doi: 10.1016/j.engstruct.2015.04.031.

[33] Q. Xie, L. Zhang, L. Wang, W. Zhou, and T. Zhou, "Lateral performance of traditional Chinese timber frames: Experiments and analytical model," Eng. Struct., vol. 186, no. February, pp. 446–455, 2019, doi: 10.1016/j.engstruct.2019.02.038.

[34] C. Chen, H. Qiu, and Y. Lu, "Flexural behaviour of timber dovetail mortise-tenon joints," Constr. Build. Mater., vol. 112, pp. 366–377, 2016, doi: 10.1016/j.conbuildmat.2016.02.074.

[35] "Chinese Metalic materials-Tensile testing-part 1: Method of test at room temperature". GB/T 228.1-2010.

Advanced Steel Construction – Vol. 18 No. 1 (2022) 465–478
DOI:10.18057/IJASC.2022.18.1.5

EFFECT OF RANDOM PRE-STRESSED FRICTION LOSS ON THE PERFORMANCE OF A SUSPEN-DOME STRUCTURE

Ren-Zhang Yan [1, 2, *], Mei-Hao Zhu [3], Ting Liu [1, 2], Jia-Qi Liu [1, 2] and Zhi-Hua Chen [4]

[1] *State Key Laboratory of Mountain Bridge and Tunnel Engineering, Chongqing Jiaotong University, Chongqing 400074, China*
[2] *School of Civil Engineering, Chongqing Jiaotong University, Chongqing 400074, China*
[3] *Design and Development Department, China Construction Science and Technology Co., Ltd. Sichuan Branch, Chengdu 610213, China*
[4] *School of Civil Engineering, Tianjin University, Tianjin 300072, China*
** (Corresponding author: E-mail: rz_yan@cqjtu.edu.cn)*

ABSTRACT

The key to the high-efficiency performance of the suspen-dome structure is to apply the pre-stressed design value to the structure accurately. However, engineering practice has found that the use of tensioning hoop cables to apply the pre-stress will produce noticeable pre-stressed friction loss (PFL), which significantly affects the safety performance of the structure. In this paper, based on a 1:10 scaled-down experiment model of a suspen-dome structure with rolling cable-strut joint installed, the random PFL (RPFL) effect of the suspen-dome on structure performance was analyzed through a probability statistics theory. First, aiming at the unequal tensioning force at both sides of the tensioned hoop cable during the tensioning process, a pre-stressed force calculation method is proposed that considers the unequal tensioning control force and RPFL at all cable–strut joints, and the reliability of this method is verified through a tension test. Then, based on the cable-joint tension test carried out in the early stage of the research group, a random mathematical model of the friction coefficient (FC) at the rolling cable–strut joint is established. And then, the cable force calculation method is used to establish the random finite element model, and independent and random changes in the FC at each rolling cable–strut joint can be considered. Subsequently, the Monte Carlo method is used to calculate the random mathematical characteristics of the mechanical performance parameters such as the member stress and joint deformation, and the obtained results are verified through a static loading experiment. In addition, to investigate the effect of random defects on structural stability, other random defects, such as the initial curvature and installation deviation, were continuously introduce based on the random finite element model. As such, we could obtain the law of the effect of multi-defect random variation coupling on the structure's ultimate bearing capacity.

ARTICLE HISTORY

Received: 17 October 2020
Revised: 27 May 2021
Accepted: 27 May 2021

KEYWORDS

Suspen-dome;
Friction coefficient;
Ultimate bearing capacity

1. Introduction

A new type of hybrid space structure, the suspen-dome, enhances the structural stability and ease of construction of buildings [1]. Since its proposal by Kawagucki [2], the suspen-dome has been widely used in more than 20 engineering projects [3, 4]. The high efficiency of the suspen-dome structure is achieved by accurately applying the pre-stressed design values to increase its stiffness and bearing capacity [5-7]. However, pre-stressed friction loss (PFL) is generated while tensioning the hoop cables (HCs). Zhang et al. studied the PFL of the 2008 Olympic Games Badminton Gymnasium and found, through on-site monitoring, that the total PFL of each HC was more than 35%, causing the ultimate bearing capacity of the structure to reduce by approximately 15% [8]. The PFL from the construction process of the suspen-dome structure can have a large negative effect on its performance, even threatening its safety. Zhang et al. reduced PFL by changing the type of joint and pointed out that friction results in unevenness of the internal force distribution of the structure [9]. Liu et al. analyzed the friction loss at the rolling cable–strut joint and its effect on the suspen-dome [10, 11].

Till date, studies on the analysis of the effect of PFL on the performance of the suspen-dome structure remain at the qualitative level. Therefore, the conclusions drawn by various studies vary with the analytical methods used. Existing studies use only theoretical analysis to study the PFL effect, which cannot simulate all the possible problems that could occur in the actual design and construction process[12]. Therefore, to gain a more accurate understanding of the mechanical properties of the suspen-dome structure and enable broader applications, experiments must be performed. In this study, in view of the core position of the tensegrity system in a suspen-dome and PFL in the actual construction process, the authors developed a scaled-down suspen-dome model, for which safety was accurately evaluated using specific quantitative indices, and the effect of random PFL (RPFL) on the static structure performance was explored.

2. New cable force calculation method

Several force-finding methods have been developed in the last decade. For example, Chen et al. presented an improved symmetry method that only requires the symmetry type and connectivity of the structure for analysis [13]. Zhang et al. presented an optimization approach that can easily find various equilibrium shapes [14, 15]. Liu et al. developed a double control form finding method considering the construction process for controlling both the configuration and force balance [16]. However, few methods consider the friction of the cable–strut joints [17]. When pre-stress is applied by tensioning the HCs, the actual control values at the tensioning points on both sides of the same tensioned cable may not be equal, owing to the limitations of the tensioning equipment and cable force-monitoring system. In addition, inevitable differences appear between cable–strut joints during the manufacturing process, and the friction coefficients of cable-strut joints (FCCJ) are not completely equal, increasing the complexity of the internal force distribution of the passive-tensioning cable segments. However, accurate determination of the internal force distribution of each cable segment is a prerequisite for precisely evaluating the effect by considering the effect of RPFL on the global structure performance. To simulate the pre-stressed distribution during the actual tensioning construction process, a new cable force calculation method is proposed that considers the unequal tensioning control force and different FCCJs.

2.1. Internal force calculation process of passive-tensioning cable segments

Fig. 1 shows the schematic of a continuous tensioning cable consisting of (n−1) cable – strut joints and n cable segments. The tensioning values at tensioning points 1 and 2 are not equal, i.e., [T1] ≠ [T2], and the friction coefficients (FCs), μ_i, of the cable–strut joints are not equal, and μ_i represents the No. i cable – strut joints. To conduct the simulations and experiments, the following assumptions were made: (i) [T1] ≥ [T2]. (ii) The tension is applied simultaneously on both sides of the tensioning cable; this does not cause any large changes in the positions of the cable–strut joints during the tensioning process.

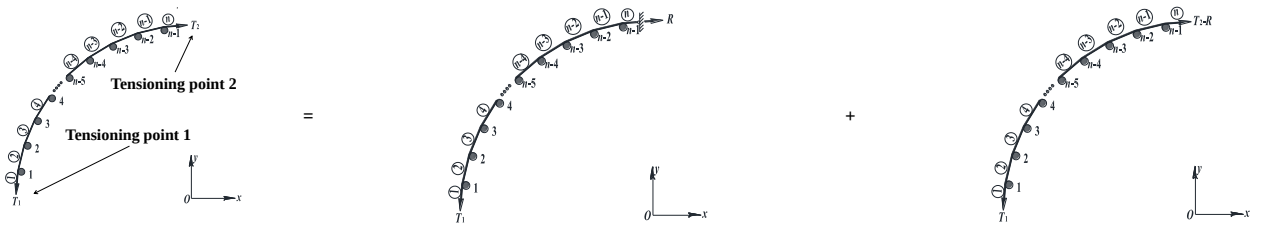

a) Tensioning cable b) Tensioning cable with temporarily fixed tensioning point 2 c) Tensioning cable with temporarily fixed tensioning point 1

Fig. 1 Schematic of the tensioning cable

When the HC is tensioned, the cable force is gradually transferred from the tensioning points to the adjacent cable segments. The internal forces of the points and cable segments are not equal because of the friction loss that occurs at the cable–strut joints during the transfer. For generality, consider cable–strut joint *i* in Fig. 2 as an example. T_i is the cable force generated by the active-tensioning cable segment. Here, T_{i+1} is the cable force generated by the passive-tensioning cable segment, N_i is the vertical pressure of the cable–strut joint on the cable, and f_i is the friction force at the cable–strut joint. Assuming that the maximum static friction force at the cable–strut joint is $f_{i,max}$, and the FC is μ_i; then, according to static equilibrium and friction transfer law, the following two situations must occur:

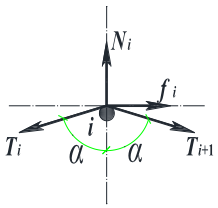

Fig. 2 Force schematic of cable–strut joint *i* during the tension process

① No cable sliding occurs, i.e., $T_{i+1} = 0$. This scenario is expressed as

$$\begin{cases} f_i \le f_{i,\max} = \mu_i N_i \\ f_i = T_i \cdot \sin\alpha \\ N_i = T_i \cdot \cos\alpha \end{cases} \tag{1}$$

As indicated in Equation (1), $\tan\alpha \le \mu_i$ and for $0° < \alpha < 90°$, $0° < \alpha < \arctan\mu_i$. That is, if $0° < \alpha < \arctan\mu_i$, the cable cannot slide, and pre-stress cannot be applied; this scenario should be avoided during the construction process.

② Cable slides, i.e., $T_{i+1} > 0$, which is expressed as

$$\begin{cases} f_i = \mu_i N_i \\ f_i + T_{i+1} \cdot \sin\alpha = T_i \cdot \sin\alpha \\ N_i = T_i \cdot \cos\alpha + T_{i+1} \cdot \cos\alpha \end{cases} \tag{2}$$

The friction force at cable–strut joint *i* and the internal force of cable segment *i* + 1 can be derived from Equation 2, as shown in Equations 3 and 4, respectively.

$$f_i = \mu_i T_i \frac{2\sin\alpha}{\tan\alpha + \mu_i} = k_i^1 \cdot T_i , \tag{3}$$

$$T_{i+1} = T_i \cdot \frac{\tan\alpha - \mu_i}{\tan\alpha + \mu_i} = k_i^2 \cdot T_i , \tag{4}$$

where k_i^1 is the FC and is written as $k_i^1 = \mu_i \dfrac{2\sin\alpha}{\tan\alpha + \mu_i}$.

In addition, k_i^2 is the transfer coefficient and is written as $k_i^2 = \dfrac{\tan\alpha - \mu_i}{\tan\alpha + \mu_i}$.

Here, k_i^1 and k_i^2 are only related to μ_i and α. If a tensioning cable is fixed at one end and tensioned at the other, as shown in Fig. 1b, all cable forces can be calculated in turn according to Equation 4. However, in practice, the tensioning cable is long. To reduce the effect of the friction force, both ends of the tensioning cable must be tensioned simultaneously, as shown in Fig. 1a. The transfer of cable force is bidirectional, and both ends of a tensioning cable can be the active-tensioning ends. The steps to calculate the cable internal force are as follows, which is also shown in Fig. 3.

1) Calculate α and determine μ_i, k_i^1 and k_i^2 at each cable–strut joint.

2) Temporarily fix tensioning point 2 and make the internal force of tensioning point 1 T_1 = [T1]. The internal force is transferred from tensioning point 1 to tensioning point 2, as shown in Fig. 1-b).

3) Calculate the internal force T_2~T_n from cable segment 2 to *n* according to Equation 4. The support reaction at the temporary fixed tensioning point 2 can be derived from the static equilibrium equation, i.e., $R = T_n$.

4) Calculate friction force f_{n-1}~f_1 from joints $n-1$ to 1 in the reverse order by using Equation 3.

5) Keep the internal force of each cable segment unchanged, release the fixed constraint at tensioning point 2, and temporarily fix tensioning point 1. Then, apply $[T_2]$ and R to tensioning point 2. The unbalanced tension at tensioning point 2 will be ΔT_n = [T2] − R. This unbalanced tension is transferred from tensioning point 2 to tensioning point 1.

6) The unbalanced tension, $\Delta T_i = k_i^2 \cdot \Delta T_{i+1}$, of each cable segment is calculated from cable segment *n*-1 in reverse order by using Equation 4.

7) If $\Delta T_i > f_i$, the tension at tensioning point 2 can continue to be transferred to tensioning point 1, and the final internal force of cable segment *i* is $T_i + \Delta T_i$. If $\Delta T_i < f_i$, the tension at tensioning point 2 can no longer be transferred to tensioning point 1; the internal force from cable segments 1 to *i* is T_i, and the internal force from cable segments *i*+1 to *n* is $T_i+\Delta T_i$.

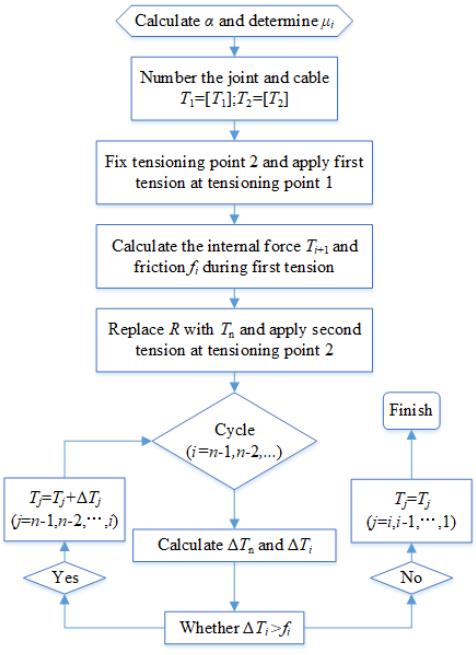

Fig. 3 Flow chart of the calculation of cable internal force

Further, if there are only two tensioning points in the HC, or the tension force in adjacent cable segments is equal to the tension segment, the internal forces of other cable segments can be directly obtained using the symmetry [18-21].

2.2. Tension test on scaled-down model

2.2.1. Experimental model

A 1:10 scaled-down suspen-dome model of the Chiping Stadium was fabricated, as shown in Fig. 4. The upper reticulated shell was assigned the Levy form, and for the lower part, a tensegrity system with seven circles of cables was used, whose HCs were numbered 1 to 7 from inside to outside. Φ12 steel wire ropes were used for the 1st and 2nd HCs, and 1×7/Φ12.7 steel strands were used for the 3rd to 7th HCs. Pre-stress was applied by tensioning the HC. One tensioning point was set at the 1st and 2nd HCs, two were symmetrically set at the 3rd HC, and four tensioning points were set at the 4th to 7th HCs. The layout diagrams of the tensioning and measurement points of the cable force are shown in Fig. 5. By combining the results of the pre-stress optimization and similarity ratio theory of the model experiment, the pre-stressed control values of HCs during the construction process were determined in Table 1. The specific tensioning equipment and control methods are detailed in [5].

a) Photograph of experimental model

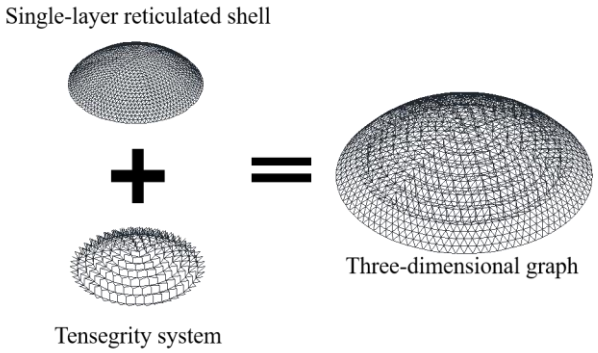

b) Three-dimensional graph of experimental model

Fig. 4 Photograph and diagram of experimental model

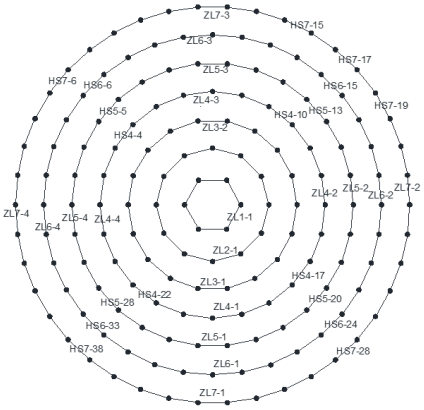

Fig. 5 Layout of tensioning points and measurement points for cable force

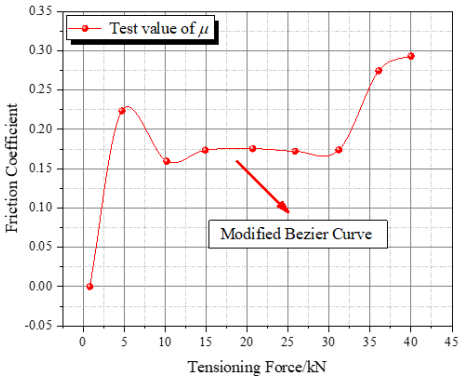

Fig. 6 Change curve of FC μ with the change of tension

Table 1
Pre-stressed control values

Level	1st circle	2nd circle	3rd circle	4th circle	5th circle	6th circle	7th circle
1st level (N)	100	370	495	945	1,270	2,220	4,950
2nd level (N)	300	1,770	1,600	2,000	2,470	5,040	1,1500

To reduce PFL during the tensioning process and ensure the uniform transfer of cable force, the authors independently developed a rolling cable–strut joint and used it in the model experiment. The authors had systematically studied the new joint, obtaining the changing trend of its FC fitted by the modified Bezier curve [22], as shown in Fig. 6. As indicated in Fig. 6, the FC changes with the tension force, and when the tension is small, the FC changes more drastically and presents unstable characteristics, only when the tension increases will the FC stabilize. As the FC is unstable when the internal force of the HC is small, and considering that the number of segments and joints of the outermost HC in the tension test is the largest, the internal force is the largest. Therefore, the FCs are taken as the corresponding FC when the pre-stress is 10 kN, that is, μ = 0.165 when the FC has begun to stabilize. At the same time, further analysis showed that when the FC is taken as μ = 0.165, this is the mean value of all the FCs measured during the cable-joint tension test. Therefore, the use of this mean value to calculate the combined effect of friction loss is considered representative.

2.2.2. Calculation results and comparative analysis

To verify the validity of the cable force calculation method for μ = 0.165, the APDL of ANSYS was used to compile the internal cable force calculation program according to the calculation process shown in Fig. 3. First, the tension value at both sides of the cable is assigned according to the actual tension control value. Next, the calculated value of the internal cable force of each cable segment is calculated and compared with the actual test value. The results of the calculation, which are displayed in Fig. 7, were compared with the experimental values. The change curves of the internal cable force are shown in Fig. 8. Relative errors between the experimental and theoretical values at the measurement points are shown in Table 2.

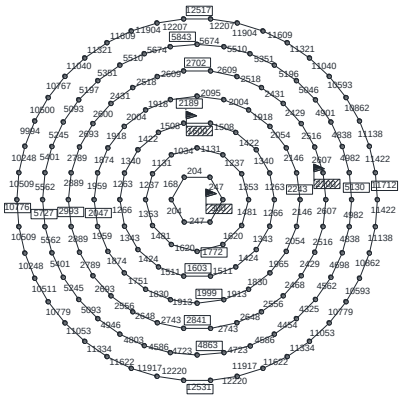

Fig. 7 Calculated values of cable force

Note: The value in [ ] is the actual tensioning control value at the

tensioning point on each HC. The value in  is the theoretical control value in Table 1 which could not be monitored due to equipment fault.

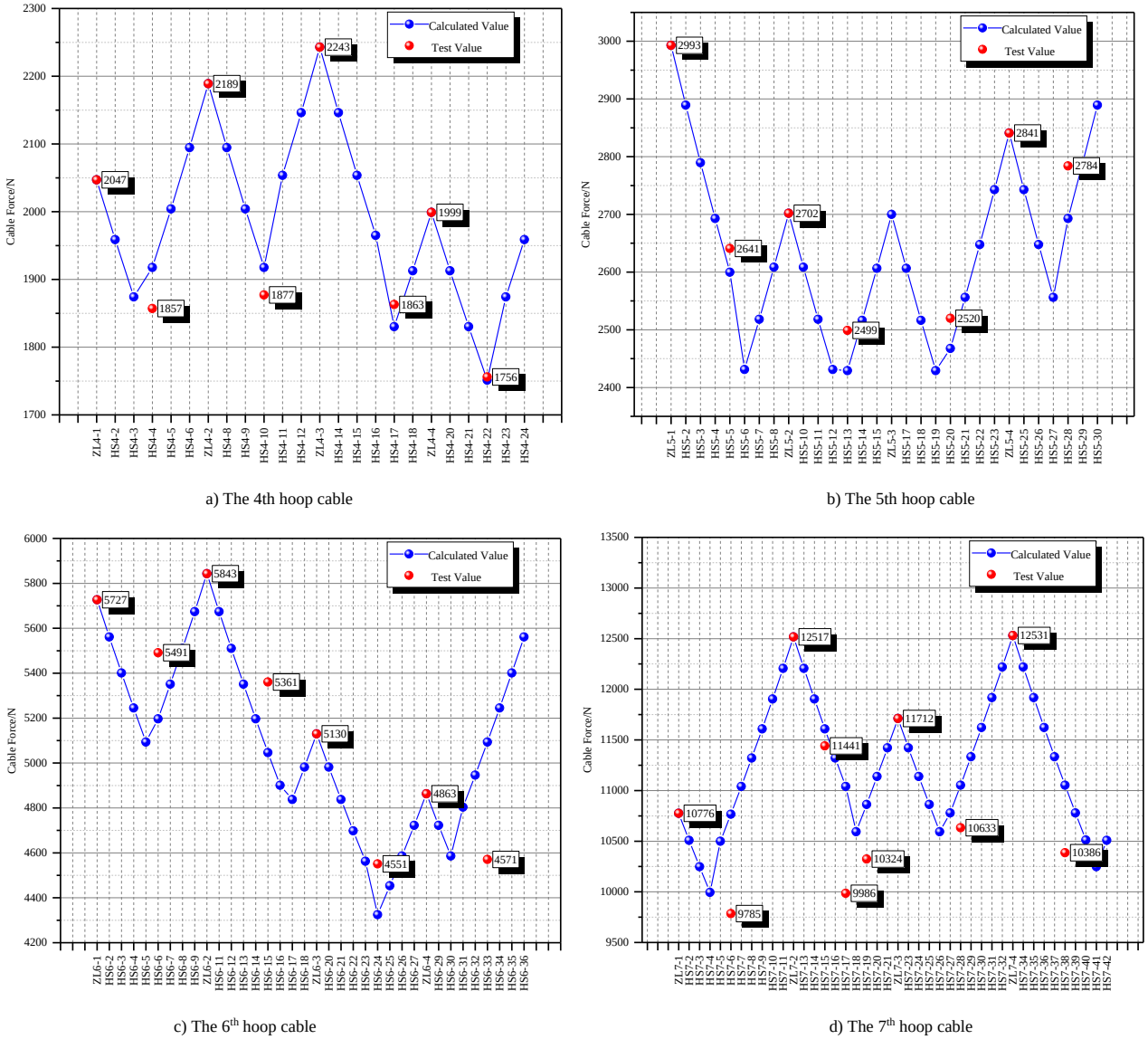

a) The 4th hoop cable

b) The 5th hoop cable

c) The 6th hoop cable

d) The 7th hoop cable

Fig. 8 Change curve of internal cable force

Table 2
Relative errors in cable force calculations

Number of the measurement point	Test value/N	Calculated value/N	Relative error/%
HS4-4	1,857	1,918	-3.2%
HS4-10	1,877	1,918	-2.1%
HS4-17	1,863	1,830	1.8%
HS4-22	1,756	1,751	0.3%
HS5-5	2,641	2,600	1.6%
HS5-13	2,499	2,429	2.9%
HS5-20	2,520	2,468	2.1%
HS5-28	2,784	2693	3.4%
HS6-6	5,491	5,197	5.7%
HS6-15	5,361	5,046	6.2%
HS6-24	4,551	4,325	5.2%
HS6-33	4,671	5,093	-8.3%
HS7-6	9,785	10,767	-9.1%
HS7-15	11,441	11,609	-1.4%
HS7-17	9,986	11,040	-9.6%
HS7-19	10,324	10,862	-5.0%
HS7-28	10,633	11,053	-3.8%
HS7-38	10,386	11,053	-6.0%

As shown in Fig. 8, owing to the effect of friction, both the calculated and test values indicate that in the same tensioning cable, the cable force exhibits an approximate linear decrease while being transferred from the tensioning points to the midsection of the tensioning cable. When the tensioning cable is long, such as the 7th HC, the maximum relative error of the cable force, occurred at HS7-4, compared with the pre-stressed control value is up to 20.2%; this cannot be ignored when studying the global structure performance. As observed in Table 2, the relative errors between the test and calculated values are small, and the absolute values of them are kept within 10%. This suggests that the cable force calculation method is reliable and lays a foundation for further analysis of the effect considering the cable force errors on the global structure performance.

From the values in Table 2, the following laws are observed:

1) With the gradual increase of the pre-stressed control value from inside to outside of the HCs, the relative errors between the calculated and test values gradually increase. The absolute values of the average relative errors from the 4th to 7th HCs are 1.8, 2.5, 6.4, and 5.8%, respectively.

2) The cable force of the outermost HC is the largest. The calculated values are larger than the test values, indicating that the former underestimates the real

effect of friction. The main reason for the underestimation is that the FCCJs were taken as 0.165 uniformly throughout the theoretical calculation model. However, the FC increases with the increase in the internal cable force, as shown in Fig. 6. Therefore, for the outermost HC with the larger pre-stressed control value, using the same FC as that in the inner HC will underestimate the friction loss.

3. Random mathematical model of PFL

The FC is related to the type of contact material and the joint construction. At present, the FC is mostly determined based on actual engineering experience. The FC of the contact surface in the cable–strut joint comes down to a tribological problem. Theoretical research on this topic, however, did not start until the 15th century. Later, Amontons and Coulomb made important contributions to the field and summarized well-known classical friction laws. However, with the progress of research in tribology, it has been found that the classical law is not a general law but only suitable for special cases. New tribological theories view the FC as a comprehensive characteristic of the friction pair system, instead of an inherent characteristic of the material. It is affected by the pairing properties of material pair, static contact time, normal load, loading speed, stiffness of friction pair, sliding speed, contact geometry and physical properties of surface layer, chemical actions of environmental medium, and so on [23-26]. During the sliding process of the HC, a friction pair is formed at the cable–strut joint. In addition to being subjected to the axial tensile force, the HC is compressed by the cable–strut joint along the normal direction. This causes the cross section shape of the HC to change continuously with the progress of the tensioning process. This, in turn, changes the FC of the friction pair. Therefore, it is difficult to obtain the exact values of FCCJ.

3.1. Value-picking study on the FC

3.1.1. FC at the traditional sliding cable–strut joint

Wang [27] and Qin et al. [28] analyzed the pre-stressed loss in the HCs of the 2008 Olympic Games Badminton Gymnasium, obtaining the value of PFL at each cable–strut joint. Liu et al. measured the FCCJ with a scaled-down suspen-dome model of the 2008 Olympic Games Badminton Gymnasium [29]. Guo et al. performed the construction monitoring service on the entire tensioning process of the Ji'nan Olympic Center Gymnasium [30]. With this, they obtained the internal forces of all HCs during the tensioning process with a magnetic flux monitor. Zhang et al. conducted experiments to study the friction generated at the cable–strut joint in a sunflower-patterned suspen- dome, and obtained PFLs of the new rolling cable–strut joints as well as the traditional sliding cable–strut joints [9]. Yuan et al. conducted an experiment on a full-scale model of the Xuzhou Olympic Center Gymnasium to derive the sliding FC at the cable–clamp joint [31]. According to the references above, the authors calculated the FCs at the traditional sliding cable–strut joints with the formula for Coulomb friction, as shown in Table 3.

Table 3
FCs at the sliding cable–strut joint in various suspen-dome constructions

Engineering	Joint model diagram	Joint position	On-site data (average value)	Experimental value	Remarks
2008 Olympic Badminton Gymnasium [27-29]		1st circle	0.019	0.110	
		2nd circle	0.010	0.192	
		3rd circle	0.004	0.157	
		4th circle	0.024	0.115	
		5th circle	0.034	0.198	
Ji'nan Olympic Center Gymnasium [30]		Inner circle	0.012	--	
		Middle circle	0.032	--	
		Outer circle	0.036	--	
A sunflower-patterned suspen-dome [9]	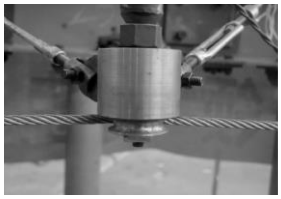	1st circle	--	0.178	The roller was welded to simulate the traditional sliding cable–strut joint
		2nd circle	--	0.146	
Shandong Chiping Stadium [5][32]		Joint test	--	0.199	The roller was welded to simulate the traditional sliding cable–strut joint
Xuzhou Olympic Center Gymnasium [31]	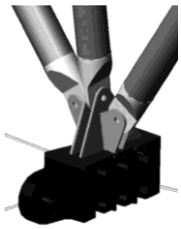	Joint 1	--	0.123	
		Joint 2	--	0.126	
		Joint 3	--	0.129	
		Joint 4	--	0.130	
		Joint 5	--	0.130	

As indicated in Table 3, FCCJ is highly variable but follows certain laws:

1) Due to the effect of complex on-site factors, the variability of the FC observed by on-site monitoring is higher than that obtained by the experiment.

2) The FC is related to the joint position. In other words, it is related to the internal force of the HC. For example, FCCJs of the 2008 Olympic Badminton Gymnasium and Ji'nan Olympic Center Gymnasium gradually increased from the inner circle to the outer circle. This changes the cross section shape of the HC under large normal pressures.

3) The FCs obtained through the model experiments are relatively steady, varying from 0.11 to 0.20 for the same joint type.

3.1.2. FC at the new rolling cable–strut joint

Rolling friction replaces sliding friction at the rolling cable–strut joint, effectively decreasing the FCCJ. In a previous study, the research group tested the rolling cable–strut joint, which sleeve no PTFE between the pin and the roller, in the suspen-dome structure of Shandong Chiping Stadium, obtaining the values of FCCJ [5]. Fig. 7 shows the change law of the FCCJ, whose mean value is 0.165. Zhang of the Zhejiang University also measured the FC of another new rolling cable–strut joint with an experimental model [9], as shown in Table 4.

Table 4
FCs at rolling cable–strut joints

Engineering	Joint model diagram	Experimental value	
Shandong Chiping Stadium [2]		No PTFE sleeve between the pin and the roller.	0.165
		Set PTFE sleeve between the pin and the roller.	0.095
Sunflower-patterned suspen-dome [9]	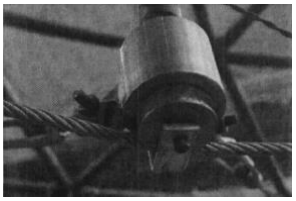		0.041

Compared with the values in Tables 3 and 4, it is easy to see the rolling cable–strut joint can effectively decrease the FC. Meanwhile, the FC can be further reduced by, for example, installing a PTFE sleeve.

3.2. Random mathematical model of FC at the rolling cable–strut joint

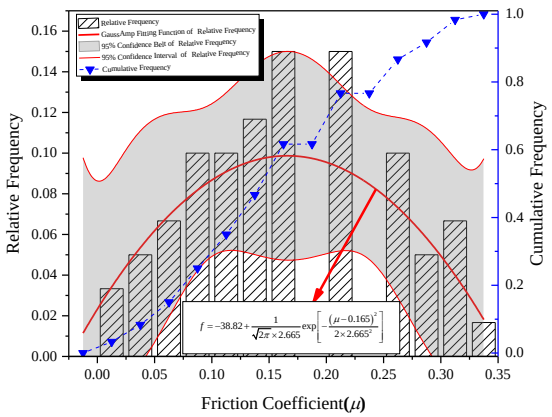

Fig. 9 Probability distribution diagram of the FC at the rolling cable–strut joint

The above analysis reveals the large discreteness of FCCJ. Different constructions have different joint structures, and therefore different FCs. However, for the same type of joint, such as the rolling cable–strut joint, the coefficient fluctuates randomly within a certain range and remains relatively uniform. In this paper, the effect of the new rolling cable–strut joint in reducing the friction loss of the suspen-dome was analyzed. Therefore, the authors further studied previous research works and analyzed the statistical law related to the FC of the rolling cable–strut joint. A sample library of the FCCJ was created through an experiment, and a histogram of the probability distribution was drawn as shown in Fig. 9. Several factors contribute to the random fluctuation of the FC, such as the material of the contact pair, surface treatment, the angle of the adjacent cable segments, cable force, and so on. The effect of each factor in the total effect is small. Therefore, the authors assumed the FC approximately obeys the normal distribution according to the central limit theorem. In this paper, the FC μ at each cable joint is regarded as an independent random variable. As indicated in Fig. 9, the FC with no PTFE sleeve obeys the normal distribution approximately, the mean value $\bar{\mu}$ = 0.165 and the mean square deviation σ = 2.665.

4. Analysis and experiment of effect of RPFL on suspen-dome structure performance

4.1. Analysis method

Since the FCCJ are random variables, the random characteristic of variables should be considered to accurately evaluate the effect of friction loss on structural performance. With the advancement of computers, numerical experiments such as the Monte Carlo method have enabled the simulation of the random characteristic of parameters, greatly promoting the development of engineering reliability. In addition, the method is a random finite element method (FEM), and there is no need to consider the complex non-linear correlations between parameters affecting the structural performance. It need only substitute the random number of each random variable into the finite element control equations repeatedly, to obtain the solution of a group of variables. Then, the distribution characteristics of the variables can be evaluated using statistical methods.

The basic idea of the Monte Carlo method is as follows: For a basic variable, i.e., the FC μ_{i_j}, at each cable–strut joint taken from 1,000 samples according to the normal distribution in the random mathematical model of Section 3. Then, the structure considering the effect of friction was calculated 1,000 times to verify the mean and the mean square deviation of each output variable. The mechanical properties of the structure were extracted as per the requirement. 1000 groups of structural-performance indices were obtained to form a sample library for the statistical analysis.

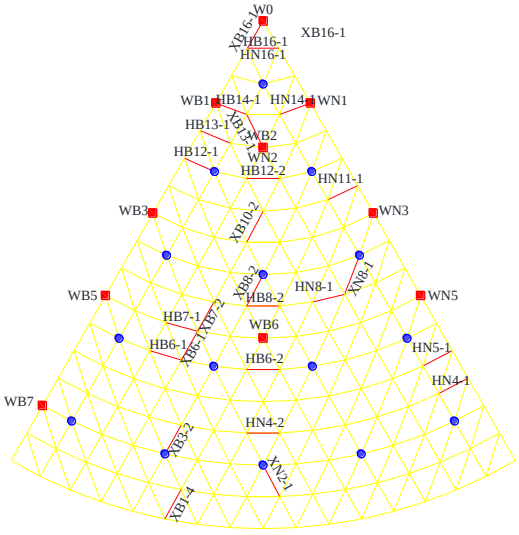

Fig. 10 Arrangement of loading points and measurement points

4.2. Parameter sensitivity analysis

To study the effect of FCCJ on the performance of the global suspen-dome structure, and to calculate the structural response considering the coupling effect of the full-span uniform load and the random variation of FCCJ, the authors extracted the key joint vertical deformations (JVDs), typical member axial stresses (MASs) of the upper reticulated shell, and key radial tension bar internal forces (RBFs), and then their sensitivities to FCCJ were analyzed [33]. To compare JVDs, MASs, and RBFs with the experimental results, a uniform load was simulated as the experimental load and applied to 80 joints as an equivalent concentrated load. The schematic diagram of the loading points is shown in Fig. 10. The blue circles in Fig. 10 indicate the loading points, and a concentrated

load of 1 kN was applied on each point. By considering the symmetry of the structure itself and of the load, the measurement points were concentrated in 1/6th of the area of the K6 reticulated shell, which further simplified the evaluation of PFL [34], and the measurement points are also shown in Fig. 10. By fully considering the stress characteristics of K6, the authors selected two types of measuring members: the ring member (HB) and radial member (XB).

4.2.1. Sensitivity analysis of JVDs to FCs

According to the internal force distribution of the suspen-dome, the lower tensegrity system can play the role of an elastic support for the upper reticulated shell [35], reducing the vertical deformations of the structure under vertical load. Therefore, JVDs are closely related to the pre-stress distribution of the lower tensegrity system, and the friction loss at the cable–strut joint will inevitably affect the vertical deformations of the structure. The graphs of the sensitivity of key JVDs and maximum JVDs to FCCJ are shown in Fig. 11. Owing to space limitation, the graphs show only the most significant results.

As indicated in Fig. 11, all the key JVDs are sensitive to the FCs of the 7th HC, i.e., the outer-most HC, and other FCs near the joint. Specifically, besides the FC of the 7th HC, the JVD w_0 at the mid-span displayed a certain sensitivity to the FC of the 2nd HC near the mid-span, albeit small. The FC at the other cable–strut joints have almost no effect on w_0. The w_4 between the 3rd and 4th HCs is the most sensitive to the FCs μ_{2_1} and μ_{2_2}, followed by the FC of the outer-most HC. It should be noted that the sensitivity of w_4 to the FC of the 2nd HC is stronger than that of the 3rd HC. There are two main reasons for this phenomenon. On the one hand, the pre-stressed design value of the 2nd HC is larger than that of the 3rd HC, causing the strut of the 2nd HC to have a stronger supportive effect on the upper reticulated shell. Therefore, the FC of the 2nd HC had a more profound effect on the mechanical properties of the upper reticulated shell. On the other hand, the radial tension bars at the cable–strut joints corresponding to μ_{2_1} and μ_{2_2} of the 2nd HC are just connected to the area near w_4, and therefore the changes of μ_{2_1} and μ_{2_2} will directly affect w_4. In addition, w_8 between the 6th and 7th HCs is the most sensitive to the FC of the 7th HC near w_8, i.e., μ_{7_33}, μ_{7_34}, μ_{7_35}, μ_{7_36}, μ_{7_37}, μ_{7_42}, followed by the FC of the 6th HC.

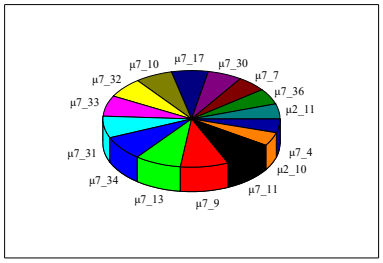

a) w_0

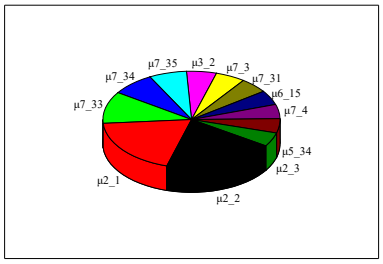

b) w_4

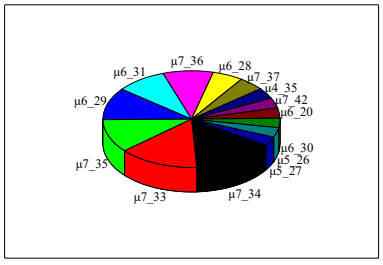

c) w_8

Fig. 11 Sensitive of key JVDs to the FCs

Fig. 12 is a plot of the sensitivity of the maximum JVD w_{max} to the FC. Obviously, w_{max} is mainly sensitive to the FC of the 2nd and 7th HCs. One reason for this is that the pre-stressed value of the outer-most HC is the largest, and the effect on the upper reticulated shell is the most significant. The other reason is that FCs at all cable–strut joints changed to arbitrary values during the calculation process, causing w_{max} to change its position and appear randomly in the area between the 1st and 2nd HCs. The pre-stressed design value of the 2nd HC affecting this area is larger than that of the 1st HC, and therefore w_{max} shows a more significant sensitivity to the FC of the 2nd HC.

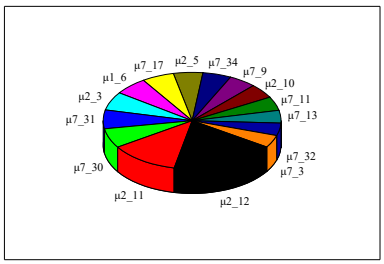

Fig. 12 Sensitivity of maximum JVD w_{max} to the FCs

As shown in Fig. 11, the FC of the outer-most HC has a remarkable effect on the vertical deformations of the entire structure, while those of the other HCs only affect the JVDs near the cable–strut joints. There are two main reasons for this phenomenon. On the one hand, the FC of the outer-most HC affects the design value of its internal force more than that of the other HCs. On the other hand, the outer-most HC is near the edge of the support where all loads born by the reticulated shell are gathered. The outer-most HC plays a decisive role in the structure. Therefore, special attention should be paid to the effect of the FC of the outer-most HC on the suspen-dome structure in the pre-stress construction process.

4.2.2. Analysis of sensitivity of MASs to FCs

The purpose of introducing the tensegrity system into the suspen-dome is to improve the mechanical properties of the upper single-layer reticulated shell. Therefore, the changing of FC will inevitably affect the internal force of the lower HC, which in turn will influence the MASs of the upper reticulated shell. To study the effect of FC change on MASs from the inside to the outside of the reticulated shell, HB16-1 and XB16-1 near the mid-span, HB1-1 and XB1-1 near the outermost HC, HB6-1 between the 5th and 6th HCs, XB8-1 between the 4th and 5th HCs were selected. The graphical plots of sensitivity of a typical MAS to the FC were drawn, as shown in Fig. 13.

As indicated in Fig. 13, the radial MAS is as sensitive to the FC as the ring MAS, i.e., the MASs are sensitive to the FC in the adjacent area. The larger the pre-stressed design value in the adjacent area, the more sensitive the MAS. For example, the axial stress of HB6-1, $\sigma_{HB6\text{-}1}$, is sensitive to μ_{5_j}, and even more so to the FC μ_{6_j} of the 6th HC, with a larger pre-stressed design value. $\sigma_{XB8\text{-}1}$ is sensitive to μ_{4_j} and more sensitive to μ_{5_j} of the 5th HC, with a larger pre-stressed design value. The stresses $\sigma_{HB16\text{-}1}$ and $\sigma_{XB16\text{-}1}$ near the mid-span display remarkable sensitivity to μ_{2_j}, followed by μ_{1_j}. The reason why $\sigma_{HB16\text{-}1}$ and $\sigma_{XB16\text{-}1}$ are less sensitive to μ_{1_j} is that the pre-stressed design value of the 2nd HC is much larger than that of the 1st HC. The stresses $\sigma_{HB1\text{-}1}$ and $\sigma_{XB1\text{-}1}$ show a certain degree of sensitivity to the FCs of the 5th and 6th HCs, and more so to the FC of the 7th HC, which is closer to the area and has a larger pre-stressed design value. As illustrated in Fig. 13, although the JVDs exhibit a more obvious sensitivity to the FC of the outermost HC, most MASs also display a certain degree of sensitivity to the FC of the outermost HC. This also indicates that the effect of FC of the outermost HC on the mechanical properties of the structure needs attention.

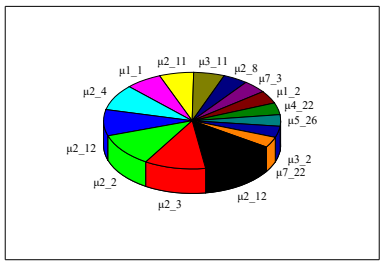

a) $\sigma_{HB16\text{-}1}$

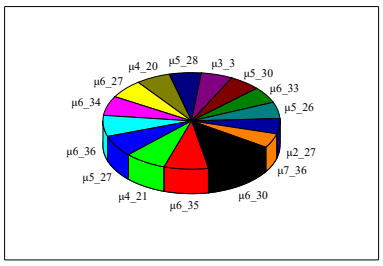

b) $\sigma_{HB6\text{-}1}$

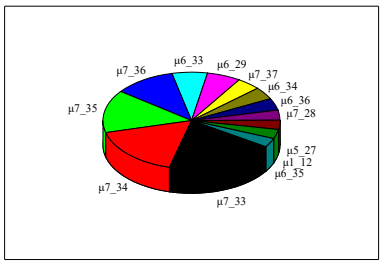

c) $\sigma_{HB1\text{-}1}$

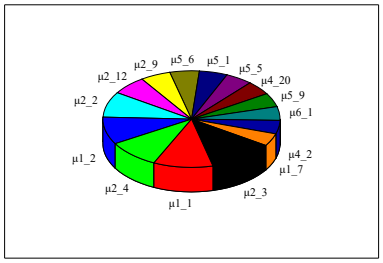

d) $\sigma_{XB16\text{-}1}$

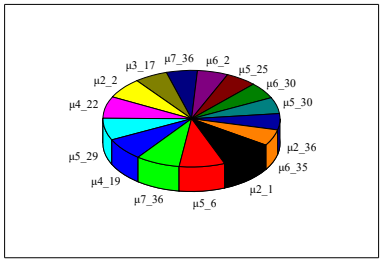

e) $\sigma_{XB8\text{-}1}$

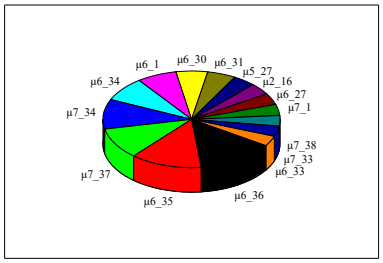

f) $\sigma_{XB1\text{-}1}$

Fig. 13 Sensitivity of typical MASs to the FCs

To comprehensively evaluate the effect of FC at all cable–strut joints on the MASs of the upper reticulated shell, a graphical plot of sensitivity of the maximum MAS σ_{wq_max} of the upper reticulated shell to the FC was drawn, as shown in Fig. 14. Fig. 14 reveals that the maximum MAS is most sensitive to the FCs of the 2nd and 3rd HCs. The reason for this might be that when the FC changes randomly, the stress σ_{wq_max} appears in the area between the 2nd and 3rd HCs, and the FC change will mainly affect the MAS in the adjacent area.

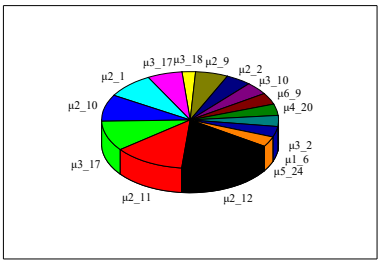

Fig. 14 Sensitivity of maximum MAS σ_{max} to the FCs

The graphs of sensitivity of MAS to FC are similar to those of the JVDs. That is, a change in FC will greatly affect the MASs in the adjacent area but have a smaller effect on the MASs at a position away from the cable–strut joint.

4.3. Effect of random PFL on static structure performance

To investigate the change law of the global structure performance with the change in FCCJ, the probability distribution characteristics of the maximum JVD w_{max}, the maximum MAS σ_{wq_max} and the maximum RBF N_{xls_max} varying randomly with the FCs were obtained [33,36], as shown in Figs. 15–17. The probability distribution index of performance of the suspen-dome is shown in Table 5. Figs. 15–17 show that when the FCCJ of the suspen-dome change arbitrarily, w_{max}, σ_{wq_max}, and N_{xls_max} also vary randomly but follow a broad set of rules. In general, the sample frequency histograms of various mechanical performance indices are low on both sides of graphics, high in the middle, and symmetrical on the left and right sides. The K–S test result shows that the sample data of all mechanical performance indices obey normal distribution in the concentration area, and only a few results are discrete.

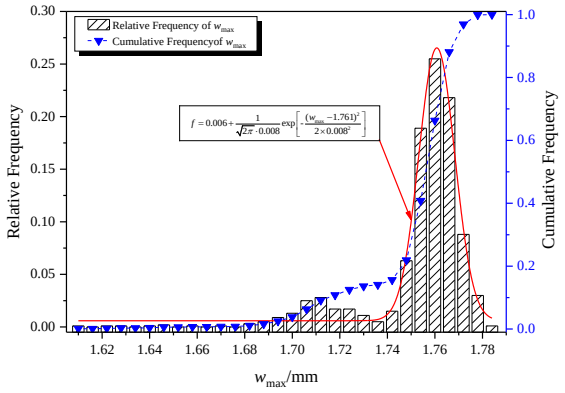

Fig. 15 Probability distribution of w_{max}

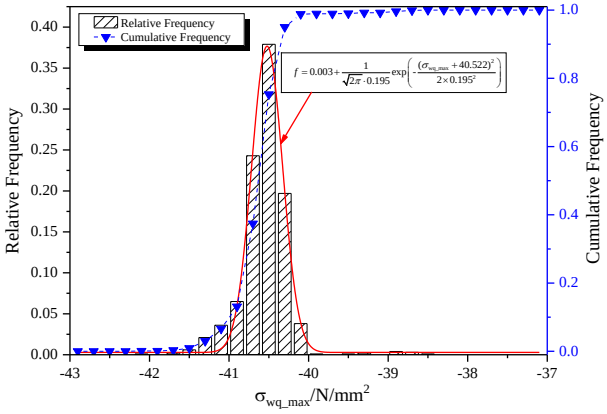

Fig. 16 Probability distribution of σ_{wq_max}

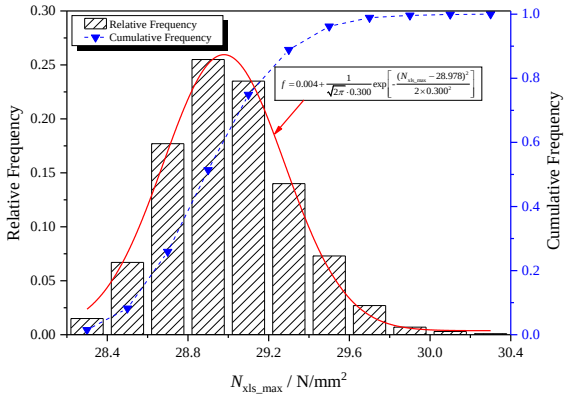

Fig. 17 Probability distribution of N_{xls_max}

Table 5
Probability distribution parameters of various performances

Item	w_{max} (mm)	σ_{wq_max} (N/mm^2)	N_{xls_max} (N/mm^2)
Mean /μ	1.761	-40.522	28.978
Mean square deviation /σ	0.008	0.195	0.3
Maximum error /R	0.154	1.487	1.021
Percentage increase in maximum error	8.67%	3.67%	4.4%
Exceeding probability (μ-3σ, μ+3σ)	14.20%	1.90%	0.6%

According to the analysis, the structure mainly arches upwards under the action of pre-stress and load, and the maximum JVD is also an upwards arching deformation. The main reason for this is that the global stiffness of the structure is large, and the load applied during the experiment is small. The structural deformation is mainly controlled by the arching effect upon the application of pre-stress. As indicated in Fig. 15, for w_{max}, the mean value μ is 1.761 mm, the mean square deviation σ is 0.008, the maximum value is 1.785 mm, and the minimum value is 1.608 mm. Therefore, the maximum error in the maximum vertical deformation of the upper reticulated shell due to the change of FCCJ, R_{w_max} = | 1.608-1.761 | = 0.153 mm, and the percentage increase in maximum error is 8.67%. In order to investigate the discrete degree of w_{max}, the exceeding probability (μ-3σ, μ+3σ) should be calculated, i.e., the probability of exceeding (1.738, 1.784) is 14.2%; it can be seen that the discrete degree of w_{max} is small.

To investigate the specific mechanism of the effect of FCCJ on structural deformation, two cases including the absence of friction loss at all cable–strut joints, i.e., μ_{i_j} = 0, and the FC without random variation with all FCCJs taken as μ_{i_j} = 0.165 were analyzed. The vertical deformation nephogram was drawn as shown in Figs. 18 and 19. A comparison of Fig. 18 with Fig. 19 reveals that the two cases follow the same deformation distribution laws. That is, under the action of pre-stress and load, the mid-span has the largest upwards arching, and the deformation gradually changes to downwards deflection from inside to outside. However, friction at the cable–strut joint reduces the upwards arching deformation of the structure and adversely affects the structure. When μ_{i_j} = 0, the maximum upwards arching deformation occurs on the reticulated shell between the 1st and 2nd rings, which is 2.011 mm. When μ_{i_j} = 0.165, even though it still occurs in the same area, the deformation value reduces to 1.774 mm. By simultaneously comparing this trend with Fig. 15, the authors found that the probability of sample data of the maximum upwards arching deformation considering the RPFL (μ_{i_j} = random) being smaller than that considering μ_{i_j} = 0 is 100%. That is, the friction loss has an inevitable and adverse effect on structural deformation. In addition, if the mean of the sample data is taken as the comprehensive performance index [37], the pre-stressed random friction loss can reduce the upwards arching deformation by (2.011-1.761)/2.011=12.43%. By comparing Fig. 15 with Fig. 19, the authors found that the probability of sample data of the maximum upwards arching deformation considering μ_{i_j} = random being smaller than that considering μ_{i_j} = 0.165 is 96.1%. That is, the actual upwards arching deformation is probably smaller than that considering the FC without random variation. Obviously, if the RPFL is not considered, the effect on the structure will be underestimated.

In summary, although PFL cannot change the deformation distribution law of the entire structure, it will weaken the favorable effect of pre-stress and reduce the upwards arching deformation of the structure under the action of pre-stress and small load. Moreover, it is highly probable that the global upwards arching deformation is smaller when the FC is considered with random variation than without.

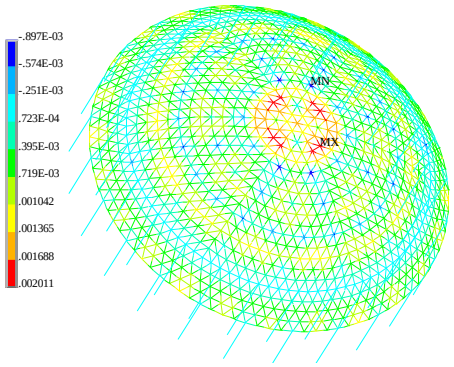

Fig. 18 Vertical deformation nephogram of the upper reticulated shell for μ_{i_j} = 0 (m)

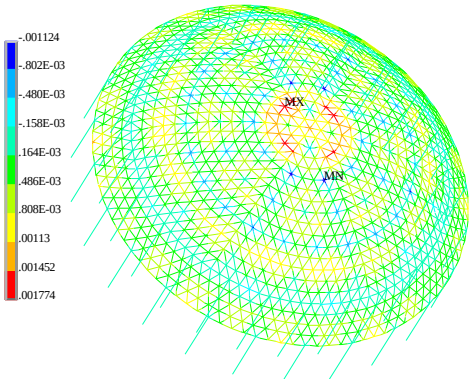

Fig. 19 Vertical deformation nephogram of the upper reticulated shell for μ_{i_j} = 0.165 (m)

Since the members of the upper reticulated shell are mainly subjected to axial force, and the stress measured by the experiment is axial stress, the maximum MAS σ_{wq_max} was extracted and analyzed. The axial-stress nephograms in the two cases of μ_{i_j} = 0 and μ_{i_j} = 0.165 were captured, as shown in Figs. 20 and 21. A comparison of Figs. 20 and 21 reveals that the friction loss does not have a major effect on the stress distribution law of the structure, which is similar with the findings of the structural deformation analysis. In both cases, the stress σ_{wq_max} occurs at the members of the 5th ring of the reticulated shell, and the maximum axial stresses are -42.6 MPa when μ_{i_j} = 0 and -41.1 MPa when μ_{i_j} = 0.165, respectively. If the mean value of the sample data in Fig. 16, i.e. -40.522 MPa, were taken as the comprehensive performance index considering the RPFL, the maximum axial stress relative difference of the upper reticulated shell in the three cases would be less than 5%, which can be ignored. This indicates that if or how to consider the friction loss has little effect on the stress σ_{wq_max}.

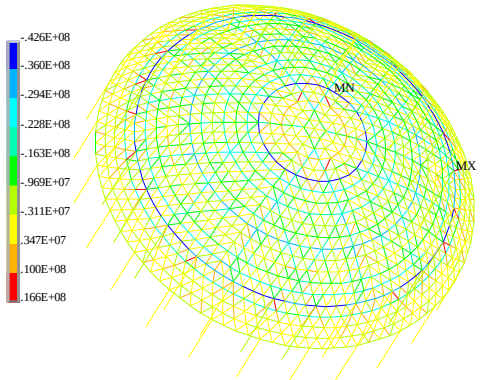

Fig. 20 MAS nephogram of the upper reticulated shell considering μ_{i_j} = 0 (Pa)

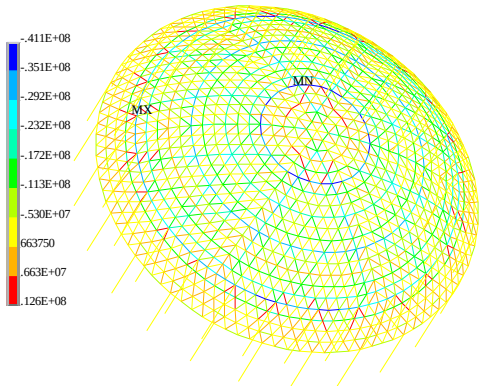

Fig. 21 MAS nephogram of the upper reticulated shell considering μ_{i_j} = 0.165 (Pa)

The absolute values of the typical MASs of the upper reticulated shell in the three cases were further extracted, and a bar chart was drawn for comparison, as shown in Fig. 22, incorporating PFL or RPFL increases the axial stresses of the upper reticulated shell. For example, when μ_{i_j} = random, the axial stresses of XB13-1 and XB7-2 are increased by 159.24% and 93.83%, respectively. However, by comparing the two ways of considering the friction loss, the authors found that, in most cases, considering μ_{i_j} = random will further increase the axial internal force of the upper reticulated shell. For example, when μ_{i_j} = 0.165, the axial stresses of XB13-1 and HB8-2 are −0.72 and −4.14 MPa, respectively. However, when considering μ_{i_j} = random, the axial stresses are −0.99 and −4.40 MPa, respectively, which are increased by 37.5% and 6.28%, respectively. Therefore, although PFL has little effect on the maximum MAS, it will increase the typical MASs. However, considering the RPFL will greatly increase the member axial stresses, which cannot be ignored.

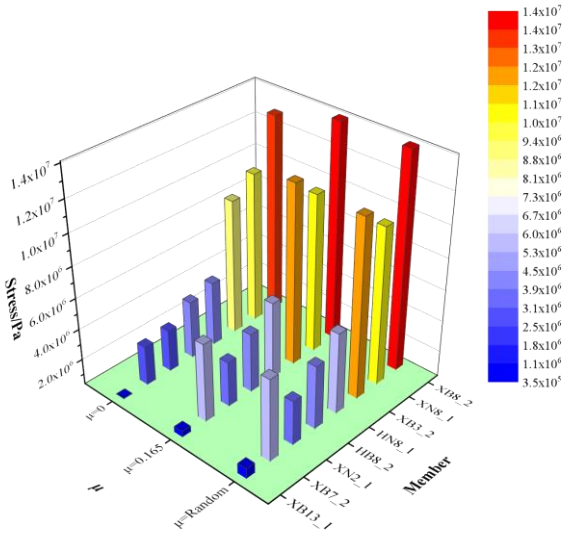

Fig. 22 Bar chart of typical member axial stresses

The RBFs are closely related to the internal forces of the HCs. For the tensegrity system of the structure, the pre-stressing effect should be fully realized to minimize the internal force under the external load. As shown in Table 5, the exceeding probability (μ-3σ, μ+3σ) of the sample data of N_{xls_max} is only 0.6% closer to the normal distribution. The RBF nephograms considering μ_{i_j} = 0 and μ_{i_j} = 0.165 were extracted and are illustrated in Figs. 23 and 24, respectively. The distribution law is that the RBFs gradually increase from inside to outside, and the maximum RBFs are 28.2 and 28.9 MPa, respectively. By comparing these results with the random analysis ones in Fig. 17, the probability of sample data greater than 28.2 and 28.9 MPa are 100% and 60%, respectively. Therefore, PFL will increase the RBFs, and RPFL will increase the maximum RBF to a great extent. However, in general, the extent of increase of the maximum RBF is smaller than the maximum JVD.

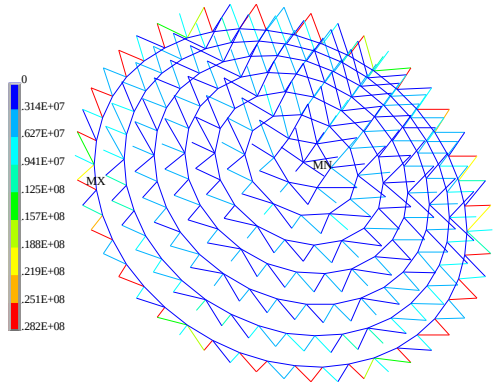

Fig. 23 Radial tension bars internal force nephogram considering μ_{i_j} = 0 (Pa)

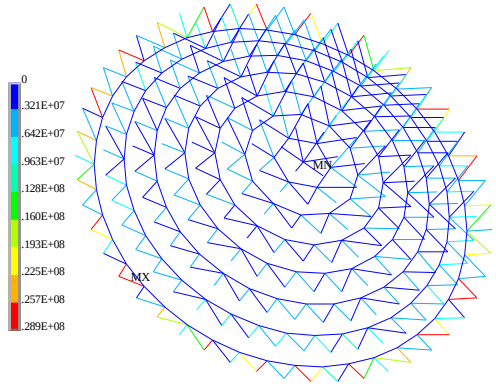

Fig. 24 Radial tension bar internal force nephogram considering μ_{i_j} = 0.165 (Pa)

4.4. Static loading experiment on scaled-down model

To study the law governing the effect of FCs with random variation on the actual structure's performance, a static loading experiment was carried out after the tension test shown in Fig. 4. During the experiment, a uniform load was applied to 80 joints as the equivalent concentrated load on the upper reticulated shell. The loading points were arranged as shown in Fig. 10. Each loading point was divided into five levels, and a total load of 1 kN was applied. A photograph of the loading experiment is presented in Fig. 25. The representative members and joints of the upper reticulated shell were selected as the stress and deformation measurement points, respectively, and the arrangement of measurement points corresponds to the previous theoretical analysis, as shown in Fig. 11. Since the static loading experiment was an elastic loading experiment, the stresses were obtained by converting the strains measured by a resistance strain gauge attached to the members, and the deformations were obtained by a laser tracker to an accuracy of 0.01 mm [5].

Fig. 25 Photograph of model during loading experiment

To verify the feasibility of the Monte Carlo method to analyse the effect of random friction loss on global structure performance, the experimental results were compared with the finite element calculation results. Firstly, the authors

applied the actual tensioning control force shown in Fig. 7 using a force-finding analysis considering RPFL on ANSYS. Then, the static loading process was simulated according to the experimental loading process, and a random database of structural mechanical responses was generated by the Monte Carlo method. Finally, the random mathematical characteristics were analyzed. Moreover, to clarify the effect of PFL on the structural performance, theoretical values 1 with μ_{i_j} = 0 and 2 with μ_{i_j} = 0.165 of the member stresses and joint deformations were calculated. The results of the Monte Carlo calculations of representative member stresses and joint deformations were used to construct a box plot which can reflect the characteristics of the original data distribution. The Monte Carlo calculations were then compared with the experimental values, theoretical values 1 and 2, as shown in Figs. 26–28. As a general trend, the representative member stresses and joint deformations based on μ_{i_j} = random in 1,000 groups were mostly located in the whiskers of the Box plot, in which, the insides of the two whiskers are normal values, while the outsides are outliers. Moreover, the Monte Carlo calculations were basically consistent with the trend of the experimental values, which confirms to a certain extent the feasibility of the probability distribution model of FC μ and Monte Carlo method.

4.4.1. Monte carlo calculations of joint deformation

In Fig. 26, under the action of pre-stress and load, the structural deformation is dominated by upwards arching, and all the deformations of the selected measurement points are positive values. All Monte Carlo calculations of joint deformation of the 11 measurement points selected from the inside to the outside of the reticulated shell obey the normal distribution revealed by the K–S test. Most Monte Carlo calculations are located in the whiskers of the box plot. The general discrete degree of the calculated results is not considerably large. The discrete points of the Monte Carlo calculations at the inner ring of the reticulated shell are close to the lower limit of the normal range. With transition to the outer ring of the reticulated shell, the discrete points become closer to the upper limit of the normal range, such as the change trend of discrete points WN3, WB5, and WB6.

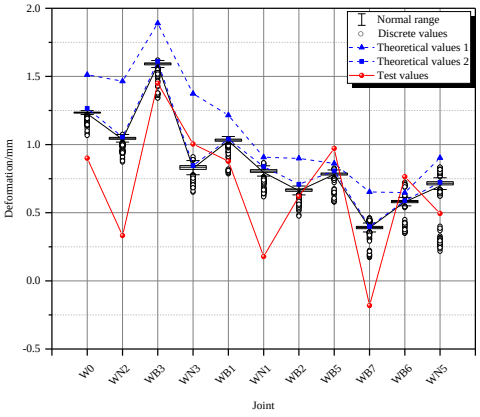

Fig. 26 Distribution contrast diagram of joint deformations

From the comparison of the Monte Carlo calculations, and theoretical values 1 and 2, the authors found that their structural deformation distributions follow the same trend. Both theoretical values 1 and 2 are close to the upper limit of normal range of the Monte Carlo calculations. Most theoretical values 2 are located in the upper whisker of the box plot and are closer to the means. The deformations of all measurement points show that theoretical values 1 are larger than 2 and slightly larger than the Monte Carlo calculations. Obviously, this is because the friction loss was not considered when calculating theoretical values 1, the pre-stressing effect was the largest, and the upper reticulated shell had the largest degree of arching. However, although theoretical values 2 were the deformation responses when all FCs were taken as 0.165, they still slightly deviated from the Monte Carlo calculations, indicating that the relationship between the pre-stress and structural response is non-linear, and the effect of friction loss on the structure performance is also inevitably non-linear.

By comparing the experimental values with the Monte Carlo calculations, the authors found that the structural deformation distribution law reflected by the experimental values was basically consistent with the Monte Carlo calculations, while the experimental values were more discrete. However, the experimental values of WB1, WB2, and WN5 are in the normal range. The experimental values of WB3 and WB6 are in the discrete area, which can be used to verify to a certain extent the feasibility of the random numerical simulation analysis. The experimental values of other measurement points were larger than the Monte Carlo calculations. The reason might be that the change law of the FCCJ in the experimental model is far more complex than that of the normal distribution model in the calculated model.

As indicated in Fig. 6, μ varies non-linearly with the tension, but it does not always maintain the mean value of 0.165. When the pre-stress is less than 10 kN, μ is more discrete. When the pre-stressed design value is approximately 5 kN, μ is approximately 0.22, and the tension of the six HCs in the inner structure are less than 5.04 kN, the FC will be greater than the mean, but the tension of the outermost HC is 11.5 kN, whose FC is closer to the mean of 0.165, and it will agree with the normal distribution random mathematical model of FC.

In Section 4.2, the PFL of each HC mainly affects the deformation of the reticulated shell in the adjacent area. In the experimental model, the upwards arching deformation of the inner HC under the action of pre-stress and light load is small than that of the outer HC, because the actual friction loss of the inner HC is larger. This implies that most of the experimental values of the HCs are close to the lower limit of normal range of the Monte Carlo calculations, but the experimental values of the inner HC are farther away from the lower limit of the normal range than that of the outer HC.

4.4.2. Monte carlo calculations of radial member stress

Five representative radial members were selected, and the member stresses were extracted. A distribution contrast diagram of Monte Carlo calculations, theoretical values 1, theoretical values 2 and experimental values was drawn, as shown in Fig. 27. It shows that the representative radial member stresses of the upper reticulated shell based on 1,000 groups of random values of μ_{i_j} through the K–S test display an approximate optimal normal distribution, which is more conducive to data analysis. Only a few values of the members are beyond the normal range, albeit without large discreteness. In general, because of the small experimental load, the representative radial member stresses are small, and the Monte Carlo calculations were basically consistent with the distribution law of experimental values, which verifies the correctness of the theoretical analysis.

The calculated value of the inner-most radial member, XB16-1, deviates remarkably from the experimental value, when compared with the other representative members. The main reason for this phenomenon is that the pre-stressed design value of the inner HC is small, and the corresponding FCs are extremely unstable, causing the stresses in the corresponding area of the reticulated shell to fluctuate. This is consistent with the fact that the experimental values of the representative joint deformation near the mid-span deviates from the calculated values as shown in section 4.4.1. In addition, the comparison of theoretical values 1 and 2 and the Monte Carlo calculations showed that both theoretical values 1 and 2 were close to the upper limit of the normal range, while theoretical value 2 was basically distributed within the normal range. However, theoretical value 2 deviates from the mean of the Monte Carlo calculations; the reason being similar to that for the joint deformations. The means of the Monte Carlo calculations were slightly greater than theoretical values 1 and 2 and were closer to the experimental values. Moreover, considering that the selected radial members were all under pressure, the calculated result considering RPFL was more conservative, and therefore more suitable for the actual situation.

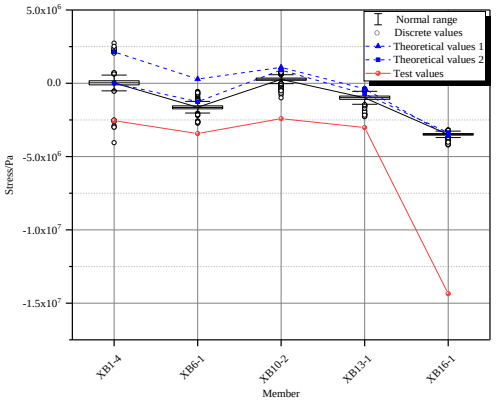

Fig. 27 Distribution contrast diagram of radial member stresses

4.4.3. Monte carlo calculations of ring member stress

Fourteen representative ring members were selected, and the member stresses were extracted, and the corresponding distribution contrast diagram is shown in Fig. 28. According to the box plot of the Monte Carlo calculations, the ring member stresses change from the tension at the supports to the compression near the mid-span of the reticulated shell. Tensioned ring members appeared at the mid-span with small absolute values. There were few differences between the Monte Carlo calculations of the ring members at the same ring, such as HN4-

1 and HB4-2, HB6-1 and HB6-2, HB12-1 and HB12-2, HB14-1 and HN14-1, HB16-1 and HN16-1, and so were the experimental values. The trend of experimental values was almost the same as those of the Monte Carlo calculations, and the two values did not differ much. This indicates that the experimental design and process met the requirements, and the probability distribution model of FC μ and the Monte Carlo method are feasible within a certain extent. Here, the authors emphasize that the calculated values of the inner-most HCs, HB16-1 and HN16-1, deviate significantly from the experimental values. The reason for this is the same as that of the representative joint deformations and radial member stresses near the mid-span. The comparison of the Monte Carlo calculations with theoretical values 1 and 2 showed that theoretical value 1 was almost entirely within the normal range of the box plot. This in turn indicates that the ring member stresses in the two cases with μ_{i_j} = 0 and μ_{i_j} = 0.165, respectively, are not considerably different. As displayed in Figs. 27–28, the Monte Carlo calculations are more volatile than theoretical value 1, indicating that PFL would make the internal force distribution of the structure uneven.

In general, the absolute values of calculated results, such as the joint deformations and radial and ring member stresses, considering RPFL and based on the Monte Carlo method are smaller than the experimental values. This occurred because of the exposure of the experimental model to corrosion outdoors for one year. In addition, installation errors may have exaggerated the experimental values. The smaller value shows that, in an actual suspen-dome structure, there are factors besides FCCJ which may cause additional pre-stressed losses. This fact cannot be ignored in engineering practice. Initial defects such as the initial eccentricity, member initial curvature and RPFL will be considered throughout Section 5, along with an analysis of the effect of coupling on the ultimate bearing capacity of the suspen-dome.

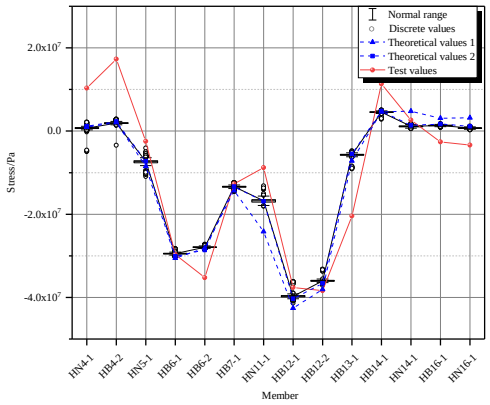

Fig. 28 Distribution contrast diagram of ring member stresses

5. Analysis of effect of multi-defect random variation coupling on ultimate bearing capacity of suspen-dome structure

According to the analysis in Section 4.4, the experimental values are slightly different from the calculated values. The reasons cited included the possible deviation of FCCJ in the theoretical calculation model from that in the actual experimental model. In addition, there inevitably exist initial defects, such as the member initial curvature, installation and positioning deviations, and section-size deviation of members in the experimental model during manufacturing and installation. Among them, the section size of members is small and the slenderness ratio is large in the scaled-down model, causing initial curvature during the process of transportation and installation. The upper reticulated shell is a defect-sensitive structure [38]. Therefore, the effect of joint installation deviation on the structure performance cannot be ignored. To obtain the actual performance of the structure and establish a theoretical model which can characterize the true operational performance of the structure, this paper introduces the member initial curvature and joint installation deviations based on RPFL, to evaluate the actual structure performance.

5.1. Initial curvature and installation deviation

Initial curvature is inevitable during the processes of manufacturing, transportation, and installation of members, causing members to produce a *P–Δ* effect under an axial force. The initial curvature strongly influences the structure's mechanical properties [39]. The shape of the member during the initial curvature is random. For ease of calculation and structural safety, the *sine* half-wave curve was used to simulate the initial curvature, as shown in Fig. 29. The multi-segment beam method was used to simulate the initial curvature defect [40]. That is, after the ideal straight rod element was subdivided into multi-segment beam elements with a rigid connection, the coordinates of the intermediate connection nodes were adjusted by a *sine* half-wave curve. To ensure accurate analysis, this paper assumes the number of segments as 10.

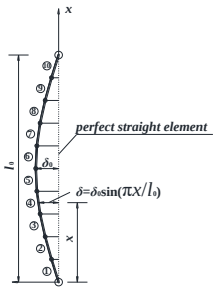

Fig. 29 Schematic diagram of initial curvature defect of member

After determining the initial curvature form of the member, the authors found that the key parameter affecting the initial curvature defect degree was the bending amplitude δ_0 in the mid-span. Apparently, δ_0 of each member changes randomly. However, to ensure structural safety, the literature [41] has set a limit on the axial bending height of the space grid structure member, i.e., $\delta_0 \le l_0 / 1{,}000$, where l_0 is the original length of the member. Combined with the actual on-site installation conditions and the size effect of the scaled-down model, the δ_0 of the experimental model was appropriately enlarged to $\delta_0 = l_0 / 600$. Because there are few published material on the random parameters of a member's initial curvature, this paper refers to the literature [41] and assumes that the random variable δ_0 obeys the extreme value I-type distribution. Its probability density function $f(\delta_0)$ is as follows.

$$f(\delta_0) = \frac{1}{\sigma} \cdot e^{\frac{\delta_0-\mu}{\sigma}} \cdot e^{-e^{\frac{\delta_0-\mu}{\sigma}}} \tag{5}$$

Assuming that the exceeding probability of bending amplitude $\delta_0 = l_0 / 600$ is 2.5%, and the exceeding probability of $\delta_0 = 0$ is 1%, the mean μ and mean square deviation σ of δ_0 of each member were calculated as follows.

$$\mu = 0.78(\frac{l_0}{600}) \approx \frac{l_0}{770} \tag{6}$$

$$\sigma = \frac{l_0/600}{5.9} = \frac{l_0}{3540} \tag{7}$$

The upper reticulated shell had a total of 3,504 members. The Monte Carlo method was used to analyze the effect of random variation of the member initial curvature on the structural ultimate bearing capacity. Assuming that the ultimate bearing capacity's sample library was formed by iteratively and randomly running the calculations *n* times, for each random simulation, a group of initial curvature amplitude random-sample library $\{\boldsymbol{\delta}_0\}=(\delta_{1,j}, \delta_{2,j}, \delta_{3,j}, \ldots \delta_{i,j}, \ldots \delta_{3504,j})$ was generated, where *i* is the member number and *j* is the *No. j* random simulation iterative calculation. Moreover, $\delta_{i,j}$ is independent and obeys the extreme value I-type distribution. Fig. 30 shows the FEM of the random simulation process.

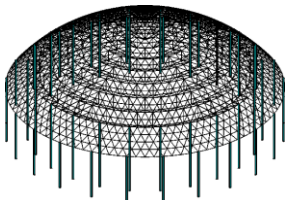

Fig. 30 Model diagram of member initial curvature (×10)

5.2. Analysis of effect of multi-defect random variation coupling on ultimate bearing capacity

To accurately evaluate the ultimate bearing capacity of the structure, an

FEM of the experimental model was constructed, and defects such as the member initial curvature random defect, RPFL, and installation deviation were introduced. The member initial curvature amplitude δ_0 and the FC μ_{i_j} at each cable–strut joint are random, independent variables. In general, to analyze the ultimate bearing capacity considering the double non-linearity of the material and the geometry is analyzed, the arc-length method is used. However, given that the calculation is not easy to converge, and the cost is relatively high, the authors assumed that when the calculation does not converge in the analysis process, i.e., the stiffness matrix of the structure appears singular, the structure has lost its stability. Meanwhile, the load corresponding to the load step can be considered as the structural ultimate bearing capacity.

Fig. 31 illustrates a probability distribution curve of the ultimate bearing capacity, which tended to converge when the simulation time was 100. The sample data distribution is similar with the normal distribution, except that it moves to the right and forms a peak in the interval (4.5, 5.0). The results at the tail are called *stragglers*. Furthermore, most of the relative frequency curve of the sample data is located in the 95% confidence interval of the fitted LogNormal curve. Therefore, P_{cr} obeys the LogNormal distribution with the parameter (ln(4.62),0.19), and the maximum and minimum values are 5.454 and 2.965 kN, respectively.

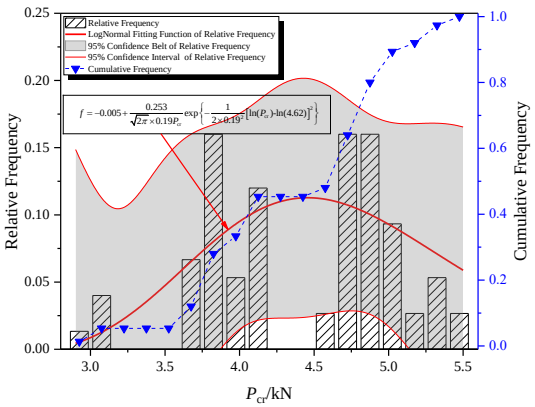

Fig. 31 Probability distribution diagram of ultimate bearing capacity

To further analyze the effect of initial defects on the ultimate bearing capacity of the suspen-dome, the ultimate bearing capacity under two conditions, without friction loss, i.e., ideal structure with μ_{i_j}=0, and with the same friction loss at all cable–strut joints, i.e., defining all μ_{i_j}=0.165, were calculated. The results were compared with those considering the friction loss, member initial curvature, and joint installation deviation simultaneously, which can be seen in Table 6. The ultimate bearing capacity with μ_{i_j} = 0, which is 9.05 kN is larger than that with μ_{i_j} = 0.165, which is 5.49 kN. The ultimate bearing capacity with the same friction loss at all cable–strut joints is reduced by 39.34%, when compared with that of an ideal structure. Then, the axial stress and deformation nephograms of the upper reticulated shell were extracted to analyze the specific effect of friction loss on the structure's performance. As shown in Table 6, when structural failure occurs, the inner members are mainly subjected to compression, while the outer members are subjected to tension. However, the ideal structure has a uniform stress distribution at failure, and the maximum compressive stress appears in the area to which the concentrated load was applied. Further, the stress level of the ideal structure is significantly higher than that of the structure with friction loss at structural failure occurs. Obviously, this is because the stress distribution of the ideal structure is uniform and the structural stiffness is large, thus allowing the structure to bear larger loads. Therefore, its stress level is significantly improved, which greatly improves the structure's performance.

A comparison of the deformation nephograms of the upper reticulated shell reveals that the maximum deformation of the ideal structure reaches 60.998 mm, which occurs in the area in which the maximum axial stress is generated. Moreover, it is much larger than the maximum deformation of 14.214 mm, considering the friction loss. In addition, deformation in the ideal structure is mainly concentrated in the load-bearing mid-span. After the introduction of friction loss, the deformation range of the structure was expanded, which illustrates the adverse effect of PFL on structural stiffness.

The model state is the closest to the actual state of the structure when simultaneously considering multiple random defects. Meanwhile, the ultimate bearing capacity sample data of 100 groups were all less than 9.05 and 5.49 kN, indicating that the ultimate bearing capacity of the suspen-dome reduces when incorporating multi-defect random variation coupling. If the mean of bearing capacity is taken as a comprehensive performance index of the structure, the bearing capacities reduce by 51.16% compared with the ideal structure and 19.49% compared with the structure with the same FCCJ. If the friction loss at the cable–strut joint is neglected, the safety of the suspen-dome structure will be seriously overestimated. Likewise, the structural bearing capacity will also be overestimated without considering the random characteristics of each defect.

Table 6
Comparison of structure performance in three cases

Items	Ultimate bearing capacity (kN)	Axial stress nephogram at structural failure (Pa)	Deformation nephogram at structure failure (m)
μ_{i_j} = 0	9.05	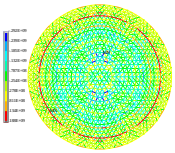	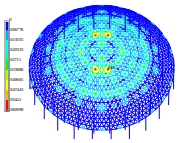
μ_{i_j} =0.165	5.49	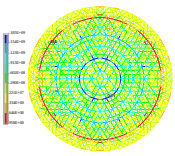	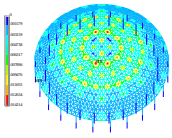
Multiple random defects	mean	mean square deviation	
	4.42	0.6201	

6. Conclusions

The high efficiency of the suspen-dome structure lies in the accurate introduction of pre-stress. However, due to the inevitable friction loss at cable–strut joints during the construction process, the structure's mechanical properties are affected. Based on the random characteristics of FCCJs, the random analysis of structural mechanical performance of a suspen-dome 1:10 scaled-down experiment model was carried out in this paper. The main conclusions are as follows:

1) Based on the static force balanced relationship and the friction transmission law, a cable force calculation method considering the unequal tension at both sides and the independent change of the FCCJs was proposed, and the reliability of this method was verified by comparing and analyzing the distribution law and relative error of the calculated values and the test values.

2) Engineering and experimental investigations have found that the FCCJs have a large variability, and the investigation data of the rolling cable–strut joint showed that the FCCJs used in the model approximately follows a normal distribution. The mean value is 0.165, and the mean square deviation is 2.665.

3) Random finite element analysis considering the random friction loss of the suspen-dome structure found that when the FCs at all cable–strut joints change randomly, the maximum deformation of the structure will approximately obey the normal distribution. The probability of the random calculation result of the pre-arching deformation value of the structure being less than the deterministic calculation result is as high as 96.1%, a high probability event. The MASs and the RBFs are sensitive to the FCCJs in the adjacent area. Although the maximum MAS of the upper reticulated shell and the maximum RBF follow the normal distribution, compared with the pre-stressed friction loss deterministic analysis results, the random friction loss of the pre-stress will further increase the MASs of the upper reticulated shell and the RBFs. This makes the internal force distribution of the structure uneven. Overall, the effect of random friction loss on the internal force of the structure is less than its effect on deformation. The static loading experiment results of the structure showed that most of the experimental values of key member stress and key joint deformations are within the normal range of the Monte Carlo random simulation calculation results. The changing trend of the calculated values and the experimental values are the same, verifying the feasibility of the Monte Carlo simulation.

4) When simultaneously considering friction loss, member initial curvature, and joint installation deviation, the ultimate bearing capacity with the random variation of each defect of the suspen-dome is reduced by 51.16% compared with the ideal structure and 19.49% compared with the structure with the same friction coefficient at cable–strut joints.

5) In this study, the effect of random pre-stressed friction loss on structural performance was investigated for a specific suspen-dome scaled-down experiment model. The probability distribution model of the FC is obtained from a cable-joint tension test, which was carried out by our research group earlier,

but the amount of the test data is relatively small. In the meantime, owing to the size effect, the random mathematical model of joint friction coefficients in the scaled-down model may differ from the actual project. In the next step, the group will investigate and establish a sample library of slip FCs of various types of cable-support joints in real projects and establish a more accurate probability distribution model of FCs to verify the influence law of random friction losses on actual engineering structures.

Acknowledgments

The research described in this paper was financially supported by the National Natural Science Foundation of China (No. 51708067), General Program of Chongqing Natural Science Foundation (cstc2020jcyj-msxmX0089).

References

[1] J. G. Cai, Y. Q. Liu, J. Feng, et al., "Nonlinear stability analysis of a radially retractable suspen-dome", *Advanced Steel Construction*, Vol. 13, No. 2, pp. 117-131, 2017.
[2] M. Kawaguchi, M. Abe, and T. Ikuo, "Design, tests and realization of 'suspend-dome' system", *Journal of the International Association for Shell and Spatial Structures*, Vol. 40, No. 3, pp. 179-192, 1999.
[3] H. N. Li, C. L. Yuan, L. Ren et al., "Structural health-monitoring system for roof structure of the Dalian Gymnasium", *Advances in Structural Engineering*, Vol. 22, No. 7, pp. 1579-1590, 2019.
[4] Z. H. Chen, "Cable-supported Structure system", *Science Press*, Beijing, China, 2013.
[5] Z. H. Chen, R. Z. Yan, X. D. Wang et al., "Experimental researches of a suspen-dome structure with rolling cable-ctrut joints", *Advanced Steel Construction*, Vol. 11, No. 1, pp. 15-38, 2015.
[6] R. Montuori and R. E. Skelton, "Globally stable tensegrity compressive structures for arbitrary complexity", *Composite Structures*, Vol. 179, pp. 682-694, 2017.
[7] S. D. Guest, "The stiffness of tensegrity structures", *IMA Journal of Applied Mathematics*, Vol. 76, No. 1, pp. 57-66, 2010.
[8] A. L. Zhang, X. C. Liu, D. M. Wang et al., "Static experimental study on the model of the suspend-dome of the Badminton Gymnasium for 2008 Olympic Games", *Journal of Building Structures*, Vol. 28, No. 6, pp. 58-67, 2007.
[9] G. F. Zhang, S. L. Dong, X. Zhuo et al., "Experimental research on sliding cable prestress losses of suspen-dome structures", *Spatial Structures*, Vol. 26, No. 4, pp. 36-41, 2020.
[10] H. B. Liu and Z. H. Chen, "Structural behavior of the suspen-dome structures and the cable dome structures with sliding cable joints", *Structural Engineering and Mechanics*, Vol. 43, No. 1, pp. 53-70, 2012.
[11] H. B. Liu, Q. H. Han, Z. H. Chen et al., "Precision control method for the pre-stressing construction of suspen-dome structures", *Advanced Steel Construction*, Vol. 10, No. 4, pp. 404-425, 2014.
[12] Z. W. Zhao, B. Liang, R. Z. Yan et al., "A novel numerical method for considering friction during pre-stressing construction of cable-supported structures", *International Journal of Steel Structures*, Vol. 18, No. 5, pp. 1699-1709, 2018.
[13] Y. Chen, Q. Sun, and J. Feng, "Improved form-finding of tensegrity structures using blocks of symmetry-adapted force density matrix", *Journal of Structural Engineering*, Vol. 144, No. 10, pp. 04018174.1-04018174.13, 2018.
[14] J. Y. Zhang and M. Ohsaki, "Force identification of prestressed pin-jointed structures", *Computers & Structures*, Vol. 89, No. 23, pp. 2361-2368, 2011.
[15] M. Ohsaki and J. Y. Zhang, "Nonlinear programming approach to form-finding and folding analysis of tensegrity structures using fictitious material properties", *International Journal of Solids and Structures*, Vol. 69-70, pp. 1-10, 2015.
[16] H. J. Liu, L. F. Yang, Y. L. Li et al., "Geometrically nonlinear analysis on a double controlled form finding method considering construction process of suspen-domes", *Advanced Materials Research*, Vol. 904, pp. 524-527, 2014.
[17] J. M. Guo and D. Zhou, "Pretension simulation and experiment of a negative Gaussian curvature cable dome", *Engineering Structures*, Vol. 127, pp. 737-747, 2016.
[18] Y. Chen, P. Sareh, J. Feng et al., "A computational method for automated detection of engineering structures with cyclic symmetries", *Computers & Structures*, Vol. 191, pp. 153-164, 2017.
[19] Y. Chen, J. Feng, and Q. Sun, "Lower-order symmetric mechanism modes and bifurcation behavior of deployable bar structures with cyclic symmetry", *International Journal of Solids and Structures*, Vol. 139, pp. 1-14, 2018.
[20] Y. Chen, J. Feng, R. Ma et al., "Efficient symmetry method for calculating integral prestress modes of statically indeterminate cable-strut structures", *Journal of Structural Engineering*, Vol. 141, No. 10, pp. 04014240.1-04014240.11, 2014.
[21] Y. Chen, J. Feng, H. Lv et al., "Symmetry representations and elastic redundancy for members of tensegrity structures", *Composite Structures*, Vol. 203, pp. 672-680, 2018.
[22] M. Elhoseny, A. Tharwat, A. E. Hassanien et al., "Bezier curve based path planning in a dynamic field using modified genetic algorithm", *Journal of Computational Science*, Vol. 8, No. 4, pp. 1-41, 2017.
[23] S. Z. Weng and P. Huang, "Principles of Tribology", T*singhua University Press*, Beijing, China, 2002.
[24] S. V. Shil'ko, D. A. Chernous, T. V. Ryabchenko et al., "Estimation of the friction coefficient of a nanostructured composite coating", *Mechanics of Composite Materials*, Vol. 53, No. 5, pp. 579-588, 2017.
[25] D. Prayogo and Y. T. T. Susanto, "Optimizing the prediction accuracy of friction capacity of driven piles in cohesive soil using a novel self-tuning least squares support vector machine", *Advances in Civil Engineering*, Vol. 2018, 6490169.1-6490169.9, 2018.
[26] Y. Chen, J. Feng, P. Sheng et al., "Anti-sliding performance of cable clips of inner concave cable arches in the New Guangzhou Railway Station", *Journal of Building Structures*, Vol. 34, No. 5, pp. 27-32, 2013.
[27] S. Wang, G. J. Zhang, A. L. Zhang et al., "The prestress loss analysis of cable-strut Joint of the Badminton Gymnasium for 2008 Olympic Game", *Journal of Building Structures*, Vol. 28, No. 6, pp. 39-44, 2007.
[28] J. Qin, Z. Q. Wang, R. Zhang et al., "Study on prestress construction monitoring of Badminton Gymnasium for 2008 Olympic Games", *Journal of Building Structures*, Vol. 28, No. 6, pp. 83-91, 2007.
[29] X. C. Liu, A. L. Zhang, and W. L. Fu, "Cable tension preslack method construction simulation and engineering application for a prestressed suspended dome", *Advances in Materials Science and Engineering*, Vol. 2015, No. 2015, pp. 1-17, 2015.
[30] Z. X. Guo, Y. Q. Wang, B. Luo et al., "Prestressed cable construction of large-span suspend-dome in Ji'nan Olympic Center Gymnasium", *Construction Technology*, Vol. 37, No. 5, pp. 133-135, 2008.
[31] Y. B. Yuan, X. Z. Hu, X. D. Cai et al., "Test study on the stress of cable-clamp joint in Xuzhou Olympic Gymnasium", *Low Temperature Building Technology*, Vol. 35, No. 8, pp. 81-83, 2013.
[32] Z. H. Chen, X. X. Wang, H. B. Liu, et al., "Failure test of a suspendome due to cable rupture", *Advanced Steel Construction*, Vol. 15, No. 1, pp 23-29, 2019.
[33] R. Z. Yan, Z. H. Chen, X. D. Wang et al., "Analysis of static performances of suspen-dome structures considering the random errors influence of prestressing construction", *Spatial Structures*, Vol. 21, No. 1, pp. 39-89, 2015.
[34] Y. Chen, J. Feng, and R. J. Ma, "A unified criterion for movability of kinematically indeterminate frameworks with symmetry", *Journal of Building Structures*, Vol. 36, No. 6, pp. 101-116, 2015.
[35] Z. H. Chen, "Suspen-dome Structure", *Science Press*, Beijing, China, 2010.
[36] A. Petcherdchoo, "Probability-based sensitivity of service life of chloride-attacked concrete structures with multiple cover concrete repairs", *Advances in Civil Engineering*, Vol. 2018, 4525646.1-4525646.17, 2018.
[37] G. C. Wu, "Probability and Mathematical Statistics", *China Renmin University Press*, Beijing, China, 2011.
[38] M. Zhang, Y. P. Liu, Z. X. Yu, et al. "Study of seismic resistance of Kiewit-8 dome considering key structural design parameters", *Advanced Steel Construction*, Vol., 15, No. 4, pp. 386-397, 2019.
[39] Y. Ding, T. L. Zhang, "Research on influence of member initial curvature on stability of single-layer spherical reticulated domes", *Advanced Steel Construction*, Vol. 15, No. 1, pp. 9-15, 2019.
[40] J. C. Yan, F. Fan, and Z. G. Cao, "Research on influence of initial curvature of members on elasto-plastic stability of reticulated shells", *Journal of Building Structures*, Vol. 33, No. 12, pp. 63-71, 2012.
[41] Ministry of Housing and Urban-Rural Development of the People's Republic of China, "JGJ 7-2010 Technical Specification for Space Frame Structures", *Architecture & Building Press*, Beijing, China, 2010.

Advanced Steel Construction – Vol. 18 No. 1 (2022) 479–487
DOI:10.18057/IJASC.2022.18.1.6

A SIMPLE METHOD FOR A RELIABLE MODELLING OF THE NONLINEAR BEHAVIOUR OF BOLTED CONNECTIONS IN STEEL LATTICE TOWERS

Farshad Pourshargh [1], Frederic P. Legeron [1, 2], Sébastien Langlois [1, *] and Kahina Sad Saoud [1]

[1] *Université de Sherbrooke, Department of Civil and Building Engineering,*
2500 boul. de l'Université, Sherbrooke, QC J1K 2A1, Canada
[2] *PMC – Bridge & Tunnel UAE District Manager, Parsons, Abu Dhabi PO5498, UAE*
** (Corresponding author: E-mail: Sebastien.Langlois@USherbrooke.ca)*

ABSTRACT

The behaviour of bolted connections in steel lattice transmission line towers affects their load-bearing capacity and failure mode. Bolted connections are commonly modelled as pinned or fixed joints, but their behaviour lies between these two extremes and evolves in a nonlinear manner. Accordingly, an accurate finite element modelling of the structural response of complete steel lattice towers requires the consideration of various nonlinear phenomena involved in bolted connexions, such as bolt slippage. In this study, a practical method is proposed for the modelling of the nonlinear response of steel lattice tower connections involving one or multiple bolts. First, the local load-deformation behaviour of single-bolt lap connections is evaluated analytically depending on various geometric and material parameters and construction details. Then, the predicted nonlinear behaviour for a given configuration serves as an input to a 2D/3D numerical model of the entire assembly of plates in which the bolted joints are represented as discrete elements. For comparison purposes, an extensive experimental study comprising forty-four tests were conducted on steel plates assembled with one or two bolts. This approach is also extended to simulate the behaviour of assemblies including four bolts and the obtained results are checked against experimental datasets from the literature. The obtained results show that the proposed method can predict accurately the response of a variety of multi-bolt connections. A potential application of the strategy developed in this paper could be in the numerical modelling of full-scale steel lattice towers, particularly for a reliable estimation of the displacements.

ARTICLE HISTORY

Received: 11 December 2020
Revised: 26 May 2021
Accepted: 27 May 2021

KEYWORDS

Steel lattice tower;
Nonlinear behaviour;
Bolted connection;
Failure modes;
Bolt slippage;
Finite element modelling

1. Introduction

Steel lattice towers are widely used all over the world as transmission line supports. The structural integrity of such towers is a key factor in the reliability of a power transmission system. To minimize the risk of power supply disruptions that may occur because of tower failure, structural reliability of towers should be evaluated properly. In the standard simplified method of analysis and design, commonly used by tower engineers, lattice towers are idealized as linear trusses in which angle members are assumed to be connected to each other by frictionless joints acting as hinges. Moreover, the influence of end bending moments in members is generally ignored in simplified structural analyses, and leg members, which are supposed to be continuous, are assumed to be hinged in nodal points. Because of the simplifying assumptions used for design and analysis of lattice towers, it is a common practice among electric network operators to perform experimental tests on full-scale towers for the validation of new design concepts, which turns out to be a long and costly process.

Leg members in towers are connected via lap spliced bolted joints and the bracing members are usually connected to legs via single bolted joints to ensure a hinged connection. Assuming hinged joints does not represent their real behaviour and modelling bolted connections as rigid is also inadequate. In fact, an accurate numerical modelling of the behaviour of real joints is complex due to numerous interactions taking place locally.

The complex behaviour of bolted joints can be split into three categories: eccentricity, rotational stiffness and joint slippage. In practice, angle members in lattice towers are often loaded eccentrically, which causes a biaxial bending in addition to axial loads. The combined action of axial and bending forces may cause a plastic hinge in the cross-section and the bolted leg of the angle could undergo a local post-elastic deformation under the bearing force of bolts, causing displacement and rotation in the connection and shear lag in the member [1].

Additionally, most of the bolt holes are in practice slightly larger than the diameter of bolts, which makes joint slippage inevitable. The slippage may happen gradually or at a specific level of loading and it depends on different parameters such as: structural loading, workmanship, the constitutive properties of the bolts and connections, nature and condition of the faying surfaces and bolt torqueing [2, 3].

Because of the lack of experimental data and the complexity of describing the actual slippage phenomenon in a real structure, simplified models have to be used. For example, in a study by Kitipornchai et al. [4], the slippage is modeled as a random process. The authors concluded that joint behaviour does not have a significant influence on the ultimate strength of the structure, but it influences deflections. In a comparison of numerical predictions with experimental results, Jiang et al. [5] investigated the effect of joints on structural analysis model. The results of their study showed that to predict the tower sway displacement, joint behaviour must be considered. This will drastically increase the predicted tower deformation but will not affect its failure load, failure mode and sequence. In a subsequent study, Jiang et al. [6] numerically investigated the impact of the combination of various joint effects, including connections' semi-rigidity, joint slippage, and initial geometric imperfections, on the structural behaviour of an ultrahigh-voltage steel lattice tower. Their study revealed second order effects should be considered to accurately predict the behaviour of slender transmission line towers.

To account for the joint stiffness, Kang et al. [7] found that the connection rigidity may have a considerable effect on the ultimate horizontal loading capacity of a lattice tower. The rigid connection increases the buckling capacity, thus the assumption on connection rigidity must be realistic. Otherwise, the buckling capacity of the structure may be over or underestimated.

Knight and Santhakumar [8] concluded that neglecting the joint effects may be responsible for the premature failure in towers and must thus be considered in the analysis. The results of their study showed a good correlation with experiments when joint effects are considered. An et al. [9] carried out an experimental and numerical study on the nonlinear axial stiffness of multi-bolted leg joints typically employed in classical 500 kV lattice transmission towers in China. A simplified model was also proposed in this study for the characterization of the load-deformation relationship. However, the proposed model does not cover configurations including a reduced number of bolts, which is commonly the case in steel lattice transmission line towers. Ungkurapinan et al. [10] investigated the behaviour of various configurations of connections involving one to four bolts. Unfortunately, there is not a complete database of slippage parameters for angle member connections. Some limited numbers of tests are available on specific angle sections and bolt arrangements. From the literature, it is observed that the behaviour of bolted joints influences deflections of steel lattice towers most of the time, and failure modes and ultimate loading only in some cases. It is recognized that the tower connections are different from ordinary steel connections in other types of steel structures [10].

In lattice transmission towers, the members are mostly connected directly via their flange or through the gusset plates which provide a connection flexibility. In addition, the slippage effect should be included in the numerical model, because lattice towers are constructed by bearing type connections instead of friction type ones. In this respect, recent studies conducted by Abdelrahman et al. [11], and Gan et al. [12], among others, have highlighted the

importance of appropriately considering the influential factors in the design process.

The general objective of this article is to propose a simple method to predict the complex behaviour of bolted connections in steel lattice towers. The procedure detailed in this paper comprises two main aspects. First, the nonlinear load-deformation behaviour of single-bolt connections is characterized based on their geometric/material properties and some construction details. This characterization includes the identification of the pre-slip, slip and post-slip regions of the behaviour. Then, the calculated behaviour is applied to finite element models of bolted assemblies, where the connections are represented using nonlinear spring elements. The finite element method can involve multiple bolts with various arrangements. The accuracy of developed method is verified by conducting experimental tests on plate assemblies including single-bolt and two-bolt configurations. The prediction method is also compared to datasets from experimental tests performed on four-bolt connections provided by Cai and Driver [13] as well as a detailed three-dimensional finite element modelling of two-bolt connections considering multiple interactions between the assembled plates and the bolts.

The proposed method is intended to be easily implemented for a wide range of joint configurations and may find broader application in the context of numerical modelling of complete lattice towers with the aim of evaluating precisely their complex structural behaviour.

This article starts by presenting the approach developed for the representation of the behaviour of multi-bolt connections. Then, the experimental program investigating the response of different plate assemblies involving one or two bolts is briefly described. Finally, various configurations involving single and multiple bolts are examined and the obtained numerical results are compared with reference results.

2. Modelling and prediction of the nonlinear behaviour of bolted connections

In the present study, a nonlinear discrete element is employed to model the bolted connections. The paper particularly investigates the effect of varying the following geometric parameters: the plate thickness t_p, the plate width W, the bolt diameter D, the end distance of plate (distance from the center of the hole to plate edge) L_e, and the number of bolts n (the configurations analysed are summarized in Table 1 and Table 2). The nonlinear spring element should also be able to include the deflection due to slippage of connection and the near-field behaviour of plate in the vicinity of the bolt. The local behaviour of single-bolt connections, from loading to failure, is first predicted analytically as described subsequently. Then, the predicted load-deformation law is applied to numerically model the nonlinear response of plate assemblies using nonlinear spring elements. Code_Aster [14], an open-source finite element software package developed by "Electricité de France" (EDF), is used in this research. Code_Aster [14] has a powerful nonlinear spring element that can model the connection behaviour. The methodology is to first predict the behaviour of single-bolt connection using equations available in the literature based on its properties and considering the near-field behaviour. At the second step, a series of specimens is tested in laboratory to validate the prediction model. The third step proposes a method to categorize multi-bolt connections and predict their behaviour based on one bolt predicted model. This step is done with the help of a finite element plate model. At the next step, the method is evaluated by conducting experiments on several two-bolt joints. In the final step, predictions are compared to experimental results of four-bolt connection tests which have been reported by a research at the University of Alberta, Canada [13].

2.1. Prediction method for one-bolt connections

Fig.1 illustrates the typical force-displacement relationship of a bolted connection under uniaxial tensile load. This graph may be divided into two main regions: pre-contact and post-contact. The pre-contact region is characterized by a frictional load transfer followed by a significant bolt slippage and ends at the contact point defining the threshold value for establishing contact between the bolt and the plate. Beyond the contact point begins the post-contact region, in which the load is mainly transferred by bearing up to the failure of the joint.

To characterize the local response of a bolted connection, the values of the load at which bolt slippage occurs P_{slip}, the peak load $P_{failure}$, the elastic displacement reached before the onset of slippage $D_{preslip}$, the displacement at the end of the pre-contact region D_{slip} and the ultimate displacement $D_{failure}$ should first be determined based on the geometric and material properties of the connection and some construction details.

Once evaluated, the parameters defining the curve depicted in Fig.1 will be used in a two-dimensional finite element model, where the bolted joints are represented using spring elements, to deeply investigate the global response of assemblies. This may be done by assigning these values to the discrete elements through the nonlinear behaviour law ASSE_CORN implemented in Code_Aster [14].

To determine the limit values associated with the pre-contact region, it is proposed to use equations developed by Rex and Easterling [15] to predict the slip behaviour of a single bolt bearing on a plate. They proposed the value of 0.193 mm for $D_{preslip}$ based on various experiments performed on a single plate assembled using one bolt. D_{slip} directly depends on the bolt hole clearance. Normally, the bolt holes are drilled larger than the diameter of bolts to satisfy the requirements in terms of erection tolerance. For example, common industry practices consider the value of 1.6 mm as a standard hole clearance in North American steel construction. Unless otherwise specified, the values of $D_{preslip}$ and D_{slip} in this work will be taken as 0.193 mm and 1.6 mm respectively.

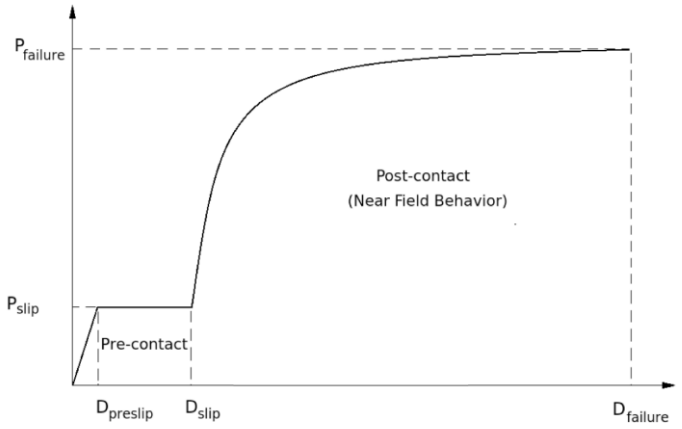

Fig. 1 Behaviour of connection under axial load

The value P_{slip} is here calculated using the method of AISC code [16] as follows:

$$P_{slip} = K_s \times m \times n \times T_i \tag{1}$$

Where:

$$T_i = \frac{Bolt\ Torque}{C \times D} \tag{2}$$

And m = number of slip surfaces (two for the cases handled in this paper), n = number of bolts (one bolt in this case); K_s = slip coefficient (for a typical steel surface, K_s is taken as 0.33); C = nut factor (0.2, as given by [17]); and D = bolt diameter.

The amount of bolt torque in equation (2) is taken as 100 N-m, in accordance with the experimental tests carried out in this study.

For the post-contact region, the following empirical equation proposed by Rex and Easterling [18] will be used to predict the behaviour of a single-bolt connection [following equations use units of mm and kN]:

$$\frac{R}{R_n} = \frac{1.74 \times \bar{\Delta}}{(1+(\bar{\Delta})^{0.5})^2} - 0.009 \times \bar{\Delta} \tag{3}$$

In which, R is the plate load, and R_n the plate nominal strength which may be evaluated as follows:

$$R_n = D \times t_p \times F_b \tag{4}$$

And $\bar{\Delta}$ is the nominal deformation which is defined in equation (5).
In equation (4), the bearing/tear-out strength of the plate F_b is defined by the following relationship:

$$\bar{\Delta} = \frac{\Delta \times \beta \times K_i}{R_n} \tag{5}$$

$$F_b = F_u \times \frac{L_e}{D} \leq 2.4 \times F_u \tag{6}$$

$$K_i = \frac{1}{\frac{1}{K_{br}} + \frac{1}{K_b} + \frac{1}{K_v}} \tag{7}$$

$$K_{br} = 120 \times t_p \times F_y \times (D/25.4) \tag{8}$$

$$K_b = 32 \times E \times t_p \times (L_e/D - 1/2)^3 \tag{9}$$

$$K_v = 6.67 \times G \times t_p \times (L_e/D - 1/2) \tag{10}$$

In equation (5), Δ stands for the hole elongation and β denotes the steel correction factor, which is taken as 1.0 for typical structural steel. Equation (7) evaluates the initial stiffness of the connection K_i, from the bearing stiffness K_{br}, the bending stiffness K_b, and the shearing stiffness K_v. In this analysis, the modulus of elasticity E and the shear modulus G of steel are taken equal to 210,000 MPa and 80,000 Mpa, respectively. The material grade of steel plates is CSA-G40-400W and the bolt grade is ASTM-A325

2.2. Prediction method for multi-bolt connections

The main contribution of this research is to predict the behaviour of multi-bolt connections based on the near field behaviour of one bolt. None of the literature reviewed considered the prediction of full behaviour for the connections. In this section, the behavior of multi-bolt connections is predicted. The behaviour of one-bolt joint is applied to a finite element model through a nonlinear spring element. The properties of the spring elements are determined according to the method discussed in the previous section.

The finite element model is built using quadrilateral shell elements named "DKT" in Code_Aster [14]. Each element has four nodes with six degrees of freedom and a bi-linear behaviour law is considered for the inelastic material. The mesh size is adjusted considering geometrical complexity of the model, especially around holes. Mesh refinement is applied where needed based on a preliminary mesh size sensitivity analysis and the mesh size varies between 4 mm and 10 mm. Fig.2 compares the results obtained for a connection involving two bolts based on three mesh trials. In this case, since the nonlinearity is mostly due to the spring elements, mesh size and density does not have a noticeable effect on the behaviour. The central nodes of bolts are represented as fixed support and a uniformly distributed tensile load is applied on the right side of the model. In reality, the near field zone is connected continuously to the surrounding area on the plate. To capture this, a rectangular cut out is created which provides extra nodes from the finite element model to connect the spring and avoid stress concentration. The rectangular shape also makes the mesh more structured. To illustrate this point, an example of a two-bolt connection is shown in Fig.3. The green lines in the figure, represent the rigid link elements to connect the non-linear spring element to nodes of near field behaviour zone. The rigid links work under tension and compression and they link the degrees of freedom of two nodes.

The model is also able to consider different types of bolts with different diameters in the same connection. The near field behaviour of one bolt can be predicted first based on the method described in section 2.1 and then it will be assigned to nonlinear spring elements, in any location on the plate. The efficiency of the proposed method is evaluated in section 4.3 by comparing to the tests on 4 two-bolt connection configurations.

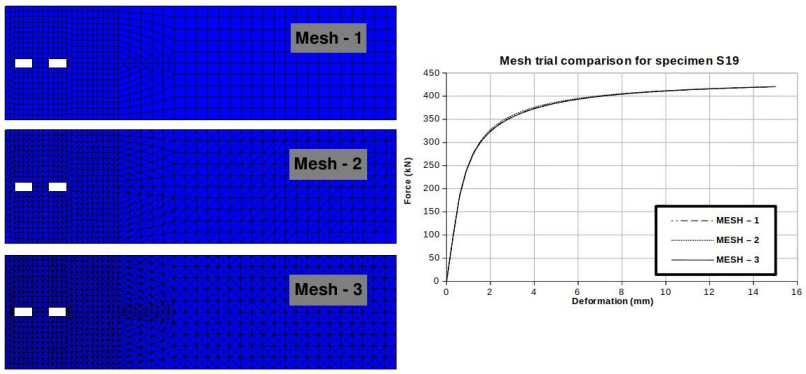

Fig. 2 Comparison of different mesh refinement and sizes

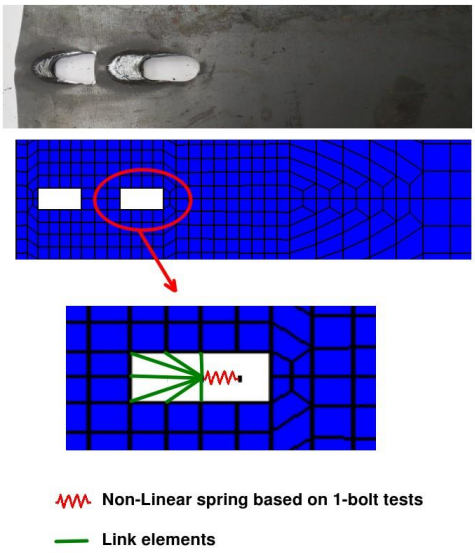

Fig. 3 2D modelling of a two-bolt connection using a plate and spring elements

The method proposed in this study is also verified by predicting the response of 10 four-bolt specimens which have been tested by Cai and Driver [13]. The researchers have used I-sections with bolt holes in the web, and the sections were loaded in tension to determine the capacity of connection. Fig.4 shows one of the specimens and the geometry of model which is proposed for the prediction. As one can notice, the four-bolt configuration presented in Fig.4 is not representative of lattice towers' typical connections. The main purpose here is to take advantage of the experimental results reported in the article by Cai and Driver [13] in order to evaluate the reliability of the method proposed in this paper. Three-dimensional shell elements of Code_Aster [14] were used to mesh the model due to the complex geometry of the analysed samples. Each element has nine nodes with six degrees of freedom per node. The central node of bolts is modeled as a fixed support and a uniformly distributed tensile load is applied to the nodes located at the free end of the I-sections. The size of the near field zone in this case is equal to edge distance of the bolt hole. In this case, the spring is connected to the sides of the zone since the end distance was too small to provide adequate support at the end of the rectangular holes (see Fig. 4).

The prediction method and procedure for these specimens is the same as two-bolt specimens. First, the near field behaviour of one bolt is calculated using equations 1 to 3. Then the behaviour is applied to the four-bolt model through the nonlinear spring elements. Properties of the specimens analysed are presented in Table 1 and Fig. 5.

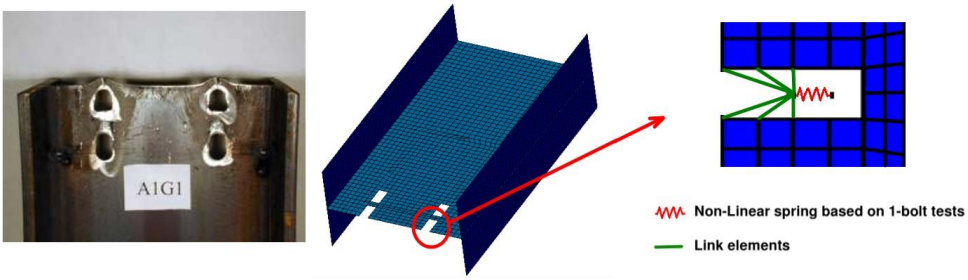

Fig. 4 FE modelling of a connection involving four bolts

Table 1
Properties of four-bolt specimens [8]

Section	D (mm)	W (mm)	t_p (mm)	L_e (mm)	*Fy* (MPa)	*Fu* (Mpa)
A1G1	19	305.4	7.48	28.3	439	519
A2G1	19	305.4	7.52	29.27	439	519
A7G1	19	304	7.43	28.55	411	494
A5E1	19	248.5	7.55	31	343	487
A11E1	19	249.9	7.30	28.27	376	500
A8G2	19	304.5	7.44	27.08	411	494
A3R1	19	310	6.30	28.15	379	472
A9R1	19	311.6	6.54	27.56	369	478
A6E2	19	248	7.51	47.73	343	487
A12E2	19	249.5	7.34	44.0	376	500

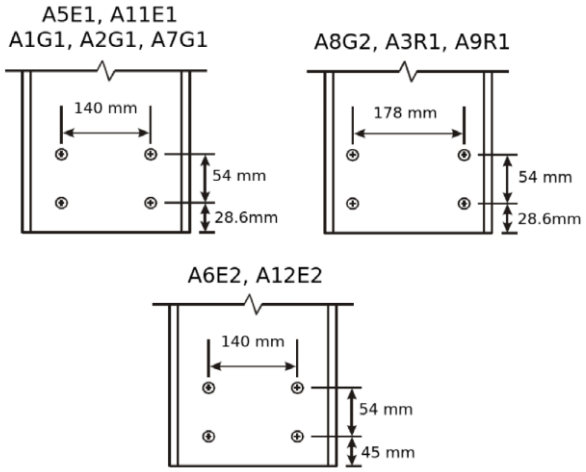

Fig. 5 Configuration of four-bolt specimens [8]

3. Experimental program

This section reports the experimental investigations carried out on double lap connections. These tests will serve for the validation of the method developed in this paper for the prediction of the complex behaviour of multi-bolt connections.

3.1. Specimens

In this research, bolt plate specimens were tested under uniaxial tensile loading. The experimental program consists of eighteen one-bolt and four two-bolt configurations. To ensure the quality and the reproducibility of the results, each configuration was tested twice. Fig.6 summarizes the dimensions and configurations of test specimens.

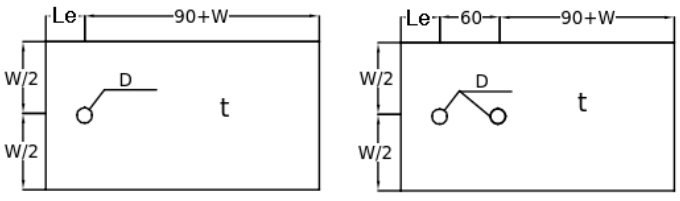

Fig. 6 Configuration of the tested specimens

The one-bolt specimens were used to validate the analytical modelling method proposed in this article. A uniaxial load was applied to all of the specimens. The main variables are plate thickness, plate width, bolt diameter and end distance. The specimens were designed to fail under three different failure modes: (i) bearing; (ii) cleavage and (iii) end bearing [16]. The complete description of one-bolt specimens is provided in Table 2. The second group of specimens were designed to evaluate the prediction method for two bolts. These specimens were designed in a way that the near field behaviour of bolts is already predicted from the previous one-bolt tests. The objective is to define a prediction method for connections with more bolts based on near field behaviour of one bolt. The properties for this group of tests are provided in Table 3.

Table 2
Properties of one-bolt test specimens

Configuration	D (mm)	W (mm)	t_p (mm)	L_e (mm)	F_y (MPa)	F_u (Mpa)	Failure Scenario
S1	16	152	9.5	40	396	555	B
S2	16	127	9.5	40	404	529	B
S3	16	127	7.9	40	417	560	B
S4	19	152	9.5	47.5	396	555	B
S5	19	127	9.5	47.5	404	529	B
S6	19	127	7.9	47.5	417	560	B
S7	16	152	9.5	24	396	555	C+S
S8	16	127	9.5	24	404	529	C+S
S9	16	89	6.35	24	370	578	C+S
S10	19	152	12.7	28.5	383	520	C+S
S11	19	127	7.9	28.5	417	560	C+S
S12	19	89	6.35	28.5	370	578	C+S

Note: (B: Bearing failure, C+S: Cleavage and End shear failure)

3.2. Test set-up

The specimens were tested in a tension jig. To prevent the prying action of plates, the setup was prepared so as to apply only a uniaxial force on the specimens, without eccentricity or bending moments. Fig.7 and Fig.8 show the layout of experimental setup.

Plates PL-2 and PL-3, were used in all the test cases, but PL-1 was changed according to the thickness of each specimens. The thickness of plates PL-2 and PL-3 is 25mm and they are connected to PL-1 by six M16 bolts. The dimensions of the plates are 500 mm for length and 250mm for width. Each bolt was tensioned manually to a torque of 100 N-m to match common practice in the transmission line industry. To acquire accurate torque, a calibrated torque wrench was used. All the surfaces are normal bare steel without any preparation.

To measure the deformation of specimens, a high accuracy laser displacement transducer was used. The transducer rested on PL-2 or PL3 and the probe mounted on the specimen by using a small aluminium angle. Therefore, the relative deformation between the specimen and the connection plates was measured accurately. Fig.3 shows the set-up and location of displacement transducer.

An MTS hydraulic testing machine was used to apply tension to specimens. The capacity of the machine is 500 kN. The loading was displacement controlled with a loading rate of 1mm/min. The maximum value of displacement that was provided by the machine was set equal to the bolt diameter, although most of the specimens failed before this value was reached.

Table 3
Two-bolt test specimens

Configuration	Corresponding one-bolt configuration	D (mm)	W (mm)	t_p (mm)	L_e (mm)	F_y (Mpa)	F_u (Mpa)	Failure Scenario
S19	S1	16	200	9.5	40	387	516	B
S20	S3	16	200	7.9	40	452	482	B
S21	S4	19	250	9.5	47.5	374	521	B
S22	S6	19	250	7.9	47.5	390	465	B

Note: (B: Bearing failure)

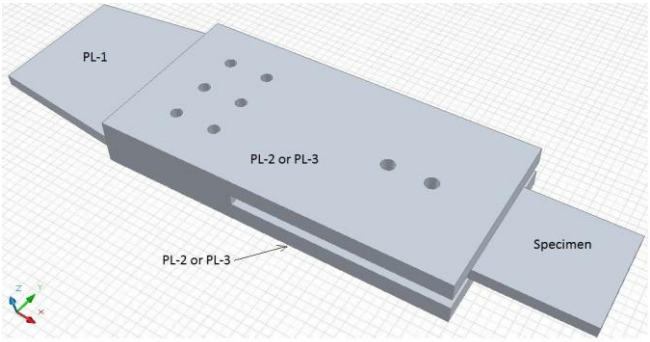

Fig. 7 Layout of experimental set-up

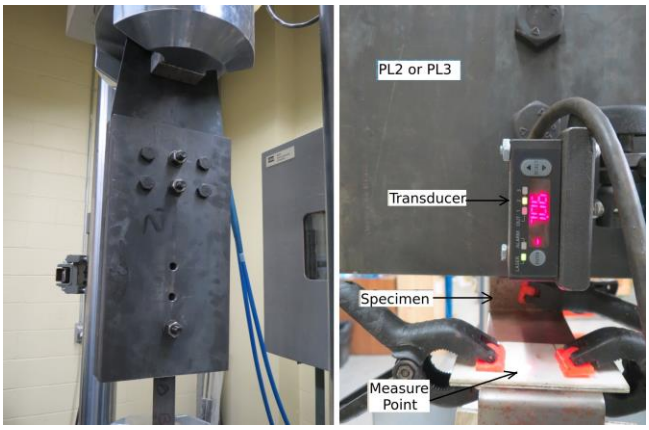

Fig. 8 Final setup and transducer location

3.3. Material property tests

Two tension coupons were cut and prepared from each batch of steel material and tested according to ASTM A370-02 standard [19]. The values of yield strength F_y and ultimate tensile strength F_u of steel obtained from tensile coupon tests were used in the prediction method. These values are indicated in Tables 1 and 2.

4. Results and discussion

4.1. Analysis of configurations involving one bolt

Figs. 9a and 9b depict the force-displacement curves of twelve one-bolt specimens (S1 to S12). These figures show that the proposed method can predict the full behaviour of the connections with high accuracy compared to the results obtained from the experimental tests. The predicted curve is also able to consider slip behaviour during the loading phase and the trend of the curve is similar to the behaviour of specimens. As shown in Fig. 3, the specimens in this study were tested using a vertical test setup and the effect of gravity minimized the gap between the bolt and the contact surface of the hole. So in this case, to have a more realistic evaluation of the force-deflection relationship, the value of 1.6 mm gap is not introduced to the prediction method. As a result, the slippage behaviour is not significant in the predictions. The pre-tensioning force in the bolts also causes the slippage to happen gradually.

In Figs. 9a and 9b, the predicted curves are stopped at a displacement equals to bolt diameter because the method does not provide an estimate for final displacement. Even though the objective of this research is to predict the complete behaviour of connection, it is clear that the method can provide the values of ultimate capacity with a significant accuracy. Table 4 presents a comparison for the ultimate capacity between the prediction method and the experimental tests. The ratio of prediction to test capacity is on average 0.98. The following symbols are used in the tables, P_{ut} (ultimate capacity of test specimens), D_{ft} (final deflection of test specimens), P_{upr} (ultimate capacity predicted by the method). It is clear from Fig. 9b, that while the maximum load is well captured for all failure modes tested (B or C+S), the ultimate displacement is not captured accurately by the method for mode C+S.

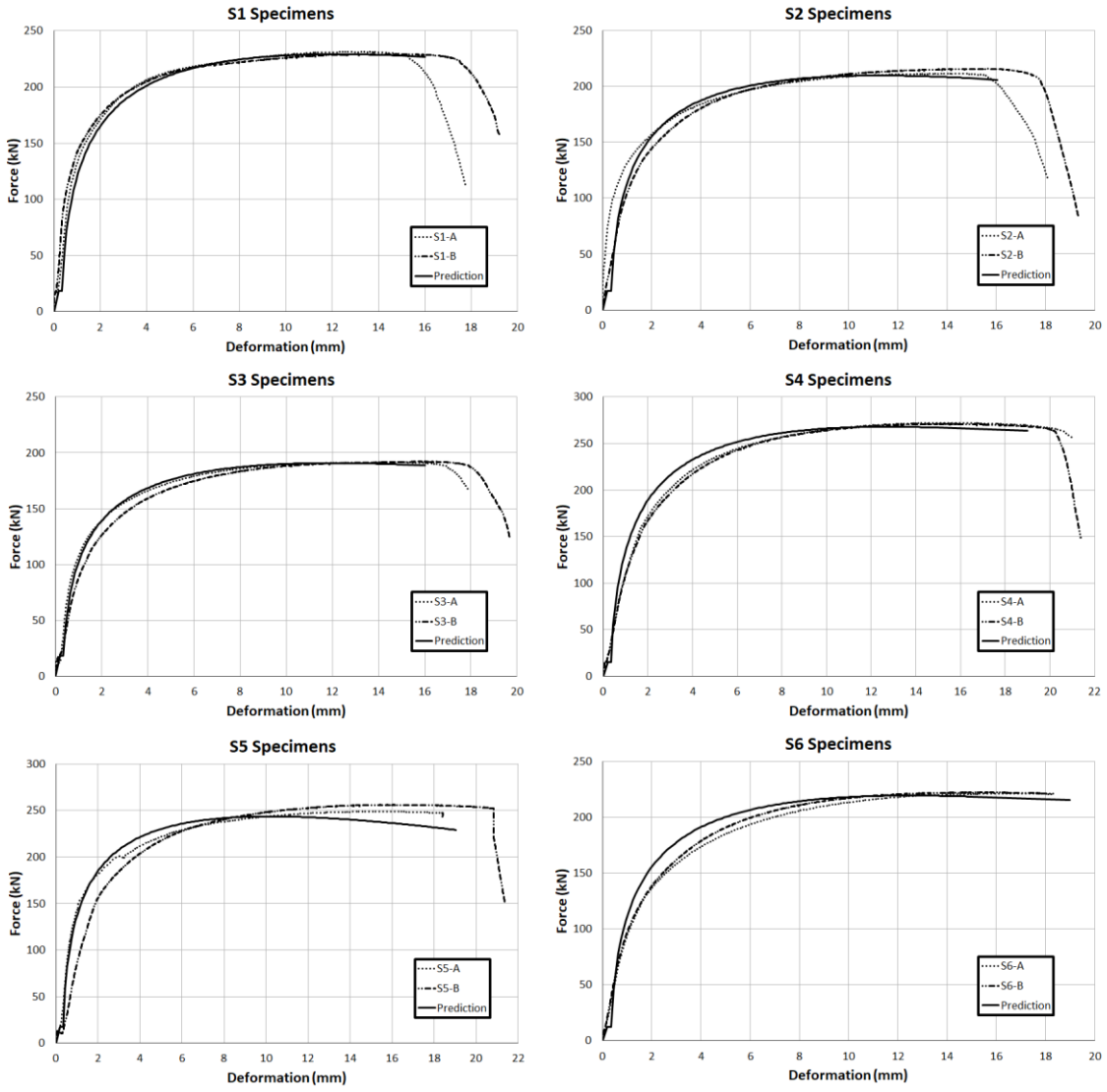

Fig. 9a Comparison of prediction and experimental behaviour of single-bolt connections

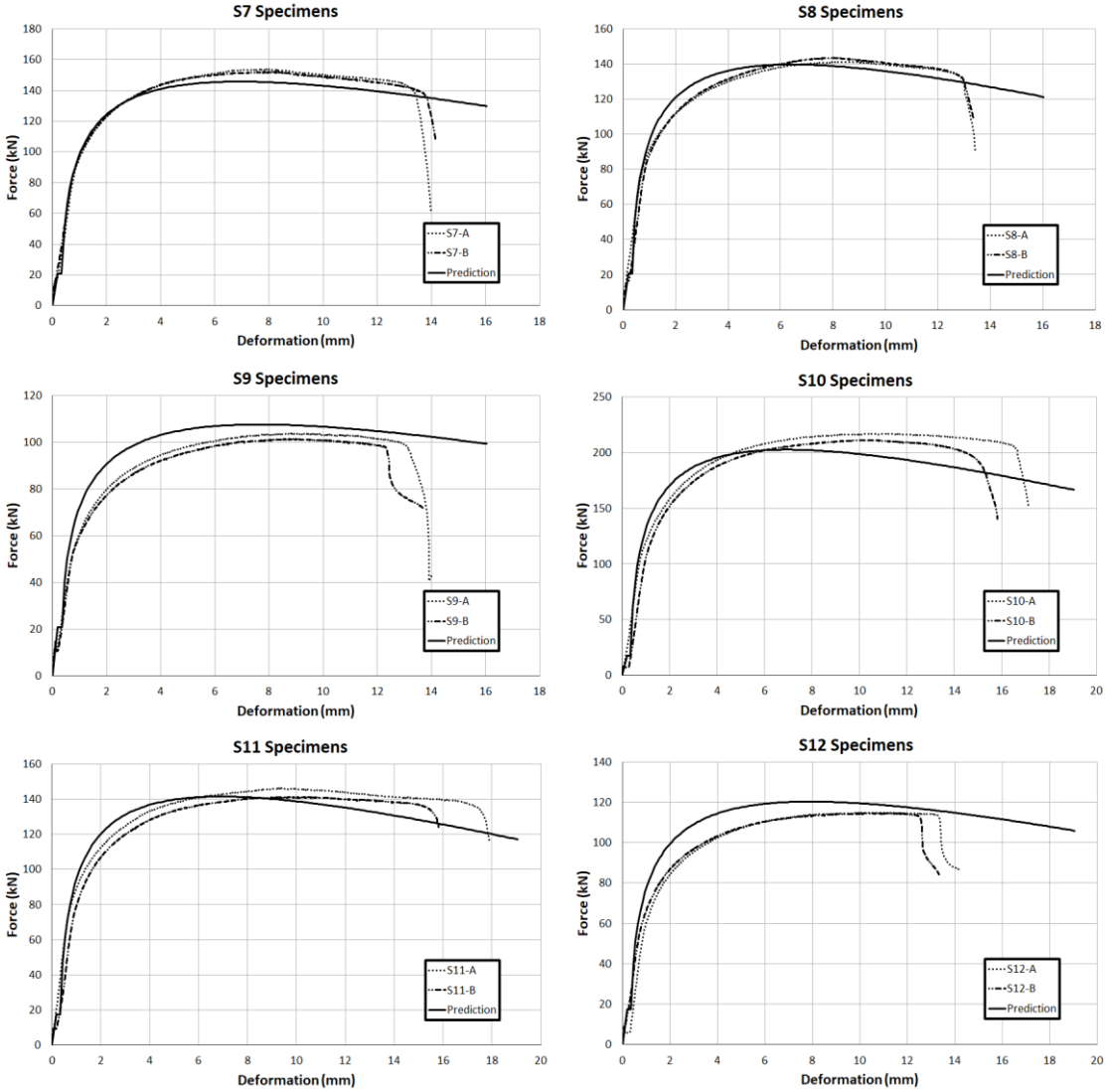

Fig. 9b Comparison of prediction and experimental behaviour of single-bolt connections

Table 4
Comparison of predicted and experimental ultimate capacity for one-bolt specimens

Specimen	P_{ut} (kN)	D_{ft} (mm)	P_{upr} (kN)	P_{upr}/P_{ut}
S1	230	16	219	0.95
S2	214	16	209	0.98
S3	192	17	188	0.98
S4	272	18	255	0.94
S5	253	18	244	0.97
S6	222	18	217	0.98
S7	153	13	146	0.95
S8	142	12	140	0.98
S9	103	12	107	1.04
S10	214	15	203	0.94
S11	144	15	142	0.99
S12	115	12	120	1.05
Average				0.98
COV (%)				3.6

COV: Coefficient of variation

4.2. Analysis of configurations involving two bolts

The method proposed for the prediction of the behaviour of connections with two bolts is derived using a finite element model. As described previously, the near field behaviour of each bolt was assigned to the model by means of a nonlinear spring and the remaining parts of the specimen were modelled by shell elements. The prediction of specimen S19 has been performed based on the predicted near field behaviour of S1, which has the same bolt diameter, plate thickness, plate width and end distance. Similarly, the specimens S20, S21 and S22 have been predicted based on S3, S4 and S6 predictions, respectively.

In addition a detailed 3D numerical modelling of the analysed two-bolt samples is performed in this case using three-dimensional solid finite elements. Fig.10 shows the geometry and mesh of the model. The numerical model is developed using Code_Aster [14] and the adopted mesh scheme is constituted of 8-node isoparametric brick elements. To diminish the computational costs, each component of the connections is meshed individually with a fine mesh around the contact area and a coarse mesh elsewhere. In this formulation, the principle of virtual work is expressed in the current configuration accounting for finite strains. The inelastic behaviour of the structural steel composing the plates is approximated by a multi-linear stress-strain relationship derived from the tensile coupon tests carried out on the analysed specimens (S19 to S22). In the absence of relevant details on the material behaviour of the high-strength bolts, they are modelled using a bi-linear elastoplastic constitutive law characterised by the modulus of elasticity E=200 GPa, Poisson's ratio ν=0.3, yield strength F_y=800 MPa, and the tangent modulus H=1 MPa. Finally, the von Mises yield criterion in conjunction with a linear isotropic hardening rule is adopted herein to simulate the plastic behaviour of the steel.

Plate PL-1 shown in Fig.7 is not represented in this modelling as it does not produce any direct effect on the behaviour of the connection. In accordance with the experimental tests, the uniaxial tensile loading is applied as an imposed displacement, while the surfaces of plates PL-2 and PL-3 are fully clamped in the side opposite to the loaded surface. The different parts constituting each connection are assembled using two bolts and the contact/friction behaviour, between plates PL-2/PL-3 and the bolts' head/washer, the three plates and the bolts' shank, and at interfaces between the central plate and plates PL-2/PL-3, is treated using the augmented Lagrangian method.

Fig.11 illustrates the comparison of the axial load-displacement results for the tests conducted on specimens with two bolts (S19 to S22). The numerical and experimental deformed configurations of the specimen S20, for instance, are shown in Fig.12. From Fig.12 it may be observed that the proposed method (Fig.12b) is in line with the experimental (Fig.12c) and the numerical (Fig.12a) deformed shapes.

As shown in Fig.11, good agreement is generally obtained between the developed method (using shell elements) and the experimental tests.

For specimen S21, the final displacement measured experimentally is smaller than the expected value. Since the operational capacity of testing machine was about 450 kN, this test was terminated to avoid damage to the machine. Also, one of the experimental tests performed on specimen S21 provided unreliable output due to misalignment of transducer. Therefore, only one experimental load-displacement curve is presented for this configuration. By contrast, the numerical results obtained using 3D solid elements are somewhat different from the experimental ones.

Despite its simplicity, the proposed method thus appears to be computationally more efficient than a detailed numerical modelling using three-dimensional solid elements. Finally, Table 5 summarizes the ultimate capacity obtained with the proposed method. Average difference of connection capacity between the prediction method and experimental results is 2 percent.

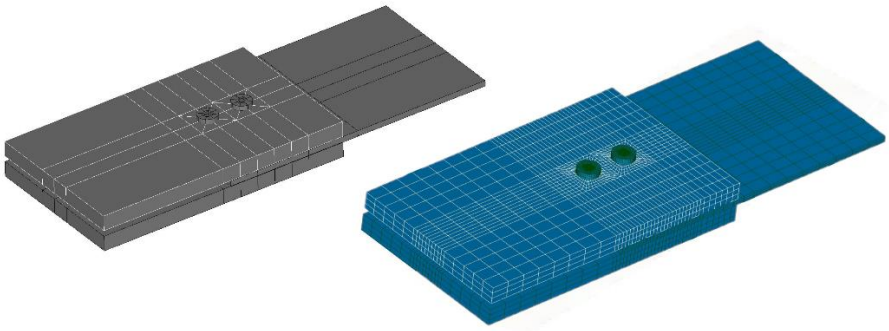

Fig. 10 Numerical model of the two-bolt tests using 3D solid elements

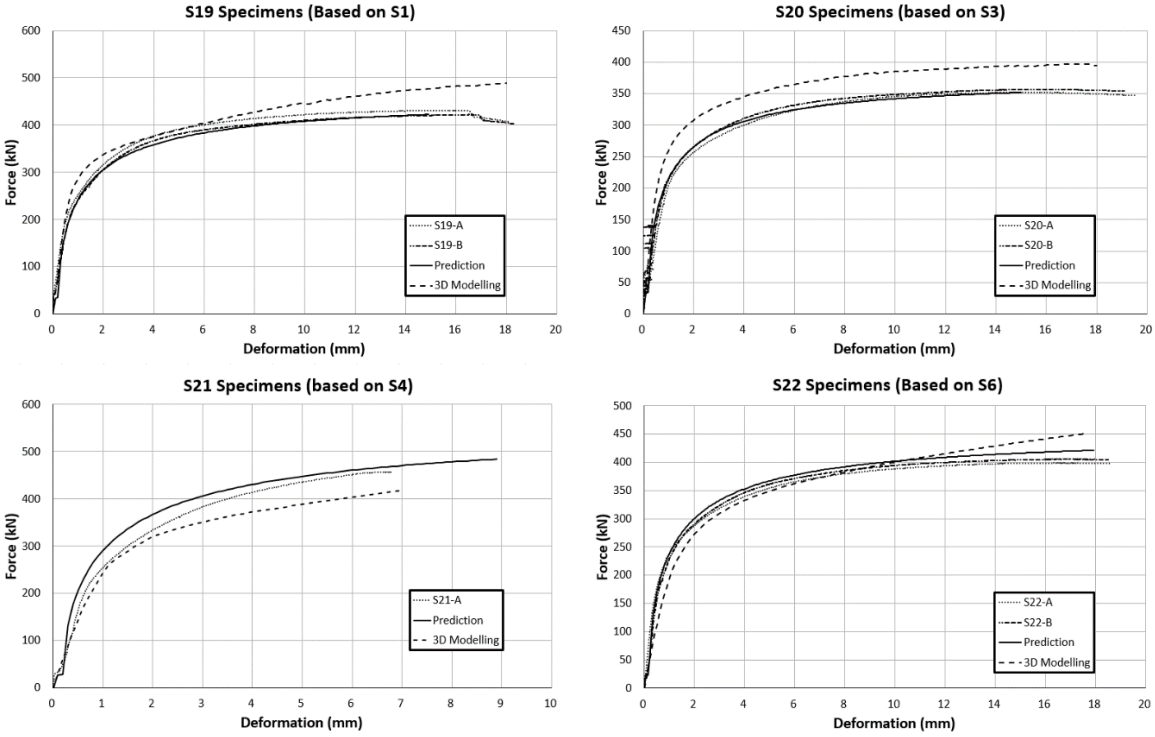

Fig. 11 Comparison of two-bolt connections

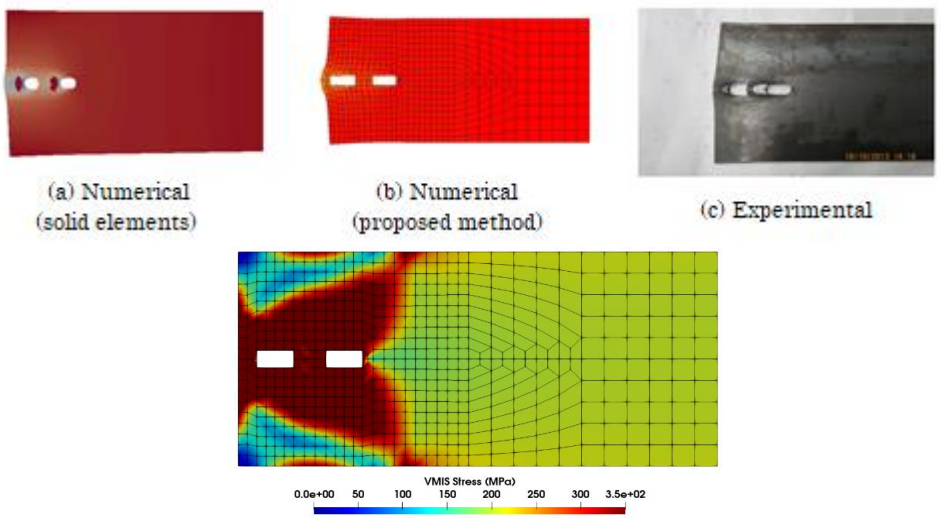

Fig. 12 Deformed configuration and yielding stress map of a two-bolt connection (specimen S20)

Table 5
Comparison of predicted and experimental ultimate capacity for two-bolt specimens

Specimen	P_{ut} (kN)	D_{ft} (mm)	P_{upr} (kN)	P_{u_3D} (kN)	$\frac{P_{upr}}{P_{ut}}$
S19	427	17	420	486	0.98
S20	354	19	363	397	1.03
S21	450	6.79*	475	417	1.06
S22	402	19	420	451	1.04
Average					1.02
COV (%)					3.31

P_{ut}: ultimate capacity of test specimens
D_{ft}: final deflection of test specimens
P_{upr}: ultimate capacity predicted by the method
P_{u_3D}: ultimate capacity of FE model using 3D solid elements
COV: Coefficient of Variation
* This specimen did not reach complete failure due to capacity of testing machine

4.3. Analysis of configurations involving four bolts

Fig.13 compares the predictions of four-bolt specimens with the tests results of the study from Cai and Driver [13]. Table 6 summarizes the results for the ten specimens considered in this study. Since the size of bolt hole for each specimen was not mentioned in their report, the amount of D_{slip} parameter is considered approximately to fit the experimental results. This set of tests also shows that the method can predict the behaviour of multi-bolt connections with acceptable accuracy. As it is observed from Table 6, the prediction method underestimates the ultimate capacity by 12 percent on average. The slippage behaviour of specimen A8G2 is obvious for both test and predicted results.

Table 6
Comparison of predicted and experimental ultimate capacity for four-bolt specimens

Specimen	P_{ut} (kN)	D_{ft} (mm)	P_{upr} (kN)	$\frac{P_{upr}}{P_{ut}}$
A1G1	691	14	610	0.88
A2G1	724	9	675	0.93
A7G1	665	16	645	0.97
A5E1	698	9	600	0.86
A11E1	691	14	600	0.87
A8G2	622	12	611	0.98
A3R1	634	11	475	0.75
A9R1	633	16	500	0.79
A6E2	776	7	680	0.88
A12E2	793	16	715	0.90
Average				0.88
COV (%)				8.15

COV: Coefficient of variation

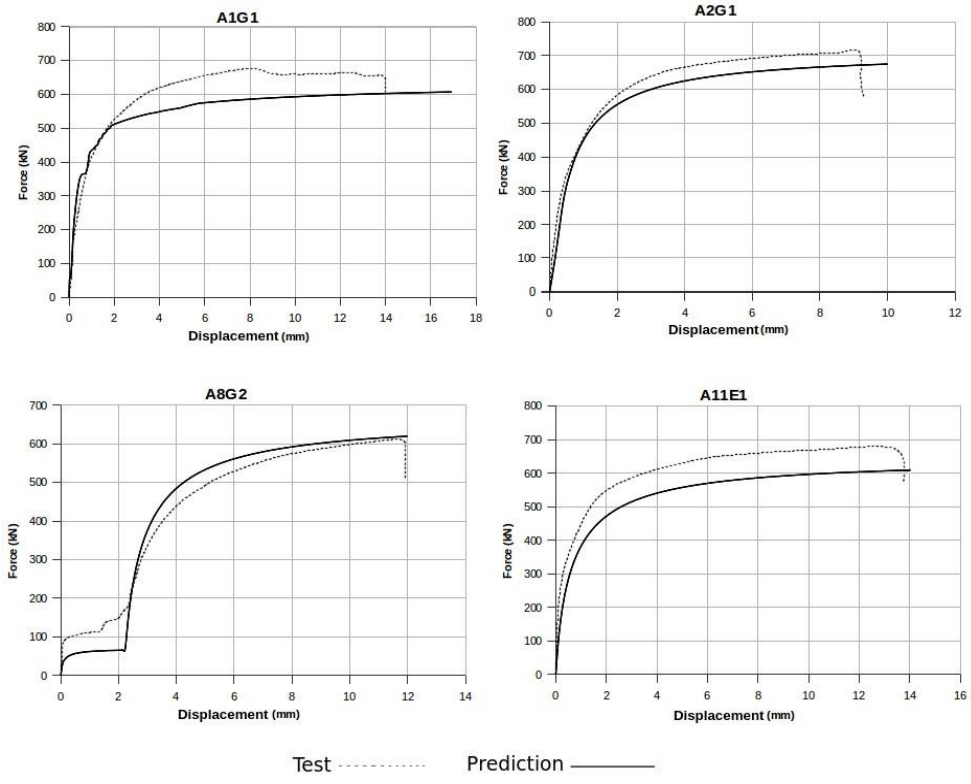

Fig. 13 Comparison of four-bolt Specimens

4.4. Potential application of the proposed method in modelling of a steel lattice tower

Once the nonlinear behaviour of multi-bolt connections is predicted using the method described in sections 4.2 and 4.3, one may take advantage of these results to accurately analyse the structural behaviour of lattice structures. Depending on the software used, this can be done by introducing the full curve of the connection's behaviour or, as it is done in Code_Aster [14], by introducing the key parameters defining the curves, as described in sections 4.2 and 4.3. The proposed method allows to obtain the properties for a unique spring element that captures the overall nonlinear behaviour of a given multi-bolted connection. This spring can easily be implemented at the end of a beam element in a complete lattice tower model.

The parameters to be evaluated are P_{slip}, $P_{failure}$, D_{slip} and $D_{failure}$, and should be assigned to each spring element. Let us recall that the parameters $P_{failure}$ and $D_{failure}$ are the maximum capacity of the connection and the corresponding displacement, respectively. The values of P_{slip} and D_{slip} depend on the amount of slippage in the connections. If there is substantial and obvious slippage in the predicted behaviour, these values can be extracted directly from the curve. Otherwise, these values are assumed to be zero which means that near field behaviour initiates from the beginning and there is no slippage. Tables 7 and 8 indicate the mentioned parameters to calibrate nonlinear springs for two-bolt and four-bolt connections of this study.

Table 7
Parameters to calibrate the nonlinear spring (two-bolt)

Specimen	P_{slip} (kN)	D_{slip} (mm)	$P_{failure}$ (kN)	$D_{failure}$ (mm)
S19	0	0	420	15
S20	0	0	363	15
S21	0	0	475	9
S22	0	0	420	19

Table 8
Parameters to calibrate the nonlinear spring (four-bolt)

Specimen	P_{slip} (kN)	D_{slip} (mm)	$P_{failure}$ (kN)	$D_{failure}$ (mm)
A1G1	0	0	610	17
A2G1	0	0	675	10
A7G1	65	2.1	645	16
A5E1	0	0	600	9
A11E1	0	0	600	14
A8G2	66	2.2	611	12
A3R1	0	0	475	12
A9R1	0	0	500	15
A6E2	0	0	680	8
A12E2	0	0	715	15

5. Concluding remarks

This article presents a method to predict the full force-deformation behaviour of multi-bolt connections under uniaxial tension. The method is based on adding the near field behaviour of each bolt through a nonlinear spring element in the finite element model of the connection. Several experimental tests on single-bolt connections were conducted and the results showed that their behaviour can be evaluated with existing theoretical and empirical relations. The near field behaviour is then applied as a nonlinear spring to the finite element model of various connections. Next, the results for the finite element model were compared to experimental tests performed on two-bolt connections and to existing four-bolt tests. The method accurately predicted the full behaviour of one-, two- and four-bolt connections with different configurations and properties. It also allowed to match closely the ultimate capacity of the connection.

The proposed method allows to predict the full force-displacement curve of multi-bolt connections using a finite element model and starting from the geometry and mechanical properties of each individual bolt. This force-displacement curve for the multi-bolt connection can be used to calibrate a nonlinear spring that will reproduce the connection behaviour in a large-scale tower model. For future work, more experimental tests with different bolt numbers and arrangements should be conducted. Also, tests on models should be performed to study the rotational behaviour of steel angle connections. Moreover, this study focused on bearing and end-shear failure. For the net section failure, another approach needs to be developed. It is also recommended that the predictions of the present study be applied to a finite element model of a complex lattice tower and compared to full scale experimental tests.

References

[1] N. Prasada Rao, S. J. Mohan, N. Lakshmanan, A study on failure of cross arms in transmission line towers during prototype testing, International Journal of Structural Stability and Dynamics 5 (3) (2005) 435–455.
[2] W. Kang, F. Albermani, S. Kitipornachi, L. Heung-Fai, Modeling and analysis of lattice towers with more accurate models, Advanced Steel Construction 3 (2) (2007) 565–582.
[3] N. Prasad Rao, K. G. M. Samuel, N. Lakshmanan, R. I. Nagesh, Effect of bolt slip on tower deformation, Practice Periodical on Structural Design and Construction 17 (2) (2012) 65–73.
[4] S. Kitipornchai, F. Albermani, A. H. Peyrot, Effect of bolt slippage on ultimate behaviour of lattice structures, Journal of structural engineering 120 (8) (1994) 2281–2287.
[5] W. Jiang, Z. Q. Wang, G. McClure, G. Wang, J. Geng, Accurate modeling of joint effects in lattice transmission towers, Journal of Engineering Structures 33 (2011) 1817–1827.
[6] W.Q. Jiang, Y.P. Liu, Chan SL, Z.Q. Wang, Direct analysis of an ultrahigh-voltage lattice transmission tower considering joint effects. Journal of Structural Engineering (2017) 143(5): 04017009. https://doi.org/10.1061/(ASCE)ST.1943-541X.0001736.
[7] W. Kang, F. Albermani, S. Kitipornchai, H.F. Lam, Modeling and analysis of lattice towers with more accurate models, Advanced Steel Construction. 3 (2007) 565–582.
[8] G. M. S. Knight, A. R. Santhakumar, Joint effects on behaviour of transmission towers, Journal of structural engineering 119 (3) (1993) 698–712.
[9] L. An, J. Wu, W. Jiang, Experimental and numerical study of the axial stiffness of bolted joints in steel lattice transmission tower legs. Engineering Structures (2019) 187: 490-503. https://doi.org/10.1016/j.engstruct.2019.02.070
[10] N. Ungkurapinan, S. S. Chandrakeerthy, R. Rajapakse, S. Yue, Joint slip in steel electric transmission towers, Journal of Engineering Structures 25 (2003) 779–788.
[11] A.H. Abdelrahman, Y.P. Liu, S.L. Chan, Advanced joint slip model for single-angle bolted connections considering various effects. Advances in Structural Engineering (2020) 23(10): 2121-2135. https://doi.org/10.1177/1369433220906226.
[12] H. Gan, H.Z. Deng, C. Li, Simplified joint-slippage model of bolted joint in lattice transmission tower. Structures (2021) 32: 1192-1206. https://doi.org/10.1016/j.istruc.2021.03.022
[13] Q. Cai, R. G. Driver, End tear-out failures of bolted tension members, Tech. Rep. Structural Engineering Report 278, University of Alberta (2008).
[14] Code_Aster Open Source - general FEA software, www.code-aster.org
[15] C. O. Rex, W. S. Easterling, Behavior and modeling of a single plate bearing on a single bolt, Tech. Rep. Rep. CE/VPI-ST 96/14, Virginia Polytechnic Institute and State Univ., Blacksburg, Va. (1996).
[16] G. L. Kulak, et al., Guide to Design Criteria for Bolted and Riveted Joints, AISC, 2001.
[17] SAE Fastener Standards Manual, SAE International - ISBN: 978-0-7680-2170-7, 2009.
[18] C. O. Rex, W. S. Easterling, Behavior and modeling of a bolt bearing on a single plate, Journal of Structural Engineering 129 (6) (2003) 792–800.
[19] ASTM A370-02, Standard Test Methods and Definitions for Mechanical Testing of Steel Products, ASTM International, West Conshohocken, PA, 2001

Advanced Steel Construction – Vol. 18 No. 1 (2022) 488–494
DOI:10.18057/IJASC.2022.18.1.7

TENSILE BEHAVIOUR OF TMCP Q690D HIGH-STRENGTH STRUCTURAL STEEL AT STRAIN RATES FROM 0.00025 TO 760 S^{-1}

Jing-Si Huo [1, *], Xiang Zeng [2] and Hai-Tao Wang [3]

[1] *College of Civil Engineering, Huaqiao University, Xiamen, 361021, China*
[2] *College of Civil Engineering and Architecture, Hainan University, Haikou, 570228, China*
[3] *College of Civil Engineering, Hunan University, Changsha, 410082, China*
** (Corresponding author: E-mail: jingsihuo@gmail.com)*

ABSTRACT

The application of Q690D high-strength structural steel (HSSS) has been increasing in engineering structures. The lack of knowledge of the strain rate behaviour limits the application to the extreme loading conditions such as blast and impact loadings. This paper presents a series of tensile tests on the dynamic tensile behaviour of Q690D HSSS produced through the thermo-mechanical control process (TMCP). The stress-strain relationships of TMCP Q690D in the strain rate range of 0.00025 to 760 s^{-1} were measured by using the universal and servo-hydraulic high speed testing machines. The experimental results verified the sensitivity to strain rate of TMCP Q690D and the dynamic increase factor (DIF) for yield stress is identical to that of QT (Quenched and Tempered) S690 HSSS. However, TMCP Q690D behaves in a much different way in the strain hardening stage. The commonly-used Cowper-Symonds model was calibrated for the DIFs of yield stress and ultimate tensile strength. The Johnson-Cook (J-C) model was modified and a new rate-dependent constitutive model was proposed. The proposed model was validated successfully to predict the true stress-strain relationship, providing better prediction results than the modified J-C model.

ARTICLE HISTORY

Received: 16 October 2020
Revised: 1 June 2021
Accepted: 5 June 2021

KEYWORDS

TMCP Q690D steel;
Strain rate effect;
Dynamic tensile test;
Dynamic increase factor;
Rate-dependent constitutive model

1. Introduction

The mechanical behaviour of steel had been proved to be sensitive to strain rate [1-2], which mainly manifests with the increase of the yield and ultimate tensile strengths and the variation of strain hardening with the strain rate. Structural steel is a typical rate-dependent material and the strain-rate effect significantly influences the dynamic behaviour of steel structures under impact and explosion [3-4], even the strong earthquake action [5]. Thus, the rate-dependent behaviour is vital to evaluate the performance of steel and steel-concrete composite structures subjected to the accidental loads.

The utilisation of high-strength structural steel (HSSS) in engineering structures has been increasing due to its many advantages [6]. The 690 MPa grade HSSS, which has been developed in different countries [7-10], has been used in buildings, bridges, and towers [11-12] as well as offshore structures [13-14]. To promote the application of 690 MPa grade HSSS to the engineering structures subjected to dynamic loading conditions, it is of significance to investigate the strain rate-dependent behaviour.

The strain rate-dependent behaviours of structural steel of different grades with the yield strength ranging from 321 to 906 MPa have been investigated [15-23]. The existing references show that structural steel is sensitive to strain rate and its yield stress is more sensitive to strain rate than the ultimate tensile strength. The post-yielding behaviour is significantly different from that at a static loading condition. For the strain rate-dependent mechanical behaviour of 690 MPa grade HSSS, the efforts have been made to investigate quenched and tempered (QT) HSSS S690 in the past three years [15-17]. Alabi et al. [15] pointed out that more test data is imperative to validate the reliable strain rate effect on the QT S690QL and S960QL HSSS at strain rates from 4 to 100 s^{-1}. Yang et al. [16-17] examined the tensile behaviour of QT S690 at the wider strain rates from 0.00025 to 4109 s^{-1} and provided the model of dynamic increase factor (DIF) for yield stress and constitutive model.

Although the yield stress has a certain degree of influence on the strain rate effect, there is still under discussion on the relationship between yield stress and strain-rate behaviour [17]. Furthermore, Alabi et al. [15] concluded that the sensitivity to strain rate is affected by the chemical compositions, production routes, and microstructure. Especially, the thermo-mechanical control process (TMCP) and QT process are the two important ways to improve the strength of steel from the point of metallurgy. For TMCP steel, the high strength and comprehensive properties result from the mechanism of grain refinement, precipitation strengthening, or phase-transformation strengthening. The strengthening mechanism is realized by combining controlled rolling and controlled cooling methods. For QT steel, the high strength stems from the tempered martensite microstructure which forms after reheating, quenching, and further tempering heat treatment of hot-rolled steel. The tempering process for QT steel aims to improve the toughness of martensite (being high strength and brittle) produced in the quenching process and to balance the strength and toughness of steel. Even though QT and TMCP steels have the similar chemical compositions, there are differences in grain size and microstructure between them, and therefore, QT and TMCP steels behave in different mechanical properties [24]. The strain rate-dependent behaviour of 690-MPa QT steel (S690) has been investigated, but the strain rate-dependent behaviour of 690-MPa TMCP steel still needs to be clarified.

The present paper aims to study the mechanical behaviour of TCMP Q690D HSSS at different strain rates. A series of tensile tests were conducted to obtain the stress-strain curves within the strain rate range from 0.00025 to 760 s^{-1}. A comparison of the strain-rate behaviour between TCMP Q690D and QT S690 reported in previous studies was performed. According to the measured results, the models for the DIFs for yield and tensile strengths as well as the rate-dependent constitutive model of TCMP Q690D are discussed and proposed.

2. Experimental programme

2.1. Specimens preparation

TMCP Q690D HSSS was used in the tests. Table 1 summarizes the chemical composition and carbon equivalent value (CEV), which meet the requirements of Standard GB/T 1591-2008 [7].

The geometry of all specimens was determined according to the Standard ISO 26203-2:2011 [25]. The thickness of the specimen is 3 mm and the width over the parallel length is 6 mm. As shown in Fig. 1, the parallel length and gauge length are 15 mm and 12 mm, respectively.

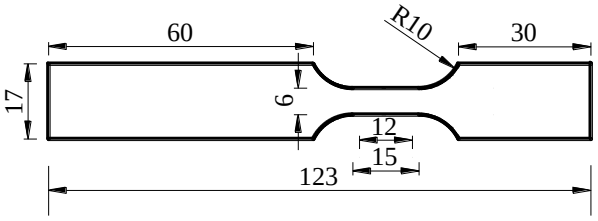

Fig. 1 Specimen geometry (unit: mm)

2.2. Test setup and instrumentation

Different test methods were used for the tension tests. A universal electromechanical machine walter+bai ag (LFM- TOP 50 kN) was used to produce the strain rates of 0.00025 and 0.002 s^{-1}. The tension tests with a wide

range of strain rates (from 0.1 to 760 s^{-1}) were conducted by means of a servo-hydraulic high-speed testing machine (Fig. 2) which has been used by other researchers [17, 20, 21, 26, 27]. The tested results at the strain rate of 0.00025 s^{-1} can be taken as the quasi-static properties [28-29].

As shown in Fig. 2, the dynamic tension was activated by the movement of the upper accelerated grip, which was fixed to the hydraulic actuator. A piezoelectric force cell was installed inside of the fixed grip to measure the dynamic tensile force when the strain rate is lower than 100 s^{-1}. Due to the limitation of the frequency response of the piezoelectric force cell, two strain gauges were mounted onto the lower end of the specimen to determine the tension force at strain rates above 100 s^{-1}. Meanwhile, the measurement of the strain in the gauge length was realized through the 3D non-contact deformation measurement system [26] which is equipped with a high speed video camera, image acquisition software, and digital image correlation software.

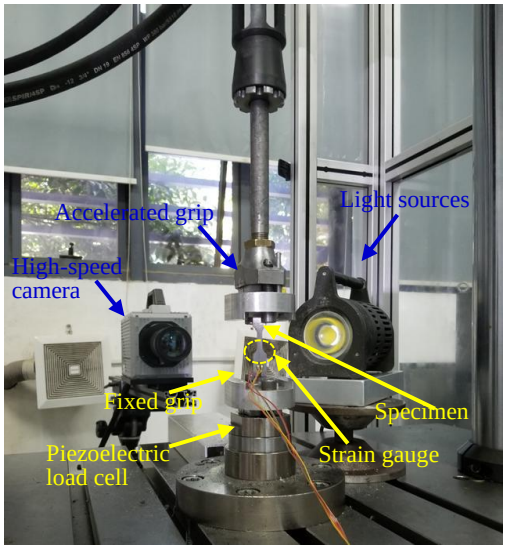

Fig. 2 Setup of high-speed tensile test

3. Results and discussion

3.1. Engineering stress-strain curves at various strain rates

Fig. 3 shows the engineering stress-strain curves at strain rates ranging from 0.00025 to 763 s^{-1}. The measured curves of repeated specimens at different strain rates have good consistency and repeatability, which demonstrates the reliability of the test data. The curves with oscillation were processed, and the processed curves keep in consistency with the original ones. The average curve of the three repeated stress-strain curves at each strain rate was taken as the representative curve (indicated by the green line in Fig. 3), which was used for the following analysis.

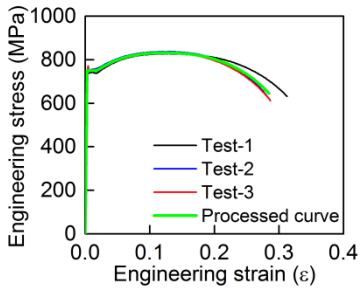

(a) 0.00025 s^{-1} (Quasi-static)

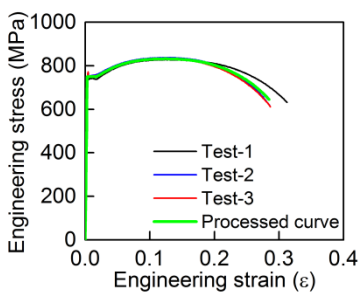

(b) 0.002 s^{-1}

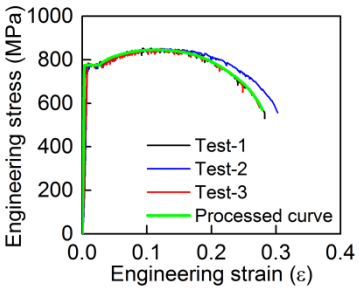

(c) 0.08 s^{-1}

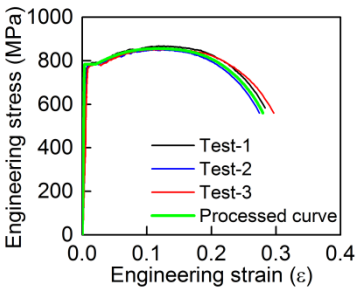

(d) 0.99 s^{-1}

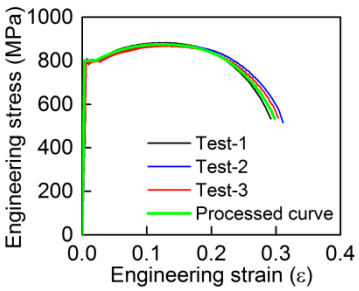

(e) 7.9 s^{-1}

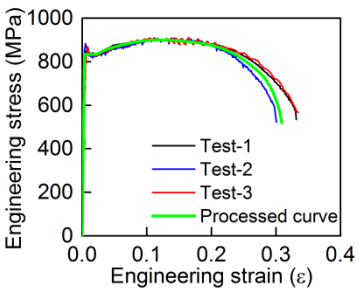

(f) 75.6 s^{-1}

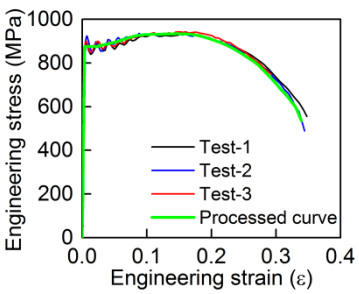

(g) 466 s^{-1}

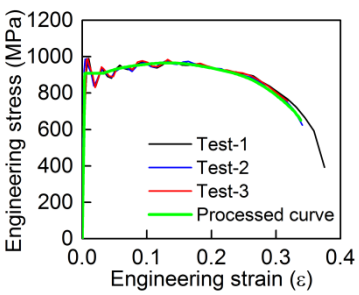

(h) 763 s^{-1}

Fig. 3 Raw and processed engineering stress-strain curves of TMCP Q690D

Fig. 4 compares the stress-strain curves of TMCP Q690D at different strain rates. It can be observed that the increase in strain rate results in the increased yield and tensile strengths. The yield plateau can be seen in all curves (Fig. 3 and Fig. 4) and its length increases with the strain rate. The phenomenon is similar to that of QT S690 at different strain rates [16-17].

The yield strength (f_y), ultimate tensile strength (f_u), and uniform elongation (ε_u) of TMCP Q690D steel at various strain rates are summarized in Table 2. The dynamic increase factors for the three mechanical indexes, abbreviated as DIF_y, DIF_u, and $DIF_{\varepsilon u}$ respectively, are also given in Table 2. Conventionally, the DIF for a mechanical index is expressed as the ratio of its dynamic value to its quasi-static value. The table shows that the raising of strain rate leads to the increased yield and tensile strengths. When the strain rate increases from 0.00025 to 763 s^{-1}, yield strength and tensile strength increase obviously, from 724 to 908 MPa (increased by 25.4%) and from 812 to 968 MPa (increased by 19.2%), respectively. The sensitivity to strain rate of the yield strength is more significant than that of the tensile strength. However, the uniform elongation does not change in a monotonic manner with the strain rate increasing, which is similar to Q420 steel [21]. The uniform elongation is between 11% and 15% and the corresponding $DIF_{\varepsilon u}$ is between 0.904 and 1.173 at different strain rates.

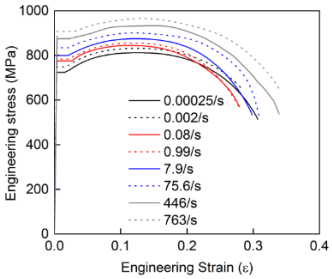

Fig. 4 Stress-strain curves of TMCP Q690D at various strain rates

Table 1
Chemical composition and CEV of TMCP Q690D (in weight %)

Element	C	Si	Mn	P	S	Nb	V	Ti	Cr	Cu	Mo	Ni	B	CEV
%	0.07	0.09	1.5	0.013	0.003	0.046	0.003	0.099	0.02	0.013	0.01	0.02	0.0001	0.329

Table 2
Mechanical properties of TMCP Q690D steel at various strain rates

Strain rate (s^{-1})	Yield stress (MPa)	Ultimate tensile strength (MPa)	Uniform elongation ε_u	DIF_y	DIF_u	$DIF_{\varepsilon u}$
0.00025	724	812	0.1255	1.000	1.000	1.000
0.002	749	831	0.12561	1.035	1.023	1.001
0.08	775	845	0.11345	1.070	1.041	0.904
0.99	784	855	0.11796	1.083	1.053	0.940
7.9	799	875	0.12362	1.104	1.078	0.985
75.6	834	903	0.12084	1.152	1.112	0.963
446	875	933	0.14719	1.209	1.149	1.173
763	908	968	0.13249	1.254	1.192	1.056

3.2. Models for DIF_y and DIF_u

In order to clarify the difference of DIF_y and DIF_u between TMCP Q690D and QT S690 steel, Fig.5 illustrates a comparison of the test results from the present experiment and References [16-17]. In addition, the quasi-static strain rate is set as 0.00025 s^{-1}. Fig. 5 depicts that the DIF_y versus strain rate curves of TMCP Q690D are identical to those of QT S690, and the DIF_u of QT S690 steel is also identical to the corresponding DIF_y at the same strain rate. The DIF_u of TMCP Q690D is fairly lower than that of QT S690.

C-S model proposed by Cowper and Symonds in 1957 [30] had been widely used to predict the DIF of the strength of steel and is expressed as

$$DIF_y = 1 + \left(\frac{\dot{\varepsilon}}{D}\right)^{\frac{1}{q}} \quad (1)$$

where $\dot{\varepsilon}$ stands for the strain rate, D and q are material constants which can be calibrated by the test data. Yang et al. [16-17] calibrated the parameters

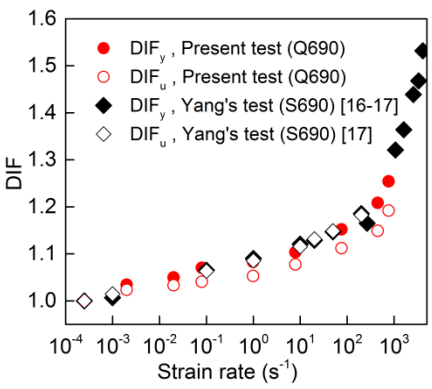

Fig. 5 Comparison of DIF_y and DIF_u between TMCP Q690D and QT S690

of the C-S model for the DIF_y and DIF_u of QT S690 at different strain rate ranges (seen in Table 3). The model is adopted for the comparison with the test results of TMCP Q690D, as shown in Fig. 6 and Fig. 7. Fig. 6 shows that the C-S model [17], which is calibrated based on the measured results of QT S690 when $\dot{\varepsilon} \leq 200$ s^{-1}, underestimates the DIF_y seriously at larger strain rates. The calibrated C-S model [16] based on the test results of QT S690 at $\dot{\varepsilon}$ from 266 to 4109 s^{-1} underestimates the DIF_y at lower strain rates. Thus, the existing C-S model for DIF_y of QT S690 can not exactly describe the DIF_y in the entire strain rate range. Combining the DIF_y test data of TMCP Q690D with that of QT S690, an attempt to calibrate the C-S model is made to predict the DIF_y exactly over the entire test strain rate range. But it is found that the C-S model is not suitable in the entire strain rate range. In Fig. 6, it is observed that there exists a distinct turning point in the DIF_y versus strain rate curves. Therefore, a modified C-S model based on a piecewise function is proposed for the DIF_y. Through fitting the DIF_y test data of TMCP Q690D and QT S690, the parameters of C-S model for them are obtained, as shown in Table 4. When $\dot{\varepsilon} \leq 264$ s^{-1}, $D = 1.141 \times 10^8$ s^{-1} and q=7.57. And when $\dot{\varepsilon} > 264$, D=22946 s^{-1} and q=2.6. The comparison between the modified C-S model and test results shown in Fig. 6 demonstrates that the modified model provides an excellent prediction accuracy for their DIF_y.

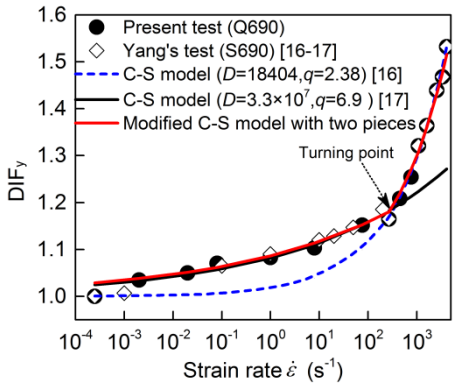

Fig. 6 Predicted DIF_y at strain rates from 0.00025 to 4109 s^{-1} in comparison with test results

Fig. 7 presents the comparison of DIF_u between the existing models and experimental results. The Malvar model was presented according to the experimental results of steel reinforcing bars with yield stresses between 290 and 710 MPa and with strain rates between 10^{-4} and 10 s^{-1} [1]. As shown in Fig. 7, the margin of error is not acceptable for the predicted DIF_u based on the malvar model with a linear formula. The C-S model of DIF_u for QT S690 (Table 3) [17] overestimates the DIF_u of TMCP Q690D. Therefore, the parameters in C-S model of DIF_u for TMCP Q690D are recalibrated with D=5.9×10^7 and q=6.33 (summarized in Table 4). Fig. 7 shows that the recalibrated C-S model provides good predicted results of DIF_u of TMPC Q690D.

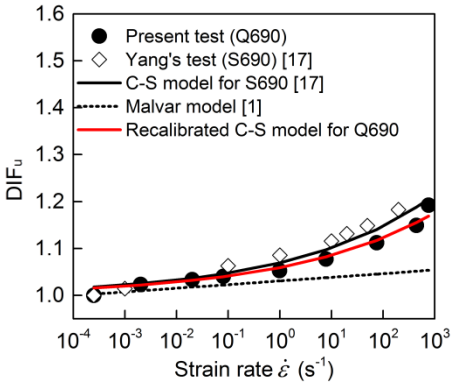

Fig. 7 Comparison of DIF_u from models and test results

Table 3
C-S models for DIF_y and DIF_u of QT S690

Test	Strain rate (s^{-1})	Parameters for DIF_y		Parameters for DIF_u	
		D (s^{-1})	q	D (s^{-1})	q
SHPB Test [16]	0.00025, 266 to 4109	18404	2.38	-	-
Tension test [17]	0.001 to 200	3.3×10^7	6.9	1.2×10^7	6.1

Table 4
Calibrated parameters of C-S model for TMCP Q690D

Strain rate (s^{-1})	Parameters for DIF_y		Parameters for DIF_u	
	D (s^{-1})	q	D (s^{-1})	q
≤264	1.141×10^8	7.57	5.9×10^7	6.33
>264	22946	2.6		

3.3. Rate-dependent constitutive laws for TMCP Q690D steel

When steel or composite structures subjected to high dynamic loads are evaluated using an explicit nonlinear dynamic finite element procedure, the true rate-dependent mechanical properties of steel are required. In order to simulate the true mechanical properties, a rate-dependent constitutive model is usually developed based on the measured stress-strain curves.

3.3.1. J-C model

J-C model proposed by Johnson and Cook in 1983 [31] is widely applied to simulate the true stress-strain constitutive behaviour of steel in the nonlinear finite element simulations of dynamic cases. The flow stress (σ) can be expressed as

$$\sigma = \left[A + B(\varepsilon_p)^n\right]\left[1 + C\ln(\frac{\dot{\varepsilon}}{\dot{\varepsilon}_0})\right](1 - T^{*m}) \quad (2)$$

where $\dot{\varepsilon}$ is the strain rate, ε_p is the plastic strain, $\dot{\varepsilon}_0$ is the reference strain rate. Here, $\dot{\varepsilon}_0$ is taken as the quasi-static strain rate 0.00025 s^{-1}. T^* is the homologous temperature. The material constants include A, B, C, n, and m. Eq. 2 contains the strain hardening effect under quasi-static load (denoted by the first bracket), strain-rate, and thermal softening effects on the strain hardening behaviour (described by the second bracket and third bracket, respectively). The thermal softening effect described by the third bracket is for the metal materials under high temperatures. The present test is performed at room temperature and thus the thermal softening effect is not considered in the constitutive model and the value of the third bracket is taken as 1. Then, Eq. 2 can be simplified into Eq. 3,

$$\sigma = \left[A + B(\varepsilon_p)^n\right]\left[1 + C\ln(\frac{\dot{\varepsilon}}{\dot{\varepsilon}_0})\right] \quad (3)$$

Heat is generated in specimens when plastic deformation occurs, and the adiabatic heating effect at a high strain rate will increase the temperature in the specimens, but for simplicity, the temperature effect is generally considered to be contained in the effect of strain rate, namely, the stress-strain curves described by Eq. 3 automatically considers the increase of temperature due to the adiabatic heating effect.

Eq. 3 has been used to describe the constitutive behaviour of QT S690 steel [16-17] and the coefficients A, B, C, and n in the equation were calibrated and modified by fitting the test results. The values of those coefficients in Eq. 3 are listed in Table 5. Furtherly, a modified J-C model (Eq. 4) with $(1 + J\dot{\varepsilon}^K)$ instead of $(1 + C\ln(\dot{\varepsilon}/\dot{\varepsilon}_0))$ for the strain rate effect (denoted by S690-M-J-C model hereafter) [17] was proposed for describing the constitutive behaviour at the strain rates ranging from 0.001 to 4109 s^{-1} (Table 5).

$$\sigma = [A + B(\varepsilon_p)^n](1 + J\dot{\varepsilon}^K) \quad (4)$$

To discover whether the constitutive model of QT S690 steel [17] is able to describe the constitutive behaviour of TMCP Q690D steel, a comparison between the S690-M-J-C model and the test results of TMCP Q690D is performed, as shown in Fig. 8. The figure shows that the true stress-strain curves predicted by the S690-M-J-C model are quite different from the test curves of TMCP Q690D. S690-M-J-C model has been demonstrated to be well consistent with the test curves of QT S690. Therefore, the comparison indicates that TMCP Q690D and QT S690 have different strain hardening behaviour.

The strain rate term of the standard J-C model is linear in the logarithm of the strain rate (Eq.2). The linear strain rate term is not always suitable for describing the effect of strain rate on the true stress-strain curve of any mental, and thus it can be modified into other forms such as the exponential forms in strain rate [16-17, 32] and the quadratic form in the logarithm of the strain rate [33]. To accurately predict the true stress-strain curves of TMCP Q690D, the J-C models should be recalibrated or modified to acquire the appropriate quasi-static strain hardening term and strain rate term. The coefficients A, B, and n in the model can be obtained through fitting the quasi-static true stress-strain curve with the power function $(A + B(\varepsilon_p)^n)$ in Eq. 3.

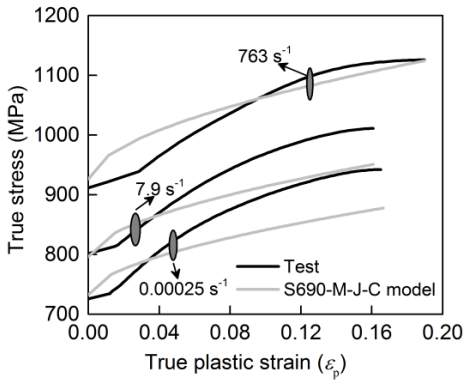

(a)

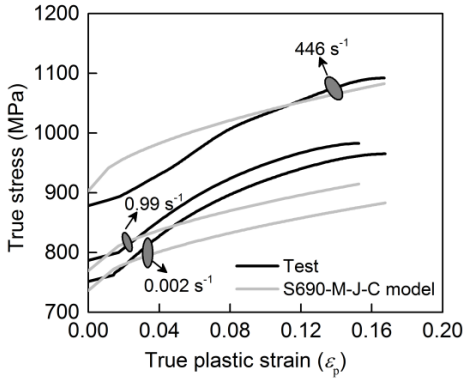

(b)

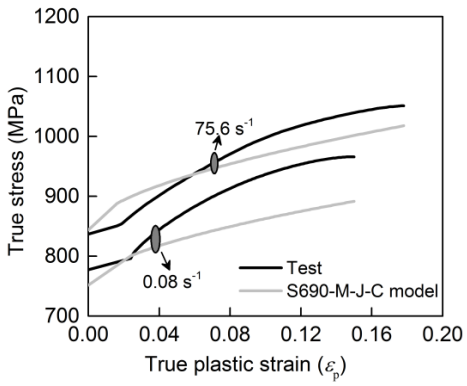

(c)

Fig. 8 Comparison between S690-M-J-C model and test results of TMCP Q690D

Table 5
J-C model for true stress-strain curve of QT S690

J-C Model	Strain rate /s^{-1}	*A* (MPa)	*B* (Mpa)	*n*	*C*	*J*	*K*
Eq. (3)	0.00025, 266 to 4109[16]	722	400	0.57	$0.0041\dot{\varepsilon}^{0.217}$	-	-
	0.001 to 200 [17]	727	400	0.57	0.012	-	-
Eq. (4)	0.001 to 4109 [17]	727	400	0.57	-	0.06	0.23

Fig. 9 illustrates the ratio of true stress-strain curves at different strain rates to the curve at quasi-static strain rate in the whole strain range. In other words, it presents the strain rate term of the J-C model for TMCP Q690D at different strain, which is denoted by $\mathrm{DIF}(\dot{\varepsilon},\varepsilon_p)$ in Fig. 9. The $\mathrm{DIF}(\dot{\varepsilon},\varepsilon_p)$ of the curves are different at different strain, especially for those at high strain rates. Therefore, an average of $\mathrm{DIF}(\dot{\varepsilon},\varepsilon_p)$ ($\mathrm{DIF_{ave}}$) for each strain rate is used to alleviate the difference of $\mathrm{DIF}(\dot{\varepsilon},\varepsilon_p)$ in the entire strain range. The $\mathrm{DIF_{ave}}$ is shown in Fig. 9 and can be fitted with an exponential form in $\dot{\varepsilon}$ $(1+0.0564\dot{\varepsilon}^{0.1803})$, as shown in Fig. 10. Hence, the modified J-C model for TMCP Q690D is described as Eq. 4 with J=0.0564 and K=0.1803. Table 6 summarizes all the coefficients in the modified J-C model for TMCP Q690D. A comparison between the modified J-C model and test results is made in Fig. 11. The figure shows the modified J-C model provides better-predicted results than the S690-M-J-C model shown in Fig. 8.

Table 6
Modified J-C model for TMCP Q690D

Modified J-C Model	*A* (MPa)	*B* (MPa)	*n*	*J*	*K*
Eq. (4)	f_y	873	0.7272	0.0564	0.1803

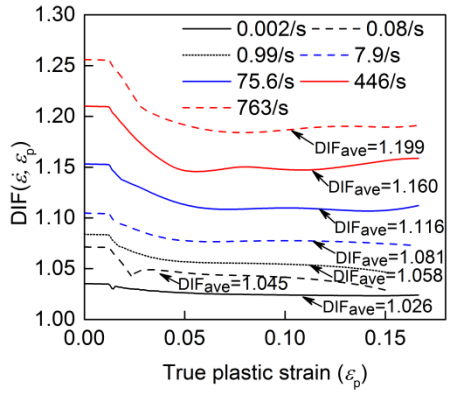

Fig. 9 $\mathrm{DIF_{ave}}$ at various strain rates

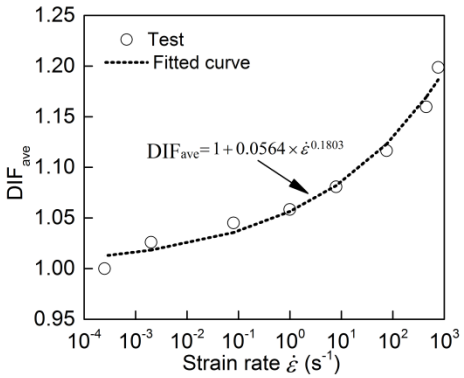

Fig. 10 Fitting $\mathrm{DIF_{ave}}$

3.3.2. Proposed constitutive model

A new constitutive model is necessary to forecast the true stress-strain curve of TMCP Q690D at different strain rates more precisely. From Fig. 4 and Fig. 11, it can be observed that the stress-strain curves at different strain rates are approximately parallel, namely, the strain hardening rate of the curves is approximately consistent in the entire plastic strain range. Hence, the true stress-strain curve can be expressed as Eq. (5) [34].

$$\sigma = \sigma_0(\dot{\varepsilon}) + \alpha(\varepsilon_p) = \sigma_s M(\dot{\varepsilon}) + \alpha(\varepsilon_p) \tag{5}$$

where $\alpha(\varepsilon_p)$ represents the consistent strain hardening curve at different strain rates and $\sigma_0(\dot{\varepsilon})$ means the stress at the initiation of the curve at a strain rate $\dot{\varepsilon}$. The $\alpha(\varepsilon_p)$ can be obtained by subtracting the quasi-static yield stress from the quasi-static curve. Fig. 12 illustrates Eq. (5), namely, the true stress-strain curve at the strain rate $\dot{\varepsilon}$ can be obtained by translating the $\alpha(\varepsilon_p)$ with a distance of $\sigma_0(\dot{\varepsilon})$ upwards. Furtherly, the $\sigma_0(\dot{\varepsilon})$ can be expressed by the product of σ_s and $M(\dot{\varepsilon})$, where the σ_s means the quasi-static yield stress and the $M(\dot{\varepsilon})$ represents the strain rate effect.

The $\alpha(\varepsilon_p)$ can be expressed by Eq. (6) with El-Magd quasi-static flow model [35] for reference.

$$\alpha(\varepsilon_p) = A_1\varepsilon_p + B_1(1 - exp(-\beta\varepsilon_p)) \tag{6}$$

where A_1, B_1, and β are material constants. A_1, B_1, and β are acquired by fitting the quasi-static test results, which are listed in Table 7. Fig. 11(a) shows that Eq. 6 is more suitable for the quasi-static strain hardening curve of TMCP Q690D than is the exponential expression ($A+B(\varepsilon_p)^n$) in the J-C model.

Table 7
Coefficients in Eq. (6)

Parameters	A_1 (MPa)	B_1 (MPa)	β
Value	-8741	9707	1.139

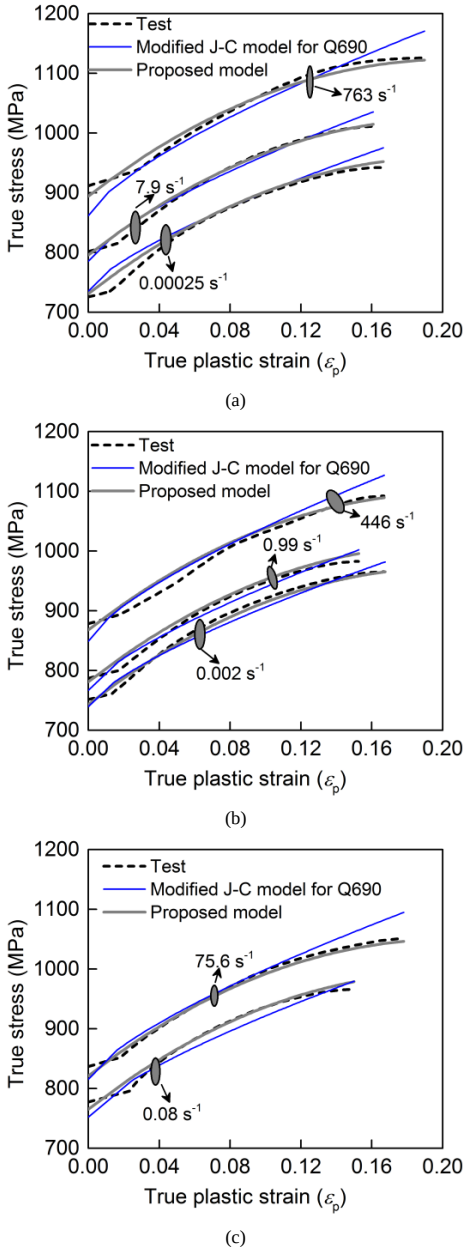

Fig. 11 Comparison between Modified J-C model, proposed model, and test results of TMCP Q690D

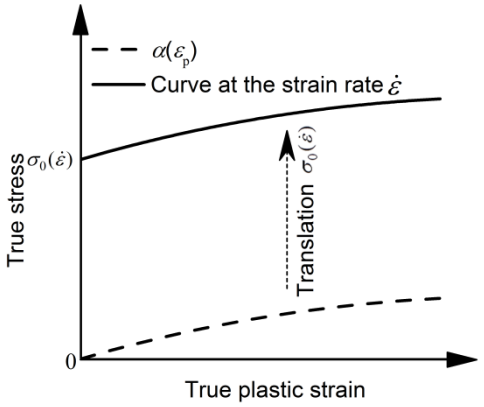

Fig. 12 Relationship between the true stress-strain curve and $\alpha(\varepsilon_p)$

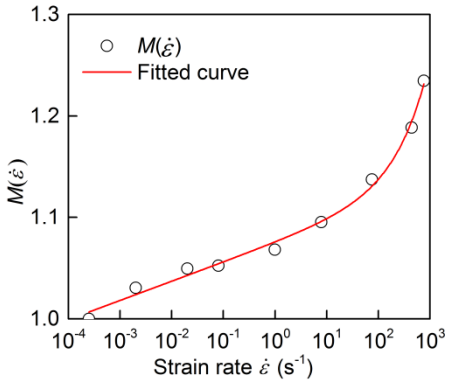

Fig. 14 Fitting $M(\dot{\varepsilon})$

Fig. 13 depicts the true stress difference ($\Delta\sigma(\dot{\varepsilon},\varepsilon_p)$) between dynamic and quasi-static curves at the same plastic strain. It is observed from Fig. 13 that the $\Delta\sigma(\dot{\varepsilon},\varepsilon_p)$ is not a constant for every dynamic curve, which indicates that the true stress-strain curves are not strictly parallel. So, an average of $\Delta\sigma(\dot{\varepsilon},\varepsilon_p)$ ($\Delta\sigma_{ave}(\dot{\varepsilon})$) is used, which is suitable to represent the $\Delta\sigma(\dot{\varepsilon},\varepsilon_p)$ in the entire plastic strain range. The $\Delta\sigma_{ave}(\dot{\varepsilon})$ is calculated and given in Fig. 13. Then, $\sigma_0(\dot{\varepsilon})$ in Eq. 5 can be express as ($\sigma_s+\Delta\sigma_{ave}(\dot{\varepsilon})$) and $M(\dot{\varepsilon})$ is expressed as

$$M(\dot{\varepsilon})=\frac{\sigma_0(\dot{\varepsilon})}{\sigma_s}=1+\frac{\Delta\sigma_{ave}(\dot{\varepsilon})}{\sigma_s} \tag{7}$$

Introducing the σ_s from test and $\Delta\sigma_{ave}(\dot{\varepsilon})$ shown in Fig. 13 into the Eq. (7), and the value of $M(\dot{\varepsilon})$ can be computed, which is depicted in Fig. 14. Through fitting $M(\dot{\varepsilon})$ with the data in Fig. 14, an expression for $M(\dot{\varepsilon})$ is obtained as Eq. 8.

$$M(\dot{\varepsilon})=1.007+(\dot{\varepsilon}/20106)^{1/1.4336}+0.00821\ln(\dot{\varepsilon}/\dot{\varepsilon}_0) \tag{8}$$

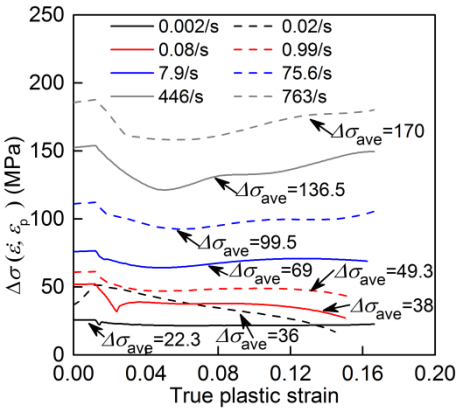

Fig. 13 Difference of true stress ($\Delta\sigma(\dot{\varepsilon},\varepsilon_p)$) between dynamic and quasi-static curves

Fig. 11 shows a comparison among the proposed model (Eqs. 5-8), modified J-C model, and the test results. The comparison demonstrates that the proposed model predicts the true stress-strain curves with good accuracy within the range of strain rates from 0.00025 to 760 $s^{-1}$and it is much better for TMCP Q690D than the modified J-C model.

4. Conclusions

In this paper, the dynamic behaviour of TMCP Q690D steel at different strain rates (from 0.00025 to 760 s^{-1}) has been tested and stress-strain curves were measured. Based on the experimental and analytical results, the conclusions can be obtained as follows:

(1) The strain-rate sensitivity of yield stress of TMCP Q690D steel is exactly similar to that of QT S690 steel. The strain-rate sensitivity of tensile strength of TMCP Q690D steel is fairly lower than that of QT S690 steel. The strain hardening response of TMCP Q690D steel at different strain rates are very different from those of QT S690 steel, which behaves in the way that the strain hardening rate of TMCP Q690D steel is higher than that of QT S690 steel.

(2) Based on the test data of TMCP Q690D and QT S690, the material constants in the C-S model for two different strain rate ranges (≤264 s^{-1} and >264 s^{-1}) are exactly calibrated to predict the DIF_y. Moreover, the C-S model employed to represent the DIF for tensile strength of TMCP Q690D is calibrated.

(3) The existing J-C model for QT S690 is not suitable to simulate the true stress-strain relationship of TMCP Q690D. The modified J-C model based on the test results of TMCP Q690D provides a better prediction than the J-C model for QT S690 does.

(4) A newly proposed constitutive model can predict the true stress-strain curves of TMCP Q690D with higher accuracy than the modified J-C model.

Acknowledgments

The authors gratefully acknowledge the support provided by the National Natural Science Foundation of China (51678256, 51438010, and 51608156).

References

[1] Malvar L.J., “Review of static and dynamic properties of steel reinforcing bars”, ACI Materials Journal, 95, 609-616, 1998.
[2] Ritchie C.B., Packer J.A., Zhao X.L., Heidarpour A. and Chen Y.Y., “Dynamic material performance of cold-formed steel hollow sections: a state-of-the-art review”, Frontiers of Structural and Civil Engineering, 11, 209-227, 2017.
[3] Ribeiro J., Santiago A., Rigueiro C., Barata P. and Veljkovic M., “Numerical assessment of T-stub component subjected to impact loading”, Engineering Structures, 106,450-460, 2016.
[4] Liew J.Y.R., “Survivability of steel frame structures subject to blast and fire”, Journal of Constructional Steel Research, 64, 854-866, 2008.
[5] Lamarche C.P. and Tremblay R., “Seismically induced cyclic buckling of steel columns including residual-stress and strain-rate effects”, Journal of Constructional Steel Research, 67, 1401-1410, 2011.
[6] Li G.Q., Wang Y.B. and Chen S.W., “The art of application of high-strength steel structures for buildings in seismic zones”, Advanced Steel Construction, 11, 492-506, 2015.
[7] GB/T 1591-2008, High strength low alloy structural steels, Standards Press of China, Being, 2009. (in Chinese).
[8] GB/T 16270-2009, High strength structural steel plates in the quenched and tempered condition, Standards Press of China, Being, 2010. (in Chinese).
[9] BS EN 10025–6: 2004, Hot rolled products of structural steels - Part 6: Technical delivery conditions for flat products of high yield strength structural steels in the quenched and tempered condition, British Standards, 2004.
[10] ASTM A514/A514M-00a, Standard specification for high-yield-strength, quenched and tempered alloy steel plate, suitable for welding, American Society for Testing and Materials, West Conshohocken, PA, 2000.
[11] Shi G., Hu F.X. and Shi Y.J., “Recent research advances of high strength steel structures and codification of design specification in china”, International Journal of Steel Structures, 14, 873-887, 2014.
[12] Schröter F. and Lehnert T., “Trends in the application of high-performance steel in european bridge building”, In: Petzek E., Bancila R. (eds), The Eight International Conference "Bridges in Danube Basin", Springer Vieweg, Wiesbaden, 2014.
[13] Chiew S.P., Zhao M.S. and Lee C.K., “Mechanical properties of heat-treated high strength steel under fire/post-fire conditions”, Journal of Constructional Steel Research, 98, 12-19, 2014.
[14] Wang Y., MacDonald A., Xu L., Wright M. and Shenoi R.A., “Engineering critical assessment and variable sensitivity analysis for as-welded S690 steels”, Engineering Failure Analysis, 109, 104282, 2020.
[15] Alabi A.A., Moore P.L., Wrobel L.C. and He W., “Tensile behaviour of S690QL and S960QL under high strain rate”, Journal of Constructional Steel Research,150, 570-580, 2018.
[16] Yang X., Yang H. and Zhang S., “Rate-dependent constitutive models of S690 high-strength structural steel”, Construction and Building Materials, 198, 597-607, 2019.

[17] Yang X., Yang H., Lai Z. and Zhang S., "Dynamic tensile behavior of S690 high-strength structural steel at intermediate strain rates", Journal of Constructional Steel Research, 168, 105961, 2020.
[18] Chen J., Shu W. and Li J., "Experimental study on dynamic mechanical property of Q235 steel at different strain rates", Journal of Tongji University (Natural Science) 44, 1071-1075, 2016. (In Chinese).
[19] Singh N.K., Cadoni E., Singha M.K. and Gupta N.K., "Dynamic tensile and compressive behaviors of mild steel at wide range of strain rates", Journal of Engineering Mechanics, 139, 1197-1206, 2013.
[20] Chen J., Shu W.and Li J., "Constitutive model of Q345 steel at different intermediate strain rates", International Journal of Steel Structures, 17, 127-137, 2017.
[21] Chen J., Li J. and Li Z., "Experiment research on rate-dependent constitutive model of Q420 steel", Construction and Building Materials, 153, 816-823, 2017.
[22] Forni D., Chiaia B. and Cadoni E., "Strain rate behavior in tension of S355 steel: base for progressive collapse analysis", Engineering Structures, 119, 164-173, 2016.
[23] Yang H., Yang X. and Varma A.H., "Strain-Rate effect and constitutive models for Q550 high-strength structural steel", Journal of Materials Engineering and Performance, 28, 6626-6637, 2019.
[24] Xiong M. X., and Liew J.Y.R., "Experimental study to differentiate mechanical behaviours of TMCP and QT high strength steel at elevated temperatures", Construction and Building Materials, 242:118105, 2020.
[25] ISO 26203-2: 2011, Metallic materials - Tensile testing at high strain rates - Part 2: Servo-hydraulic and other test systems, International Organization for Standardization (ISO/TC 164/SC 1), Switzerland, 2011.
[26] Zeng X., Huo J.S., Wang H.T., Wang Z. and Elchalakani M., "Dynamic tensile behavior of steel HRB500E reinforcing bar at low, medium, and high strain rates", Materials. 13, 185, 2020.
[27] Zeng X., Wang Z. and Huo J.S., "Tensile behavior of 400 MPa-grade anti-earthquake hot-rolled ribbed bar (HRB400E) over a wide strain rate range", Construction and Building Materials, 249 (2020) 118729.
[28] ASTM E8/E8M-16a, Standard Test Methods for Tension Testing of Metallic Materials, ASTM International, West Conshohocken, PA , 2016.
[29] ISO 6892-1: 2016, Metallic materials - Tensile testing - Part 1: Method of test at room temperature, International Organization for Standardization (ISO/TC 164/SC 1), Switzerland, 2016.
[30] Cowper G. and Symonds P.S., Strain hardening and strain rate effects in the impact loading of the cantilever beams - Technical Report 28, Providence, RI: Brown University, Division of Applied Mathematics, 1957.
[31] Johnson G.R. and Cook W.H., "A constitutive model and data for metals subjected to large strains, high strain rates and high temperatures", Proceedings of the 7th International Symposium on Ballistics, 1983.
[32] Allen D.J., Rule W.K. and Jones S.E., "Optimizing material strength constants numerically extracted from taylor impact data", Experimental Mechanics, 37, 333-338, 1997.
[33] Huh H. and Kang W.J., "Crash-worthiness assessment of thin-walled structures with the high-strength steel sheet", International Journal of Vehicle Design, 30, 1-21, 2002.
[34] Paul S.K., "Predicting the flow behavior of metals under different strain rate and temperature through phenomenological modeling", Computational Materials Science, 65, 91-99, 2012.
[35] Totten G.E., Xie L. and Futanani K., Modeling and simulation for material selection and mechanical design, Marcel Dekker, NewYork, 2004.

Advanced Steel Construction – Vol. 18 No. 1 (2022) 495–505
DOI:10.18057/IJASC.2022.18.1.8

NUMERICAL STUDY OF TWO NOVEL CONNECTIONS WITH SHORT END I OR H STUB IN STEEL STRUCTURES

Mehrdad Taheripour [1], Farzad Hatami [1, 2, *] and Reza Raoufi [1]

[1] *Department of Civil Engineering, Ahvaz Branch, Islamic Azad University, Ahvaz, Iran*
[2] *Department of Structures and Earthquake Research Center, Amirkabir University of Technology, Tehran, Iran*
** (Corresponding author: E-mail: hatami@aut.ac.ir)*

ABSTRACT

In this study, two novel steel connections are introduced by replacements in the conventional end-plate connection with an H-or I-shaped cross-section as a Short Stub Column (SSC). In the first connection, the SSC flange is bolted to the column flange, and the beam is welded to the stub flange. In the second connection, after welding the SSC flange to the column flange and welding the beam to an end-plate, the end-plate is bolted to the SSC flange. The flange and web of the stub are reinforced using horizontal stiffeners to transfer the beam moment. Stiffeners could be employed with various thicknesses and configurations such that the strength and ductility of the joint could be adjusted. In this study, the Finite Element Model (FEM) model of a conventional welded and bolted end-plate connection, subjected to cyclic loading, is primarily calibrated using experimental data from previous studies. After confirming the model's performance, the behavior of the two proposed connections, in comparison with it, has been studied. The hysteresis diagrams have been obtained for each case, followed by extracting the effective parameters and comparing them. The results show that the two Proposed Connections reduce the stress in the panel zone and increase the ductility compared to the previously confirmed end-plates. All the samples in this study satisfy the fundamental requirements for rigid beam-to-column connections, according to AISC.

ARTICLE HISTOR

Received: 17 December 2020
Revised: 16 June 2021
Accepted: 4 July 2021

KEYWORDS

Bolted end-plate connection;
Stub steel connections;
Panel zone;
Hysteresis diagrams;
PEEQ

1. Introduction

The seismic performance of steel frames is determined mainly by the connecting properties of the structures. The results of previous studies have shown that semi-rigid connections have outstanding properties, which make them proper substitutions for fully rigid connections. These properties are necessary for a smaller base shear, a better economy, and a better capability to absorb energy [1]. In addition to resisting shear, bending, and torsional forces to successfully transfer these internal forces from the beam to the column, connections must have sufficient capacity for deformation and provide the required ductility. Therefore, specific regulations have been formulated for connections under static and dynamic loading. Accordingly, extensive studies have been conducted, and several novel connections for connecting I-beams to columns have been proposed since the 1994 Northridge earthquake [2]. However, there is a need for more laws to be regulated for newly proposed connections [3]. Nevertheless, researchers are yet looking for a suitable beam-to-column joint [4]. Yielding is necessary for plastic energy to be absorbed. Brittle fracture of the connection prevents bending connections from exhibiting the non-elastic behavior required for resisting earthquake loads. Triaxial stresses have a substantial effect on ductility reduction and the appearance of brittle behavior. When steel is loaded simultaneously in two or three directions, it could not exhibit its inherent ductility; instead, it experiences brittle fracture without elongation [5]. Tremblay et al. [6,7] investigated steel structure performance during several earthquakes. Fractures caused by weak joints during the cyclic loading process demonstrated that, before the 1994 Northridge earthquake, design criteria did not practically result in the establishment of plastic hinges in the beam. After the Northridge earthquake, the primary goal was to move the plastic hinge inside the beam at a specified location from the column in the conventional connection. In these connections, placing the plastic hinge establishment farther from the column reduces strain concentration in the weld, hence, prevents the distribution of cracks in the weld and brittle fracture in the connection [8]. Various methods have been proposed for transferring the location of the plastic hinge formations. These methods are generally divided into two categories. In the first category, the connections are designed so that components' addition to the connection improves the beam strength. Thus, it transfers the plastic hinge inside the beam and prevents the rotation of the connection components concerning each other (beam concerning column). In the second group, a specific pre-determined region is weakened by reducing the section in areas of the flanges; therefore, the plastic hinge is transferred inside the beam. Various Reduced Beam Section (RBS) connections belong to this group [9].

Moreover, several attempts have been made to transfer the connections at a specific distance from the column using a stub. Behrooz et al. [10] used a short beam stub for steel connection. Shen [11] investigated two types of experimental replaceable connections using the reduced beam cross-section theory. This connection is a combination of end-plate and stub. Moreover, a replaceable link with a smaller cross-sectional area (than the beam) was used to generate the plastic hinge in the link. Li [12] studied a particular type of reverse channel connection in which the UNP webs are welded to box columns, and the UNP flanges are connected to the beams. Yılmaz et al. [13] used a stub in the form of a short beam along the weak axis of the column. Moghadam et al. [1] used two parallel connection plates welded vertically to the column and connect them to the beam using a flash end-plate. Gaoxing et al. [14] presented a replaceable energy dissipation system for connections of beams to concrete columns using a steel stub consisting of a short link and an H-shaped steel section with an open web. Han et al. [15] utilized a stub made of a shear hinge and a couple of buckling-restrained plates to present a beam-to-column connection for controlling seismic damages.

Qiang et al. [16] proposed a semi-rigid joint along the weak axis of the column, where the beam was attached to the web column by a combination of the transverse, vertical stiffeners, and flash end-plate connection, which formed a stub. Jiang et al. [17] proposed a novel connection in which vertical pair through-plates pass within box-column, and these plates bolted to web beam. Zhang et al. [18], using a stub attached to the beam and steel strands, suggested a premade self-centering steel structure with a novel floor system that includes movable minor beams for frame development. Liu et al. [19] proposed connection consists of two identical half-cylindrical parts connected to the column on one side with an end-plate and on the other side with a fin-plate to the beam. By rotating the fin plate relative to the end-plate, the half-cylindrical parts provide axial ductility.

In conventional rigid joints, the bending moment is transmitted from the beam to the column as a combination of compressive and tensile forces. Consequently, the two concentrated forces are applied to the column at the connection location, leading to higher stress in the panel zone. Moreover, an increase in the strength and hardness of the connection reduces its ductility. Additionally, a strong connection results in transferring all of the forces and moments, especially to the panel zone of the column, making it damageable. Therefore, using the extended surface section in the connection increases the contact surface between the connection, the column flange, and the force's distribution applied to the column. In addition to improved ductility, this reduces the stress involved in the panel zone. Thus, the idea of a flexible connection and reducing the damage to the column was proposed. This study attempted to combine the stub and end-plate connections to introduce two novel connections with a straightforward design and various behavior. The two Proposed Connections consist of an H- or I-shaped cross-section placed between the beam and column along its main axis. This connection prevents damage to other structural components by changing to plastic behavior. Upon using a stub, the plastic hinge moves far from the column. Moreover, the stress

in the panel zone is reduced by increasing the column's force transfer surface. Rolled profiles in the connection (where redundant parts could also be used) with a stiffening plate facilitate flexibility in the connection behavior, and the ductility and rigidity of the connection could be easily modified if required.

2. Two proposed connections

2.1. Proposed connection model (I)

The proposed connection Model (I), as illustrated in Fig. 1, is located between the beam and column along its main axis as a Short Stub Column (SSC) using an H- or I-shaped cross-section. This stub is placed so that one of its flanges bolted to the column, and the other welded to the beam. Therefore, the web and flanges are reinforced with stiffeners to compensate for the stub inertia moment lack related to the beam. These stiffeners are directed along the beam flanges so that eccentricity does not generate moment and pry action in the stub flanges. If the thickness of the stiffeners is greater than the thickness of the beam flanges, the SSC connection acts as fully rigid, and a plastic hinge is an establishment in the beam. Furthermore, if the thickness of stiffeners is less than that of the beam flanges, the stub acts as a damper, and a plastic hinge gets formed in it. The height of the stub is more than that of the beam in the two Proposed connections. The connection quality is high due to the performance of all the weldments before assembling the structure. The width of the stub flanges must be more than the width of the beam flanges and at most equal to the flange width of the column. Complete Joint Penetration (CJP) groove welds are used to connect the web and flanges of the beam to the stub flange and the continuity plates to the stub. In this connection, a panel zone similar to that in the column is created in the stub web. This reduces stress in the panel zone of the column. The pry action due to the bolts causes bending between the two bolts, wherever the stub flange is bolted to the column. The stub's presence of stiffener plates causes the redistribution of stress among the flanges, the stub's web, and all the connection parts in resisting the exerted forces. Moreover, different thicknesses can be used for the stiffeners. The extended parts outside the beam height in the stub act as a haunch connection and transfer a considerable force to the outside bolts. The significant displacement at the beam's end causes substantial, large deformation and plastic strain at the extended part outside the beam height on the one hand and buckling at the opposite extended part on the other hand. This leads to a more considerable contribution of the stiffener plates to the force transfer and creating the stub flange's pry action. The increase in the displacement leads to the fracture of extended parts in the stub web, and tensile and compressive forces are transferred using stiffener plates. Finally, with an increase of pry action due to the bolts, the stub web suffers a fracture between the bolts, and the connection fails.

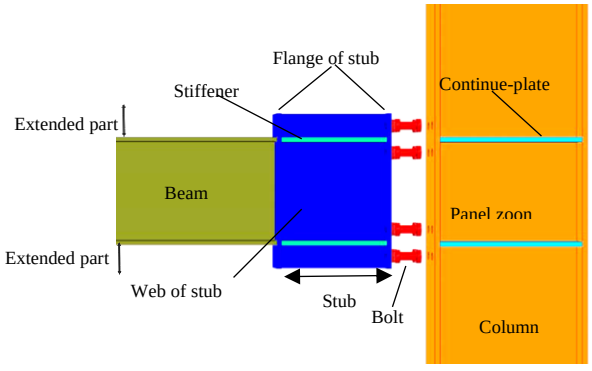

Fig. 1 configuration setup of proposed Connection model(I)

2.2. Proposed connection model (II)

In the proposed connection Model (II), as illustrated in Fig.2, one of the stub flanges is welded to the flange of the column, and the beam with the end-plate welded is bolted to the other stub flange. The end-plate width is equal to the stub flange width. Similar to model (I), the stub's web and flange are reinforced using stiffeners, and all the welds are applied at the factory. Moreover, the presence of a bolt layer in the connection results in better ductility. This connection is a suitable alternative to the tree connection. Like model (I), a panel zone formed in the stub web resembles this connection in the column. Due to the bending of the beam, the tensile and compressive forces are passed to the end-plate, then transmitted from the end-plate to the stub flange using bolts. Then, pry action causes the bending of the stub flange between the bolt rows. The stiffeners and stub web presence create a cross-shaped stiffener, which reduces the pry action in the bolts and redistributes the stress among the stub section elements. Therefore, the stress is transferred to the beam on a greater surface (equal to the surface area of the stub flange), finally reducing stress in the column's panel zone.

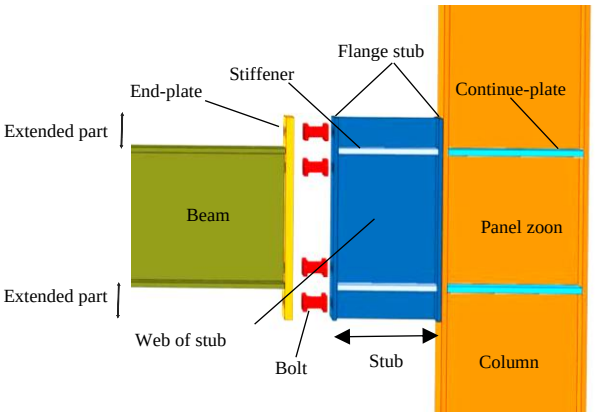

Fig. 2 configuration setup of proposed Connection model(II):

3. Numerical modeling

The experiments for parameters study on the behavior of the connection are time-consuming and costly. With the technological advancement in recent years and the FEM development, computer simulation could be a proper alternative to experimental methods. Accordingly, finite element software with the nonlinear analysis capability was employed in this research.

3.1. Part modeling

All sections are modeled as separate mechanical parts. The part type is 3D and deformable. The section drawing type, which determines the element base, is set to solid. The critical point in the initial drawing of the section is modeling the bolt since it acts as the interface between the stub with other parts of the connection and is in contact with all. Every bolt consists of a head, body, and a nut. The stub flange is in contact with the head, the nut is in contact with the column flange or end-plate, and the body of the bolt is in contact with the hole. Since modeling the bolt parts increases the number of modeled parts individually and increases the analysis time, all three parts are modeled as one part. The next point is modeling the weld. In the first few models, the weld was modeled with a triangular solid section. However, since it did not affect the results but increased the analysis time exponentially, modeling the weld was avoided in the final models, and the constraining property was used.

3.2. Material properties

The material properties are introduced using a stress-strain curve. This curve is defined in two separate sections: elastic and plastic. In the elastic state, the material properties are isotropic, and the only inputs are the Poisson's ratio and modulus of elasticity. The data for plastic stress and strain are obtained in several points by utilizing the stress-strain curve. It must be noted that the introduced strain must not be the sum of elastic and plastic strain, and only the plastic strain must be introduced. Accordingly, the first input plastic strain corresponds to the yield stress and is equal to zero. The plastic properties of materials can change with the strain rate. Flow plasticity theory was used as the nonlinear behavior in this research. According to this theory, the response of materials after the initial yield leads to the redistribution of stress and forms a new yield level. With an increase in loading, this process continues up to the whole section's yielding and fracture. The reason for the resistance of steel after yielding is the hardening phenomenon. Accordingly, the stress-strain curve has been idealized using three lines to introduce the hardening behavior. The Von Mises yield criterion is used to evaluate whether a material has become plastic. Kinematic and isotropic hardening has been combined for consideration in the nonlinear behavior of materials. Two types of stress-strain curves have been used in this model. The first curve corresponds to common steels with which structural components are built. They are considered low-carbon steels and used in all parts of the beam, column, end-plate, and stiffeners (Fig. 3.a). The second curve (Fig. 3.b) was idealized for high-strength steels (bolts) [20].

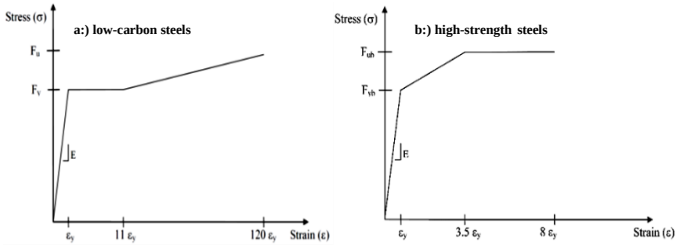

Fig. 3 Stress-strain curves

3.3. Step analysis

The analysis type is determined by the model conditions, loading, contacts, and supports. Loading on the experimental model is performed at a low rate. Therefore, the static general analysis type is appropriate. This type of analysis could solve and simulate lateral buckling, rotational loading, and nonlinear behavior of materials. Two analysis steps have been considered in this model. In the first step, the bolt pretension force is applied. The end of the beam was subjected to cyclic loading in the second step. The effect of nonlinear geometry was taken into account in the second step to compute the large displacements more accurately.

3.4. Contact modeling

One of the complicated steps in simulating bolted connections is introducing the contact elements. Both models have 62 interactions. A contact element includes two critical parameters. The normal contact behavior parameter causes hard contact and prevents the surfaces from penetrating each other. The tangential behavior parameter defines the friction coefficient, which is 0.3. Overall, there will be three contact groups in this model. The first group corresponds between the stub flange with the column flange and the end-plate. The second group is the head's contact and the bolts' nut with the plates and the column flange. The third group is the contact between the bolt bodies and the holes. All the contacts are defined as surface-to-surface. The small sliding mode is defined as the contact between the plates, the bolts, and holes. This mode makes it possible for the bolts and plates to slide along each other. The finite sliding mode is used to contact the nut and the bolt head to prevent sliding and looseness. The tolerance for the adjustment zone factor is taken to be 0.05 for all three groups. The weld is not modeled in this research; thus, we must define the corresponding components of the connection. We use the constraint property for this purpose. The beam's connections with the end-plate and the column web's continuity plates are defined using this property. This property indicates the constraints applied to the Degrees of Freedom (DOFs) in the analysis because of a part's motion in the model. Furthermore, the tie constraint is used. This constraint makes it possible to combine two regions with different meshes. In this mode, the DOFs of the slave surface nodes are constrained by the DOFs of the master surface nodes. In this mode, the node-to-node constraint will be used, and only the beam borderlines are selected so that the force transfer is similar to that in weld lines.

3.5. Loading and boundary conditions

Displacement control is used to apply load to the end of the beam, and the displacement perpendicular to the load direction is limited to prevent lateral torsional buckling. The pretension force is applied in the first loading step. The bolt pretension force is applied to a virtual plane in the bolt body. The force must create stress equal to 70% of the bolt's maximum capacity [21]. This force is obtained 613 kN using trial and error in this model. In the second step, loading is applied using displacement control. The loading history is suggested by AISC 341-10 [22] and the SAC / BD-97/02 [23]. This protocol is based on the relative rotation of the beam end. The sample was loaded statically using displacement control. Besides, the beam end displacement is obtained by multiplying the drift angle by the beam length. The moment exerted on the connection is equal to the resulting force, multiplied by the distance between the beam end and the column center.

3.6. Meshes and element types

The last step in modeling is meshing and assigning elements to parts. The number of meshes and elements has a direct impact on the accuracy of the responses. Since meshing is carried out in three-dimensional space, and regular meshing has the highest quality, one must partition the parts into simpler components. Regular meshing partitions the part using hexahedral elements and provides 8-node and 20-node elements. The higher the seed density, the finer the created meshes, the more realistic the deformations, and the longer the analysis time. Therefore, seed density must be optimized. To this end, fine meshing will be selected only around the connection core. Thus, partitioning is implemented in the beam and the column at a distance equivalent to the beam height from the connection center. The seeding density was considered 10 in this part (the connection has been modeled on a mill metric scale) and 20 in other parts. Moreover, the seed density of the bolt is equivalent to four. Two element types have been used in this model: The C3D8R element, which is linear with eight nodes, and the C3D20R element, which is quadratic with 20 nodes. The beam and the bolt have been modeled using 20-node elements, and the other members have been modeled using 8-node elements. Both element types have plastic, hardening, and extensive deformation capabilities with 3 DOFs in each node. They could exhibit nonlinear behavior with reduced Gaussian integration points.

3.7. Verification

The crucial point in a simulation is examining and verifying the results. Thus, the SSC connection was compared to a pre-verified AISC connection to evaluate seismic behavior. The connections in this study are combinations of bolt and weld and are based on end-plate theory. Therefore, the model selected for verification was a beam-to-column connection using an extended unstiffened end-plate connecting to the column flange with four bolts on both sides of each beam flange. This connection is unidirectional and subjected to cyclic loading, in which the moment-rotation curve was investigated. The finite element model was validated using Sumner's [20] experimental model. This experiment involves a beam with a length of $432\,mm$ (from the beam tip to the column center) with a cross-section of $w24 \times 68$. It is connected in cantilever configuration to a column with a length of $556\,mm$ and a $w14 \times 120$ section using an extended end-plate with a thickness of $39\,mm$ and bolts with diameters of $38\,mm$. The structure is assembled horizontally, and a hydraulic jack is used to apply force to the beam's end (Fig. 4). The loading location has been reinforced using stiffeners to prevent the beam flange from crushing. The end of the beam has been restrained using the side support to prevent lateral torsional buckling. The beam and the column properties presented in Table 1, and those of the end-plate displayed in Fig. 5 and Table 2.

Table 1
Dimensions of the Sumner sample's beam and column

	Length	Section depth	Width flange	Flange thickness	Web thickness
Beam(mm)	4128	606	233	15	11
Column(mm)	5553	368	375	24	15

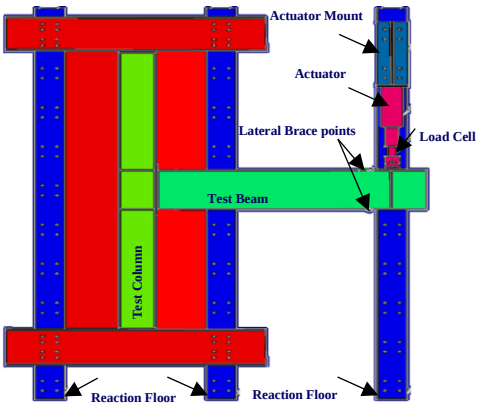

Fig. 4 Geometric typical test setup of the Sumner sample [20]

Table 2
Data of extended end-plate used in the Sumner specimen [20]

Parameter	tp	bp	Lpl	g	pf	pt	g	pf	pt
Built-Up(mm)	39	254	857	152	43.4	71.4	151	53	63

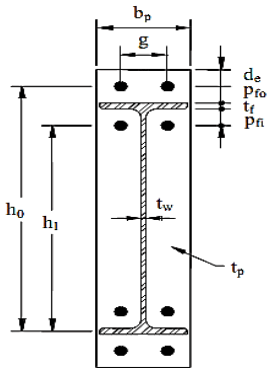

Fig. 5 Details of extended end-plate

The modeling results in this study were validated by comparison with the results of the described sample. The rotation hysteresis curve against the bending moment was plotted (Fig. 6). In this curve, the rotation is obtained by dividing the beam's displacement by the distance between the beam's free end and the center of the column (sum of the beam length, end-plate thickness, and half of the column height). The moment is equivalent to the shear force product at the end of the beam and its distance from the column center. The FEM results are, as evident, compatible with the experimental results. The experimental model differs from the FEM model for a variety of reasons. One reason is that the stress-strain curve introduced to the software does not accurately represent the material's behavior. This is especially true for the bolts, which are high-strength and do not have a specific point of yield or fracture. The contact element created can also introduce errors since this element has a complex behavior, and the friction coefficient is not equivalent to the actual value. The experimental sample results can be different from the analytical results due to errors in installing the sample and measurement devices. Nevertheless, the results are consistent. A significant reason for the model's validity is the deformation mode and its agreement with the experimental model, as shown in Fig. 7.

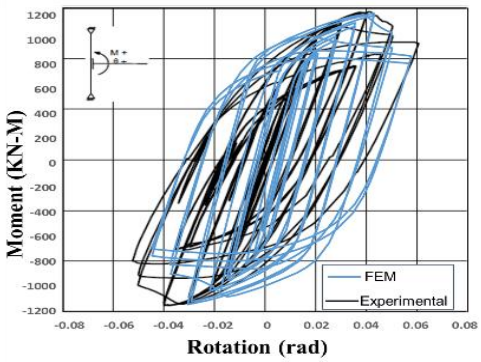

Fig. 6 Comparison hysteretic curves of experimental & FEM of Sumner specimen [20]

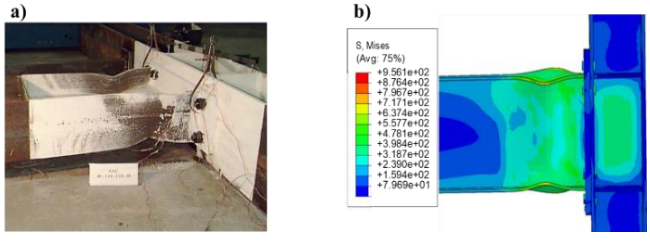

Fig. 7 Failure mode of the Sumner specimen: (a) experimental [20] & (b) FEM

4. FEM evaluation of the two proposed models

4.1. Parametric characteristics

A parametric analysis was carried out to examine the effect of changes in dimensions on the behavior of the two proposed connections. This study was performed in part 3 based on the calibration of the FEM. The IPE270 and IPE360 beam and column were selected for examining the two proposed connections, respectively. The configuration of the bolts consisted of four bolts on the sides of each beam flange. The column height, beam length from its tip to the column center, and bolt diameter was 3 m, 2.5 m, and 20 mm, respectively.

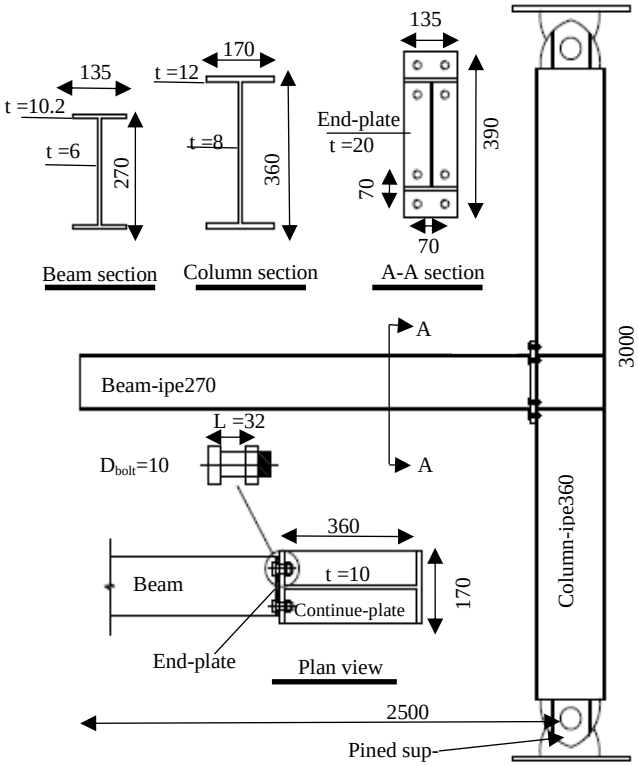

Fig. 8 End-plate connection details (unit: mm)

Since the two proposed connections are based on the properties of an extended end-plate connection with four bolts on the sides of the beam flange, we examine an end-plate connection with a thickness of 20 mm and a width equal to that of the beam, firstly (Fig. 8). This is carried out to provide a basis for comparison with the two proposed connections. Consequently, the proposed model (I) connection was examined by replacing the end-plate with a pre-built stub section (Fig. 9). Furthermore, the proposed model (II) was examined by combining the pre-built stub with the end-plate (Fig. 10). The minimum and maximum widths of the stub and end-plate are determined according to the widths of the beam flange (135 mm) and the column flange (170 mm). Therefore, IPE270, IPE360, IPB140, and IPB160 sections were used for the stub. Since the IPE's flange width is half its web height, and the IPB section has an equivalent flange width and web height, a difference was observed in behavior. A pre-built stub section with two different numbers was used to examine the effect of web height, flange width, and other section properties. The web and flange were reinforced using stiffeners to compensate for the lack of moment of inertia of the stub section concerning the beam. Three stiffener thicknesses of 10 mm, 12 mm, and 14 mm were considered for each stub. The geometric properties of the analytical samples are presented in Table 3. The sections were designed according to previous research. Moreover, the necessary controls, such as seismic compression of the beam and column sections and the Strong-Column-Weak-Beam (SCWB) rule, were applied. The stub height and bolt configuration were considered unchangeable for all samples, and the bolts were 10.9 degrees M26, based on the high-strength bolts. The modulus of elasticity and Poisson's ratio were 2.05×10e5 MPa and 0.3, respectively. The mechanical properties of the bolts are as follows: $Fy = 994\,MPa$ and $Fu = 1202\,MPa$. Furthermore, the material of other elements such as beam, column, stub, end-plate, and stiffeners was the ST37 steel with a yield strength of $Fy = 240\,MPa$ and the ultimate strength of $Fu = 370\,MPa$.

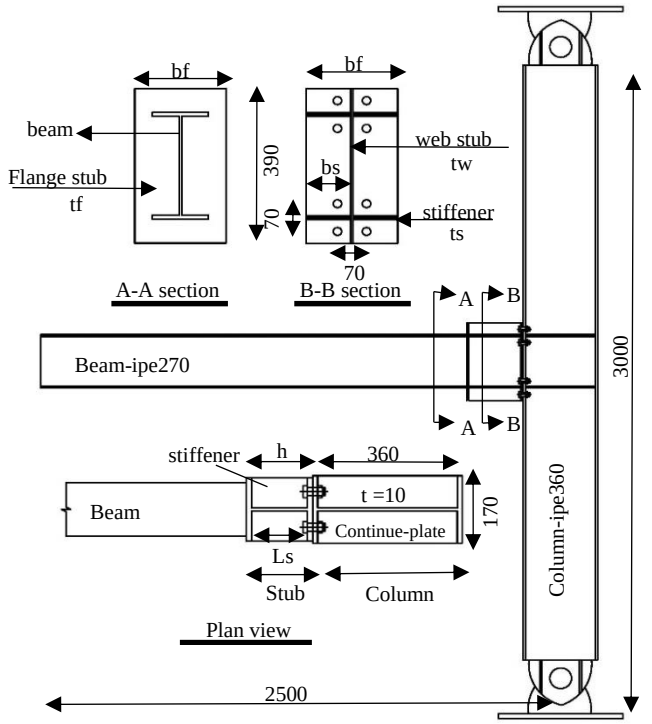

Fig. 9 Typical details of proposed connection model(I): (unit: mm)

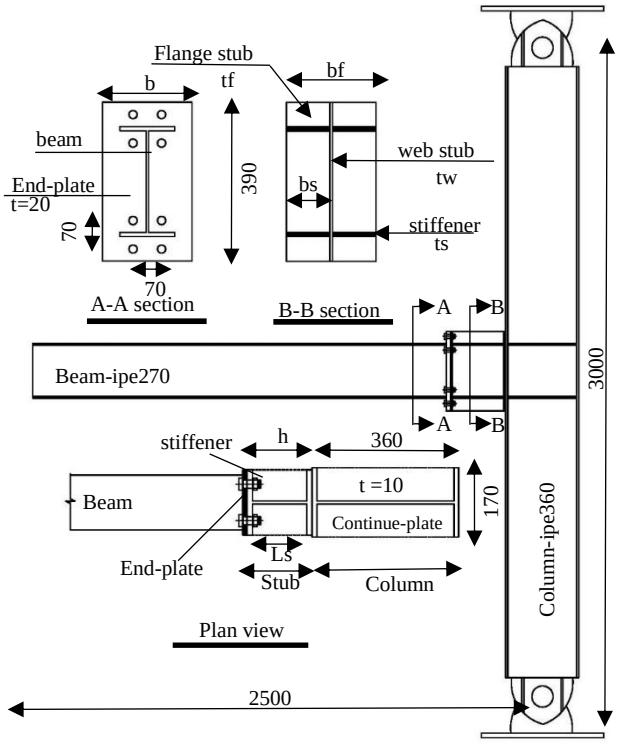

Fig. 10 Typical details of proposed connection model(II): (unit: mm)

4.2. Evaluation of results

The moment-rotation curves of all the samples have been plotted after they were exposed to cyclic loading. The backbone curve was drawn for the moment-rotation curve's positive region, and the bilinear curve was fitted according to FEMA-440 criteria [24].

Table 3
Characteristics geometric of the models

		Specimen	Stub				Stiffener			End-plate	
			h	bf	tf	tw	bs	Ls	ts	t	b
Base model		end-plate	-	-	-	-	-	-	-	20	135
Model I	Set1	m1-e27-10	270	135	10.2	6	64.5	249.6	10	-	-
		m1-e27-12	270	135	10.2	6	64.5	249.6	12	-	-
		m1-e27-14	270	135	10.2	6	64.5	249.6	14	-	-
		m1-e36-10	360	170	12	8	81	336	10	-	-
		m1-e36-12	360	170	12	8	81	336	12	-	-
		m1-e36-14	360	170	12	8	81	336	14	-	-
	Set2	m1-b14-10	140	140	12	7	66.5	116	10	-	-
		m1-b14-12	140	140	12	7	66.5	116	12	-	-
		m1-b14-14	140	140	12	7	66.5	116	14	-	-
		m1-b16-10	160	160	13	8	76	134	10	-	-
		m1-b16-12	160	160	13	8	76	134	12	-	-
		m1-b16-14	160	160	13	8	76	134	14	-	-
Model II	Set1	m2-e27-10	270	135	10.2	6	64.5	249.6	10	20	135
		m2-e27-12	270	135	10.2	6	64.5	249.6	12	20	135
		m2-e27-14	270	135	10.2	6	64.5	249.6	14	20	135
		m2-e36-10	360	170	12	8	81	336	10	20	170
		m2-e36-12	360	170	12	8	81	336	12	20	170
		m2-e36-14	360	170	12	8	81	336	14	20	170
	Set2	m2-b14-10	140	140	12	7	66.5	116	10	20	140
		m2-b14-12	140	140	12	7	66.5	116	12	20	140
		m2-b14-14	140	140	12	7	66.5	116	14	20	140
		m2-b16-10	160	160	13	8	76	134	10	20	160
		m2-b16-12	160	160	13	8	76	134	12	20	160
		m2-b16-14	160	160	13	8	76	134	14	20	160

Moreover, yield moment (M_y), maximum moment (M_{max}), yield drift (θ_y), and maximum drift (θ_{max}, corresponding to M_{max}) were obtained. Due to the stability of the two proposed connections system after the drop of the moment-rotation curve, the descending part of the backbone curve up to the 0.8 M_{pbeam} drop was considered the ultimate drift (θ_u) in the parameter calculations for plotting the bilinear curve. Moreover, the maximum and ultimate ductility (μ_{max}, μ_u) are obtained as follows:

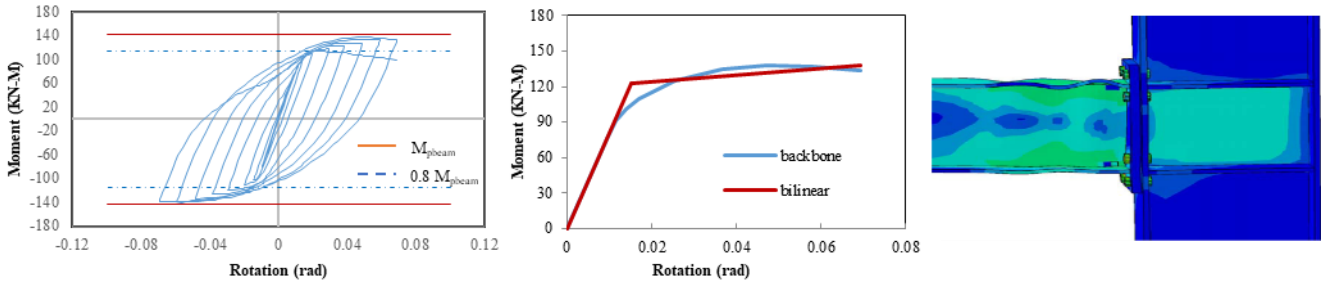

Fig. 11 Results of End-Plate Connection

$$\mu_{max} = \frac{\theta_{max}}{\theta_y} \quad (1)$$

$$\mu_u = \frac{\theta_u}{\theta_y} \quad (2)$$

Under the requirements of AISC 341-10 [25], in special earthquake resistance systems, the joints must be able to accept a thrust angle of at least 0.04 rad. In this story drift angle, the measured moment of the connection should be equivalent to at least 0.8M_P of the connected beam. M_P is the possible plastic hinge moment.

4.2.1. End-plate

The end-plate connection is used as the base model to compare the two proposed connections. According to the analyses, this sample behaves similarly to the connection in part 3. The plastic hinge in the beam is formed at an approximate distance of $d_{beam}/2$ (half of the beam web height) from the column [20]. The moment-rotation, bilinear, and backbone curves and fracture modes are displayed in Fig. 11. At a 4 percent drift, the sample's moment strength is greater than 80% of the plastic moment capacity of the beam. ($M_{0.04}/0.8M_{Pbeam}$=1.2). Moreover, the maximum bending moment strength of the sample is less than the beam's plastic moment capacity (M_{max} / M_{Pbeam} =0.96). Therefore, this connection is classified as rigid, according to AISC 341-10 [19].

4.2.2. General analysis and discussion of two proposed connections

A panel zone similar to the column's panel is formed in the stub web in the two proposed connections. Compared to the end-plate connection, it improved ductility and reduced stress in the panel zone of the column. Moreover, the bolted connection of the stub flange with the column, the bolt pry action, creates a plastic hinge between the two rows of bolts. However, this force is considerably lower than the one in the end-plate connection because the front stiffener shares the applied force among all the connection parts by redistributing the strain between the stub flange and the web. The parts extend beyond the beam's height in the connection, act as a stiffener, and transfer considerable moment to the outer bolts. The stub web presence causes more stress transfer over a larger surface of the stub flange bolted to the column flange. Subsequently, a larger area of the column is subjected to compressive stress. Therefore, the stress in the column panel zone decreases. In general, the two proposed connections resist a more significant moment and rotation compared to the end-plate. With an increase in the stiffener's thickness, the maximum moment, ultimate shear, elastic moment, and hardening will increase due to preventing the extended parts of the stub from buckling and the tensile force of the beam flange from resistance. The use of stiffeners in the stub makes it possible for the behavior to mode from semi-rigid to rigid. It is determinable that the connection behavior by changing the thickness of the stiffeners. Two sets of analyses were performed on both proposed model (I) and model (II) connections. Pre-built IPE and IPB sections were used for the first and second sets, respectively. The moment-rotation, bilinear, and backbone curves are shown in Figs. 12 to 19 and the results are summarized in Table 4. The following are observed in the results. The first set (pre-built IPE section), using a stiffener by thickness equivalent to 10mm (ST10), results in the two proposed connections having a fuse-like behavior. As a result, with simultaneous buckling of the stiffeners and the extended part, the stub fails in the compressive region. However, an Increased stiffener thickness (ST12) causes simultaneous buckling in the beam flange and stiffeners, resulting in increased ductility. Finally, by increasing the displacement, a plastic hinge is established in the approximate distance of $d_{beam/2}$ from the stub flange. This means that the plastic hinge in the two proposed connections is further away from the column by a distance equal to the stub's height compared to the end-plate connection. A stiffener with more thickness (ST14) leads to the connection exhibiting a fully rigid behavior and the plastic hinge being created completely within the beam. In comparison between IPE270 and IPE360 sections, used as the stub, the IPE270 section has greater ductility, but the IPE360 section has more bending moment strength. Compared to the end-plate connection, the two proposed connections with an IPE pre-built section have 32% more ductility and 9% more bending strength on average. In the second set (pre-built IPB section), the use of a stiffener by thickness equivalent to 10mm (ST10) has caused a semi-rigid behavior, and the fracture occurs with the simultaneous buckling of the beam flange and stiffener. The two proposed connections exhibit rigid behavior as the stiffener thickness (ST12, ST14) is increased. The behavioral parameters of the IPB140 and IPB160 sections (Table 4) are close. The behavior of the two proposed connections in the second set is unaffected by changes in section and stiffener thickness. Compared to the end-plate connection, the two proposed connections with IPB pre-built section show 13% more ductility and 8% more bending moment strength on average. Comparing the two sets, the IPE section increases the distance of the hinge formed in the beam from the column and increases the resistance against the bending moment due to its larger depth. Moreover, it provides larger deformation compared to IPB due to the thicker stiffeners. The hysteresis loops of all the samples are stable, and that show ductility and energy dissipation are acceptable. In general, the ratios M_{max} / M_P and $M_{0.04}/0.8$ M_P is larger than 1 in all samples except for m1-e27-10 and m2-e27-10. This means that the two proposed connections could transfer all the bending moment of the beam. Furthermore, they exhibit good flexibility and rotational capacities, which satisfies the deformation requirements for rare earthquakes. Therefore, the stub satisfies the criteria for a rigid connection, According to AISC. All the samples are accepted for special moment-resisting frames. The sample fracture modes are displayed in Fig. 20. As evident, in samples where the IPE270 section has been used as the stub, the plastic hinge forms at the stub location, indicating the stub's fuse-like behavior. In other samples, using a stiffener with a thickness of 10 mm leads to the creation of a plastic hinge in the beam. Despite a plastic hinge in the stub in these samples, the connection does not entirely fail and remains stable. Therefore, increasing the stiffener thickness leads to creating the plastic hinge in the beam at approximately d_{beam} /2 from the stub flange. This considerably reduces stress in the connection location, prevents the transient brittle fracture of the weld. It also significantly increases the seismic behavior of the connection. In general, the plastic hinge is formed at a greater distance from the column than the typical end-plate connection. This reduces the stress at the connection location and prevents the transient fracture of the weld, considerably improving the seismic performance of the connection.

4.2.3. Model (I)

The following occurs with an increase in the thickness of the stiffeners in the model (I)-set1: The elastic drift (θ_y), elastic bending moment (M_y), and maximum bending moment (M_{max}) increase, while the maximum drift (θ_{max}) increases with the use of the pre-built IPE270 section as the stub and decreases with the use of the IPE360 section. This indicates the negative effect of the increase in the stub depth on the Model (I) ductility. Furthermore, the maximum ductility μ_{max} and ultimate ductility μ_u decrease (considering the descending part of the moment-rotation curve). This decrease is greater when the IPE360 section is used as the stub.

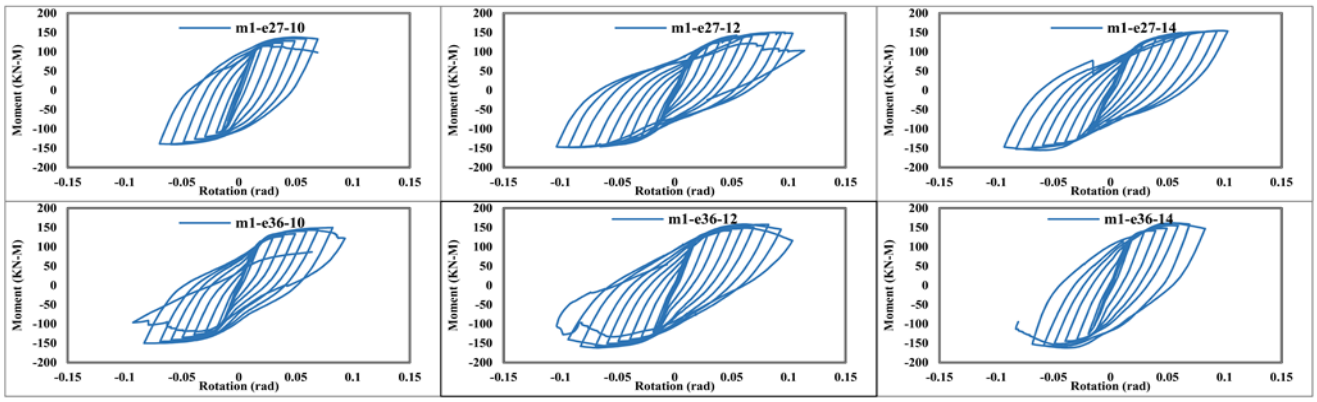

Fig. 12 Hysteretic curves of model(I)-set1 (IPE sections for stub)

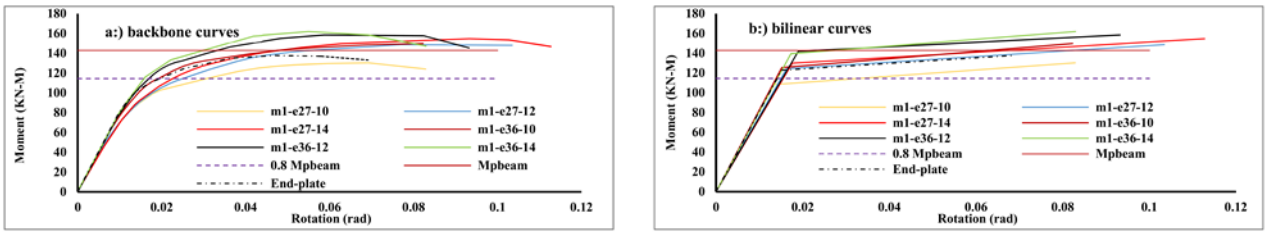

Fig. 13 Backbone & bilinear of model(I)-set1 (IPE sections for stub)

The largest values of μ_{max} and μ_u occur for samples m1-e36-10 and m1-e27-10 with 74% and 47% increases, respectively, compared to the pre-confirmed end-plate connection. The lowest values of these parameters correspond to sample m1-e36-12 with an approximate value equal to the end-plate connection. For all samples except m1-e27-10, M_{max} and My are higher than those in the end-plate connection. The largest values of M_{max} and M_y occur for m1-e36-14 and m1-e36-12 samples with $162\ kN.m$ and $142\ kN.m$, respectively. In model(I)-set2, all the parameters under study exhibit improvement compared to the end-plate connection with small variation ranges. In this set, the largest value of θ_{max} occurs in m1-b14-10 with a 7.4% drift, and its smallest value occurs in m1-b16-14 with a 4.8% drift. The largest values of M_{max} and M_y occur for m1-b14-12 and m1-b16-14 samples with $153\ kN.m$ and $131\ kN.m$, respectively.

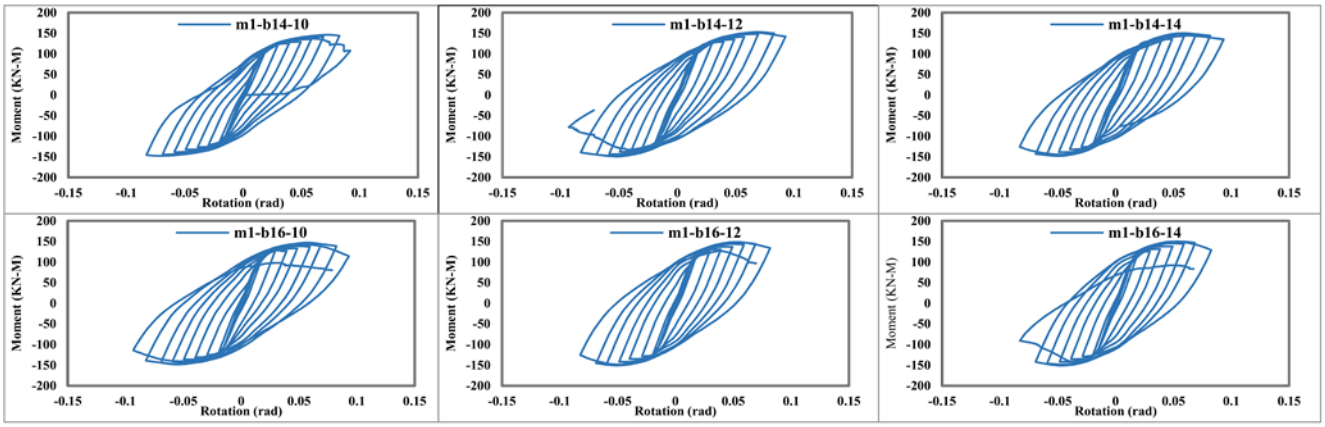

Fig. 14 Hysteretic curves of model(I)-set2 (for IPB sections for stub)

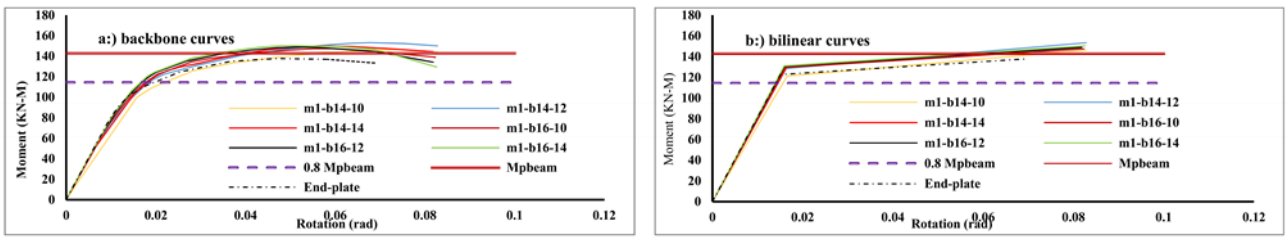

Fig. 15 Backbone & bilinear of model(I)-set2 (IPB sections for stub)

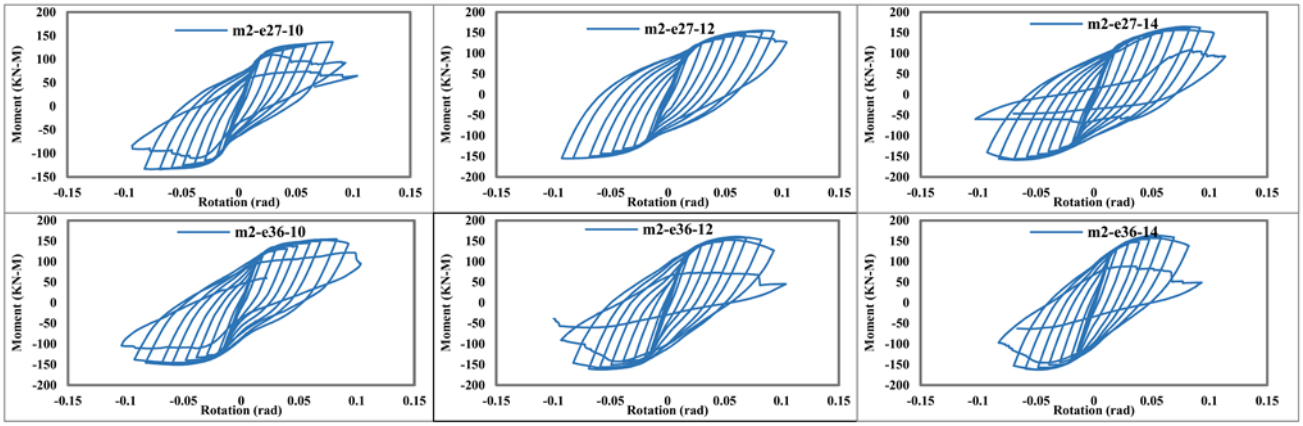

Fig. 16 Hysteretic curves of model(II)-set1 (IPE sections for stub)

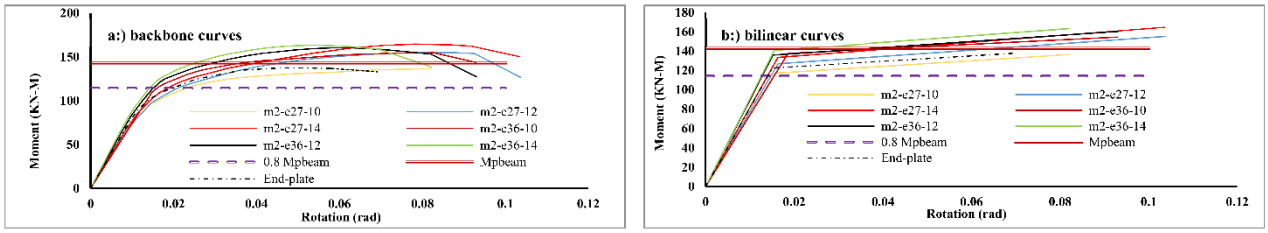

Fig. 17 Backbone & bilinear of model(II)-set1 (IPE sections for stub)

4.2.4. Model (II)

In Model (II)-set1, with an increase in the stiffeners' thickness and the stub depth, the ductility is reduced, and its bending moment strength is increased. In comparison to the end-plate connection, the largest values of μ_{max} and μ_u occur for m2-e27-10, and m2-e27-14 samples with 67% and 38% increases, respectively, and these lowest values for these parameters occur for m2-e36-14 and m2-e36-10, with a 10% decrease. The values of M_{max} and M_y are more extensive than those in the end-plate connection for all samples in this set except for m2-e27-10. The largest values of M_{max} and M_y occur for sample m2-e36-14 with the values of $163\ kN.m$ and $141\ kN.m$. The samples in Model(II)-set2 generally have a smaller ductility compared to other samples. In this set, an increase in the stiffener thickness and stub depth led to increased ductility, unlike in other samples. The largest values of M_{max} and M_y corresponding to sample m2-b16-14 are $155\ kN.m$ and $139\ kN.m$, respectively. The noteworthy point in Model(II)-set2 is the relative increase in the elastic drift (θ_y) compared to other samples. The most considerable value of this parameter belongs to sample m2-b14-10, which has a 2.2% drift and is 48% more than the value in the end-plate connection.

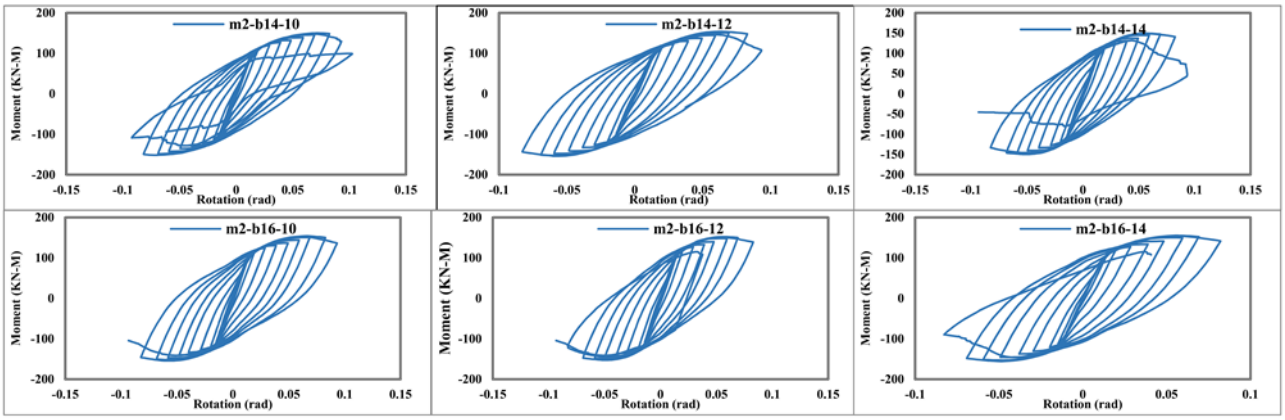

Fig. 18 Hysteretic curves of model(II)-set2 (IPB sections for stub)

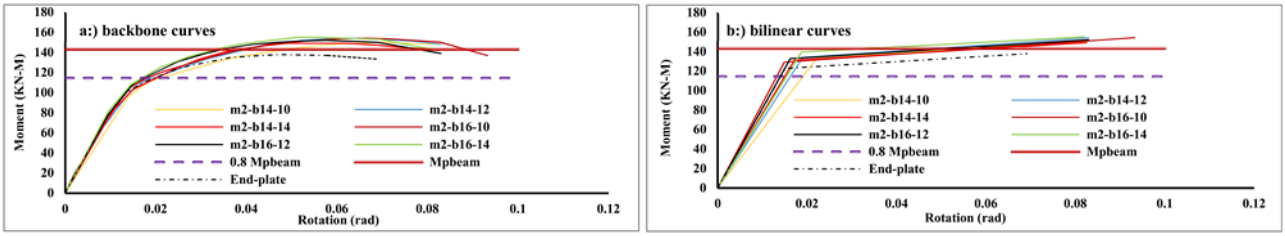

Fig. 19 Backbone & bilinear of model(II)-set2 (IPB sections for stub)

4.3. Evaluation of equivalent plastic strain (PEEQ)

The primary purpose of the two proposed connections is to reduce non-elastic deformations in the column. The non-elastic rotation in massive earthquakes causes local buckling and excessive lateral torsional buckling in the panel zone.

This potential fracture mode must be considered besides the bending buckling of the columns. Therefore, the performance of the connections under seismic loading is somewhat dependent on the panel zone behavior. Moreover, reducing the plastic strain in this area prevents the fracture of the panel zone and improves the connection's behavior. The equivalent plastic stress (PEEQ) index is used to compare the effect of the two proposed connections on the panel zone. This index is used as a tool for measuring the ductility at the local surface. It is calculated as follows:

$$PEEQ=\frac{\sqrt{\frac{2}{3}\varepsilon_{ij}^{p}\varepsilon_{ij}^{p}}}{\varepsilon_{y}} \quad (3)$$

Where ε_{ij}^{p} is the component of plastic strain in the direction specified by i and j and ε_y is yield strain under uniaxial monotonic tensile loading, respectively. In this study, the panel zone is the surface between the two continuity plates in the column web. To evaluate the PEEQ index, the curve of its maximum value was plotted and compared for the points on the panel zone surface. These curves are shown in Figs. 21 & 22. According to these curves, the equivalent plastic strain PEEQ in the end-plate connection is zero up to a drift of 1.5 percent (cycle=15), indicating the absence of yielding in the column panel zone. However, after this point, the value of PEEQ increases. In model(I)-set1, the use of the IPE270 section as the stub reduces the PEEQ in the panel zone to a great extent. A stiffener with a thickness of 10 mm decreases the PEEQ by 80% at a 6% drift (cycle=20). This is due to the fuse-like performance of the stub in this sample. With an increase in the stiffener's thickness to 12 mm and 14 mm, the value of PEEQ dropped by 60% and 40%, respectively. The IPE360 section's use as the stub with a 10 mm stiffener results in a 40% reduction in PEEQ. In this sample (m1-e36-10), the plastic hinge is formed in the stub. However, an increase in the stiffener thickness to 12 mm and 14 mm increased the connection's rigidity and increased PEEQ compared to the end-plate connection. In model(I)-set2, the IPB section's use reduced the PEEQ index by 40%. IPB140 and IPB160 sections as the stub with 10 mm, 12 mm, and 14 mm stiffeners do not significantly affect this index. This shows that the stub behaves more stably and reliably with the IPB section. Model (II) will considerably reduce PEEQ in the panel zone. This reduction occurred for all samples. In Model (II)-set1, the largest and smallest PEEQ values belonged to m2-e36-st14 and m2-e27-10 with 20% and 95% reductions, respectively, at a 6% drift. The reduction in PEEQ is continued in model (II)-set2 using the IPB section as the stub. The analytical samples with this section showed similar behaviors, and the PEEQ index decreased by approximately 80% at a 6% drift compared to the end-plate connection. Comparing the two proposed models shows that PEEQ is lower by 30% in model (II) than model (I). The second mode is when both the beam and the stub enter the plastic phase.

5. Design method

The parameters affecting the SSC connection's behavior allow the designer to design the connection according to the performance requirements of the structure. The SSC connection is capable of acting as a fuse. Therefore, the most important point in its design is determining the required bending moment. Three modes are considered for the behavior of the SSC connection. The first mode is when the SSC connection behaves as fully rigid, and the plastic hinge is formed in the beam. In this mode, the design bending moment is equal to the plastic bending moment of the beam at the plastic hinge (using the 14mm stiffener).

Table 4
Summary of numerical test results.

Specimen			θ_y	θ_{max}	θ_u	M_y	M_{max}	$M_{0.04rad}$	μ_{max}	μ_u	M_{max}/M_{Pbeam}	$M_{0.04}/0.8\ M_{Pbeam}$
			rad			kN.m						
Base model		end-plate	0.015	0.047	0.069	123	138	137	3.12	4.58	0.96	1.2
model I	set1	m1-e27-10	0.013	0.069	0.09	108	130	124	5.17	6.72	0.91	1.18
		m1-e27-12	0.016	0.077	0.103	124	149	135	4.73	6.37	1.04	1.26
		m1-e27-14	0.018	0.093	0.09	130	155	138	5.29	5.1	1.08	1.27
		m1-e36-10	0.015	0.082	0.09	125	150	139	5.43	5.93	1.05	1.24
		m1-e36-12	0.019	0.059	0.093	142	158	150	3.1	4.92	1.11	1.27
		m1-e36-14	0.017	0.055	0.09	139	162	155	3.19	5.22	1.13	1.28
	set2	m1-b14-10	0.017	0.074	0.083	121	146	135	4.47	5	1.02	1.08
		m1-b14-12	0.016	0.068	0.083	129	153	144	4.14	5.06	1.07	1.18
		m1-b14-14	0.016	0.056	0.082	130	150	145	3.43	4.98	1.05	1.21
		m1-b16-10	0.016	0.059	0.082	130	147	142	3.69	5.12	1.03	1.22
		m1-b16-12	0.016	0.051	0.082	131	149	145	3.16	5.1	1.04	1.31
		m1-b16-14	0.016	0.048	0.083	131	150	147	3.05	5.2	1.05	1.35
model II	set1	m2-e27-10	0.016	0.082	0.082	117	137	128	5.22	5.22	0.96	1.12
		m2-e27-12	0.016	0.082	0.104	127	155	139	4.99	6.34	1.09	1.22
		m2-e27-14	0.016	0.078	0.104	134	165	146	4.8	6.36	1.15	1.28
		m2-e36-10	0.019	0.072	0.093	138	155	145	3.87	5	1.08	1.27
		m2-e36-12	0.015	0.059	0.093	136	161	154	3.89	6.13	1.12	1.35
		m2-e36-14	0.015	0.053	0.082	141	163	159	3.41	5.31	1.14	1.39
	set2	m2-b14-10	0.022	0.07	0.083	134	150	137	3.14	3.7	1.05	1.2
		m2-b14-12	0.019	0.06	0.083	134	154	143	3.12	4.36	1.08	1.25
		m2-b14-14	0.017	0.054	0.083	131	149	145	3.15	4.81	1.04	1.27
		m2-b16-10	0.015	0.067	0.093	129	154	146	4.46	6.25	1.08	1.28
		m2-b16-12	0.016	0.058	0.083	133	152	147	3.54	5.11	1.06	1.28
		m2-b16-14	0.019	0.062	0.082	139	155	149	3.31	4.38	1.08	1.3

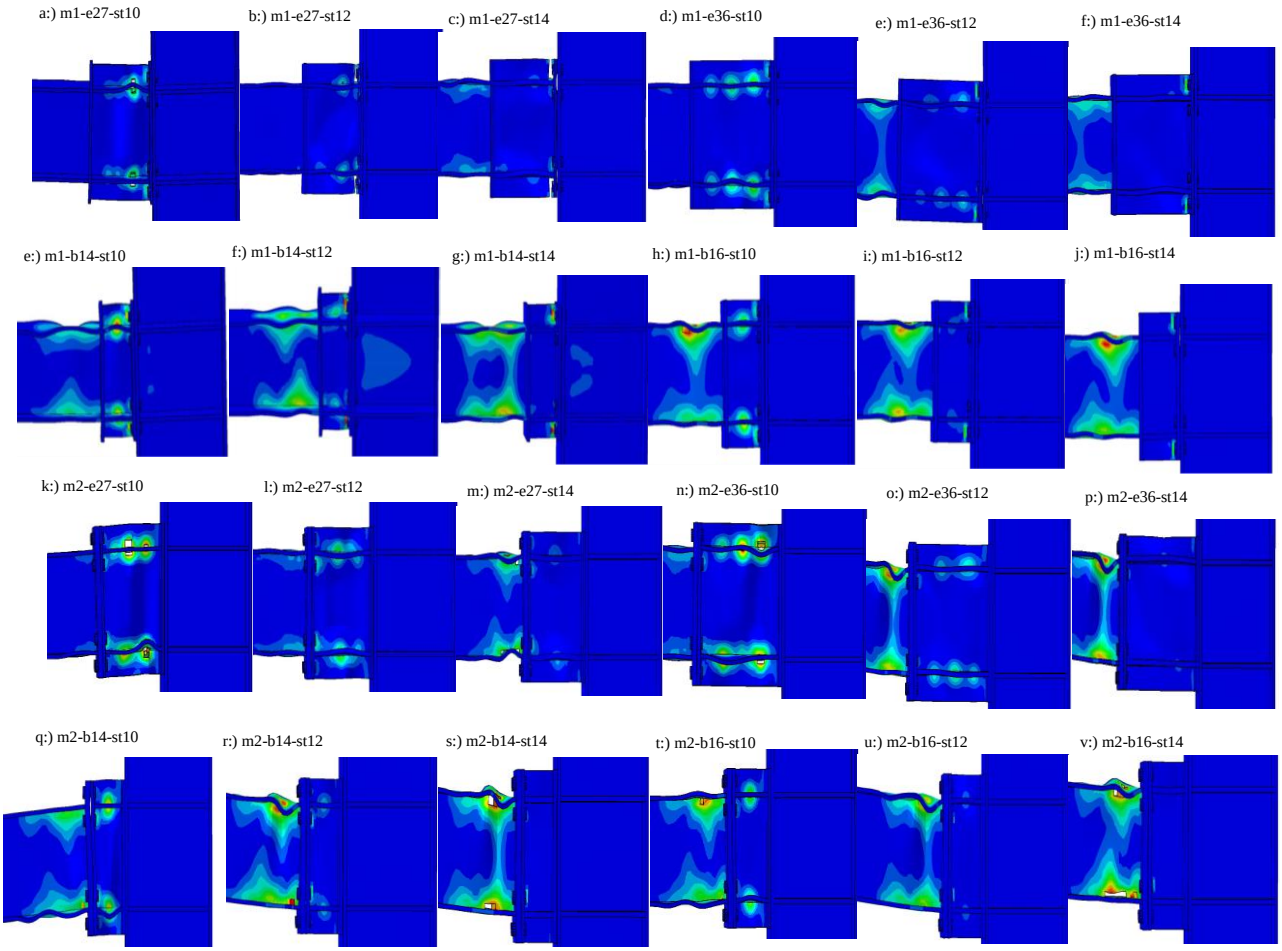

Fig. 20 Equivalent Plastic Strain (PEEQ) of Stub Models

The second mode is when both the beam and the stub enter the plastic phase. In this mode, the two proposed connections have the highest ductility (the use of the 12mm stiffener), and the design bending moment is at most equivalent to the plastic bending moment of the beam (M_{pbeam}). The third mode is when the plastic hinge is formed in the stub, and the connection acts as a fuse. In this mode, the design bending moment is between 0.8 M_{pbeam} and M_{pbeam}. According to the results of this investigation, the stub depth and stiffener thickness are the main parameters determining the behavior of the two proposed connections. The stub web behaves like the column panel zone, and the stiffeners behave similarly to the continuity plates. Thus, they can be designed based on the column panel zone rules. The other connection components, such as stiffeners, bolts, and end-plates, are designed according to the requirements of reputable rules. However, given the complexity of the exact design equations, in this study, some engineering rules are suggested for SSC connections as follows:

- In general, all the sections must be controlled concerning the width-to-thickness b/t regulations for compressed elements in highly ductile members, according to ANST/AISC341-16.
- The web and flange stub thicknesses are recommended to be at least equivalent to those of the beam.
- The stub flange width must be at least equal to the width of the beam flange and at most equivalent to the width of the column flange.
- The stub section's depth is recommended to be at least half the beam height
- and equal to the beam height. This value must not be less than 120 mm due to practical considerations.
- The stub height is recommended to be equal to the sum of the beam depth and $6d_{bolt}$ to 8 d_{bolt}.
- The bolt arrangement is controlled by the end-plate design rules as well as practical considerations. The distances of the bolt hole centers from the stub web and beam flange surfaces are recommended to be at least two times and, at most, three times the bolt diameter.

6. Conclusions

In this research, using Rolled profiles, two novel steel connections with new construction that aims to reduce damage to beams and columns and reduce plastic strain in the panel zone have been proposed. With a load transfer mechanism different from those of conventional connections, the proposed construction consists of a stub that is placed as a short column between the column and the beam (or welded beam to the end-plate) and was named Short Stub Column (SSC). The first proposed model could be an alternative to the end-plate connection, and the second proposed model could be an alternative to the tree connection.

For parametric evaluation, two sets of analyzes were performed with Pre-built IPE, and IPB sections were used for both proposed connections. The FEM software was employed to simulate 24 submodules in two sets. After each sample was subjected to cyclic loading, the moment-rotation curves were plotted, and the backbone & bilinear curves were drawn.

Based on the results obtained, the $M_{0.04}$ / 0.8 M_{Pbeam} ratio is more than one for all samples. Therefore, they provide AISC requirements for use in special moment frames. Also, by changing the stiffeners' thickness, it can be determined whether the plastic hinge is formed in the beam or the stub.

The reduction in strength of the samples is due to the fracture and local ductile buckling during cyclic loading, and no global fracture is observed in the samples.

FEM studies on the SSC connection indicate that this connection has excellent ductility. The stub region absorbs considerably more energy than the hinge in the beam due to its plastic performance. It creates a limited and controlled hinge with excellent ductility, increasing the structure's period and behavior factor. Compared to conventional bending moment connections, not only does this connection not show reduced ultimate strength and hardening, but its plastic rotation capacity can also be increased several times. Timely yielding in the stub causes a fuse-like behavior. It prevents damage to the beam and column, significantly reducing the plastic stress and strain in the panel zone and improving energy dissipation reliability. Also, this investigation of the peeq index in the panel zone showed that the SSC connection reduces the plastic strain compared to the end-plate connection.

Acknowledgments

This research has conducted in collaboration with the National Iranian South Oil Company.

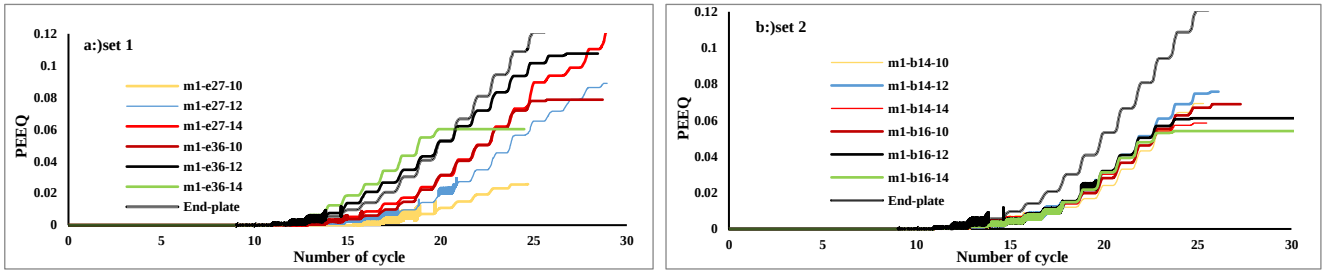

Fig. 21 PEEQ curves of model(I)

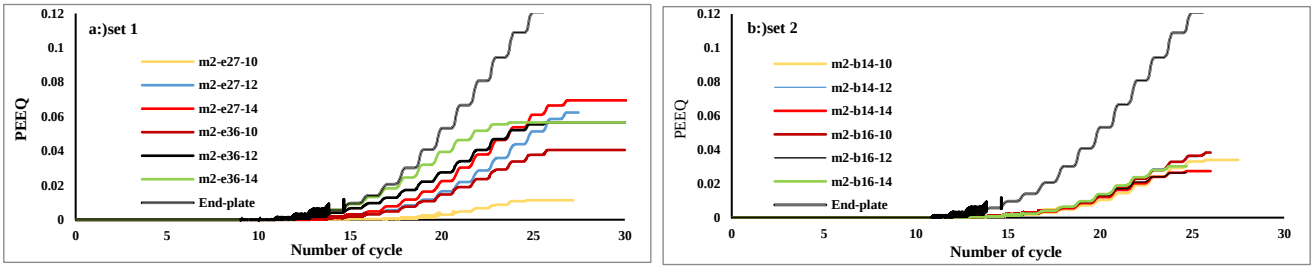

Fig. 22 PEEQ curves of model(II)

References

[1] Moghadam A, E Estekanchi H, Yekrangnia M. Evaluation of PR steel frame connection with torsional plate and its optimal placement. Scientia Iranica. 2018 Jun 1;25(3):1025-38.

[2] SAC J. State of the art report on connection performance Report No FEMA-355D. Federal Emergency Management Agency (FEMA), Washington. 2000.

[3] Alhendi H, Celikag M. Finite element prediction of reverse channel connections to tubular columns behavior. Engineering Structures. 2015 Oct 1;100:599-609.

[4] Mirghaderi SR, Torabian S, Keshavarzi F. I-beam to box–column connection by a vertical plate passing through the column. Engineering Structures. 2010 Aug 1;32(8):2034-48.

[5] Miller DK. Lessons learned from the Northridge earthquake. Engineering structures. 1998 Apr 1;20(4-6):249-60.

[6] Tremblay R, Filiatrault A, Timler P, Bruneau M. Performance of steel structures during the 1994 Northridge earthquake. Canadian Journal of Civil Engineering. 1995 Apr 1;22(2):338-60.

[7] Tremblay R, Filiatrault A, Bruneau M, Nakashima M, Prion HG, DeVall R. Seismic design of steel buildings: lessons from the 1995 Hyogo-ken Nanbu earthquake. Canadian Journal of Civil Engineering. 1996 Jun 1;23(3):727-56.

[8] American Institute of Steel Construction (AISC), Seismic Provisions for Structural Steel Buildings, AISC ANSI/AISC 341-16, Chicago, IL, 2016.

[9] Garoosi AM, TahamouliRoudsari M, Hashemi BH. Experimental evaluation of rigid connection with reduced section and replaceable fuse. InStructures 2018 Nov 1 (Vol. 16, pp. 390-404). Elsevier.

[10] Behrooz SM, Erfani S. Parametric study of Stub-Beam Bolted Extended End-Plate connection to box-columns. Journal of Constructional Steel Research. 2020 Aug 1;171:106155.

[11] Shen Y, Christopoulos C, Mansour N, Tremblay R. Seismic design and performance of steel moment-resisting frames with nonlinear replaceable links. Journal of Structural Engineering. 2011 Oct 1;137(10):1107-17.

[12] Li X. Moment-rotation behaviour of universal beam to tubular column connections using reverse channel. The University of Manchester (United Kingdom); 2012.

[13] O.Yılmaz, S Bekiroğlu. Performance Evaluation of Weak-Axis Steel Moment Connections. XVI INTERNATIONAL SCIENTIFIC CONFERENCE VSU'2016.

[14] Hu G, Huang W, Xie H. Mechanical behavior of a replaceable energy dissipation device for precast concrete beam-column connections. Journal of Constructional Steel Research. 2020 Jan 1;164:105816.

[15] Peng H, Ou J, Mahin S. Design and numerical analysis of a damage-controllable mechanical hinge beam-to-column connection. Soil Dynamics and Earthquake Engineering. 2020 Jun 1;133:106149.

[16] Shi Q, Yan S, Kong L, Bu X, Wang X, Sun H. Seismic behavior of semi-rigid steel joints—Major axis T-stub and minor axis end-plate. Journal of Constructional Steel Research. 2019 Aug 1;159:476-92.

[17] Jiang J, Chen S. Experimental and numerical study of double-through plate connections to CFST column. Journal of Constructional Steel Research. 2019 Feb 1;153:385-94.

[18] Zhang Y, Li Q, Zhuge Y, Liu A, Zhao W. Experimental study on spatial prefabricated self-centering steel frame with beam-column connections containing bolted web friction devices. Engineering Structures. 2019 Sep 15;195:1-21.

[19] Liu Y, Huang SS, Burgess I. Component-based modelling of a novel ductile steel connection. Engineering Structures. 2020 Apr 1;208:110320.

[20] Sumner EA. Unified design of extended end-plate moment connections subject to cyclic loading (Doctoral dissertation, Virginia Tech).

[21] British Standards Institution. Mechanical Properties of Fasteners Made of Carbon Steel and Alloy Steel: Set Screws and Similar Threaded Fasteners Not Under Tensile Stresses. British Standards Institution; 1999.

[22] ASCE/SEI Seismic Rehabilitation Standards Committee. Seismic rehabilitation of existing buildings. ASCE/SEI. 2007:41-06.

[23] Venture SJ. SAC. Protocol for Fabrication, Inspection, Testing and Documentation of Beam-Column Connection Test and Other Experimental Specimens. SAC Rep. SAC/BD-97/02, Sacramento, California; 1997.

[24] FEMA A. 440, Improvement of nonlinear static seismic analysis procedures. FEMA-440, Redwood City. 2005;7(9):11.

[25] AISC A. AISC 341-10. Seismic Provisions for Structural Steel Buildings, American Institute of Steel Construction. Inc., Chicago, IL. 2010.

Advanced Steel Construction – Vol. 18 No. 1 (2022) 506–516
DOI:10.18057/IJASC.2022.18.1.9

EXPERIMENTAL AND NUMERICAL INVESTIGATION ON SEISMIC PERFORMANCE OF RING-BEAM CONNECTION TO GANGUE CONCRETE FILLED STEEL TUBULAR COLUMNS

Chen Fang [1], Guo-Chang Li [2], Lei Zhang [3, 4, *] and Zhi-Jian Yang [2]

[1] *Midwest Roadside Safety Facility, University of Nebraska-Lincoln, Lincoln, Nebraska 68583, USA*
[2] *School of Civil Engineering, Shenyang Jianzhu University, Shenyang, Liaoning 110168, China*
[3] *Lecturer, Department of Civil Engineering and Architecture, Jiangsu University of Science and Technology, Zhenjiang, Jiangsu 212100, China*
[4] *Postdoctor, Institute of Geotechnical Engineering, Nanjing Tech University, Nanjing, Jiangsu 211816, China*
** (Corresponding author: E-mail: lei.zhang@just.edu.cn)*

ABSTRACT

This paper presents an investigation on seismic performance of a ring-beam connection that is used to connect reinforced gangue concrete (RGC) beam to coal-gangue concrete-filled steel tubular (GCFST) column. Two specimens, including an interior connection with two beams and an exterior connection with one beam, were designed and fabricated for experimental tests under full-reversing cyclic loads at beam ends. In addition, finite element models which corresponded to tested specimens were developed using ABAQUS to conduct numerical simulations of the composite connection subjected to the combined axial and cyclic loads. The feasibility of the developed model to predict failure modes and load-deformation response of the connection was validated by comparing with test results. The response of the ring-beam connection to cyclic loads was examined with respects to the load-bearing capacity, deformation resistance, stiffness and strength degradation, ability to dissipate energy in a seismic event, and ductility. With numerical models, parametric analysis was completed to evaluate the influences of material and structural parameters on connection resistance against cyclic loads. Based on the results of parametric studies, a restoring force model of skeleton curve for the ring-beam connection was developed in terms of ultimate capacity and corresponding deformation. The results provided practical suggestions for the application of ring-beam connection to GCFST column in the projects.

ARTICLE HISTORY

Received: 14 October 2020
Revised: 1 July 2021
Accepted: 4 July 2021

KEYWORDS

Column-beam connection;
Gangue concrete filled steel tube;
Ring-beam connection;
Seismic behavior;
Finite element analysis;
Full-scale test

1. Introduction

Coal-gangue concrete filled steel tubular (GCFST) structure is an innovative composite structure adoptable for the high-rise buildings and bridges [1]. Gangue concrete filled steel tubular structural element is designed to consist of a steel tube and gangue concrete filled in the tube. This composite structure takes advantages of steel tube and confined coal-gangue concrete. The confinement created by steel tube could significantly increase concrete strength, and the coal-gangue concrete filled in the tube provides supplementary resistance against tube buckling [2; 3]. GCFST structure exhibits benefits to achieve high strength and large ductility under cyclic loading. Furthermore, prominent merits can be found for the GCFST structures. Compared to regular concrete, the coal-gangue concrete has the superior lateral deformation resistance, resulting in the full use of the tube confinement effects and futher improve the capacity of the composite structure [4]. Another advantage which attracts the interests of researchers and designers is its less weight than the concrete filled steel tubular (CFST) structure due to the less density of gangue concrete. With the development of the society, it is a trend to develop the green building in Civil Engineering [5]. As a non-recyclable industrial waste, the use of the gangue for building construction is an economic approach to reduce environmental pollution and achieve the social benefits [6].

In the seismic design principle, a column-to-beam connection is a critical element that determines the integrity and safety of the frame building. The column-beam connection provides stiffness and strength for a building to ensure its integrity under an earthquake. Many structures collapsed due to severe damage to the column-beam connection under various earthquake events [7] such as Wenchuan in China [8]. Therefore, the strength and ductility of the column-to-beam connection should be improved to ensure the stability and safety of the entire building under earthquake events.

Many scholars and designers have conducted a series of studies on performance of various connections between CFST column and beam. Goldsworthy and Gardner [9] completed an experimental study that proposed a CFST column-to-beam connection and investigated its performance under wind or seismic loading. Kataoka et al. [10] developed a new connection between CFST column and steel beam using endplates and bolts and conducted experimental investigations on the dynamic behaviors. The study also carried out an analytical evaluation for the connection behavior based on ABNT NBR 8800. Agheshlui et al. [11] investigated the cyclic behavior of moment-resisting bolted connection between square CFST column and steel beams. The study analyzed the failure mode, hysteretic performance, capacity, stiffness of proposed connection and demonstrated its satisfactory performance to resist lateral loads for high-rise building. Tizani et al. [12] designed a new connection to CFST columns using the blind bolts and experimentally examined the performance and reliability of this new connection for the seismic design requirements. The study indicated that this new connection with an acceptable capacity to dissipate energy has adequate seismic resistance for the entire building. Khanouki et al. [13] created ABAQUS numerical model of a through-beam connection to CFST column and evaluated its cyclic behaviors using a series of parametric studies. Choi et al. [14] developed a through-type CFST column-to-beam connection and experimentally studied its failure mode and energy-dissipation capacity for earthquake-resistant applications. However, limited studies have been conducted to investigate the cyclic-loaded response of the GCFST column-to-beam connection. Due to inadequate understanding of seismic behavior, this new composite connection does not reach its full potential in the application, and more studies need to provide information on the performance of the promising composite connection for design and application in the engineering projects.

This paper proposed and designed a ring-beam connection that is used to connect RGC beams with GCFST column. The connection specimens were fabricated for experimental tests to investigate their seismic behaviors. In addition, finite element models corresponding to experimental specimens were developed using ABAQUS, and the feasibility of the developed model was verified by comparing numerical results with test data. Several critical indexes were examined to evaluate the connection performance in a seismic event for this study. Parametric analysis was conducted to examine the influences of concrete and structural parameters on the connection response. Finally, a restoring force model of skeleton curve for the ring-beam connection was developed in terms of ultimate capacity and corresponding deformation.

2. Experimental tests

2.1. Experimental specimens

The prototype of the ring-beam connection was designed in accordance with requirements of the code CECS28-2012 [15]. The ring-beam connection to GCFST column was fabricated in structural laboratory at the Shenyang Jianzhu University. Fig. 1 shows the geometries and reinforcement details of tested specimen. This composite connection consisted of a GCFST column, RGC beams of a frame building, an RGC ring beam and shear rings. The shear ring was designed as circle reinforcing bars which was welded to tube wall in the vicinity of ring beam bottom and embedded in the ring beam. The function of welded shear ring was to transfer shear stress from ring beam to GCFST

column. The number of shear ring was determined from shear stress generated by cyclic loads and design requirement provided in GB50936-2014. For the experimental program, two specimens were tested: one interior connection that includes two frame beams and one exterior connection involving one frame beam. The column was designed as a circular gangue concrete filled steel tubular column with a diameter of 325 mm. The thickness of steel tube was 6 mm, which results in a steel ratio of 0.078 for the GCFST column. The clear height of the GCFST column was 1500 mm. All beams with cross-sectional dimensions of 180×250 mm were reinforced by 2Φ20 longitudinal bars and Φ10 hoops spaced at 100 mm. The ring beam was 120 mm in width and 250 mm in depth. The ring beam was reinforced using 2Φ12 longitudinal bars and Φ6 hoops spaced at 100 mm. An axial load, which produces an axial load ratio of 0.6, was placed at the top column during the process of test.

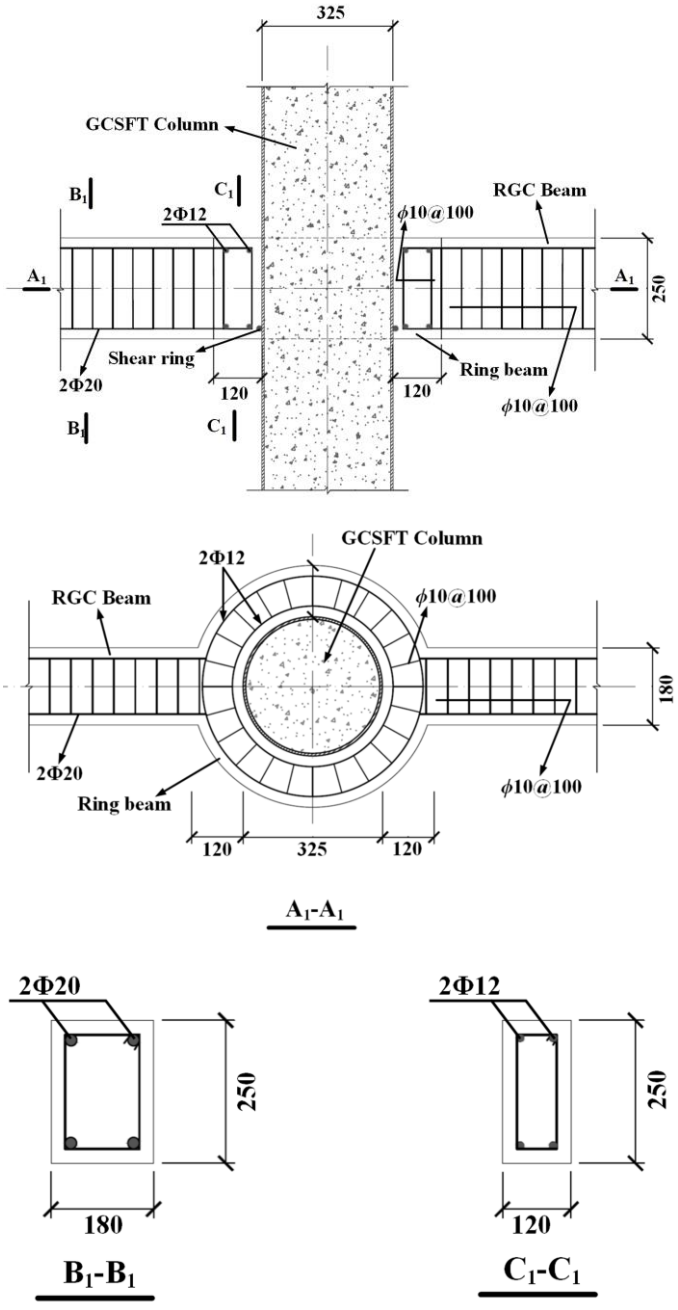

Fig. 1 Geometries and reinforcement details of tested specimen

Table 1 lists the geometries and reinforcement details of the tested connections. In this table, D is the outside diameter of GCFST column; t is the thickness of steel tube; b and h are the width and depth of the frame beam, respectively; H is column height; L is the frame beam length; A_{sf} is the area of longitudinal reinforcement for frame beam; h' is ring beam height; A_{sr} is the area of circle reinforcement for ring beam; b' is the width of the ring beam; n is the axial load ratio for the GCFST column [15].

Table 1
Dimensions of tested specimens

Specimen	$D\times t$ (mm)	H (m)	L (m)	b (m)	h (m)	A_{sf}	b' (m)	A_{sr}	hoop	n
JH-E-B	325×6	1.5	1	0.18	0.25	2Φ20	0.12	2Φ12	Φ10	0.6
JH-E-Z	325×6	1.5	2	0.18	0.25	2Φ20	0.12	2Φ12	Φ10	0.6

Based on the design code GB50011-2010 [16], the specimens were designed in accordance with the philosophy that "strong column and weak beam". Therefore, the RGC frame beam was designed to fail under earthquake events, while the column must have sufficient strength to resist the earthquake. This principle can ensure safety and stability of a building under earthquake events. Fig. 2 shows the tested specimen of JH-E-Z connection.

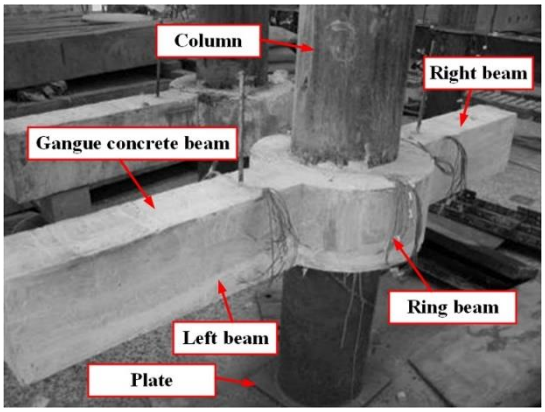

Fig. 2 Tested specimen of JH-E-Z connection

2.2. Concrete and steel properties

Tension test was conducted on the steel coupon to measure the steel properties using the code GB/T228-2002 (2003) [17]. The steel had the yield strength of 500 MPa, the ultimate strength of 650 MPa, and the Young's modulus of 215 GPa. Table 2 lists the material properties for each steel determined for this experimental investigation. Gangue concrete mix proportion that was designed by the weight included, the cement: 420 kg/m^3; sand: 412.5 kg/m^3; gangue: 412.5 kg/m^3; water: 250 kg/m^3; and coarse aggregate: 608 kg/m^3. The regular Portland cement with a grade of 32.5 and the coal gangue with an aggregate size of 5~10 mm collected in Fuxin city were used to produce the gangue concrete. The compressive cube strength test was performed on the gangue concrete block at 28 days according to GB/T50081-2002 (2003) [18]. The average strength of the coal-gangue concrete was 21.4 MPa.

Table 2
Steel material properties

Steel	f_y (MPa)	f_u (MPa)	E (MPa)
Φ20	500	650	2.17×10^5
Φ12	385	553	2.07×10^5
Φ10	325	427	2.06×10^5
Φ6	342	398	2.15×10^5
Steel tube	324	459	2.19×10^5

2.3. Test preparation

Fig. 3 illustrates experimental setup. A constant axial load (N_0) created using a hydraulic jack was imposed at the top of the GCFST column. The top and bottom of the column were restrained to the hinged boundary conditions. Two MTS hydraulic rams were set at both ends of RGC beams to generate a cyclic load. In the initial stage, the axial load was gradually increased up to the designed load prior to the cyclic load. The axial load was employed to simulate the dead load effects.

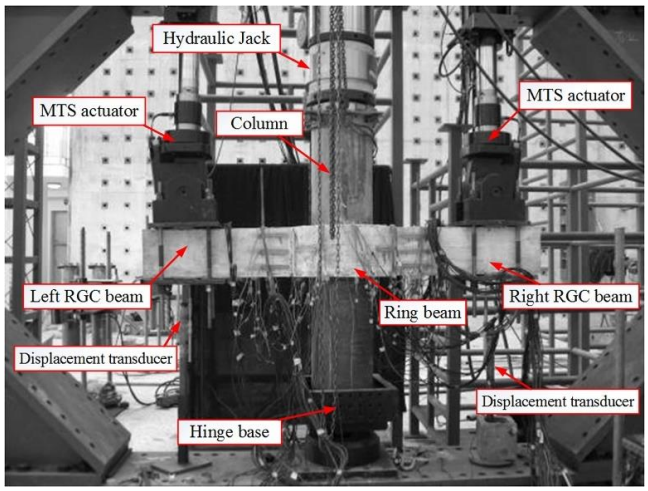

Fig. 3 Test setup

The cyclic load determined based on JGJ/T101-2015 [19] was applied at beam ends within two stages as shown in Fig. 4. At the force control stage, two cycles were employed using the load levels of $0.25P_y$, $0.50P_y$, $0.75P_y$ and $1.0P_y$ in both beam ends, where P_y is the estimated connection yield load under combined axial and cyclic loads and received from finite element models. In these specimens, P_y was close to the yield strength of RGC beam. As the cyclic load reached Py, the connection was determined to be yielded, and then the displace control was used to apply the cyclic loads. At the displacement control stage, displacement cycles with an increase rate of Δ_y were applied at the GRC beam ends, in which Δ_y represents the displacement obtained at P_y. Each displacement level had three displacement cycles before failure of the ring-beam connection. In the test, a 1-kN/s force rate was used at the force-control stage, and a 1-mm/s displacement rate was utilized at the displacement-control stage.

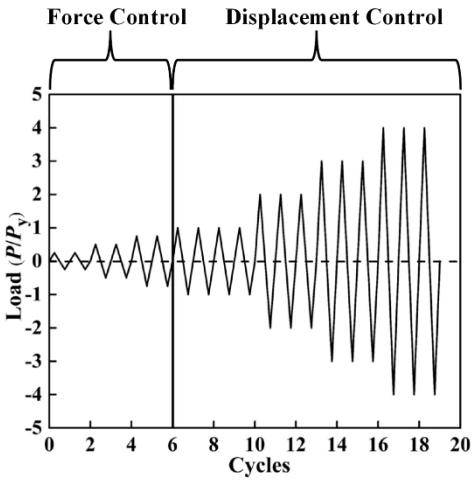

Fig. 4 Applied cyclic loading stage

The connection response was recorded and examined in the terms of the displacement of GCFST column, displacement and load at beam end, strains of concrete and reinforcing bars. Loads at both beam ends were measured using the transducers of MTS hydraulic actuators, and displacements were recorded using displacement transducers located below RCC beams. A displacement transducer was set at the top of the GCFST column to receive the column displacement. The dispacements at the RGC beams were recorded using two displacement transducers. strains for the steel tube, reinforcing bars, and coal-gangue concrete were obtained using several strain gauges. The locations of these displacement transducers are shown in Fig. 3.

2.4. Experimental observations

2.4.1. JH6-E-Z specimen

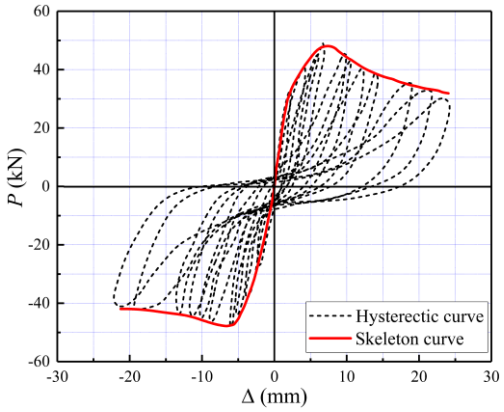

Fig. 5 Load-displacement curve for JH-E-Z connection

Fig. 5 illustrates the load-displacement time history for JH-E-Z connection. As shown in this figure, the specimen deformation demonstrated the linear characteristics at the beginning of testing, and cracking did not occur to the connection. When the cyclic force in the beams ends reached 13 kN, the first crack was observed at the end of the frame beam in the vicinity of ring beam. The 0.05 mm wide first crack was perpendicular to RGC frame beam. As the cyclic load increased to 19 kN, the concrete cracks were 0.1 mm in width and shown at the ring beam bottom. Concrete cracking was developed along the radial direction of ring beam. With the increased cyclic load, the vertical cracks and the diagonal cracks were shown in the side of ring beam. Diagonal cracks were propagated from the junction between ring beam and frame beam to the ring beam side as the cyclic load approached to 24 kN. It was clear that a wide crack along the beam depth was observed in the junction between the ring beam and the frame beam. This specimen was yielded at this load. After the yield load, the displacement control was used to impose the cyclic displacement in both beam ends. When the cyclic displacement increased to $2\Delta_y$, the composite connection reached its ultimate load bearing capacity. As the cyclic displacement increased, new cracks were created on the sides of the ring beam and the frame beam. At the cyclic displacement of $5\Delta_y$, the ring beam experienced significant concrete spalling, with the formation of lantern-shaped cracks in the ring beam side. The reinforcing bars of the connection were exposed. Failure modes of the specimen JH6-E-Z were shown in Fig. 6.

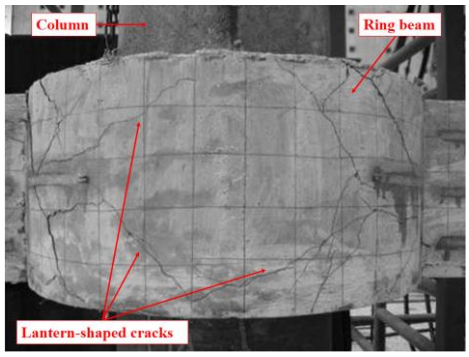

(a) Front side

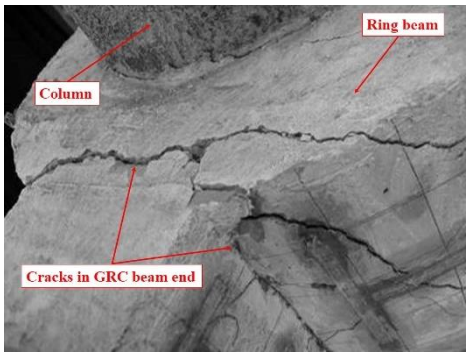

(b) Top side

Fig. 6 Failure mode for JH-E-Z connection

2.4.2. JH6-E-B specimen

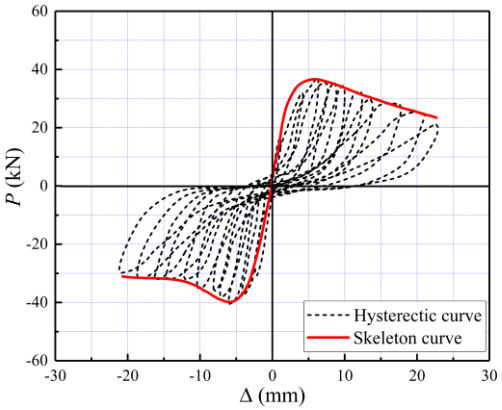

Fig. 7 Load-displacement curve for JH-E-B connection

Fig. 7 shows load-displacement time history for JH-E-B connection. The composite connection showed an elastic behavior, and the crack was not observed when the cyclic load was less than 10 kN at the force control phase. When the cyclic load increased to 11 kN, first vertical crack was noted at the ends of the frame beams. The width of the first crack was measured about 0.05 mm. The crack in the frame beam was developed to diagonal cracks from the beam bottom when the connection was subjected to cyclic load of 16 kN. These cracks were approximately 0.1 mm in width. The increase in the cyclic load resulted in the development of new cracks in the beam sides and the propagation of diagonal cracks to the ring beam side. A wide crack through the frame beam height was generated in the frame beam region that was close to ring beam at a cyclic load of 21 kN. This load was regarded as the yield load for this connection specimen. The displacement at the yield load was specified as the yield displacement for this connection specimen. After the yield load, the test was transferred to be at the displacement control phase. The existing cracks were increased and widened with the increase in the cyclic displacement. At the cyclic displacement of $2\Delta_y$, a plastic hinge was developed in the ends of the frame beams with the occurrence of ultimate connection capacity. When the cyclic displacement increased to $5\Delta_y$, the ring beam experienced concrete spalling in the vicinity of frame beam, with the formation of lantern-shaped cracks in the ring beam side. The reinforcements in the region of the plastic hinge were exposed. Fig. 8 shows failure modes for the J6-E-B specimen.

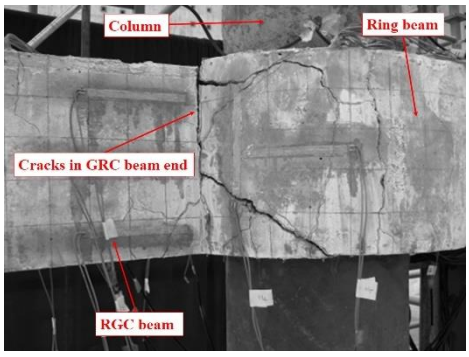

(a) Front side

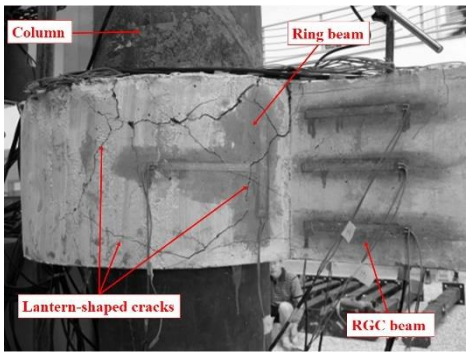

(b) Back side

Fig. 8 Failure mode for JH-E-B connection

3. Finite element model

3.1. Material constitutive model

3.1.1. Concrete

The concrete behavior under cyclic loading was modeled using the ABAQUS concrete plastic damage model, which is capable of simulating stiffness and strength degradation [20]. The core gangue concrete filled in tube was subjected to three-dimensional compressive stress due to tube confinement effect. The response of the confined coal-gangue concrete was simulated using the constitutive model for light-aggregate concrete filled steel tube provided by Fu, as shown in Eq (1).

$$\sigma = \sigma_0 \left[A\left(\frac{\varepsilon}{\varepsilon_0}\right) - B\left(\frac{\varepsilon}{\varepsilon_0}\right)^2 \right] \qquad (\varepsilon \le \varepsilon_0) \tag{1-a}$$

$$\sigma = \begin{cases} \sigma_0 (1-q) + \sigma_0 q \left(\dfrac{\varepsilon}{\varepsilon_0}\right)^{0.1\xi} & [\xi \ge 1.22] \\ \sigma_0 \left(\dfrac{\varepsilon}{\varepsilon_0}\right) \dfrac{1}{\beta\left(\dfrac{\varepsilon}{\varepsilon_0} - 1\right)^2 + \left(\dfrac{\varepsilon}{\varepsilon_0}\right)} & [\xi < 1.22] \end{cases} \qquad (\varepsilon > \varepsilon_0) \tag{1-b}$$

The details of the constitutive model were provided in the related research study. For the unconfined gangue concrete, a constitutive model of the light aggregate concrete developed by Zhang and Cao [21] was used in this study, as illustrated in Fig. 9. This material model can ensure accurate representation of failure modes obtained in the experimental tests and computation convergence during the simulation.

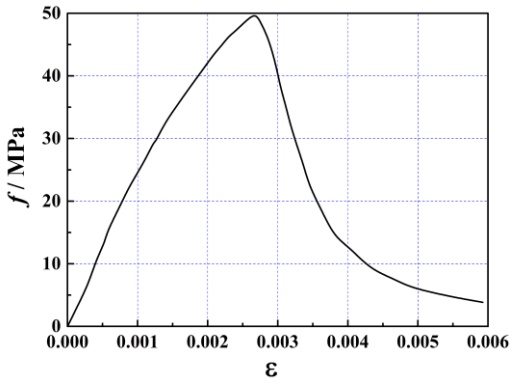

Fig. 9 Constitutive model for unconfined concrete

The concrete damage was represented through the development of the damage variable (d_c), which is in a range from 0 to 1 [22]. The unit of the damage variable indicates the total loss of stiffness and strength in concrete. The concrete damage variable can be calculated using Eq. (2) and incorporated in ABAQUS.

$$d_e = 1 - \frac{\sigma_c + n_c \sigma_{cu}}{E_c\left(\dfrac{n_c \sigma_{cu}}{E_c} + \varepsilon_c\right)} \tag{1}$$

where σ_{cu} is the ultimate compressive stress; σ_c is the compressive stress on the material; E_c is the concrete Yong's modulus; ε_c is the compressive strain; and n_c is the constant factors for compression and should be larger than 0. Based on extensive trials and previous research, n_c is taken to 2 for the confined gangue concrete in GCFST column when subjected to compressive force. n_c was taken to 1 for the unconfined gangue concrete in GC beam. The compressive stiffness recovery factor (w_c) was taken to 0 in the simulations. For the concrete brittle behavior under tension, the fracture energy cracking criterion was used in this model by specifying a fracture energy-cracking displacement curve [23], as illustrated in Eq. (3).

$$G_f = a\left(\frac{f_c'}{10}\right)^{0.7} \times 10^{-3} \quad (3)$$

where a=1.25d_{max}+10; d_{max} represents the maximum coarse aggregate diameter; and f_c' is the gangue concrete compressive strength.

3.1.2. Steel

Given the Bauschinger effects on the composite member response, a kinematic hardening model [24] was employed to represent the steel constitutive model of tube, as shown in Fig. 10. This model was incorporated with an plastic flow rule using a von Mises yield surface. Based on computation trials, the cyclic response of the reinforcement embedded in the concrete was modeled using a double linear model (USTEEL02) [25] developed by Tsinghua University to ensure computation convergence and accurate simulation results. This model (USTEEL02) demonstrates its ability to consider the deterioration of steel capacity for the hysteretic response and provide a reasonable representation of bond slip [26].

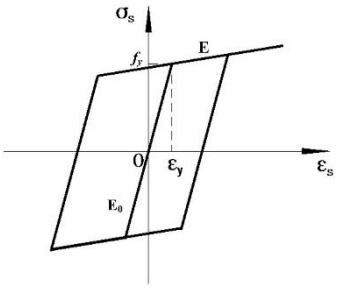

Fig. 10 Constitutive model for steel

3.2. Element formuation and contact model

The coal-gangue concrete and the rigid plates that were placed at the top and base of the GCFST column were modeled using an 8-node, reduced-integration, solid element (C3D8R). A 4-node, continuous, reduced-integration, shell element (S4R) was employed to create steel tube [23]. A truss element was used to model reinforcements embedded in RGC beams. A constraint-based coupling was used to develop the contact between the reinforcement and its surrounding concrete using embedded region constraints in ABAQUS. Fig. 11 shows the ring-beam connection model. The accuracy of finite element model depends on the proper mesh density. The mesh size for the core part of the connection was refined with the increased mesh density for other parts. The mesh sizes of steel tube and confinded coal-gangue concrete were identical to make computation convergence easy.

The tube-to-concrete contact consists of the tangential bond-slip interation and the normal contact [27]. For this model, the tube-concrete bond-slip was modeled using Mohr-Coulomb friction model [23], and the tangential force was determined with a frictional coefficient was 0.6 using a penalty friction approach [28]. The normal contact behavior was simulated using ABAQUS's hard contact to fully transfer the interfacial stresses. In the experimental tests, two hinges were set at both column ends. The plate at the column end was assumed to be rigid in the model. The Poisson's ratio of the rigid plate was 0.0001 and the plate Yong's modulus 1×10^9 GPa. The contact between the plate and the tube was modeled using a shell-to-solid coupling model, and the core concrete-plate contact was simulated using the hard contact model. The cyclic load in the form of displacement was applied on the beam ends as shown in Fig. 11. To replicate experimental boundary conditions, all translations and rotations in X and Z axes were constrained at the column bottom. At the column top, X and Z axes rotations and X and Y axes translations were constrained to model the hinged boundary condition.

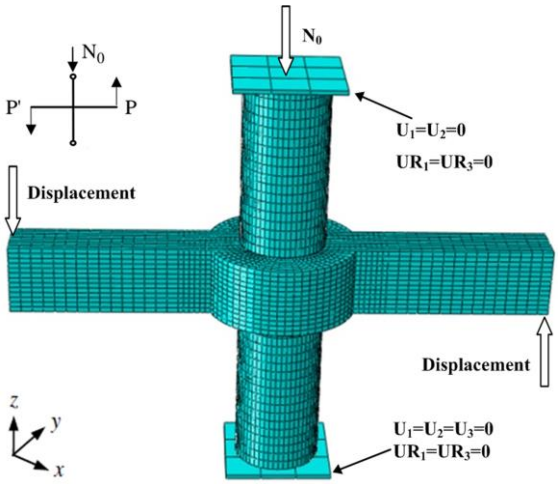

Fig. 11 Finie element model of ring-beam connection

3.3. FE model validation

3.3.1. Failure mode

A comparison of failure modes for the ring beam connection between finite element analyses and experimental tests was illustrated in Fig. 12. It was concluded that modeled failure modes achieved an acceptable agreement with tested modes. The ring-beam connection was damaged by the failure of RGC beams in the vicinity of ring beam, which matched well with experimental results. Experimental results identified that the lantern-shaped cracks were formed at ring beam side, which were observed in finite element models. In the experimental tests and finite element models, the GCFST column did not experience obvious damage. The ring beam connection to GCFST column was shown to exhibit adequate stiffness and strength against the cyclic loads. This finding satisfied the design philosophy in the seismic design code that mandates "strong column and week beam, strong connection and week members" [16].

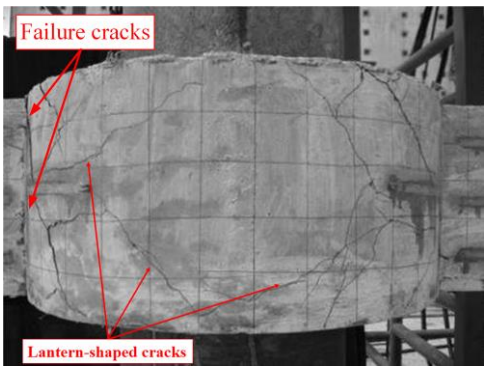

(a) Experiemntal observation

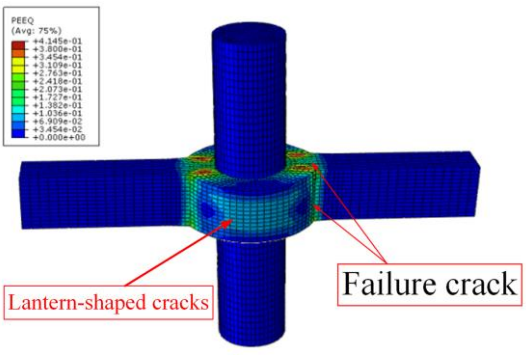

(b) Numerical results

Fig. 12 Finie element model of ring-beam connection

3.3.2. Load-displacement hysteretic curve

Fig. 13 illustrates a comparison of load (P) - displacement (Δ) curves for the ring beam connection between finite element models and experiment tests. P represents the load applied on both beam ends, and Δ is the frame beam deformation. The simulated P - Δ curve for the connection matched with the experimental curve in the terms of load, strength and stiffness degradation, and deformation. It was clear from Fig. 13 that, the stiffness degradation of ring beam connection in finite element analyses was close to those in experimental tests, and modeled strengths during the process of unloading and reloading were almost same with experimental values. The experimental curve was shown to have an obvious pinching shape, while modeled curve was relatively fuller than experimental curves. The shape of modeled curve was slightly different from experimental curve. The difference in curve shape would be caused by the deficiency of selected concrete constitutive model in simulating the large bond-slip between the reinforcements and surrounding concrete. Few research studies have been investigated on the constitutive model of the gangue concrete; therefore, a perfect concrete model was not located in the open literature. The simulated load-bearing capacity, deformation, and the strength and stiffness degradation agreed well with the tested resutls. Overall, the modeled curve obtained in simulations showed acceptable agreements with experimental curve. These FE model for the ring-beam connection were conservative but applicable to complete the research content and purpose.

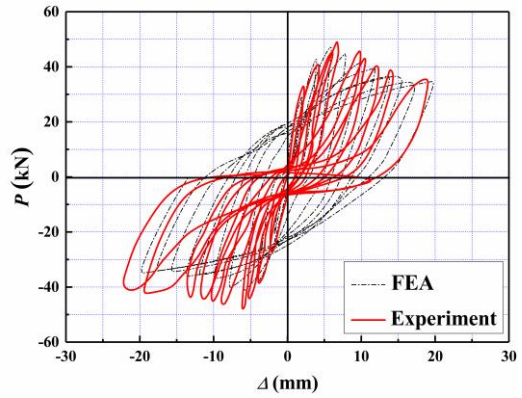

Fig. 13 Expeiremntal and simulated load-displacement curves

3.3.3. Skeleton curve

Fig. 14 compares the modeled and experimental skeleton curves for the ring-beam connection. The skeleton curve of the connection obtained in numerical simulation agreed well with experimental curve, with modeled peak value 10 % less than the recorded bearing capacity. Before the peak values, the modeled curve was identical with experimental curve. Again, the difference was due to the concrete model and simplified simulation of welding for various compnents. Overall, the developed numerical model provided conservative but acceptable predictions on failure mode and load-deformation response for the ring-beam connection under resverse cyclic loading.

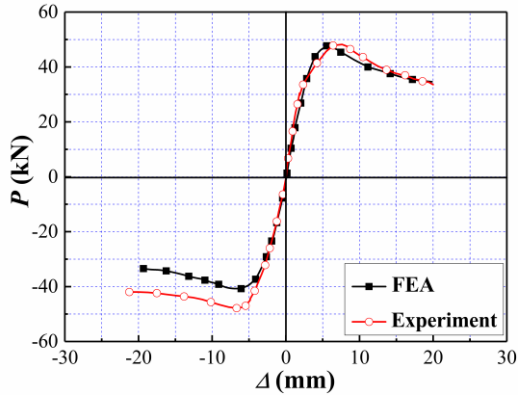

Fig. 14 Comparison of expeiremntal and simulated skeleton curves

The influences of axial load ratio on the ring beam connection behavior were analyzed with the variation of axial loads using the validated model. In this research study, finite element models with the different axial load levels were developed using the interior connection with two frame beams. In models of JH6-A-0.2 and JH6-A-0.8, the axial load was changed to develop additional models with n = 0.2 and 0.8, respectively. Table 3 lists the geometries and design detailing for the developed models.

Table 3
Geometries and design details for developed models

Specimen	$D\times t$ (mm)	H (m)	L (m)	b (m)	h (m)	A_{sf}	b' (m)	A_{sr}	hoop	n
JH-A-B	325×6	1.5	1	0.18	0.25	2Φ20	0.12	2Φ12	Φ10	0.6
JH-A-Z	325×6	1.5	2	0.18	0.25	2Φ20	0.12	2Φ12	Φ10	0.6
JH-A-0.2	325×6	1.5	2	0.18	0.25	2Φ20	0.12	2Φ12	Φ10	0.2
JH-A-0.2	325×6	1.5	2	0.18	0.25	2Φ20	0.12	2Φ12	Φ10	0.8

4. Analysis and results

4.1. Load bearing capacity

A standard method to determine yield point and failure load for the ring-beam connection has not been proposed in the open literature. The method used in the code JGJ/T101-2015 [19] for calculations of the yield strength and corresponding displacement in concrete members was selected for current study. Fig. 15 plots a typical P - Δ skeleton curve of the ring-beam connection. Point A is defined as initial yielding of the connection under cyclic loading. The connection initial yielding was found on the RGC beam. The displacement corresponds to the yield load (P_y) and is defined as the yield displacement (Δ_y). In the connection specimens, P_y approximates to the yield strength of longitudinal reinforcement embedded in the RGC beam. The peak load is the ultimate load (P_{max}) for the connetion at the peak point (B), with the appearance of the ultimate displacement (Δ_{max}). The connection failed at 85% of ultimate load (P_u = 0.85P_{max}), referenced as to the failure load at the point C, with a failure displacement (Δ_u).

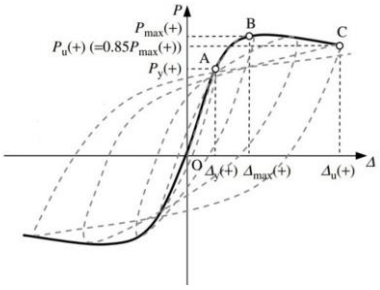

Fig. 15 Typical P-Δ skeleton curve for column-beam connection

Fig. 16 shows the load-displacement curves for these connection models. Table 4 lists critical loads and displacements for the ring-beam connection at points A, B, and C. It was concluded that, (1) Predicted bearing capacities at each stage obtained in finite element analyses were approximately 10% lower than experimental results. Before the ultimate bearing capacity, predicted displacements and loads were close to measured values in experimental tests. After the peak, predicted results were slightly less than the experimental results with the acceptable differences. (2) With an increase in the axial load magnitude, the connection ultimate capacity at n = 0.8 was 18.5% higher than that at n = 0.2 and was 1.1 times that at n = 0.6. The increase in the axial load magnitude at the column top provided a contribution to improving load-bearing capacity of the ring-beam connection. (3) For both experimental testing and numerical modeling, the yield strength, ultimate bearing capacity, and failure load of an exterior connection were larger than those of an interior connection. The exterior connection experienced more severe damage to RGC beam than the interior connection. (4) Overall, all critical displacements and loads were improved as the axial load magnitude increased. After the peak capacity, a higher decrease was shown in the bearing capacity of a connection when subjected to a larger axial load magnitude, and therefore the axial load level for a composite connection needed to be controlled in a reasonable range.

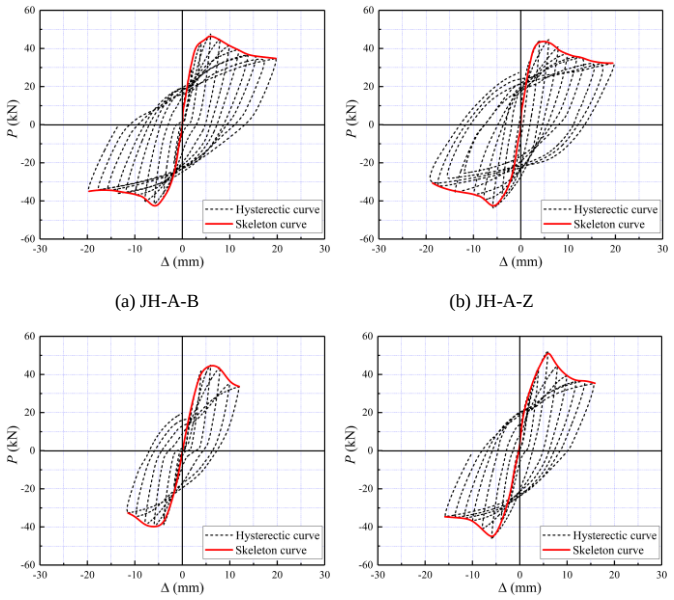

(a) JH-A-B (b) JH-A-Z

(c) JH-A-0.2 (d) JH-A-0.8

Fig. 16 Load-displacement curves for numerical connection models

Table 4
Ctcial loads and displacements at characteristic points

Specimen	N_0 (kN)	n	P_y (kN)	Δ_y (mm)	P_{max} (kN)	Δ_{max} (mm)	P_u (kN)	Δ_u (mm)
JH6-E-B	1800	0.6	21	1.9	39	6.2	32.7	11.4
JH6-E-Z	1800	0.6	24	2.1	49	6.4	42.6	12.7
JH6-A-B	1800	0.6	19	1.8	44.2	5.93	37.5	10.9
JH6-A-Z	1800	0.6	23.4	2.0	47.7	5.95	40.6	11.9
JH6-A-0.2	600	0.2	22.4	1.7	44.2	5.94	37.5	10.6
JH6-A-0.8	2500	0.8	29.4	2.2	52.5	6.0	44.6	11.6

4.2. Degradation of connection strength

The strength degradation of a column-to-beam connection is evaluated using a strength degradation coefficient [24]. The coefficient curve could be used to reflect the decrease of the load during testing and represent the characteristics of strength degradation for the ring-beam connection. The strength degradation coefficient for the column-to-beam conenction is calculated using Eq. (3).

$$\lambda_j = \frac{P_j}{P_{\max}} \tag{3}$$

where λ_j is the strength degradation of ring beam at total loads; P_j is the maximum load at the jth cycles when Δ/Δ_y at beam ends is j; and $P_{\max}$ is the ultimate connection capacity during the whole process of testing.

Fig. 17 illustrates the λ_j - Δ/Δ_y curves for the ring-beam connection. Fig. 17 indicates that, (1) Modeled curves matched well with tested results with respect to the changing trends and values, with the peak value 5% lower than experimental results. (2) After the connection reached its ultimate bearing capacity, a relatively long horizontal part was observed in the coefficient curve. The ring-beam connection possessed a large residual capacity to resist the cyclic loads after the connection experienced its failure load. The ring-beam connection exhibits desirable seismic performance for a building. (3) The strength degradation coefficient (λ_j) increased with the increas in the relative beam displacement when Δ/Δ_y was less than 3. As the relative beam displacement was larger than 3, the strength degradation coefficient began to decreasing. (4) An obvious strength degradation was shown to a connection with a higher axial load ratio. After the peak load, the strength degradation coefficient of the connection specimen was significantly reduced with the increased axial load magnitude.

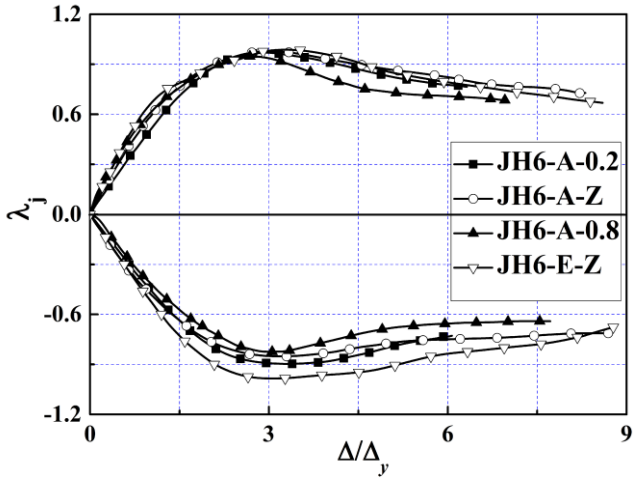

Fig. 17 Strength degradation curves for ring-beam connection

4.3. Degradation of connection stiffness

The concrete cumulative damage during cyclic loading would lead to the stiffness degradation of a column-beam connection [24]. The connection stiffness is defined in terms of maximum load and corresponding displacement at each loading cycle as expressed in Eq. (4).

$$K_j = \frac{\sum_{i=1}^{n} P_j^i}{\sum_{i=1}^{n} u_j^i} \tag{4}$$

where K_j is the stiffness of the column-beam connection; P^i_j is peak load at the jth cycle when the Δ/Δ_y in both beam ends is j; and u^i_j as maximum displacement at the jth cycle when Δ/Δ_y in both beam ends is j.

The connection stiffness (K_j) versus relative beam displacement curves are shown in Fig. 18. It was concluded from this figure that the stiffness degeneration of ring-beam connection was relatively slow, identifying its remarkable ability to resist the lateral sway. Furthermore, before the ultimate bearing capacity, the connection stiffness increased with the increased axial load magnitude. After that, the connection stiffness with a higher axial load magnitude reduced more significantly. The ring-beam connection at a higher axial load ratio experienced severer stiffness degeneration. The axial load ratio for the ring-beam connection should be desgined in a reasonable range to avoid an excessive stiffness degradation.

Overall, the ring-beam connection capacity gradually decreased after its ultimate load. The strength and stiffness degradation resulted in the comprosmised capacity of the ring-beam connection under cyclic loading. Primary factors which significantly affected the strength and stiffness degradation for the ring-beam connection included the elastic-plastic property and accumulative damage during cyclic loading. The damage was produced due to the formation and development of concrete cracking. The steel tube confinements on the coal-gangue concrete inhibited the propagation of crack. As a result, the confinement effect improved the strength and stiffness degradation of the ring-beam connection when subjected to cyclic loads.

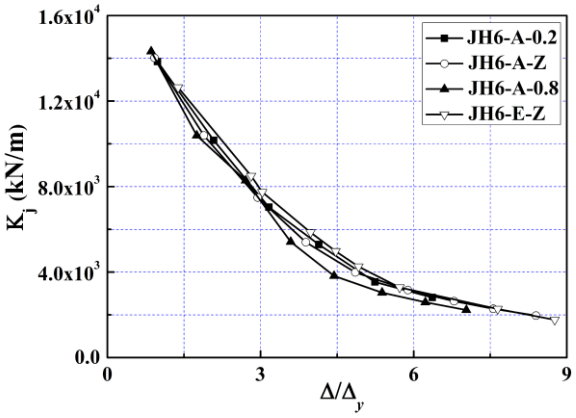

Fig. 18 Stiffness degradation curves for ring-beam connection

4.4. Ductility

The ductility is a physical property of RC structure which identifies its capacity of sustaining large permanent changes in shape. The ductility of a column-beam connection, a vital factor in the earthquake-resistant design, is evaluated using a displacement ductility coefficient [25]. The coefficient of displacement ductility (μ) is calculated using the yield and failure displacements as shown in Eq. (5).

$$\mu = \frac{\Delta_u}{\Delta_y} \tag{5}$$

in which Δ_u is failure displacement; and Δ_y is yield displacement. An angular ductility coefficient is used to evaluate the connection ductility, which is determined using yield and failure angular displacement, as shown in Eq. (6).

$$\mu_0 = \frac{\theta_u}{\theta_y} \tag{6}$$

where μ_0 is the angular displacement ductility coefficient; θ_y and θ_u is the yield and failure angular displacement, respectively. The displacement angle of the ring-beam connection (θ) can be calculated from $\theta = \arctan(\Delta/H)$ according to the code GB50011-2010 [16], in which H is the column height. Table 5 summarizes the tested and simulated ductility coefficients.

Table 5
Displacement and angular ductility coefficient

Specimen	n	Δ_y (mm)	Δ_u (mm)	μ	θ_y (rad)	θ_u (rad)	μ_0
JH6-E-B	0.6	1.9	11.4	6.0	0.0013	0.0076	5.98
JH6-E-Z	0.6	2.1	12.7	6.1	0.0014	0.0085	6.04
JH6-A-B	0.6	1.83	10.9	6.0	0.0012	0.0073	5.95
JH6-A-Z	0.6	2.02	11.9	5.9	0.0014	0.0079	5.87
JH6-A-0.2	0.2	1.75	10.6	6.1	0.0012	0.0071	6.04
JH6-A-0.8	0.8	2.21	11.6	5.3	0.0015	0.0077	5.24

It was observed from Table 5 that, (1) The displacement ductility coefficients of studied connections ranged from 5.0 to 6.1, which satisfied the principle that $\mu \geq 3$ for the RC structural components. (2) For the high-rise buildings, the design code GB50011-2010 [16] mandated the ductility limit, including an elastic angular displacement limit of 0.0033 rad, and an elastic-plastic angular displacement limit of 0.02 rad. According to Table 5, all angle displacement ductility coefficients of these studied connections satisfied requirements in the code. Results indicated that the ring-beam connection that connected the RGC beams and GCFST columns exhibited high ductility in a seismic event. (3) The ductility of the ring-beam connection slightly reduced as the axial load magnitude increased, as shown in Fig. 19. The influence of the axial load ratio was relatively insignificant to the ductility of the ring-beam connection.

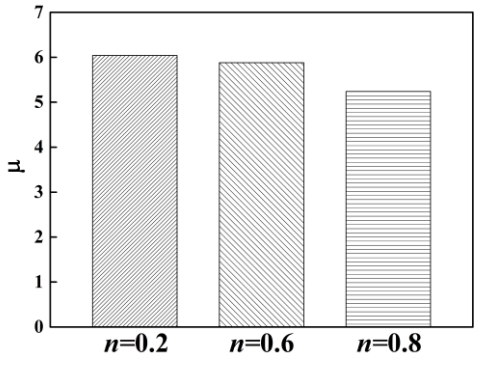

Fig. 19 Effect of axial load ratio on connection ductility

4.5. Energy dissipation

An equivalent damping coefficient and an energy dissipation coefficient recommended in JGJ/T101-2015 [19] were used to analyze the energy dissipation ability of the ring-beam connection that connected the RGC beams and GCFST columns in this study. An equivalent damping coefficient (h_e) is formulated in Eq. (7) and shown in Fig. 20.

$$h_e = \frac{1}{2\pi}\frac{S_{ABD} + S_{BCD}}{S_{OAE} + S_{OCF}} \tag{6}$$

where S_{ABD}, S_{BCD}, S_{OAE}, and S_{OCF} are areas below the corresponding curves ABD, BCD, OAE and OCF, respectively. The energy dissipation coefficient (E_{dc}) is a ratio of the total energy in a hysteretic loop to the elastic energy of the column-beam connection and calculated using $E_{dc} = 2\times\pi\times h_e$.

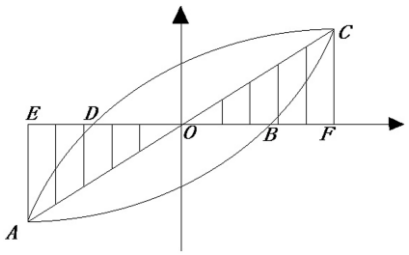

Fig. 20 Stiffness degradation curves for ring-beam connection

Table 6 lists the coefficients for the tested ring-beam connections. It was observed that the equivalent damping coefficients of all studied connections were ranged from 0.20 to 0.25. Based on the related research studies [25], the average equivalent damping coefficients were determined to 0.1 for a normal RC connection and 0.3 for a steel rigid connection. The equivalent damping coefficients of these tested connection specimens were better than the traditional RC connection, and less than the steel rigid connection. As the axial load ratio increased, the energy dissipation capacity of ring-beam connection between GCFST column and RGC beam was improved, and axial load ratio should be controlled within a reasonable range to ensure its desirable energy dissipation capacity in a seismic event. The energy dissipation coefficients of the studied ring-beam connections satisfied requirements in the seismic design code.

Table 6
Equivalent damaping coefficient for studied connections

	Specimen	n	h_e	E
Tests	JH6-E-B	0.6	0.20	1.23
	JH6-E-Z	0.6	0.25	1.57

5. Parametric studies

Parametric analysis was executed to examine the effects of material and structural parameter on the ring-beam connection response to quasi-static loads. The parameters considered in this study included: (i) axial load ratio (n); (ii) column steel ratio (α); (iii) ring beam width (b_0); (iv) confined concrete strength ($f'_{c,c}$); (vi) column slenderness ratio (λ); and (vii) column-beam stiffness ratio;); and (v) unconfined concrete strength ($f'_{c,b}$). Fig. 21 shows the results of the parametric studies, in which JH6-A-Z was used as the baseline model.

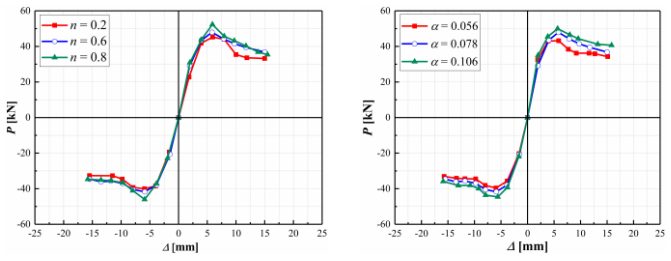

(a) axial load ratio (b) column steel ratio

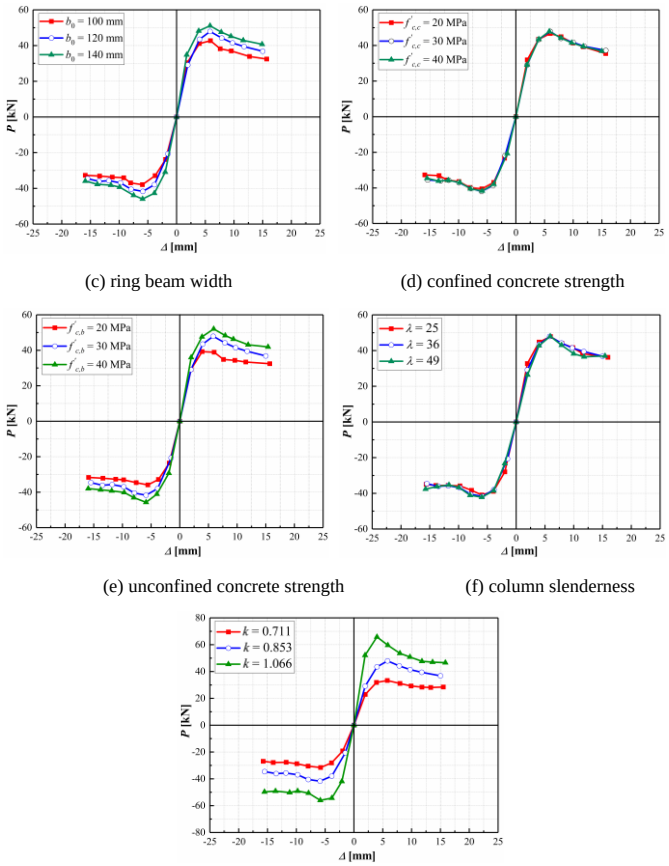

Fig. 21 Skeletion curves with effects of studied parameters

Fig. 21 (a) illustrates that, as the axial load ration increased, the load-bearing capacity of the ring-beam connection was improved. The peak load for the connection at n = 0.8 was 10.1% and 18.8% higher than that at n = 0.6 and 0.2, respectively. The increase in the preload magnitude at the top of the GCFST column resulted in the improved bending strength of the column, which contributes to the increased resistance and capacity of the ring-beam connection.

Fig. 21 (b) shows that the increase in column steel ratio led to the improvement in the connection load-bearing capacity. The peak load for the connection was increased by 11% and 4% when λ increased from 0.056 to 0.078 and from 0.078 to 0.106, respectively. The strength of the confined concrete was improved with the increased tube confinement as the steel ratio increased, resulting in the enhanced load-bearing capacity of the ring-beam connection.

Fig. 21 (c) indicates that the increase in the ring beam width resulted in the improvement of the ring-beam connection capacity. When the width increased from 100 mm to 140 mm, the peak load was improved by 19.7%. A reasonable increase in the width of the circular ring beam improves its ability to transfer internal forces to the GCFST column, which contributes to the capacity resistance of the ring-beam connection.

It was observed from Fig. 21 (d) and (f) that the influences of confined concrete strength and the column slenderness ratio were insignificant for the connection behaviors. The ring-beam connection was designed in accordance with the specifications of current codes in which the beam should be weaker than the column in the earthquake event with the intact column. Thus, the connection behavior did not significantly change with the variations of the confined concrete strength and column slenderness ratio.

Fig. 21 (e) shows that the connection capacity was improved when the unconfined concrete strength in the beam increased. The peak load for the connection with $f'_{c,b}$ = 40 MPa was 8.6% and 32.6% higher than that for $f'_{c,b}$ = 30 MPa and $f'_{c,b}$ = 20 MPa, respectively. The connection with the higher strength unconfined concrete would possess larger resistance against cyclic loads with the formation of cracks. It was seen from Fig. 21 (g) that the connection capacity was enhanced when the column-beam stiffness ratio increased. The peak load was improved by 43.8% with the increase of k from 0.771 to 0.853, and the peak load increased by 37.4% when k increased from 0.853 to 1.066.

6. Development of restoring force model

For the design purpose, seismic behavior of structural components and system can be theoretically examined using a restoring force model. The restoring force model of a structural component represents the theoretical relation between the restoring force and the deformation, which can demonstrate the structural response in the seismic event including the load-bearing capacity, degradation of strength and stiffness, ability to dissipate energy, and deformation resistance. Numerical results in parametric studies were used to derive the restoring force model of skeleton curve for the ring-beam connection to GCFST column. The maximum load-bearing capacity (P_m) and its corresponding deformation (Δ_m) were utilized as the refence point in the study to simply the comparison and development of theoretical equation. The skeleton curves of the connections considering effects of various parameters were normalized by the reference strength and deflection, as illustrated in Fig. 22, in which the skeleton curves for various connections exhibited the similar trend involving three distinct segments: linear elastic stage, plastic-hardening stage, and reducing stage.

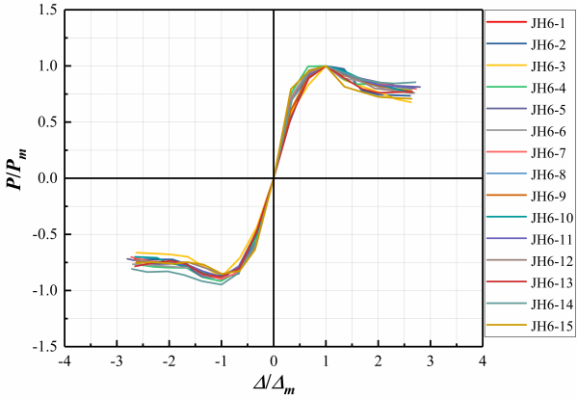

Fig. 22 Normalized skeleton curves for ring-beam connection

Based on the observations and related studies, a three-fold multilinear model was used to represent the restoring force model of skeleton curve for the cyclic-loaded ring-beam connection between the RGC beams and GCFST column. The regression analysis of numerical results from parametric studies was conducted to determine the three-fold multilinear model with the characteristic points, as illustrated in Fig. 23. According to the reference point, the $P/P_m - \Delta/\Delta_m$ interaction relation with six linear segments was developed, as shown in Eqs. (7) – (8).

(a) OABC stage

$$\frac{P}{P_m}=\begin{cases}2.2\times\dfrac{\Delta}{\Delta_m} & \text{OA segement}\\ 0.53\times\dfrac{\Delta}{\Delta_m}+0.51 & \text{AB segment}\\ 1.24-0.2\times\dfrac{\Delta}{\Delta_m} & \text{BC segment}\end{cases} \tag{7}$$

(b) OA′B′C′ stage

$$\frac{P}{P_m}=\begin{cases}1.8\times\dfrac{\Delta}{\Delta_m} & \text{OA}'\text{ segement}\\ 0.52\times\dfrac{\Delta}{\Delta_m}-0.38 & \text{A}'\text{B}'\text{ segment}\\ -0.98-0.09\times\dfrac{\Delta}{\Delta_m} & \text{B}'\text{C}'\text{ segment}\end{cases} \tag{8}$$

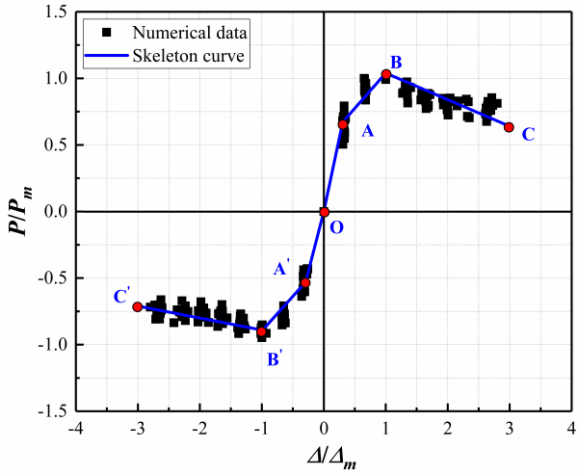

Fig. 23 Restoring force model of skeleton curves

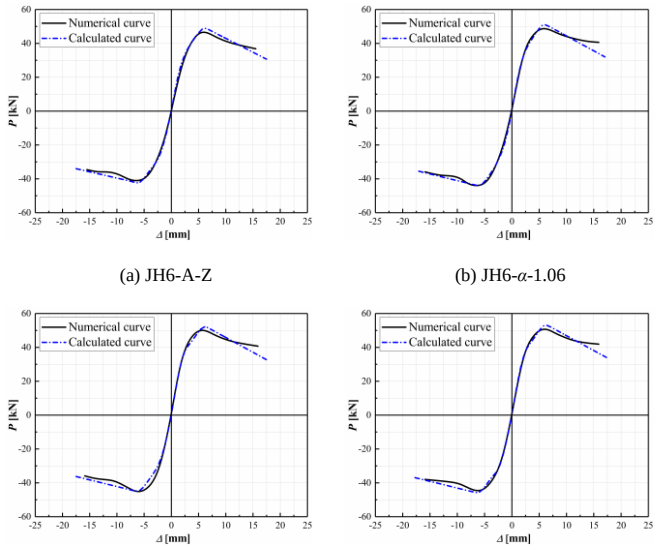

(a) JH6-A-Z (b) JH6-α-1.06

(c) JH6-b_0-1.06 (b) JH6-$f'_{c,b}$ -40

Fig. 24 Comparison of numerical and calculated skeleton curves

The developed three-fold multilinear model is useful to predict the restoring force model of skeleton curve for the ring-beam connection between RGC beams and GCFST column using the ultimate capacity and corresponding deformation when subjected to the cyclic loads. Fig. 24 compares the predicted and numerical skeleton curves for several cases. As shown in Fig. 24, the predicted skeleton curves reasonably matched with numerical results, indicating the feasibility of the developed restoring force model for the ring-beam connection. The comparison results also demonstrated the ability of the developed model to represent the deformation-cyclic load interactions for the ring-beam connection, which provides application and design suggestions of this composite connection for engineering applications.

7. Conclusions

This study conducted investigations that investigated seismic behavior of the ring-beam connection that connected the RGC beams to the GCFST column. Several behavioral indexes were examined to evalute its performance in the seismic event. The conclusions were obtained:

• The ring-beam connection that connected RGC beams to GCFST column with the full spindle-shaped hysteretic curve exhibits reasonable strength and stiffness degradation. The ring-beam connection failed with the development of a plastic hinge in RGC beam, which satisfied the requirements of the design principles that “strong column and week beams”. The ring-beam connection exhibited acceptable seismic behaviors.

• The displacement ductility coefficient for the studied ring-beam connections were higher than 5, which satisfies the seismic design requirement that the displacement ductility coefficient should be higher than 3. The angle displacement ductility coefficients of examined ring-beam connections also were larger than the required limit in the code. The equivalent damping coefficient of ring-beam connection was in a range of 0.1~0.3, which is higher than that obtained from normal RC component. The study results showed that the ring-beam connection between RGC beams and GCFST column could be effectively applied in the seismic regions.

• Detailed parametric studies indicated that the ring-beam connection seismic behaivor was significantly affected by steel ratio, ring beam width, unconfined concrete strength, and column-beam stiffness ratio. The load-bearing capacity of the ring-beam connection was improved as the steel ratio, unconfined concrete strength for the RGC beam, ring beam width, and column-beam stiffness ratio increased. The effects of the confined concrete strength and column slenderness ratio were insignificant to the connection resistance due to the seismic design fundamentals.

• A restoring force model of skeleton curve for the ring-beam connection that connected the RGC beams to the GCFST columns was developed using a three-fold multilinear model through regression analysis. The accuracy of the developed three-fold multilinear model was also validated by comparing with simulated results. This restoring force model effectively represents the load-deformation interaction relation for the ring beam connection under cyclic loading.

Acknowledgments

The authors would like to acknowledge supports for this research from the Key Projects of National Natural Science Foundation of China, China (51938009), National Natural Science Foundation of China, China (51878419) and (51578345), Natural Science Foundation of Jiangsu Province (BK20200996), and China Postdoctoral Science Foundation (2020M681566).

References

[1] Li G., Fang C., An Y., and Zhao X. (2015). "Seismic Behavior of Rebar-Penetrated Joint between GCFST Column and RGC Beam." Steel and Composite Structures, 19(3), 547-567.
[2] AL-Eliwi B.J., Ekmekyapar T., Faraj R.H., Gogus M.T., and AL-Shaar A.A. (2017). "Performance of lightweight aggregate and self-compacted concrete-filled steel tube columns." Steel and Composite Structures, 25(3), 299-314.
[3] Yu X., Tao Z., and Song T.-Y. (2016). "Effect of different types of aggregates on the performance of concrete-filled steel tubular stub columns." Materials and Structures, 49(9), 3591-3605.
[4] Li G.C., and Zhong S.T. (2002). "Strength and Lateral Deformation Coefficient of Gangue Concrete Restrained by Steel Tube." Harbin Jianzhu Daxue Xuebao/Journal of the Harbin University of Civil Engineering and Architecture, 35(3), 20-23.
[5] Nelson A.J., Rakau O., and Dörrenberg P. (2010). "Green Buildings: A Niche Becomes Mainstream."
[6] Wang C.L., Ni W., Zhang S.Q., Wang S., Gai G.S., and Wang W.K. (2016). "Preparation and properties of autoclaved aerated concrete using coal gangue and iron ore tailings." Construction and Building Materials, 104, 109-115.
[7] Miller D.K. (1998). "Lessons learned from the Northridge earthquake." Engineering Structures, 20(4), 249-260.
[8] Zhao B., Taucer F., and Rossetto T. (2009). "Field Investigation on the Performance of Building Structures during the 12 May 2008 Wenchuan Earthquake in China." Engineering Structures, 31(8), 1707-1723.
[9] Goldsworthy H., and Gardner A. (2006). "Feasibility study for blind-bolted connections to concrete-filled circular steel tubular columns." Structural Engineering and Mechanics, 24(4), 463-478.
[10] Kataoka M.N., and de Cresce El A.L.H. (2015). "Beam–column composite connections under cyclic loading: an experimental study." Materials and Structures, 48(4), 929-946.
[11] Agheshlui H., Goldsworthy H., Gad E., and Mirza O. (2017). "Anchored blind bolted composite connection to a concrete filled steel tubular column." Steel and Composite Structures, 23(1), 115-130.
[12] Tizani W., Wang Z.Y., and Hajirasouliha I. (2013). "Hysteretic performance of a new blind bolted connection to concrete filled columns under cyclic loading: An experimental investigation." Engineering Structures, 46, 535-546.
[13] Khanouki M.A., Sulong N.R., Shariati M., and Tahir M. (2016). "Investigation of through beam connection to concrete filled circular steel tube (CFCST) column." Journal of Constructional Steel Research, 121, 144-162.
[14] Choi S.-M., Park S.-H., Yun Y.-S., and Kim J.-H. (2010). "A study on the seismic performance of concrete-filled square steel tube column-to-beam connections reinforced with asymmetric lower diaphragms." Journal of Constructional Steel Research, 66(7), 962-970.
[15] CECS28-2012 (2013). "Technical Specification for Concrete-Filled Steel Tubular Structures."Beijing, China.
[16] GB50011-2010 (2011). "Code for Seismic Design of Buildings." Chinese Building Press, Beijing, China.
[17] GB/T228-2002 (2003). "Code of Metallic Materials—Tensile Testing at Ambient Temperature."Beijing, China.
[18] GB/T50081-2002 (2003). "Standard for Test Method of Mechanical Properties on Ordinary Concrete."Beijing, China.
[19] JGJ/T101-2015 (2015). "Specification of Testing Methods for Aseismic Property of Building." China Building Industry Press, Beijing, China.
[20] Yu T., Teng J., Wong Y., and Dong S. (2010). "Finite element modeling of confined concrete-II: Plastic-damage model." Engineering structures, 32(3), 680-691.
[21] Zhang J.W., and Cao S.Y. (2009). "Research on the Stress-Strain Curves of Structural Lightweight Aggregate Concrete." Building Science, 24(11), 83-85.
[22] Li W., and Han L.H. (2011). "Seismic Performance of CFST Column to Steel Beam Joints with RC Slab: Analysis " Journal of Constructional Steel Research, 67(1), 127-139.

[23] Sorenson H.K. (2003). "ABAQUS version 6.4: theory manual, users' manual, verification manual and example problems manual." Hibbitt, Karlson, Sorenson Inc. USA.
[24] Han L.H. (2004). "Concrete-filled steel tubular structure-theory and practice." Science Press, Beijing.
[25] Lu X.Z., Ye L.P., and Miu Z.W. (2009). Static-Plastic Analysis on Seismic Performance of Buildings, China Architecture & Industry Press, Beijing, China.
[26] Li G.C., Fang C., Zhao X., An Y.W., and Liu Y. (2015). "Cyclic Behavior of Rebar-Penetrated Connection between Gangue Concrete Filled Steel Tubular Column and Reinforced Gangue Concrete Beam." Advanced Steel Construction, 11(1), 54-72.
[27] Wan C.Y., and Zha X.X. (2016). "Nonlinear analysis and design of concrete-filled dual steel tubular columns under axial loading." Steel and Composite Structures, 20(3), 571-597.
[28] Johnson R.P. (2008). Composite structures of steel and concrete: beams, slabs, columns, and frames for buildings, John Wiley & Sons.

Advanced Steel Construction – Vol. 18 No. 1 (2022) 517–527
DOI:10.18057/IJASC.2022.18.1.10

LOW-CYCLE FATIGUE PROPERTIES OF AUSTENITIC STAINLESS STEEL S30408 UNDER LARGE PLASTIC STRAIN AMPLITUDE

Lei Chen [1, 2], Dong-Sheng Wang [1, 2, *], Fan Shi [1, 2] and Zhi-Guo Sun [3]

[1] *School of Civil and Transportation Engineering, Hebei University of Technology, Tianjin 300401, China*
[2] *Civil Engineering Technology Research Center of Hebei Province, Tianjin 300401, China*
[3] *Key Laboratory of Building Collapse Mechanism and Disaster Prevention, Institute of Disaster Prevention, China Earthquake Administration, Beijing 101601, China*
** (Corresponding author: E-mail: dswang@hebut.edu.cn)*

ABSTRACT

The application of stainless steel materials in civil structures for seismic protection lies in its low-cycle fatigue characteristic. However, the data of existing research are mainly based on the low-cycle fatigue in small strain amplitudes. To this end, we perform low-cycle fatigue testing of Austenitic stainless steel S30408, which has low yield point and good elongation performance, under the cyclic load with a maximum strain amplitude reaching up to 5%, to fill the gap. The stress-strain response characteristics of the stainless steel material under the cyclic load are analyzed; then, the parameters of the strain-fatigue life relationship and the cyclic-plastic constitutive model used for FEA simulation are extracted. Results show that the stainless steel's stress-strain curve is nonlinear without a yield plateau, thus presenting a high strength yield ratio and ductility. The hysteresis loops of the material are plump with a shuttle shape and are symmetric to the origin, indicating a fine energy dissipation capacity. The skeleton curve under cyclic loading with cyclic hardening can be significantly reflected by the Ramberg-Osgood model, which is affected by the strain amplitude and loading history; it is also different from the monotonic tensile skeleton curve. The strain-fatigue life curve fitted by the Baqusin-Manson-Coffin model can predict the materials' fatigue life under different strain amplitudes. The mixed hardening model, including isotropic and kinematic hardening, based on the Chaboche model, is able to simulate the cyclic stress-strain relationship. Further, its parameters can provide basic data information for the seismic design of civil structures when Austenitic stainless steel S30408 is used.

ARTICLE HISTORY

Received: 28 April 2021
Revised: 30 May 2021
Accepted: 22 July 2021

KEYWORDS

Austenitic stainless steel;
Low-cycle fatigue;
Cyclic stress-strain response;
Strain-fatigue life;
Mixed hardening;
Chaboche model

1. Introduction

The advantages of stainless steel materials, such as strong corrosion resistance, good ductility, and easy processing, have made it not only useful in the tableware, sculpture, and automobile fields but also in civil structures like bridges, ports, and underground projects [1, 2]. For example, 8,200 tons of stainless steel bars were applied to construct pile caps, tower seats, and piers for the Hong Kong-Zhuhai-Macao Bridge [3]. Stainless steel can also significantly reduce costs associated with durability maintenance and improve economic efficiency over a structure's entire life cycle.

The capability design criterion in the seismic design of structures allows designers to make full use of energy dissipation components or regions to reduce seismic responses by employing the elastoplastic hysteretic properties of materials with a rational design [4]. Under seismic loading, structures usually need to withstand short-term and huge reciprocating forces. Structural members, especially those acting as dissipation components [5], experience several large displacement cyclic loadings, which are manifested by low-cycle fatigue (LCF) with large strains at the material level. Therefore, it acts as a basis in which to investigate the stainless steel material's low-cycle fatigue performance for application in structural seismic design.

In previous studies, stainless steel exhibited an obvious nonlinear stress-strain relationship, and it is different from that of typical plain steel. Arrayago et al. [6] compiled 600 monotonic tensile tests for ferritic, austenitic, and duplex stainless steels, including grades and rolling directions of a variety of materials. They then proposed amendments for the prediction of model constitutive parameters. Under cyclic loading, the hysteresis loop of stainless steel material is plump and stable, indicating a fine hysteresis behavior; further, the cyclic skeleton curve is different from the monotonic tensile curve tension, showing an obvious strain hardening phenomenon [7-9]. In addition, it has been revealed that the cyclic hardening characteristics are greatly affected by plastic strain amplitude as well as the loading process. Further, the history and amplitude of the first load before the next cycle can influence the cyclic stress-strain curve [10, 11]. The number of times the test piece can withstand cyclic loading, i.e., the fatigue life of coupons, is a factor to be considered in its application. Julie et al. analyzed the strain-fatigue life relationship of stainless steel materials with strain below 2.0% and introduced a prediction formula for fatigue life [12, 13]. Accurate material constitutive models and parameters are the foundation for structural design and seismic performance analysis of structures. Stainless steel presents mixed hardening characteristics when reciprocated loading is applied [14]. In addition, the Chaboche constitutive model is well used currently, and its applicability have been studied by some researchers [15, 16].

Austenitic and Duplex stainless steel, which have different low-cycle fatigue characteristics, are mainly used in structures. Austenitic stainless steel with low yield point and good elongation performance has the advantage of corrosion-resistance and characteristic of low yield point steel [17]. For a high production capacity and widely used austenitic stainless steel, S30408, has good cold working performance, high toughness and good high-temperature resistance. In general corrosion, it can satisfy the requirements of corrosion resistance [18]. And the price of S30408 is lower, which represents that it is more conducive to the use and promotion of structures. It is an optimal material choice under the consideration of reliable durability performance and cost economy. In structural seismic design, it is frequently used in energy-dissipating devices, as the core of a buckling-restrained brace (BRB), where its design interface mostly consists of plate specimens [19, 20]. These devices need to withstand large plastic deformations under seismic loads [21]. However, previous studies on materials, to the best of our knowledge, have mostly focused on small strain high- or low-cycle fatigue of round bars, which cannot satisfy the needs of seismic design. Fewer studies about cyclic loading and fatigue life of plate specimens had been reported.

Therefore, three types of Austenitic stainless steel S30408 specimens, including plates and bars, are considered in this study. Three loading systems, consisting of monotonic tensile, constant, and variable strain amplitude cyclic loading with the strain amplitude reaching up to 5%, are carried out to analyze the material's characteristics. The key mechanical indexes and constitutive parameters of the monotonic model are determined through a uniaxial tensile test. We adopt the Ramberg-Osgood model to depict the cyclic hardening performance and also use it to fit the cyclic skeleton curves for obtaining the cyclic hardening parameters. The Baqusin-Manson-Coffin model is utilized to fit the strain-fatigue life equation under constant strain amplitude cyclic loading. For the variable strain amplitude cyclic loading, the Chaboche constitutive model adopted from Abaqus is used to derive the mixed hardening parameters and simulate the cyclic stress-strain relationship. The test pieces used in this test were all from the same batch.

2. Experimental details

2.1. Material and coupon specifications

Austenitic stainless steel S30408, which is being increasingly applied in buildings, bridges, energy dissipation components, and so forth, was tested in the present study. The chemical components of the stainless steel material are tabulated in Table 1. The specimens were fabricated from the same batch of material along the same orientation into flat and round coupons, including a reduced effective section area in a central region, to constrain the location of the

fracture and a smaller length of the parallel section to avoid buckling [7, 22]. Three kinds of test coupons with different specifications and sizes, defined as LF, SF, and CF, were manufactured based on the Chinese National Standard GB/T26077 [25], and their cross-section forms are a rectangle, square, and circle, respectively, as presented in Fig. 1. The length and thickness of the parallel section for LF coupons is 40 mm and 8 mm, respectively, leading to a sectional length-to-width ratio of 5. To avoid compressive buckling instability in the LF specimen, a buckling-restrained device was designed and then given a heat treatment to ensure hardness. Sandpaper was used to polish the section to reduce the roughness; grease and boron nitride powder were applied on the splint to reduce friction between the test piece and the buckling-restrained device. The SF coupons have a section width of 16 mm with a parallel segment length of 25 mm. And the CF coupons have a section diameter of 20 mm with a parallel segment length of 25 mm.

To accurately apply displacement and prevent the extensometer from sliding under large strain loading, two notches with the width and depth all equal to 0.2 mm were carved along the width direction of the coupons, as shown in Fig. 1. Their locations are at the tip of the extensometer fixed on the specimen. Another, coupon LF´, had the same size as the LF specimen, but for comparison no notch was carved.

Table 1
Chemical components of austenitic S30408

Chemicals	C	Si	Mn	P	S	Cr	Ni	N
Percentage (%)	0.04	0.37	1.10	0.032	0.001	18.17	8.03	0.05

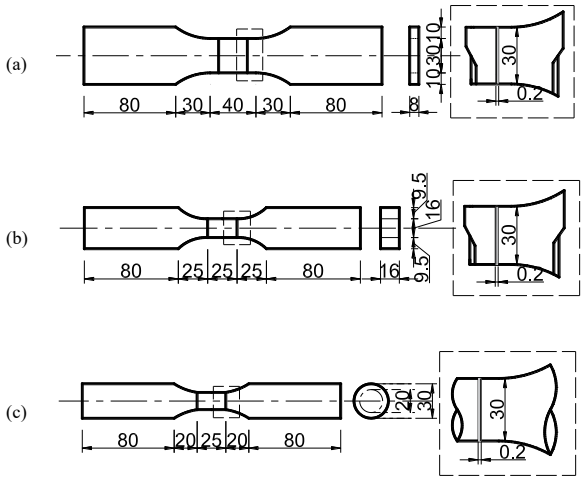

Fig. 1 Geometry of the specimens (units: mm): (a) LF; (b) SF; and (c) CF

2.2. Test setting and loading codes

Axially loaded tests were conducted for the monotonic tensile test to determine the basic mechanical parameters and for the low-cycle fatigue loading test to calibrate the hardening model parameters; then, the strain-fatigue life relationships were established. It should be noted that a larger length-to-diameter (width) ratio is necessary for the standard tensile test piece, according to the Chinese National Standard GB/T 228.1-2010 [23]. Some related literature revealed that the difference in monotonic tensile curves between the standard and reduced length-to-diameter is negligible in cases of small strain [24]. As a result, test specimens LF, SF, and CF with reduced length-to-diameter (width) were used for the monotonic tensile test. The accuracy can be guaranteed within the scope of engineering applications. Nine coupons were subjected to the monotonic tensile test. For each specimen specification, three coupons were performed to calculate the average value of the engineering stress-strain response.

In addition, a total of 88 coupons were performed for the cyclic loading test with two loading patterns, i.e., the constant and the variable strain amplitude loading systems. The constant strain amplitude cyclic loading includes 10 loading protocols, where the strain amplitude ranged from ±0.5% to ±5% with strain ratios R_ε equal to -1, as shown in Table 2. In general, three coupons were tested for obtaining the mean value under each constant amplitude scenario. The variable strain amplitude cyclic loading consists of multiple loading protocols, i.e., cyclic ascend and cyclic descend, to investigate stainless steel's hysteresis characteristics, as shown in Fig. 2.

Table 2
Constant amplitude cyclic loading system

Amplitude(%)	0.5	0.75	1.0	1.25	1.5	2.0	2.5	3.0	4.0	5.0
Label	L1	L2	L3	L4	L5	L6	L7	L8	L9	L10

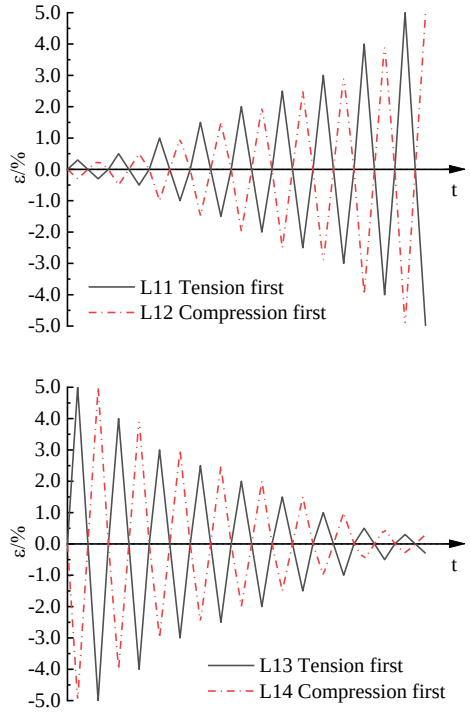

Fig. 2 Variable amplitude cyclic loading system

An MTS 793 system that can apply tension and compression loads was used to conduct monotonic tensile and cyclic loading tests, as presented in Fig. 3. The test coupons were gripped by hydraulic jaws. The monotonic tensile test coupons were executed by using an axial actuator with a loading frequency equal to 2 mm/min under displacement-control according to the Chinese National Standard GB/T228 [23]. Tests of cyclic loading were performed under nominal strain-control of the parallel segment measured by the extensometer, according to the Chinese National Standard GB/T26077 [25]. The extensometer's gauge length was 25 mm with a measuring range equal to ±20% in tension and compression. A triangular waveform loading history was adopted, and the loading frequency was set as 0.02 Hz, through which a slow strain rate can be maintained to reduce instability and heat produced in the loading process. The sampling frequency is 32 Hz. Specimens were marked before applying the load in order to measure the elongation after a fracture. All test data and input information were recorded by the MTS data acquisition system. The experimental device diagrams of the three different specifications and sizes of test specimens are shown in Fig. 4.

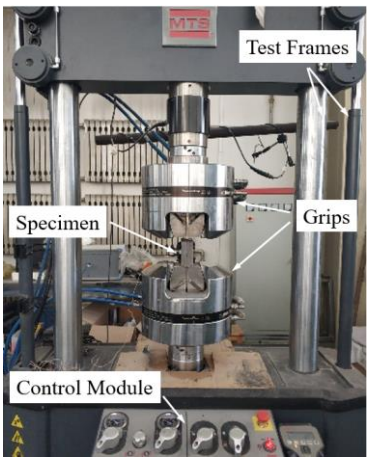

Fig. 3 Loading system with hydraulic grips (MTS793)

(a)

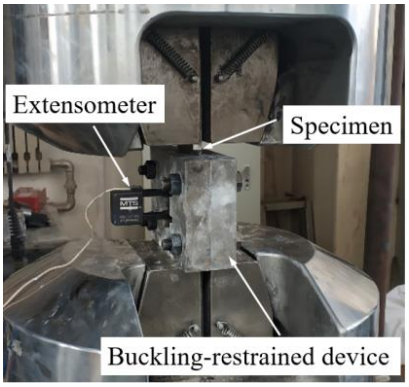

(b)

(c)

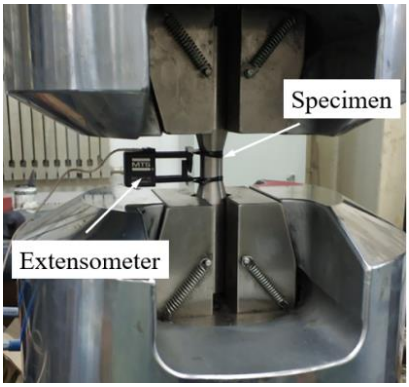

Fig. 4 Cyclic axial test setup: (a) LF; (b) SF; (c) CF

3. Experimental results and discussion

3.1. Results of monotonic experiments

Specimens of different sizes, LF-M1-3, CF-M1-3, and SF-M1-3 (where M represents the monotonic tensile test, and the numbers 1 to 3 indicate the specimen serial number), were subjected to the monotonic tensile loading until they fractured. Table 3 shows the basic mechanical parameters obtained for Austenitic stainless steel S30408. The experiment data reveals that the material has a larger strength-yield ratio of nearly 2.5, which indicates higher safety redundancy for seismic design and higher strain hardening compared with carbon steel. The elongation measured after fracture exceeded 50%, thus demonstrating better ductility and strong plastic deformation ability than the carbon steel. This result is consistent with the result of previous studies on the characteristics of the stainless steel materials [26, 27]. The test data for the LF and CF specimens are not much different from each other in strain, stress, and Young's modulus. The stress of SF was different from the other two specimens, however; the reason for this phenomenon may be that the mechanical performance of the test specimens was affected by temperature during the laser cutting process on account of thickness. When there was a small width-to-thickness ratio, a measurement deviation in the test data would be caused.

Table 3

Mechanical parameters under monotonic tensile loading

Specimen	E/GPa	$\sigma_{0.01}$/MPa	$\sigma_{0.2}$/MPa	$\sigma_{1.0}$/MPa	$\sigma_{2.0}$/MPa	σ_u/MPa	$\varepsilon_{0.2}$/(%)	$\varepsilon_{2.0}$/(%)	ε_u/(%)	n	$E_{0.2}$/GPa	n´	b	a	σ_u /$\sigma_{0.2}$
LF-M1	195	170	281	319	340	715	0.34	2.18	54.5	5.96	27.02	2.53	1447	315	2.55
LF-M2	199	180	292	335	359	708	0.36	2.20	56.5	6.19	21.08	2.53	1364	336	2.42
LF-M3	190	155	288	329	353	711	0.34	2.17	52.1	4.83	25.74	2.94	1443	329	2.49
AVG.	195	141	287	328	355	710	0.35	2.19	54.4	5.66	22.61	2.66	1418	327	2.48
SF-M1	184	102	343	401	445	747	0.38	2.24	47.9	2.47	50.41	2.16	1423	423	2.17
SF-M2	196	122	316	414	457	736	0.40	2.25	50.2	3.14	39.96	2.19	1330	437	2.33
SF-M3	172	98	337	398	456	720	0.41	2.24	51.6	2.42	49.48	2.06	1266	436	2.13
AVG.	184	107	332	430	453	734	0.39	2.24	49.9	2.68	53.62	2.13	1340	432	2.21
CF-M1	205	160	261	307	345	668	0.33	2.18	42.9	6.12	19.31	1.59	1478	320	2.55
CF-M2	189	178	259	307	343	659	0.33	2.19	46.6	7.98	14.93	1.52	1385	321	2.54
CF-M3	186	165	262	310	347	698	0.34	2.18	50.1	6.47	18.24	1.67	1446	322	2.66
AVG.	193	167	261	308	345	675	0.33	2.18	46.5	6.87	17.49	1.59	1437	321	2.58

Note: E is the Young's modulus; $\varepsilon_{0.2}$ and $\varepsilon_{2.0}$ are the strain value of offset strain of 0.2% and 2.0%; ε_u is the ultimate strain. $\sigma_{0.01}$, $\sigma_{0.2}$, $\sigma_{1.0}$, and $\sigma_{2.0}$ are the stress values corresponding to offset strains of 0.01%, 0.2%, 1%, and 2%.

The stress-strain curves of stainless steel under the monotonic tensile loading are presented in Fig. 5. Unlike carbon steel, it can be seen that 1) stainless steel exhibits nonlinear stress-strain behavior without a yield plateau and well-defined yield point; the stress corresponding to the offset strain 0.2% was usually used as the nominal yield stress; 2) it requires a more complex and suitable monotonic model than the bilinear model usually used in steel. Three commonly used nonlinear metal constitute modes [28-30], given by Eq. (1) to Eq. (3), were adopted to describe the stress-strain curves with the fitted constitute parameters obtained from the experimental tests listed in Table 3.

I) Ramberg-Osgood Model

$$\varepsilon = \frac{\sigma}{E} + 0.002\left(\frac{\sigma}{\sigma_{0.2}}\right)^{n} \tag{1}$$

II) G-N Model

$$\varepsilon = \begin{cases} \dfrac{\sigma}{E} + 0.002\left(\dfrac{\sigma}{\sigma_{0.2}}\right)^{n} & \sigma \le \sigma_{0.2} \\ \dfrac{\sigma-\sigma_{0.2}}{E_{0.2}} + \left(0.008 - \dfrac{\sigma_{1.0}-\sigma_{0.2}}{E_{0.2}}\right)\left(\dfrac{\sigma-\sigma_{0.2}}{\sigma_{1.0}-\sigma_{0.2}}\right)^{n_{0.2,1.0}} + \varepsilon_{t0.2} & \sigma_{2.0} < \sigma \end{cases} \tag{2}$$

III) Quach Model

$$\varepsilon=\begin{cases}\dfrac{\sigma}{E}+0.002\left(\dfrac{\sigma}{\sigma_{0.2}}\right)^{n} & \sigma\le\sigma_{0.2}\\ \dfrac{\sigma-\sigma_{0.2}}{E_{0.2}}+\left(0.008-\dfrac{\sigma_{1.0}-\sigma_{0.2}}{E_{0.2}}\right)\left(\dfrac{\sigma-\sigma_{0.2}}{\sigma_{1.0}-\sigma_{0.2}}\right)^{n'_{0.2,1.0}}+\varepsilon_{t0.2} & \sigma_{0.2}<\sigma\le\sigma_{2.0}\\ \dfrac{\sigma-a}{b+\sigma} & \sigma>\sigma_{2.0}\end{cases} \quad (3)$$

where E and $E_{0.2}$ are the Young's modulus and the corresponding elastic modulus when the offset strain is 0.2%. n and $n'_{0.2,1.0}$ are the coefficients of strain hardening; $\sigma_{0.2}$ and $\sigma_{1.0}$, are the stress values which correspond to offset strains of 0.2% and 1%, respectively; and a and b are parameters in the R-O constitutive model. A more detailed explanation of the monotonic tensile constitutive model is referred to in [31, 32].

A comparison between the fitting curves and the testing curves is shown in Fig. 5. It can be concluded that the Ramberg-Osgood model with a single constitutive parameter accurately represents the stress-strain curve until the strain is below 0.2%; however, it would overestimate the strain hardening degree of stainless steel with the strain increases. Both the G-N and Quach models can fit the stress-strain curve exactly while the strain is over 0.2% and less than 2.0%. However, it is not recommended to use the G-N model to represent the stainless steel in the case of large strains due to significant deviation, e.g., the strain is larger than about 5.0%. In general, the Quach model is the most accurate monotonic tensile constitutive model for stainless steel with complicated parameters and is recommended for describing the monotonic tensile stress-strain curve in cases with large strain.

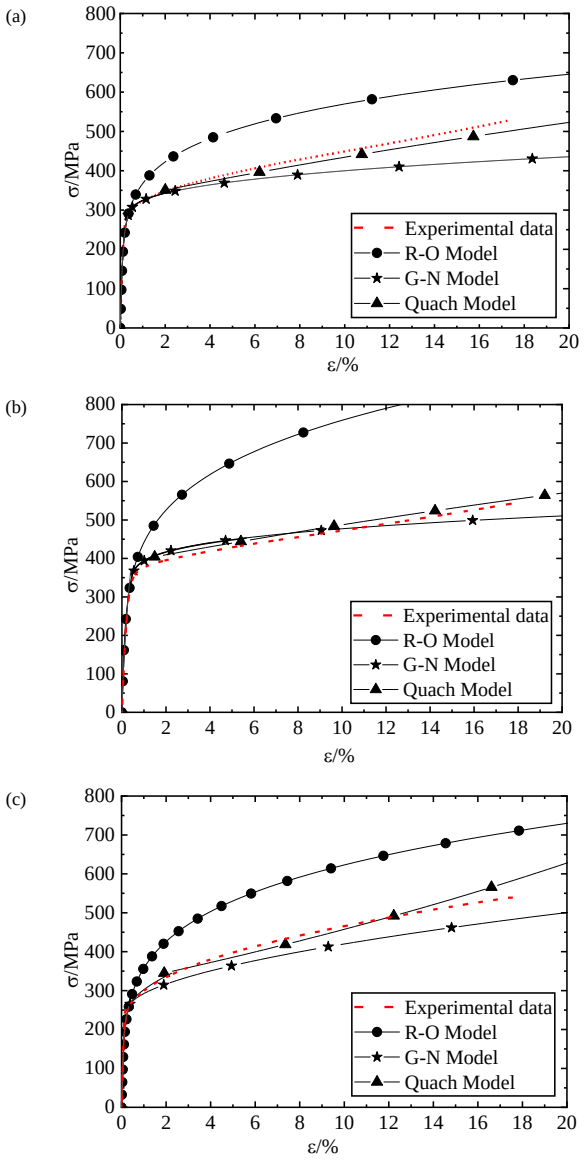

Fig. 5 Monotonic tensile σ-ε curve: (a) LF; (b) SF; and (c) CF

3.2. Results of cyclic loading experiments

In this section, the stress-strain curves of the specimens under completely reversed constant strain amplitude in the cyclic loading are illustrated and analyzed. The parameters of cyclic hardening are calibrated; the strain-fatigue life relationship is established. First, it is essential to discuss the effect of the buckling-restrained device and the notch on the test data before the analysis of the stress-strain relationship.

When the specimens were compressed under cyclic loading, the cross section along the thickness of the LF specimen enlarged, and friction force was generated between coupons and the buckling-restrained device. Further, the lateral deformation of specimens caused by the Poisson effect was restrained on account of the buckling-restrained device. As a result, the measured axial force is the summation of the compressive stress, friction force, and lateral force. In order to understand the influence of friction and lateral force on the axial compress, comparisons between stress-strain curves with and without the buckling-restrained device are plotted and shown in Fig. 6. It can be concluded that the difference between the two curves is negligible, and the stress values are approximately the same under identical strain. Therefore, the compressive stress in the present paper is directly measured by the axial stress without considering the influence of friction and the Poisson effect.

The stress-strain curves of coupons with and without the notch were shown in Fig. 7 to show the influence of the notch on the specimens' performance. The notch has little effect on the mechanical properties in the case of small strain or little number hysteresis, but it has a great impact on the specimens' strain-fatigue life, which will be introduced in detail in Chapter 3.2.3. The stainless steel's cycle characteristics in this section are analyzed with LF specimens.

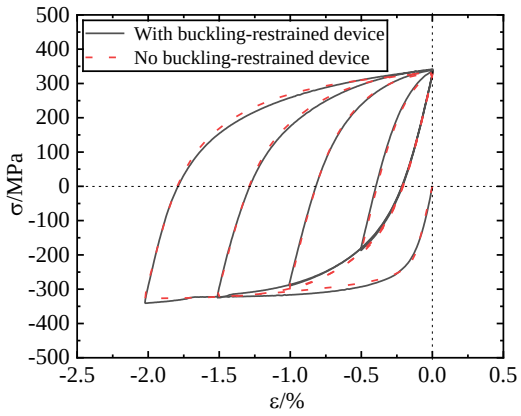

Fig. 6 Effect of buckling-restrained device on stress

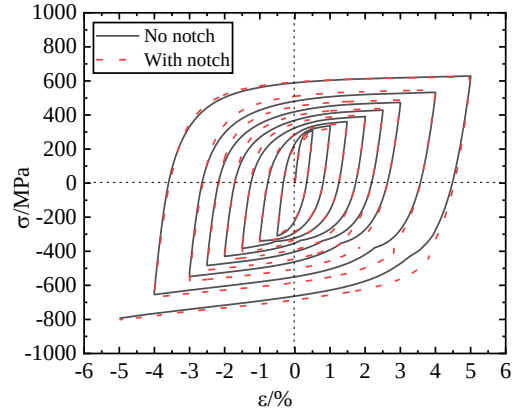

Fig. 7 Effect of the notch on stress

3.2.1. Skeleton curve

To analyze the characteristics of the stress-strain response under various strain amplitudes and to compare its difference with the monotonic tensile curve, a family of stable hysteresis loops which corresponds to the half fatigue life under each constant strain amplitude was plotted in a similar graph. The cyclic skeleton curve was generally fitted using the Ramberg-Osgood model [33], which is given in Eq. (4) by tracing the peak stress tips of each hysteresis curve (shown in Fig. 8).

$$\frac{\Delta\varepsilon}{2}=\frac{\Delta\varepsilon_e}{2}+\frac{\Delta\varepsilon_p}{2}=\frac{\Delta\sigma}{2E}+\left(\frac{\Delta\sigma}{2K'}\right)^{1/n'} \quad (4)$$

where $\Delta\varepsilon$, $\Delta\varepsilon_e$, and $\Delta\varepsilon_p$ are the total, elastic, and plastic amplitudes; $\Delta\sigma$ is the total stress amplitude; E is the Young's modulus; K' is the coefficient of cyclic strength; and n' is the exponent of cyclic strain hardening that can be fitted by the peak stress versus strain amplitude data by ordinary least squares.

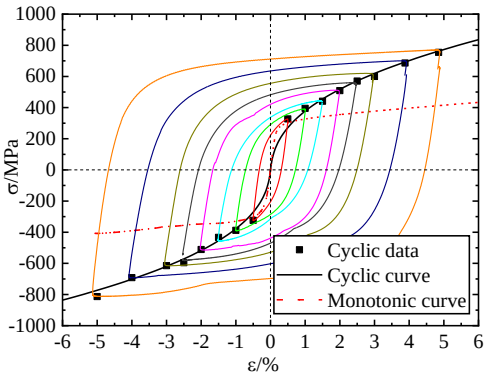

Fig. 8 Constant strain amplitude cyclic skeleton curve

It can be seen that the hysteresis curves of stainless steel are shuttle-shaped with good symmetry and plump, indicating good hysteretic performance as well as energy dissipation. The hysteresis curve width gradually increases with the increment of the strain amplitude, indicating that the share of plastic strain amplitude rises. The cyclic skeleton curve of stainless steel, observed from the above-mentioned figure, is always over the monotonic tensile curve, showing evident cyclic hardening. With the augmentation of the strain amplitude, the difference between the cyclic loading curve and monotonic tensile curve continues to grow, indicating a more obvious strain hardening. The stress under cyclic loading at the 5% strain is approximately 1.63 times the stress of the monotonic tensile loading. Therefore, it is inappropriate to apply the monotonic tensile curve of stainless steel to calculate the hysteretic behavior in elastoplastic studies, as the monotonic tensile curve would underestimate the strain hardening characteristic under cyclic tension-compression loading. The fitted cyclic skeleton curve does not accurately pass through all stress tips, the reason is that the cyclic plastic parameters were calibrated by the average value of tensile and compressive stress but are not equal to each other due to the kinematic hardening during cyclic loading.

From the test results, the calculated values of cyclic hardening parameters K' and n' under different loading cases, including constant and variable strain amplitudes were listed in Table 4. The cyclic hardening parameters fitted under various strain amplitudes were different from each other, indicating that the cyclic skeleton curve is greatly affected by strain amplitude and loading history. These cyclic hardening parameters between loading case L11 and L12 represent a small difference under the loading system with the same strain amplitude but opposite loading order. Loading cases L13 and L14 have the same phenomenon. The results reveal that the hysteretic characteristics of the stainless steel are less affected by the direction of tension and compression, and the buckling-restrained device restrained the buckling effect of the specimen under compression well.

Table 4
Cyclic loading skeleton curve parameters

Case	L1-L10	L11	L12	L13	L14	AVG.
K′/MPa	2213	1376	1375	1806	1956	1745
n′	0.428	0.405	0.413	0.468	0.519	0.447

Comparisons of the cyclic skeleton and monotonic tensile curves under several typical cyclic loading systems with different amplitudes are shown in Fig. 9. When the Ramberg-Osgood model is used to fit the cyclic skeleton curves, some results are acceptable under partial strain amplitudes, but the deviation is larger in some strain amplitudes. For example, in the small strain amplitude (the strain is less than 1.5% in Fig. 9 (a) and (b)) and a few initial loading laps (the first two loops at 4% and 5% in Fig. 9 (c) and (d)). The reason for this may be related to the cumulative plastic strain value, but further research is needed to verify this conclusion. Fig. 9 (c) and (d) show that the peak stress value of the first large strain at ±5% under variable strain amplitude loading cases L13 and L14 coincides with the stress versus large strain of monotonic tensile curve, confirming accuracy of the test.

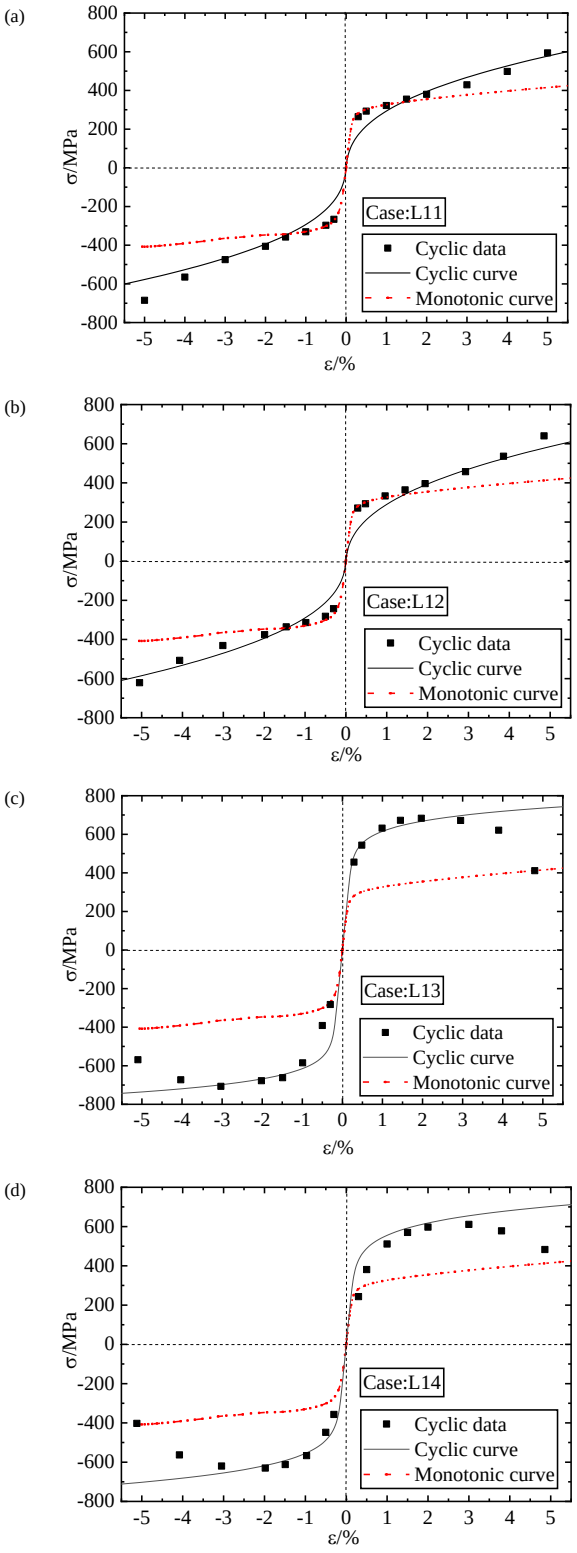

Fig. 9 Variable strain amplitude cyclic skeleton curve

3.2.2. Cycle stress-strain characteristics

The changes in the stress-strain hysteresis loop along with the increasing number of fatigue cycles (N_f) under fully reversed constant strain amplitudes are shown in Fig. 10. In terms of each given strain amplitude, the hysteresis curves do not overlap and exhibit cyclic hardening or softening as the cumulative plastic strain increases. Fig. 11 shows the stress amplitude variation against the increasing number of fatigue cycles (N_f) under each constant strain value and also explains the trend of cyclic behavior in another aspect.

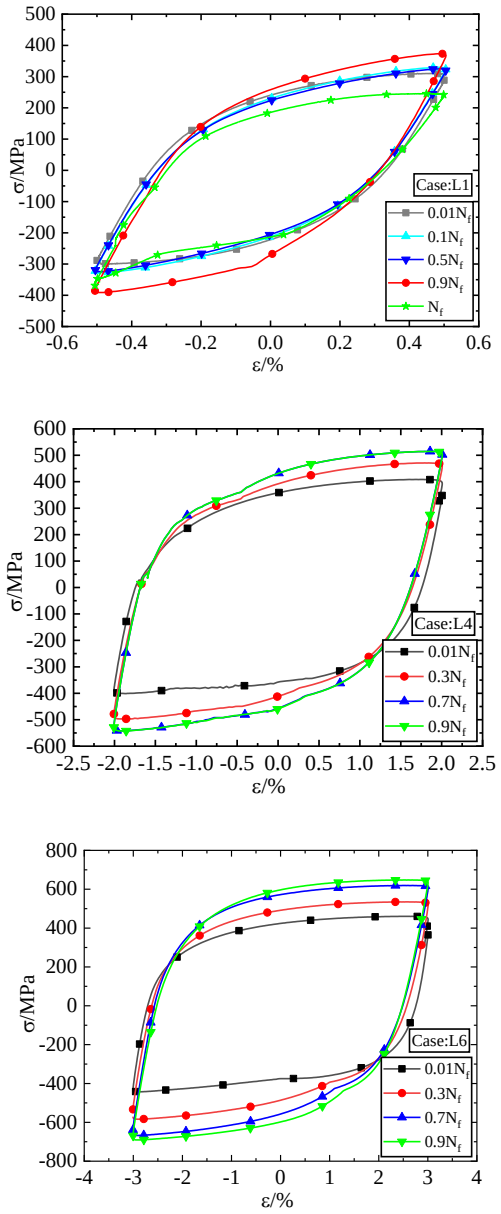

Fig. 10 Change of the hysteresis loop with an increasing number of fatigue cycles (N_f) under constant amplitude strain

The characteristics of cyclic behavior for stainless steel can be summarized from the above-mentioned figure: 1) The specimens have obvious cyclic softening before fracturing along with an increase of cumulative plastic damage if the total strain is less than 1%. The specimens have undergone four stages; slight hardening also occurred at first several cycles. And then, it came into being relatively stable for a long duration. Then, slight cyclic softening occurred before the second phase of significant cyclic hardening until fracture with a rapid drop of stress. This phenomenon is consistent with the findings in [34]. 2) When the total strain is between 1% and 2%, the specimens have undergone three stages: a greater cyclic hardening during the initial stage compared with the case where the strain is less than 1%, followed by cyclic stabilizing for a short period, then a second cyclic hardening appeared before fracture; there is no cyclic softening in the whole process. 3) In the case with a strain amplitude over 2%, the maximum cyclic stress increases until the specimen fractures, and no cyclic stabilizing and softening were observed. The specimen only undergoes one stage with cyclic hardening until fracture. It is a continuous-growth process in the peak stress where the rate grew slowly along with the number increment of fatigue cycles in the later stage.

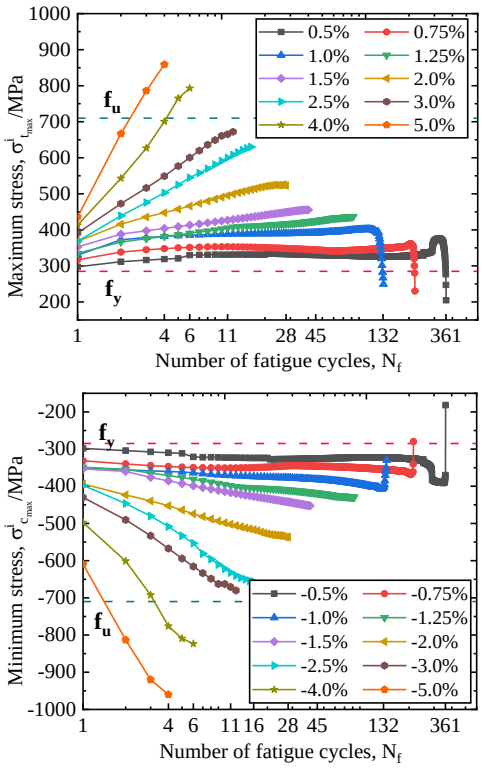

Fig. 11 Change of the peak stress with the increasing number of fatigue cycles (N_f) of LF specimen under constant strain amplitude loading: (a)Tensile stress; (b) Compressive stress

The peak value of cyclic tensile and compressive stress changes in sync with the increasing number of fatigue cycles (N_f). The cyclic stress peak exceeded the ultimate stress only when the value of strain is larger than 4%. And the peak cyclic stress remained between the yield stress and the ultimate stress if the strain amplitude is less than 4%. This phenomenon is different from the discovery in [7], which reported that the peak cyclic stress exceeds the ultimate stress after approximately thirteen load reversals at a strain amplitude of 2%.

To quantify the cyclic hardening magnitude, a measure is defined in Eq. (5), which employs the ratio of the maximum cyclic stress $\sigma_{t,\max}^{N=N_f}$ during the whole life to the stress amplitude $\sigma_{t,\max}^{N=1}$ at the first cycle corresponding to the same strain. It is also an important indicator in seismic design:

$$R = \frac{\sigma_{t,\max}^{N=N_f} - \sigma_{t,\max}^{N=1}}{\sigma_{t,\max}^{N=1}} \tag{5}$$

The cyclic hardening ratios increase gradually along with the increments of strain amplitude under fully reversed strain-control, as illustrated in Table 5. It can be fitted into a straight line roughly with a slope of 0.22 that is passing through the origin point, as shown in Fig. 12, indicating that stainless steel S30408's cyclic hardening degree increases linearly with the increase in strain amplitude.

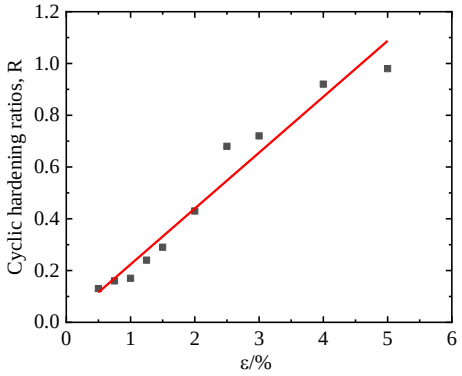

Fig. 12 The cyclic hardening ratios under different constant strain amplitude

The stiffness of the material decreases quickly after yielding when plain carbon steel is used as the core component of BRB, resulting in a large residual displacement [35, 36]. The significant cyclic hardening of stainless steel with strong post-yield stiffness can alleviate the core of BRB from generating large offset strain during cyclic loading for energy dissipation components, which can increase the safety margin of the structure.

Table 5
Degree of cyclic hardening of LF specimen

Case	L1	L2	L3	L4	L5	L6	L7	L8	L9	L10
$\sigma_{t,\max}^{N=1}$ / MPa	297	316	332	347	352	368	374	391	412	435
$\sigma_{t,\max}^{N=N_f}$ / MPa	334	369	390	431	455	525	630	672	792	858
R*	0.13	0.16	0.17	0.24	0.29	0.43	0.68	0.72	0.92	0.98

*Note: R is the ratio of the peak stress increment in the cyclic loading process to the maximum stress in the first cycle.

3.2.3. LCF life

The LCF life of specimens subjected to cyclic loading is also an important factor to be considered in the seismic structure application. The strain-fatigue life relationship is employed through the constant strain amplitude test results, which vary from 0.5% to 5.0%.

The total strain-fatigue life relationship contains two parts: the elastic part corresponding to the description of the Basquin model [37, 38]; and the plastic part, which corresponds to the description of the Manson-Coffin model [39-41]. The curves of the elastic and plastic strain vs the fatigue life (ε-2N_f) are linear on the diagram with log-log coordinates. This paper employs the Basquin-Manson-Coffin model described in Eq. (6), which takes elasticity and plasticity into account to fit the strain-fatigue life relationship of Austenitic stainless steel S30408 in all specifications mentioned above.

$$\frac{\Delta\varepsilon}{2}=\frac{\sigma_f^{'}}{E}\left(2N_f\right)^b+\varepsilon_f^{'}\left(2N_f\right)^c \tag{6}$$

where Δε is the total strain amplitude, σ′$_f$ and ε′$_f$ are the coefficients of fatigue strength and fatigue ductility, *b* and *c* are the exponents of fatigue strength and fatigue ductility, and 2N_f represents the number of reversals to failure.

The parameters shown in Table 7 were derived using the mean of the specimens' fatigue life shown in Table 6 under each strain amplitude. The plots illustrating the number of reversals against elastic, plastic, and total strain amplitudes with logarithmic coordinates are presented in Fig. 13. Then, the relative cumulative plastic deformation strain value (CPD_{rv}) [42], which is an important indicator used to measure the capacity of energy dissipation, was calculated through Eq. (7), in which ε_{pi} is the plastic strain range of the *i*th cycle, ε_y is the nominal yield strain:

$$CPD_{rv}=\Sigma\left|\Delta\varepsilon_{pi}\right|/\varepsilon_y \tag{7}$$

The results concluded that the fatigue life of stainless steel S30408 decreases gradually along with the increment of the strain amplitude, as shown in Table 6. The cumulative plastic deformation capacity and ductility also gradually decrease, which is shown by the decreasing value of CPD_{rv}, on account of the increasing plastic damage. The plastic strain, which accounts for the majority of the total strain, has a great influence on the material's low-cycle fatigue life, seen in Fig. 13; further, the Basquin-Manson-Coffin model can fit the materials' strain-fatigue life, because there is good agreement between the fitted curve (described in Eq. (6) with fatigue parameters) and the test data.

Table 6
Results of the low-cycle fatigue life

Δε/2(%)	Δε$_p$/2(%)	2N$_f$				LF′/LF	CPDrv/(LF′)			
		LF	SF	CF	LF′		LF	SF	CF	LF′
0.5	0.325	722	532	560	5024	6.95	1564	1152	1213	10855
0.75	0.535	426	365	306	2342	5.49	1221	1046	877	9293
1.0	0.735	264	204	182	1036	3.92	1108	856	764	4351
1.25	1.015	162	115	133	726	3.42	996	707	818	4466
1.5	1.26	90	62	60	474	5.27	687	473	458	3619
2.0	1.67	56	-	46	256	4.57	561	-	461	2567
2.5	2.13	32	-	20	-	-	408	-	255	-
3.0	2.58	22	-	-	-	-	325	-	-	-
4.0	3.51	12	-	-	-	-	238	-	-	-
5.0	4.45	8	-	-	-	-	204	-	-	-

Table 7
Parameters of Basquin-Manson-Coffin model

Specimen	LF	SF	CF	LF′
σ$_f$′	1108	769	819	1738
b	-0.1848	-0.1195	-0.1300	-0.1789
ε$_f$′	0.1369	0.1133	0.1006	0.3307
c	-0.5246	-0.5241	-0.4902	-0.5358

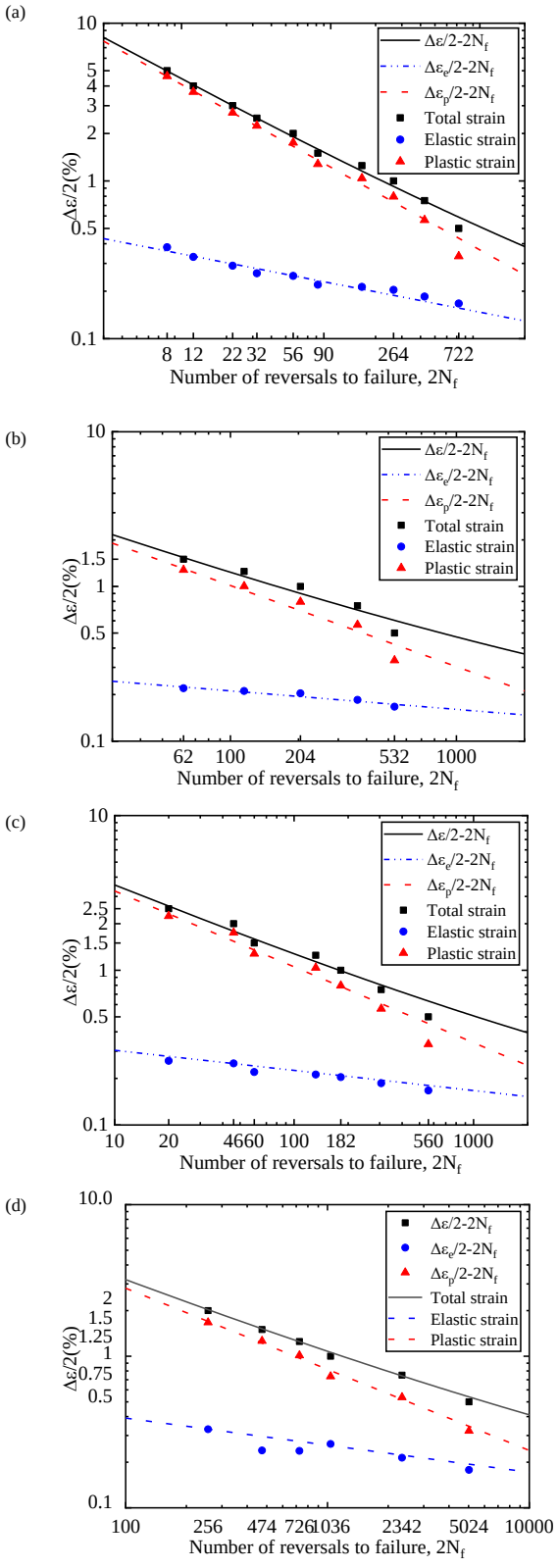

Fig. 13 Strain-fatigue life relationship: (a) LF; (b) SF; (c) CF; (d) LF´

Fig. 14 plots the test data for the number of reversals versus the constant strain for all specifications and their Basquin-Manson-Coffin curves with a total strain amplitude of 5%. By comparing the strain-fatigue life relationship of different specification specimens LF, SF, and CF, it can be summarized that the material's fatigue life is less affected by the specimen size. The hysteresis cycle number corresponding to the specimens with different sizes they can withstand is not much different. Comparing the fatigue life of specimen LF with a notch and specimen LF' without a notch in the same specification characters shows that the maximum ratio of the number of hysteresis cycles for LF' to LF can be up to about seven times at the same strain amplitude, which proves that the notch has a significant influence on the low-cycle fatigue performance, and even small damage would reduce the fatigue life of the material significantly.

Fig. 15 illustrates the comparison of strain-fatigue life curves between the test results of LF specimens and that in previous literature[7,12,13]. The results show that there exists a great difference among the fitted fatigue life curves of Austenitic stainless steel S30408 obtained by each paper, which may be related to the production batch of the material and the test process of the specimen. However, this needs further study and confirmation. It is obvious from Fig. 15 that the variation trend of fatigue life with the strain amplitude increase of Austenitic stainless steel S30408 in this test is close to that in reference [13], but the experimental fatigue life is much lower. The test result for this experiment is between the strain-fatigue life curve fitted in references [7] and [12], which proves that the deviation of the test results is not large and is reasonable. In this cyclic loading test, the peak strain value of the LF specimen reached ±5%. There are more data values and a larger strain range compared with the fitted stain-fatigue curves in the previous literature (<2%) [7,12,13]. Although the initial damage caused by the notch on the LF specimen will lead to a reduction of fatigue life, it is reliable and relatively conservative to use the fitted strain-fatigue life equation of the LF specimen to predict the fatigue cycles of Austenitic stainless steel S30408 as less than the strain amplitude of 5%. The damage is inevitable due to the cutting and welding factors in the processing of material and components, and the fatigue life is sensitive to damage under large strain loading.

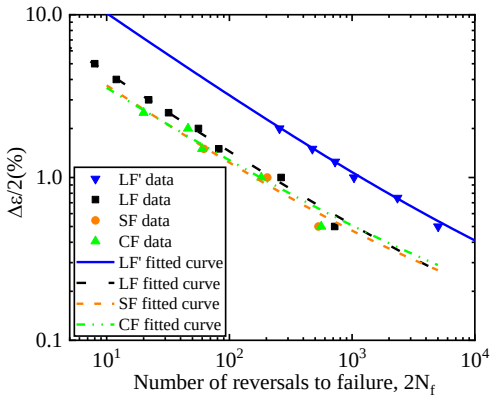

Fig. 14 Comparison of strain-fatigue life curve for different specimens

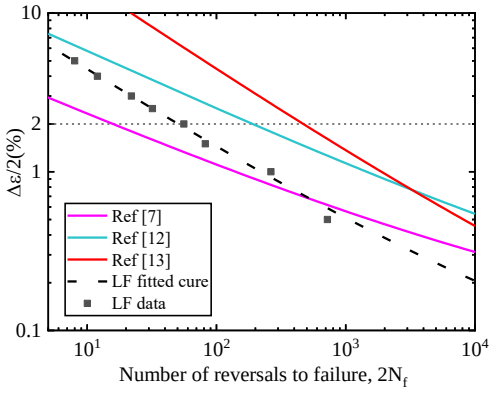

Fig. 15 Comparison of the strain-fatigue life between the test results of the LF specimen and other literature

4. Finite element modeling

The experimental results in the previous section show the basic properties of Austenitic stainless steel S30408 under axial tensile loading and the stress-strain characteristics under cyclic loading, which are useful for understanding how the material works. And it is necessary to further study the specific hardening paremeters of the material under cyclic loading for representing the hysteretic behavior accurately in finite element analysis. In addition, a numerical simulation of the structures and components under reciprocating loading is needed in the absence of tests. The precise material cyclic plasticity parameters are beneficial for the response analysis of structures. In this section, the behavior of specimens is analyzed and simulated using finite element software under variable strain amplitude cyclic loading to further understand hysteretic performance and provide basic data for the seismic analysis of stainless steel structures.

4.1. Calibration of mixed hardening parameters

It is concluded from the cyclic stress-strain relationship curve that the austenitic stainless steel S30408 exhibits a nonlinear mixed hardening behavior, which includes isotropic hardening and kinematic hardening under cyclic loading. That means the evolution rule of the subsequent yield surface includes two parts: 1) an isotropic hardening process that depicts the yield surface expansion through equivalent strain; and 2) a kinematic hardening process that describes the yield surface translation in the stress space via backstress.

The nonlinear mixed hardening model is numerically built-in Abaqus [43], which employs the Chaboche constitutive model put forward by Armstrong and Frederick [44-46] and improved by Chaboche [14]. This model can be used to describe characteristics of the material under cyclic loading, such as nonlinear strain hardening, the Bauschinger effect, the ratcheting effect, and mean stress relaxation. The cyclic plastic model parameters are calibrated, and the test and simulation curves are compared.

According to the von Mises yield criterion, the strengthening expression is calculated as follows:

$$F = f(\sigma - \alpha) - \sigma^0 = 0 \tag{8}$$

where σ denotes the tensor of stress, α represents the backstress tensor, and σ^0 refers to the current yield stress, indicating the size of the yield surface.

The plastic flow law of the model associated with von Mises yield criterion is as follows:

$$\dot{\varepsilon}^{pl} = \dot{\bar{\varepsilon}}^{pl} \frac{\partial F}{\partial \sigma} \tag{9}$$

The evolution in the yield surface size, as defined by the isotropic hardening component, is a function of the equivalent plastic strain, which is calculated by:

$$\sigma^0 = \sigma|_0 + Q_\infty \left(1 - e^{-b\varepsilon^p}\right) \tag{10}$$

where $\sigma|_0$ denotes the yield stress when the plastic strain is zero, which can be obtained from the first-quarter cycle of the test, Q_∞ and b are the model's isotropic hardening parameters, and ε^p is the equivalent plastic strain.

The determination of the elastic limit stress is dependent on the detection accuracy of the offset strain because the stainless steel has no yield platform and exhibits an obvious nonlinear stress-strain relationship. It is appropriate to use 0.55 times the nominal yield stress at a 0.2% offset strain as the yield stress $\sigma|_0$. And there gave a detailed introduction to the definition of the elastic limit stress in references [47, 48]. Q_∞ denotes the maximum change value of the yield surface size, indicating the hardening degree, and b denotes the rate of the yield surface size changes with the equivalent increase in the plastic strain.

The size of the yield surface stress σ_i^0 in the ith cycle is calculated from the average of the peak tensile stress σ_i^t and the maximum elastic limit compressive stress σ_i^c:

$$\sigma_i^0 = \frac{\sigma_i^t - \sigma_i^c}{2} \tag{11}$$

The equivalent plastic strain which corresponds to the yield surface σ_i^0 is:

$$\varepsilon_i^p = 2\Sigma\left(\Delta\varepsilon_{i-1}^p\right) + \frac{1}{2}\Delta\varepsilon_i^p \tag{12}$$

where $\Delta\varepsilon_i^p$ is the range of plastic strains corresponding to the ith cycle. The equivalent plastic strain equals the sum of twice of the plastic strain range of the (i-1)th cycle and half of the plastic strain of the ith cycle.

The isotropic hardening model formula described in Eq. (10) has been fitted by data pair (σ_i^0, ε_i^p), including the data ($\sigma|_0$,0) when the equivalent plastic strain is zero, and then hardening parameters Q_∞ and b are obtained.

To better depict the kinematic hardening under high plastic strain, multiple sets of backstress were selected, which are expressed as:

$$\alpha_k = \frac{c_k}{\gamma_k}\left(1 - e^{-\gamma_k \varepsilon^p}\right) + \alpha_{k,1} e^{-\gamma_k \varepsilon^p} \tag{13}$$

$$\alpha_{NLK} = \sum_{k=1}^{N} \alpha_k \tag{14}$$

where α_k is the backstress, C_k represents the kinematic hardening modulus in the initial stage, and γ_k represents the rate of change in the kinematic hardening modulus, along with the plastic deformation. k is the Chaboche component number.

The plastic strain corresponding to the backstress is shifted as follows:

$$\varepsilon_j^p = \varepsilon_j - \frac{\sigma}{E} - \varepsilon_p^0 \tag{15}$$

where $\varepsilon_1^p = 0$, and ε_p^0 is the value of plastic strains at the time the hysteresis loop passes through the X axis. The backstress α_j is calculated by:

$$\alpha_j = \sigma_j - \sigma_s \tag{16}$$

where $\sigma^s = (\sigma_1 + \sigma_n)/2$ is the mean value of the first data point σ_1 and last data point σ_n, representing the size of the stable yield surface. Data pairs (α_j, ε_j^p) are used to fit the model described in Eqs. (13) and (14) to calculate kinematic hardening parameters c_k and γ_k.

From general experience with stainless steel, the application of two to five backstress components may obtain a better fitting result. The stress-strain curve shows that the backstress curve contains several distinct shape features: 1) an initial part close to a straight line; 2) a curve segment with a sharp curvature; 3) a curve segment with a smaller curvature; and 4) a straight part close to flat to the end. Therefore, the number of backstresses is N=4, which corresponds to the count of the characteristic for the kinematic hardening curve. In order to prevent over-fitting while fitting the kinematic hardening parameters C and γ, it is necessary to calibrate parameters manually at first by using the endpoints of each curve segment [47]. More detailed steps are referred to in the literature [49, 50]. The final fitted results were obtained and are presented in Table 8.

Table 8
Fitted parameters of Chaboche constitutive model

Parameters	Q_∞	b	C_1	γ_1	C_2	γ_4	C_3	γ_4	C_4	γ_4
First fitted	177	7.5	13183	174	9497	83	4112	36	1271	20
Optimize	284	5	15894	432	9050	154	4359	52	1422	20

4.2. Comparison between test and simulation curves

The ABAQUS was utilized to simulate the cyclic loading test. Regarding the specimens' symmetry, half of the specimen size was simulated by using solid element C3D8R, and the material properties values were obtained based on the monotonic tensile test and the previous calibration of cyclic hardening parameters in section 4.1. The end of the specimen clamped by the actuator hydraulic jaws was applied fixed constraint in the simulation. The reference point and the loading surface were set for coupling constraint to have the same deformation, and the set displacement amplitudes were applied to the reference point. The FEM and specimen details are shown in Fig. 16.

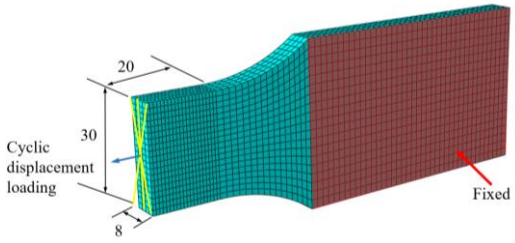

Fig. 16 FEM and specimen details

The experiments and simulation curves were carried out for comparison under the various strain amplitude cyclic loadings. Fig. 17 shows that the mixed hardening parameters obtained by fitting can depict the key behavior characteristic of the hysteresis curves and can be applied to simulate the test curve acceptably. In addition, the parameters can provide a data basis for seismic analysis of the stainless steel structure.

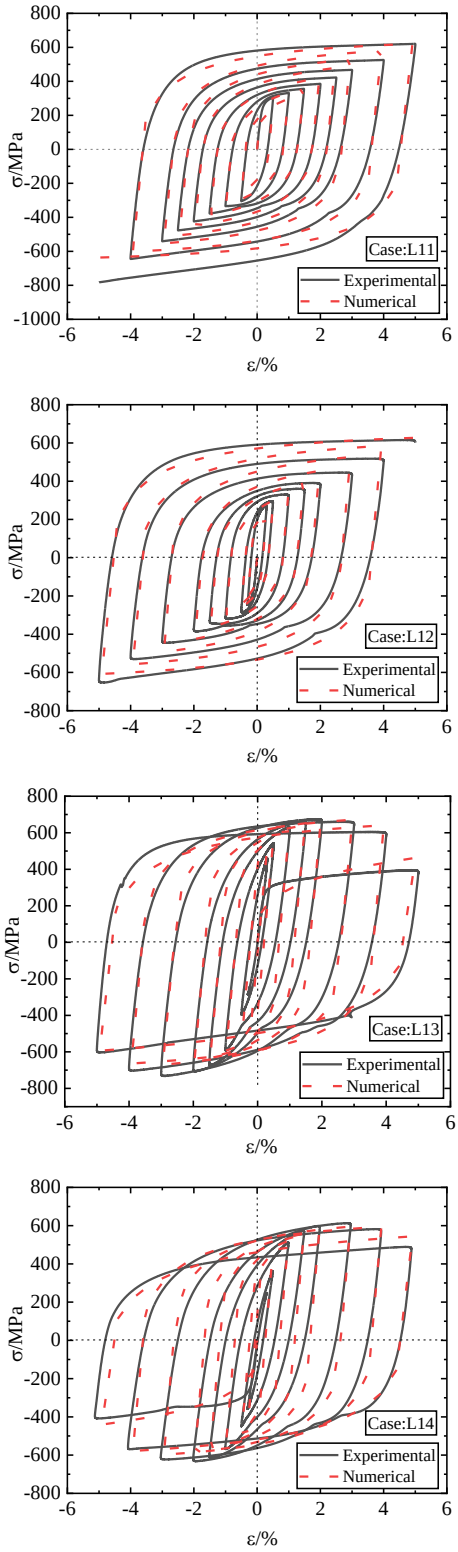

Fig. 17 Comparison of the σ-ε curve under variable strain amplitude between the test and simulation

5. Conclusion

This study analyzed the basic mechanical properties under the monotonic tensile loads, and the characteristics of the hysteretic loop under cyclic loads with a larger strain amplitude (5%) of Austenitic stainless steel S30408. We calibrated the cyclic plastic parameters, and the strain-fatigue life relationship was obtained based on the constant strain amplitude varying from 0.5% to 5.0%. Furthermore, variable strain amplitude loading tests were performed to calibrate the mixed hardening model parameters for application in numerical simulations. The above-presented investigation was summarized below.

(1) The stress-strain of Austenitic stainless steel S30408 shows nonlinear characteristics without a yield plateau, presenting a large strength yield ratio of about 2.5 and high strain hardening that indicates a higher safety redundancy in seismic design. The Quach model fits the monotonic tensile curve well.

(2) The hysteresis curve of Austenitic stainless steel S30408 is shuttle-shaped with good symmetry and plumpness with constant strain amplitude, which reveals good hysteretic behavior and energy dissipation. Cyclic hardening was observed in that the cyclic skeleton curve is above the tensile skeleton curve. The Ramberg-Osgood model employed to fit the cyclic skeleton curve was appropriate, whose hardening parameters were calibrated.

(3) The cyclic stress of the material varies along with increasing the number of reversals, which consists of cyclic hardening, cyclic softening, and cyclic stability phenomena. The cyclic hardening ratio is the peak stress throughout the whole fatigue life to the maximum stress of the first cycle versus the same strain amplitude to indicate the cyclic hardening degree. The larger the strain value, the higher the cyclic hardening degree.

(4) The fatigue life is mainly affected by plastic strain, and it declines slowly with the augment of the strain amplitude. The Basquin-Manson-Coffin model fits the strain-fatigue life well, and the calibrated fatigue parameters could predict the low-cycle fatigue life of Austenitic stainless steel S30408 in a larger plastic strain range (5%).

(5) The Chaboche constitutive model employed in Abaqus, representing a mixed hardening model comprising isotropic and kinematic hardening, can simulate the performance of Austenitic stainless steel S30408 by comparing the test data under variable strain amplitude cyclic loading.

Declaration of competing interest

The authors declare that they have no known competing financial interests or personal relationships that could have appeared to influence the work reported in this paper.

Acknowledgments

The work was financially supported by the National Natural Science Foundation of China (No. 51778206), which is gratefully acknowledged.

References

[1] L. Gardner, The use of stainless steel in structures, Progress in Structural Engineering & Materials 7(2) (2005) 45-55.
[2] A. Pramanik, A.K. Basak, Stainless steel: Microstructure, mechanical properties and methods of application (2015).
[3] Q. Jing, X. Fang, Application of Stainless Steel Reinforcements in the Hong Kong-Zhuhai-Macao Bridge, 2016 International Conference on Architectural Engineering and Civil Engineering 72 (2017) 363-366.
[4] G.P. Cimellaro, S. Marasco, Capacity Design, 2018.
[5] S. Avgerinou, I. Vayas, High-strength steel on dissipative elements in seismic resistant systems: Tests and simulations, Journal of Constructional Steel Research 172 (2020) 106173.
[6] I. Arrayago, E. Real, L. Gardner, Description of stress-strain curves for stainless steel alloys, Materials & Design 87(DEC.15) (2015) 540-552.
[7] C.-D. Annan, E. Beaumont, Low-cycle fatigue of stainless steel plates under large plastic strain demands, Journal of Building Engineering 29 (2020).
[8] F. Zhou, L. Li, Experimental study on hysteretic behavior of structural stainless steels under cyclic loading, Journal of Constructional Steel Research 122 (2016) 94-109.
[9] X. Chang, L. Yang, L. Zong, M.H. Zhao, F. Yin, Study on cyclic constitutive model and ultra low cycle fracture prediction model of duplex stainless steel, Journal of Constructional Steel Research 152(JAN.) (2019) 105-116.
[10] A. Belattar, C. Keller, L. Taleb, Multiscale analysis of the pre-hardening effect on the cyclic behavior and fatigue life of 304L stainless steel, Mat Sci Eng a-Struct 662 (2016) 468-480.
[11] H. Ban, J. Zhu, G. Shi, Cyclic loading tests on welded connections of stainless-clad bimetallic steel and modelling, Journal of Constructional Steel Research 171 (2020) 106140.
[12] Julie, Colin, Ali, Fatemi, Said, Taheri, Fatigue Behavior of Stainless Steel 304L Including Strain Hardening, Prestraining, and Mean Stress Effects, Journal of Engineering Materials & Technology 132(2) (2010) 021008-1-13.
[13] J. Colin, A. Fatemi, S. Taheri, Cyclic hardening and fatigue behavior of stainless steel 304L, J Mater Sci 46(1) (2011) 145-154.
[14] J.L. Chaboche, Time-independent constitutive theories for cyclic plasticity, International Journal of Plasticity 2(2) (1986) 149-188.
[15] A. Kumar, S. Vishnuvardhan, G. Raghava, Evaluation of Combined Hardening Parameters for Type 304LN Stainless Steel Under Strain-Controlled Cyclic Loading, Transactions of the Indian Institute of Metals 69(2) (2016) 513-517.
[16] N. Moslemi, M.G. Zardian, A. Ayob, N. Redzuan, S. Rhee, Evaluation of Sensitivity and Calibration of the Chaboche Kinematic Hardening Model Parameters for Numerical Ratcheting Simulation, Applied sciences9(12) (2019) 2578.
[17] SG. Fan, RM. Ding, YL. Han, Experimental study on bearing capacity of austenitic stainless steel lipped channel columns [j]. Advanced Steel Construction, 2020, 16(1): 65-76.
[18] SG. Jia, QH. Tan, JY. Ye, Experiments on dynamic mechanical properties of austenitic stainless steel S30408 and S31608 [J]. Journal of Constructional Steel Research, 179 (2021) 106556.

[19] J. Lanning, G. Benzoni, C.M. Uang, Using Buckling-Restrained Braces on Long-Span Bridges. I: Full-Scale Testing and Design Implications, Journal of Bridge Engineering 21(5) (2016) 04016001.
[20] Uang, Chia-Ming, Benzoni, Gianmario, Lanning, Joel, Using Buckling-Restrained Braces on Long-Span Bridges. II: Feasibility and Development of a Near-Fault Loading Protocol, Journal of Bridge Engineering (2016).
[21] R.A. Chacon, M.D. de Marco, E. Real, I. Arrayago, An experimental study on the cyclic response of austenitic stainless steel, in: Proceedings of the 9th International Conference n Advances in Steel Structures; ICASS 5–7, 2018. December 2018,Hong Kong, China
[22] P. Dusicka, A.M. Itani, I.G. Buckle, Cyclic response of plate steels under large inelastic strains, Journal of Constructional Steel Research 63(2) (2007) 156-164.
[23] C.n. standard, G.T. 228.1-2010, MaterialsTensile Testing-Part 1: Method of Test at Room Temperature 2010.
[24] R Ge, Y Xu, X Niu, Experimental study on low-cycle fatigue behavior of Chinese LYP225, China Civil Engineering Journal (1) (2017) 12-19. (in Chinese)
[25] C.n. standard, G.T. 26077-2010, Metallic materials-Fatigues testing-Axial-strain-controlled method 2010.
[26] K.H. Nip, L. Gardner, A.Y. Elghazouli, Cyclic testing and numerical modelling of carbon steel and stainless steel tubular bracing members, Steel Construction 32(2) (2010) 424-441.
[27] K.H. Nip, L. Gardner, C.M. Davies, A.Y. Elghazouli, Extremely low cycle fatigue tests on structural carbon steel and stainless steel, Journal of Constructional Steel Research 66(1) (2010) 96-110.
[28] SEI/ASCE 8-02, Specification for the Design of Cold-Formed Stainless Steel Structural Members, New York: American Society of Civil Engineers (ASCE), 2002.
[29] L Gardner, D A Nethercot. Experiments on stainless steel hollow sections-Part 1: Material and cross-sectional behavior, Journal of Constructional Steel Research, 2004, 60(9): 1291－1318.
[30] W M Quach, J G Teng, K F Chung. Three-Stage Full-Range Stress-Strain Model for Stainless Steels, Journal of Structural Engineering, 2008, 134(9):1518–1527.
[31] I. Arrayago, E. Real, L. Gardner, Description of stress-strain curves for stainless steel alloys, Materials & Design 87 (2015) 540-552.
[32] D Fernando, J G Teng, W M Quach, et al. Full-range stress-strain model for stainless steel alloys, Journal of Constructional Steel Research, 2020, 173:106266.
[33] W. Ramberg, W.R. Osgood Description of Stress-Strain Curves by Three Parameters Technical Note No.902, WashingtonDC: National Advisory Committee for Aeronautics, 1943.
[34] J.W. Pegues, S. Shao, N. Shamsaei, J.A. Schneider, R.D. Moser, Cyclic strain rate effect on martensitic transformation and fatigue behaviour of an austenitic stainless steel, Fatigue & Fracture of Engineering Materials & Structures (2017).
[35] R Tremblay, P Bolduc, Neville, R.D. , Seismic testing and performance of buckling-restrained bracing systems, Canadian Journal of Civil Engineering 33(2) (2006) 183-198.
[36] C.J. Black, N. Makris, I.D. Aiken, Component Testing, Seismic Evaluation and Characterization of Buckling-Restrained Braces, Journal of Structural Engineering 130(6) (2004) p.880-894.
[37] O. BASQUIN, The exponential law of endurance tests, Proc ASTM 10 (1910).
[38] A Kulesa, A Kurek, T Agoda, et al. Low Cycle Fatigue of Steel in Strain Controlled Cyclic Bending, Acta Mechanica et Automatica, 2016, 10(1).
[39] Manson, Behavior of Materials Under Conditions of Thermal Stress, Nat. Advis. Comm. Aero. Tech 2933 (1953).
[40] C. Jr, A study of the effects of cyclic thermal stresses on a ductile metal, A Study of the Effects of Cyclic Thermal Stresses on A Ductile Metal (1953) 931-950.
[41] Z Zheng, G Cai, Z Li, et al. Interpretation of Manson-Coffin Model of Low Cycle Fatigue Based on Damage Mechanics[J]. China Mechanical Engineering, 2011, 22(7):812-814.
[42] B Huang, Q Chen, T Li. Low-cycle fatigue test of Q235 steel buckling-restrained braces, China Civil Engineering Journal, 2013,46 (6): 29-43(in Chinese)
[43] D.C.S. Simulia, Abaqus 6.11 analysis user's manual, Abaqus 6.11 Documentation (2011) 22-22.
[44] R. Milligan, W. Koo, T. Davidson, The Bauschinger Effect in a High-Strength Steel, Journal of Basic Engineering 88 (1965) 34.
[45] P.J. Armstrong, C.O. Frederick, A mathematical representation of the multiaxial Bauschinger effect. CEGB Report RD/B/N 731, Central Electricity Generating Board. the report is reproduced as a paper: 2007, Materials at High Temperatures 24(1) (1966) 1-26.
[46] Y. Jiang, P. Kurath, Characteristics of the Armstrong-Frederick type plasticity models, International Journal of Plasticity 12(3) (1996) 387-415.
[47] A. Kalnins, J. Rudolph, A. Willuweit, Using the Nonlinear Kinematic Hardening Material Model of Chaboche for Elastic-Plastic Ratcheting Analysis, Journal of Pressure Vessel Technology 137 (2015) V01BT01A005.
[48] ASME, Boiler and Pressure Vessel Code, American Society of Mechanical Engineers, New York, 2010.
[49] T. Gilman, B. Weitze, J. Rudolph, A. Willuweit, A. Kalnins, Using Nonlinear Kinematic Hardening Material Models for Elastic-Plastic Ratcheting Analysis, ASME 2015 Pressure Vessels and Piping Conference, 2015.
[50] W.F. Weitze, T.D. Gilman, Additional Guidance for Inelastic Ratcheting Analysis Using the Chaboche Model, American Society of Mechanical Engineers, Pressure Vessels and Piping Division (Publication) PVP 1 (2014).